UNIVERSITY OF OKLAHOMA

GRADUATE COLLEGE

Single-Molecule Spectroscopic Investigation of the Influence that Charge-Charge Interactions, Solvation, and Confinement Have on Guest Molecule Rotational Mobility and Photostability within Silica Sol-Gel Host Matrices

A DISSERTATION

SUBMITTED TO THE GRADUATE FACULTY

in partial fulfillment of the requirements for the

degree of

Doctor of Philosophy

By

JAMES GILLILAND
Norman, Oklahoma
2006

INFORMATION TO USERS

The quality of this reproduction is dependent upon the quality of the copy submitted. Broken or indistinct print, colored or poor quality illustrations and photographs, print bleed-through, substandard margins, and improper alignment can adversely affect reproduction.

In the unlikely event that the author did not send a complete manuscript and there are missing pages, these will be noted. Also, if unauthorized copyright material had to be removed, a note will indicate the deletion.

ProQuest Information and Learning Company
300 North Zeeb Road
P.O. Box 1346
Ann Arbor, MI 48106-1346

Single-Molecule Spectroscopic Investigation of the Influence that Charge-Charge Interactions, Solvation, and Confinement Have on Guest Molecule Rotational Mobility and Photostability within Silica Sol-Gel Host Matrices

A DISSERTATION APPROVED FOR THE
DEPARTMENT OF CHEMISTRY AND BIOCHEMISTRY

BY

_____
Dr. Paul F. Cook

_____
Dr. Roger Frech

_____
Dr. Matthew Johnson

_____
Dr. Charles V. Rice

_____
Dr. Wai Tak Yip

Acknowledgments

Now we see but a poor reflection as in a mirror; then we shall see face to face. Now I know in part; then I shall know fully, even as I am fully known.

1 Corinthians 13:12

First, I thank my wife Sandra for her love and support. Without her I would not have started graduate school. And even though she should know better, she still believes that I am the smartest physical chemist she knows.

I thank my advisor Dr. Yip for his guidance and teaching.

I thank my Graduate committee members (Dr. Cook, Dr. Frech, Dr. Johnson, Dr. Rice, and Dr. Yip) as well as Dr. Fung and Dr. Wheeler for their advice and patience over the years.

I thank my co-workers for their friendship and for enduring my compulsiveness: Becky, John, Kazushige, Natalie, Qiong, Ricardo, Tami, Tim D, and Yongyao.

I thank my friends for the fun we've had, which keeps me sane: AJ, Eric, James, Jason, Jiang Zhe, Steve, Steven, Tao, Tod, Tim C., and countless others.

I thank Carl, Dean, John, Greg, Kevin and Preston for their help in learning new skills and instrumentation.

Thank you to the OU Alumni Fellowship program, Oklahoma EPSCoR NanoNet, and GSS for their financial support.

And thanks be to God, for He is my hope in dark places.

Table of Contents

Table of Contents

Table of Contents

Table of Contents

List of Tables

List of Figures

List of Figures

List of Figures

Abstract

Silica sol-gel is an amorphous silicon oxide glass formed at room temperature using the sol-gel process. The sol-gel process consists of hydrolysis and condensation reactions, which bind the starting alkoxide monomers into a three dimensional polymer network that spans the sample volume (the solution becomes a gel, sol-gel). The random hydrolysis and condensation reactions leave behind solvent filled pores within the silica sol-gel matrix, within which guest molecules can be trapped. Silica sol-gel encapsulation has been found to stabilize both fluorescent dye molecules and enzymes; however the guest properties are strongly influenced by interactions with the heterogeneous host environment.

We have chosen to investigate guest-host interactions within silica sol-gel thin films using single molecule spectroscopy. Using single molecule fluorescence polarization, we identified the intermediate molecule mobility population, which expands our understanding beyond simple fixed and tumbling motions. Thus, intermediate molecules help reveal the guest's rich dynamic interactions with the local environment. Investigation into the influence that charge-charge interactions have on guest molecule mobility showed that anionic repulsion away from the negative silica surface has a greater influence on mobility than cationic attraction toward the surface. The limited influence of charge-charge attraction on mobility indicates that charge-charge attraction is only one among many interactions that foster dye immobilization. By controlling buffer pH, the anionic guest protonation state and charge could be altered, influencing guest mobility. Solvent equilibration was found to increase the observed fixed population, due to preferential leaching of highly mobile molecules. Solvation also

revealed the importance of guest molecule dissociation from the counter ion to achieve optimal charge-charge interaction. Guest molecule hydrogen bonding with the surface was found to reduce the influence of solvent dynamics on the guest rotational mobility and photostability. In all samples studied there remains a 20 %, or greater, population physically immobilized by molecular templating, pore collapse, or matrix incorporation.

To investigate physical immobilization further, guest behavior was monitored within the more highly branched silica nanoparticle matrix, when covalently bonded to silica nanoparticles, and within pores templated by gold nanoparticles. The silica nanoparticle environment was found to enhance mobility by increasing the intermediate population relative to the silica thin films, while covalent bonding to the silica nanoparticle surface did not significantly alter the mobility distribution relative to guests physically doped within silica nanoparticles. The guest survival lifetime increased with covalent bonding, but the photobleaching quantum yield did not change, indicating that covalent attachment does not improve photostability. In contrast, guest trapped in pores templated by gold nanoparticles showed increased survival lifetimes and decreased photobleaching quantum yields, indicating greater guest stability within the templated pores. Investigation will continue on the gold nanoparticle templated samples to reveal the role that nanoscopic confinement plays in determining guest mobility and photostability. By developing an accurate model of guest-host interactions, we hope to gain control over the interactions, guest behavior, and eventually material properties.

Chapter I

Introduction

Silica sol-gel is an amorphous silicon oxide glass formed at room temperature using the sol-gel process. The sol-gel process is a general method used to form inorganic metal oxide materials from metallic alkoxide precursors (for example, silica glass from tetraethyl orthosilicate).[1-4] While the sol-gel process is applicable to many metals, this dissertation focuses on silicon based sol-gel materials (referred to as silica sol-gel, or sol-gel silicate).

The sol-gel process consists of two steps, hydrolysis and condensation, which bind the starting alkoxide monomers into a three dimensional polymer network that spans the sample volume (the solution becomes a gel, sol-gel). To make the sol-gel, a "sol" solution is prepared by combining the alkoxide precursor, water, a co-solvent (generally an alcohol such as ethanol), and a catalyst. When combined, the alkoxide functional groups (Si-OR) are first hydrolyzed to silanol groups (Si-OH), as shown in Figure 1.1. When catalyzed by an acid, hydrolysis occurs rapidly through "a bimolecular displacement mechanism which substitutes a H^+ (hydronium ion) for an alkyl group (R)."[3] In contrast, base catalyzed hydrolysis occurs more slowly with hydroxide functioning as the attacking nucleophile in a nucleophilic substitution reaction.[3,5] The hydrolysis rate increases for each sequentially removed alkyl group, since each group that leaves increases the silicon atom positive charge and decreases the steric hindrance.[5] Condensation proceeds by silanol dehydration, simultaneously forming the silica bond and releasing water (Figure 1.1). It is worth noting that if a monomer bonds with a large

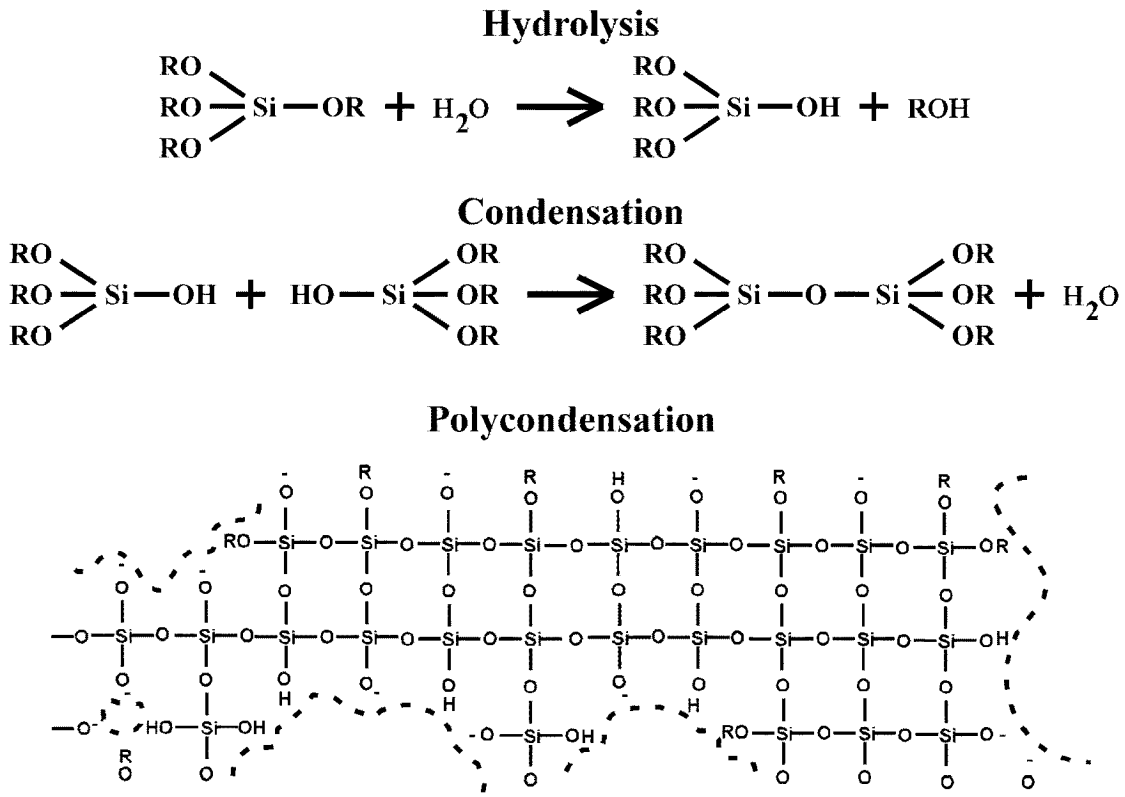

Figure 1.1. The sol-gel hydrolysis and condensation reactions are depicted above. In hydrolysis, a monomer alkoxy group is converted into a silanol, while in condensation two silanols undergo dehydration to link the monomers and release water. Repeated random condensation (polycondensation) forms a porous three dimensional silica structure.

polymer species before all alkyl groups hydrolyze, the resulting steric hindrance can prevent the remaining alkyl groups from hydrolyzing.[5]

The final silica sol-gel structure depends on the relative hydrolysis and condensation rates. These rates can be influenced by the type of catalyst, alkyl group identity, temperature, and starting reagent concentrations.[3,4] Altering these conditions changes the gelation time, the matrix structure, and the final pore size distribution. For an acid catalyst, hydrolysis is much more rapid than condensation, leading to a more linear and cross-linked network structure.[3] On the other hand, with a base catalyst, condensation is faster than hydrolysis, leading to a more highly branched structure that

favors silica nanoparticle formation.[3,6] Whether the reaction is acid or base catalyzed, random silanol group condensation leaves behind solvent filled pores of various dimensions within the silica sol-gel matrix. The final structure and properties, including the porosity, can be modified by introducing additives to the initial sol preparation. One specific type of silica sol-gel material uses organically modified silane (ORMOSIL) additives, which co-condense with the alkoxy silane for direct incorporation into the silica matrix.[1,7-19] Other additives that modify the final structure or functionality include; surfactants,[20-29] polymers,[7,12,24] charged species,[5,30,31]crown ethers,[32,33] and metal salts or alkoxides.[25,34-37]

The ease with which silica sol-gel properties can be modified is one reason for the interest in silica sol-gel as a host material. Other attractive properties include silica sol-gel's low non-linear refractive index, low strain birefringence, near zero coefficient of thermal expansion, low impurity levels, high mechanical stability, relative inertness, porosity, ability to dope with guest molecules, restricted guest translational and rotational freedom, optical clarity, and processability.[4,38-40] These properties make silica sol-gel especially attractive for optical sensor development.[41] Adding buffers to the sample preparation makes it possible to encapsulate proteins, functioning enzymes, and live cells within the silica sol-gel matrix.[34,42-49] Silica sol-gel encapsulation has been found to stabilize both fluorescent dye molecules[1,50,51] and enzymes.[47,52-56] However, dye leaching from the matrix and protein denaturation remain major concerns that slow wider application. [10,46,56] Nonetheless, optical and non-optical sensors based on silica sol-gel have been made to measure pH,[13,57-61] gases,[36,37,62-66] moisture,[31] temperature,[67] metals,[59,68-70] ions,[32,33,64,71] pharmaceutical compounds,[72,73] and glucose.[72,73] In addition,

photoconductive[24,29] and stereo selective [11,74] silica sol-gel materials have also been produced.

To optimally utilize silica sol-gel in a wide range of applications, a fuller understanding of the silica sol-gel host properties and interactions with guest molecules is necessary. While differences in preparation make it difficult to directly compare different investigations, a general description of the silica sol-gel environment can be assembled. Before gelation, the silica network is built through aggregation and cross-linking of small sub-nanometer primary particles that form in the sol solution.[75,76] After gelation, the silica network continues to evolve and develop through ongoing condensation between neighboring polymer species. Pores are left behind in the silica matrix due to incomplete hydrolysis and condensation, within which guest molecules can be trapped. While full incorporation directly within the silica host matrix is possible, guests primarily reside within the pores in non-ORMOSIL silica sol-gel materials.[77] Four

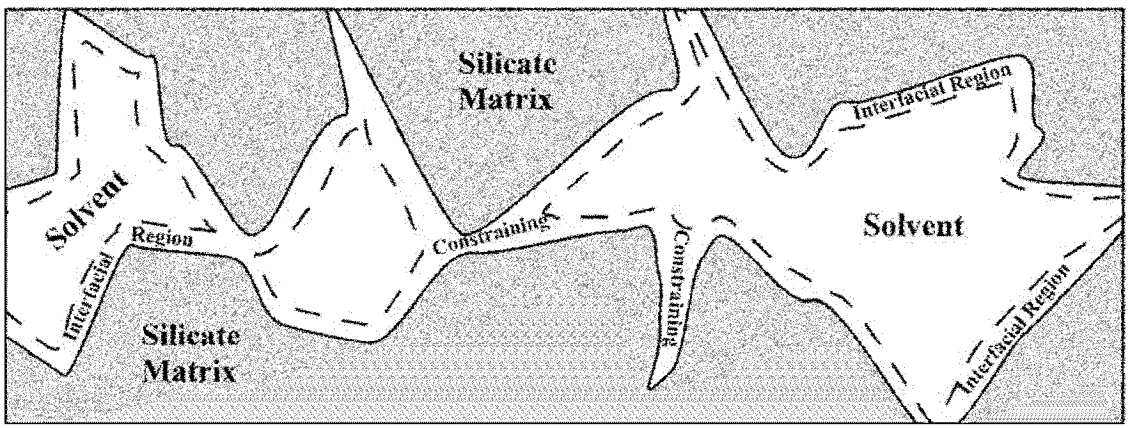

Figure 1.2. Diagram of the four pore guest environments. There is the pore surface, which defines the pore and on which guest can adsorb. The pore interior is filled with solvent that behaves as if it were unconfined bulk solvent. The interfacial region comprises the surface to solvent transition zone where the surface still influences behavior. Finally, the constraining regions are areas where the pore walls are separated by a distance comparable to the guest molecule dimensions. (Figure based on Dunn, B.; Zink, J. I. *Chem. Mater.* **1997**, *9*, 2280.)

primary pore regions have been identified as potential environments experienced by guest molecules (Figure 1.2), they are; (i) the pore surface, (ii) solvent within the pore, (iii) interface zone between the solvent and surface, (iv) constrained areas with dimensions comparable to the guest molecule.[4] Gradual solvent evaporation as the sol-gel ages and dries leads to pore collapse as the supporting solvent is removed.[4,78] Thus the pore size will vary depending on the sample age. The sol-gel can be densified through high temperature treatment to provide pores between 1.5 – 10 nm in diameter,[39] but many groups forego densification to protect trapped guest molecules. Within the silica sol-gel, external solvent and small molecules are able to diffuse through the interconnected pores to interact with the trapped guest, making silica sol-gel materials ideal for sensing applications.[57,79-82] However, there remains a small guest population trapped within pores that are inaccessible to external reagents.[47,57]

Confinement within small pores alters the confined molecule's behavior. Time-resolved measurements indicate slowed solvation dynamics near pore surfaces and reduced diffusion rates for confined molecules.[82-85] In addition, guest molecule studies typically display bi-exponential anisotropy decays, which are often interpreted as free and hindered rotation.[15,16,27,86] Since the pore environment is heterogeneous, the need for multiple decay components to describe the guest rotational behavior is not surprising. Much of the information describing the silica sol-gel environment comes from bulk techniques that measure the average response; however the average response does not necessarily reflect the guest environment accurately in a heterogeneous matrix. Take for example a study using Nile Red to investigate ORMOSIL polarity.[17] Since Nile Red fluorescence decreases with increased polarity, the average fluorescence measured was

biased toward the less polar (more fluorescent) population, while the most common (less fluorescent) population was more polar than the average.[17] Given the silica sol-gel structural and environmental complexity, it is unlikely that a full description of the environment can be obtained through bulk techniques alone.

Single molecule spectroscopy reveals details unattainable by bulk techniques, because single molecule spectroscopy removes the bulk averaging effect.[87-89] Since a single molecule can exist in only one state at a time, the individual response for each molecule is known and can be combined with the response from other molecules to reveal the distribution of responses in the system.[87-89] Single molecule spectroscopy also removes the need to synchronize molecular behavior,[89] reveals spatial and temporal dynamic response fluctuations,[87,88] permits direct comparison to theoretical calculations,[88] and obtains information from a local environment point source probe.[87] For these reasons we chose to investigate individual molecule rotational mobilities using single molecule spectroscopy. By monitoring the guest mobility at a single-molecule level, we can identify how guest-host interactions influence the mobility distribution. Single molecule measurements also allow us to directly correlate molecule behavior and properties. By developing an accurate model of guest-host interactions, we hope to gain control over those interactions, guest behavior, and material properties.

Chapter I References

(1) Yariv, E.; Schultheiss, S.; Saraidarov, T.; Reisfeld, R. *Opt. Mater.* **2001**, *16*, 29.
(2) Dulebohn, J. I.; Haefner, S. C.; Berglund, K. A.; Dunbar, K. R. *Chem. Mater.* **1992**, *4*, 506.
(3) Gallagher, D.; Ring, T. A. *Chimia* **1989**, *43*, 298.
(4) Dunn, B.; Zink, J. I. *Chem. Mater.* **1997**, *9*, 2280.
(5) Van Blaaderen, A.; Kentgens, A. P. M. *J. Non-Cryst. Solids* **1992**, *149*, 161.
(6) Stöber, W.; Fink, A.; Bohn, E. *J. Colloid Interface Sci.* **1968**, *26*, 62.
(7) Keeling-Tucker, T.; Brennan, J. D. *Chem. Mater.* **2001**, *13*, 3331.
(8) Lobnik, A.; Wolfbeis, O. S. *J. Sol-Gel Sci. Technol.* **2001**, *20*, 303.
(9) Walcarius, A.; Delacote, C. *Chem. Mater.* **2003**, *15*, 4181.
(10) Tapec, R.; Zhao, X. J. J.; Tan, W. H. *J. Nanosci. Nanotechnol.* **2002**, *2*, 405.
(11) Fireman-Shoresh, S.; Avnir, D.; Marx, S. *Chem. Mater.* **2003**, *15*, 3607.
(12) Baker, G. A.; Pandey, S.; Maziarz, E. P., III; Bright, F. V. *J. Sol-Gel Sci. Technol.* **1999**, *15*, 37.
(13) Gulcev, M. D.; Goring, G. L. G.; Rakic, M.; Brennan, J. D. *Anal. Chim. Acta* **2002**, *457*, 47.
(14) De Matteis, F.; Prosposito, P.; Sarcinelli, F.; Casalboni, M.; Pizzoferrato, R.; Furlani, A.; Russo, M. V.; Vannucci, A.; Varasi, M. *J. Non-Cryst. Solids* **1999**, *245*, 15.
(15) del Monte, F.; Ferrer, M. L.; Levy, D. *J. Mater. Chem.* **2001**, *11*, 1745.
(16) Ferrer, M. L.; del Monte, F.; Levy, D. *J. Phys. Chem. B* **2001**, *105*, 11076.
(17) Higgins, D. A.; Collinson, M. M.; Saroja, G.; Bardo, A. M. *Chem. Mater.* **2002**, *14*, 3734.
(18) Yariv, E.; Reisfeld, R. *Opt. Mater.* **1999**, *13*, 49.
(19) Zayat, M.; Levy, D. *J. Mater. Chem.* **2003**, *13*, 727.
(20) Lu, Y. F.; Ganguli, R.; Drewien, C. A.; Anderson, M. T.; Brinker, C. J.; Gong, W. L.; Guo, Y. X.; Soyez, H.; Dunn, B.; Huang, M. H.; Zink, J. I. *Nature* **1997**, *389*, 364.
(21) Garcia, J. A. M.; Valverde, G.; Zink, J. I. *Langmuir* **2003**, *19*, 4411.
(22) Minoofar, P.; Hernandez, R.; Franville, A. C.; Chia, S. Y.; Dunn, B.; Zink, J. I. *J. Sol-Gel Sci. Technol.* **2003**, *26*, 571.
(23) Yokoi, T.; Yoshitake, H.; Tatsumi, T. *Chem. Mater.* **2003**, *15*, 4536.
(24) Garcia, M. J.; Valverde, G.; Cruz, D.; Franco, A.; Zink, J. I.; Minoofar, P. *J. Phys. Chem. B* **2003**, *107*, 2249.
(25) Minoofar, P. N.; Dunn, B. S.; Zink, J. I. *J. Am. Chem. Soc.* **2005**, *127*, 2656.
(26) Chakrabarty, D.; Hazra, P.; Chakraborty, A.; Sarkar, N. *J. Phys. Chem. B* **2003**, *107*, 13643.
(27) Sahu, K.; Roy, D.; Mondal, S. K.; Halder, A.; Bhattacharyya, K. *J. Phys. Chem. B* **2004**, *108*, 11971.
(28) Huang, M. H.; Dunn, B. S.; Soyez, H.; Zink, J. I. *Langmuir* **1998**, *14*, 7331.
(29) Valverde, G.; Garcia Macedo, J.; Cruz, D.; Zink, J. I.; Hernandez, R. *J. Sol-Gel Sci. Technol.* **2003**, *26*, 605.
(30) Shibata, S.; Taniguchi, T.; Yano, T.; Yamane, M. *J. Sol-Gel Sci. Technol.* **1997**, *10*, 263.

(31) Tao, S.; Winstead, C. B.; Singh, J. P.; Jindal, R. *Opt. Lett.* **2002**, *27*, 1382.
(32) Kimura, K.; Sunagawa, T.; Yokoyama, M. *Anal. Chem.* **1997**, *69*, 2379.
(33) Kimura, K.; Sunagawa, T.; Yajima, S.; Miyake, S.; Yokoyama, M. *Anal. Chem.* **1998**, *70*, 4309.
(34) Tang, Y.; Dave, B. C. *Adv. Mater.* **1998**, *10*, 1536.
(35) Yanagi, H.; Hishiki, T.; Tobitani, T.; Otomo, A.; Mashiko, S. *Chem. Phys. Lett.* **1998**, *292*, 332.
(36) McDonagh, C. M.; Shields, A. M.; McEvoy, A. K.; Maccraith, B. D.; Gouin, J. F. *J. Sol-Gel Sci. Technol.* **1998**, *13*, 207.
(37) MacCraith, B. D.; McDonagh, C. M.; O'Keeffe, G.; Keyes, E. T.; Vos, J. G.; O'Kelly, B.; McGilp, J. F. *Analyst* **1993**, *118*, 385.
(38) Reisfeld, R.; Yariv, E.; Minti, H. *Opt. Mater.* **1997**, *8*, 31.
(39) Avnir, D.; Levy, D.; Reisfeld, R. *J. Phys. Chem.* **1984**, *88*, 5956.
(40) Casalboni, M.; DeMatteis, F.; Francini, R.; Prosposito, P.; Senesi, R.; Grassano, U. M.; Pizzoferrato, R.; Gnappi, G.; Montenero, A. *J. Lumines.* **1997**, *72-4*, 475.
(41) MacCraith, B. D.; McDonagh, C.; McEvoy, A. K.; Butler, T.; Okeeffe, G.; Murphy, V. *J. Sol-Gel Sci. Technol.* **1997**, *8*, 1053.
(42) Ellerby, L. M.; Nishida, C. R.; Nishida, F.; Yamanaka, S. A.; Dunn, B.; Valentine, J. S.; Zink, J. I. *Science* **1992**, *255*, 1113.
(43) Gill, I. *Chem. Mater.* **2001**, *13*, 3404.
(44) Smith, K.; Silvernail, N. J.; Rodgers, K. R.; Elgren, T. E.; Castro, M.; Parker, R. M. *J. Am. Chem. Soc.* **2002**, *124*, 4247.
(45) Chia, S. Y.; Urano, J.; Tamanoi, F.; Dunn, B.; Zink, J. I. *J. Am. Chem. Soc.* **2000**, *122*, 6488.
(46) Zheng, L.; Flora, K.; Brennan, J. D. *Chem. Mater.* **1998**, *10*, 3974.
(47) Zheng, L.; Brennan, J. D. *Analyst* **1998**, *123*, 1735.
(48) Dave, B. C.; Miller, J. M.; Dunn, B.; Valentine, J. S.; Zink, J. I. *J. Sol-Gel Sci. Technol.* **1997**, *8*, 629.
(49) Edmiston, P. L.; Wambolt, C. L.; Smith, M. K.; Saavedra, S. S. *J. Colloid Interface Sci.* **1994**, *163*, 395.
(50) Mei, E.; Bardo, A. M.; Collinson, M. M.; Higgins, D. A. *J. Phys. Chem. B* **2000**, *104*, 9973.
(51) Rahn, M. D.; King, T. A.; Gorman, A. A.; Hamblett, I. *Appl. Optics* **1997**, *36*, 5862.
(52) Lloyd, C. R.; Eyring, E. M. *Langmuir* **2000**, *16*, 9092.
(53) Lan, E. H.; Dave, B. C.; Fukuto, J. M.; Dunn, B.; Zink, J. I.; Valentine, J. S. *J. Mater. Chem.* **1999**, *9*, 45.
(54) Chen, J.-P.; Wang, H.-Y. *Biotechnol. Tech.* **1998**, *12*, 851.
(55) Badjic, J. D.; Kostic, N. M. *Chem. Mater.* **1999**, *11*, 3671.
(56) Nguyen, D. T.; Smit, M.; Dunn, B.; Zink, J. I. *Chem. Mater.* **2002**, *14*, 4300.
(57) Villegas, M. A.; Pascual, L. *J. Mater. Sci.* **2000**, *35*, 4615.
(58) Ben-David, O.; Shafir, E.; Gilath, I.; Prior, Y.; Avnir, D. *Chem. Mater.* **1997**, *9*, 2255.
(59) Yang, L.; Saavedra, S. S. *Anal. Chem.* **1995**, *67*, 1307.
(60) Lee, J. E.; Saavedra, S. S. *Anal. Chim. Acta* **1994**, *285*, 265.
(61) Kowada, Y.; Ozeki, T.; Minami, T. *J. Sol-Gel Sci. Technol.* **2005**, *33*, 175.

(62) von Bueltzingsloewen, C.; McEvoy, A. K.; McDonagh, C.; MacCraith, B. D.; Klimant, I.; Krause, C.; Wolfbeis, O. S. *Analyst* **2002**, *127*, 1478.
(63) Bailey, R. T.; Cruickshank, F. R.; Deans, G.; Gillanders, R. N.; Tedford, M. C. *Anal. Chim. Acta* **2003**, *487*, 101.
(64) Collinson, M. M.; Howells, A. R. *Anal. Chem.* **2000**, *72*, 702A.
(65) Onida, B.; Borello, L.; Fiorilli, S.; Bonelli, B.; Arean, C. O.; Garrone, E. *Chem. Commun.* **2004**, 2496.
(66) Shahriari, M. R.; Ding, J. *Opt. Lett.* **1994**, *19*, 1085.
(67) Liebsch, G.; Klimant, I.; Wolfbeis, O. S. *Adv. Mater.* **1999**, *11*, 1296.
(68) Yeh, T.-C.; Tien, P.; Chau, L.-K. *Appl. Spectrosc.* **2001**, *55*, 1320.
(69) Jeronimo, P. C. A.; Araujo, A. N.; Montenegro, M. C. B. S. M.; Satinsky, D.; Solich, P. *Anal. Chim. Acta* **2004**, *504*, 235.
(70) Stozhko, N. Y.; Morosanova, E. I.; Kolyadina, L. I.; Azarova, Z. M. *Journal of Anaytical Chemistry (Translation of Zhurnal Analiticheskoi Khimii)* **2004**, *59*, 865.
(71) Kim, W.; Chung, S.; Park, S. B.; Lee, S. C.; Kim, C. *Anal. Chem.* **1997**, *69*, 95.
(72) Wen-xu, L.; Jian, C. *Anal. Chem.* **2003**, *75*, 1458.
(73) Wu, X.; Choi, M. M. F.; Xiao, D. *Analyst* **2000**, *125*, 157.
(74) Fireman-Shoresh, S.; Popov, I.; Avnir, D.; Marx, S. *J. Am. Chem. Soc.* **2005**, *127*, 2650.
(75) Geddes, C. D.; Karolin, J.; Birch, D. J. S. *J. Phys. Chem. B* **2002**, *106*, 3835.
(76) Birch, D. J. S.; Geddes, C. D. *Phys. Rev. E: Stat. Phys., Plasmas, Fluids, Relat. Interdiscip. Top.* **2000**, *62*, 2977.
(77) Suratwala, T.; Gardlund, Z.; Davidson, K.; Uhlmann, D. R.; Watson, J.; Bonilla, S.; Peyghambarian, N. *Chem. Mater.* **1998**, *10*, 199.
(78) Narang, U.; Wang, R.; Prasad, P. N.; Bright, F. V. *J. Phys. Chem.* **1994**, *98*, 17.
(79) McKiernan, J.; Simoni, E.; Dunn, B.; Zink, J. I. *J. Phys. Chem.* **1994**, *98*, 1006.
(80) Hellriegel, C.; Kirstein, J.; Braeuchle, C.; Latour, V.; Pigot, T.; Olivier, R.; Lacombe, S.; Brown, R.; Guieu, V.; Payrastre, C.; Izquierdo, A.; Mocho, P. *J. Phys. Chem. B* **2004**, *108*, 14699.
(81) Kanungo, M.; Collinson, M. M. *Langmuir* **2005**, *21*, 827.
(82) Koone, N. D.; Zerda, T. W. *J. Sol-Gel Sci. Technol.* **1997**, *8*, 883.
(83) Loughnane, B. J.; Farrer, R. A.; Fourkas, J. T. *J. Phys. Chem. B* **1998**, *102*, 5409.
(84) Loughnane, B. J.; Farrer, R. A.; Scodinu, A.; Reilly, T.; Fourkas, J. T. *J. Phys. Chem. B* **2000**, *104*, 5421.
(85) Koone, N.; Shao, Y.; Zerda, T. W. *J. Phys. Chem.* **1995**, *99*, 16976.
(86) Baumann, R.; Ferrante, C.; Kneuper, E.; Deeg, F.-W.; Braeuchle, C. *J. Phys. Chem. A* **2003**, *107*, 2422.
(87) Orrit, M. *J. Chem. Phys.* **2002**, *117*, 10938.
(88) Jung, Y.; Barkai, E.; Silbey, R. J. *J. Chem. Phys.* **2002**, *117*, 10980.
(89) Moerner, W. E.; Orrit, M. *Science* **1999**, *283*, 1670.

Chapter II

Experimental: Preparation, Instrumentation, Skills, and Analysis

2.1 CHAPTER ABSTRACT

This chapter details the experimental techniques and processes that make the subsequent investigations possible. The preparation procedures for acid hydrolyzed TEOS and TMOS thin films as well as base hydrolyzed silica nanoparticles are presented. My success in constructing our second single molecule confocal instrument is documented, as well as modifications made to both instruments to better support our testing needs. Many of the instrument modifications involved computer control program changes in Labview©. I was also responsible for developing and revising our Visual Basic© data analysis programs that operate in Excel©. Recent revisions have simplified program use while saving time and decreasing the saved file size. My research also required me to gain familiarity with AFM and TEM techniques in order to characterize our samples.

2.2 INTRODUCTION

While each project has unique background and preparation, there are common threads that run throughout the investigations. This chapter enumerates the common techniques and instrumentation background for later reports. Coming into a new lab I had the opportunity to perform significant laboratory and instrumentation setup, including the planning and assembly of our second instrument. While not new and exciting discoveries, these details elaborate the processes that went on behind the scenes and they form the foundation on which the final results rest. This chapter is organized into three main sections: silica sol-gel sample preparation and identification (2.3),

instrumentation (2.4), and data analysis (2.5). Some techniques and skills that I have acquired over the past five years are mentioned, but this cannot be considered an exhaustive list of all I have learned. Much of my effort was focused on building our second confocal instrument, and updating our equipment and programs to better fit our needs.

2.3 SAMPLE PREPARATION

2.3.1 Materials

99.9+% Tetraethyl orthosilicate (TEOS), spectrophotometric grade 95% ethanol, 85 wt% phosphoric acid, citric acid, hydrogen tetrachloroaurate (III) trihydrate, sodium citrate, sodium cyanide, 2-[4-(2-Hydroxyethyl)-1-piperazine]ethanesulfonic acid (HEPES), tetramethylrhodamine-5-isothiocyanate (TRITC), Nile Red (NR), and sulforhodamine B 75% (SRB), were purchased from Sigma-Aldrich or Fisher Scientific. Didodecyl-3,3,3',3'-tetramethylindo-carbocyanine ($DiIC_{12}$), Oregon Green 514 (ORG) and rhodamine 6G (R6G) were purchased from Molecular Probes. 100% ethanol was purchased from AAPER. All chemicals were used without further purification. TEOS

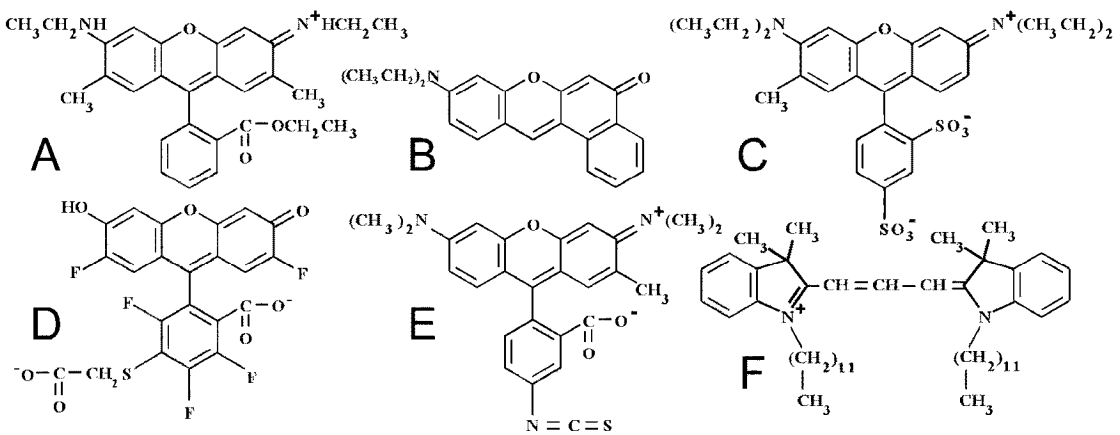

Figure 2.1. The laser dye molecules used to probe the silica sol-gel matrix are shown above. They are A: rhodamine 6G, B: Nile Red, C: sulforhodamine B, D: Oregon Green 514, E: tetramethylrhodamine-5-isothiocyanate, and F. didodecyl-3,3,3',3'-tetramethylindo- carbocyanine.

hydrolysis was catalyzed by a 1 to 100 v/v phosphoric acid dilution in double distilled water. All aqueous reagents, buffers, and sample preparations were prepared using either double distilled or deionized water. Microscope cover glasses, Fisher Premium Grade purchased from Fisher Scientific, were thoroughly cleaned by consecutive sonication in 10% sodium hydroxide, distilled water, acetone, and deionized water before use. The cleaned coverslips showed no fluorescent impurity response under normal testing conditions. Phosphate, citrate, and HEPES buffer stock solutions were prepared to provide a wide pH range. All buffers were diluted to 50 mM concentration before us.

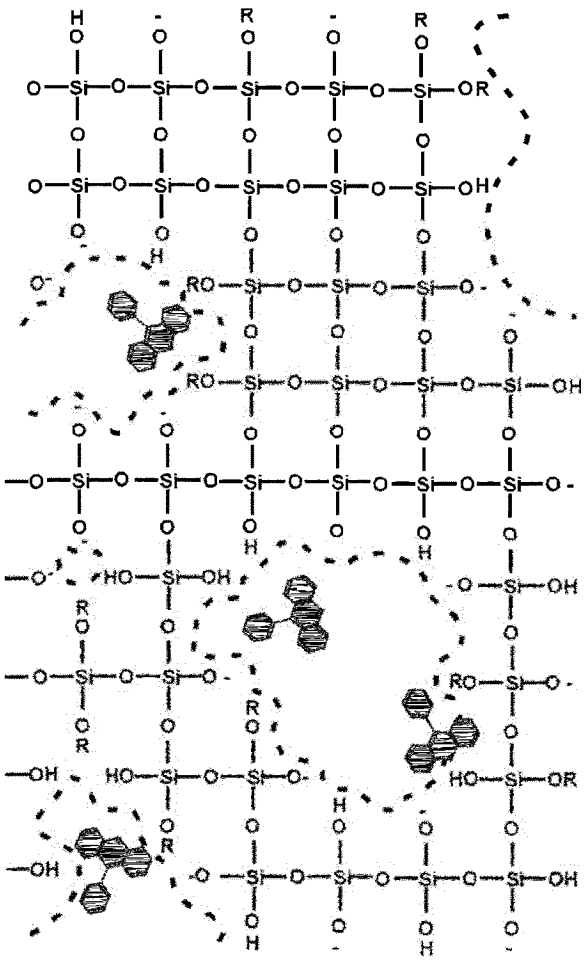

Figure 2.2. By including the probe molecules in the sol solution, they become entrapped within the silica pores as the matrix forms. Thus providing more information about the silica sol-gel environment, than that obtained by dye which diffuses into already formed pores.

The R6G, SRB, NR, ORG, TRITC, and $DiIC_{12}$ probe molecules (Figure 2.1) were selected for their high fluorescence quantum yields and photostability. As shown in Figure 2.2, the guest molecules are assumed to reside within the solvent filled silica sol-gel pores left behind after the sample matrix has solidified. Since each probe has the possibility to experience unique silica sol-gel matrix interactions, many

studies must be performed to help elucidate the interactions occurring between the guest molecule and host matrix.

2.3.2 Silica Sol-Gel Thin Films

Since the sol-gel process was described in detail in Chapter 1 (Figure 1.1) the silica sol-gel hydrolysis and condensation reactions will not be repeated here. All TEOS thin film samples were prepared using the procedure outlined below. An acid hydrolyzed TEOS sol solution (8.8 wt% SiO_2) was prepared to provide a 1:8:7 molar ratio TEOS:ethanol:water solution. It was prepared by combining 1.95 µL 1/100 v/v phosphoric acid dilution, 100.0 µL double distilled water, 357.1 µL 95% ethanol, and 176.35 µL TEOS. These volumes were calculated using the liquid densities and assuming that the other 5% solution of the 95% ethanol was water. This procedure can be used with other organically modified silane precursors by replacing the TEOS volume with the appropriate silane volume indicated in Table 2.1. Not all the organically modified silanes were found to gel under these conditions. Thus, a combination of TEOS and the organically modified silane may be required for the solution to gel.

Table 2.1. Listed below are the silane volumes required to maintain the 1:8:7 sol-gel preparation ratios for TEOS and organically modified triethoxy silanes (TES).

Silane	Volume
TEOS	176.35 µL
Methyl-TES	158.04 µL
Propyl-TES	184.35 µL
Pentyl-TES	208.23 µL
Phenyl-TES	193.13 µL

To facilitate hydrolysis, and minimize condensation, the sol solution was sonicated for 2 hours at 0 °C (ice bath) to ensure a single phase. Single molecule samples were prepared by doping the sol solution after sonication to between 1.7-8.5 nM final dye concentration. Thus 352.1 µL ethanol was added before sonication, and the additional ~5

μL ethanol added as the solvent for the dye after sonication to bring the total ethanol volume to 357.1 μL.[1] The exact dye concentration used was determined empirically, based on film fluorescence imaging and testing conditions. Solvent equilibrated films often required a higher initial dye concentration to counter solvent quenching or dye leaching. "Bulk" concentration ORG silica sol-gel films used in Chapter 5 for pH testing had a 34 nM final ORG concentration.

Regardless of the final dye concentration, the dye-doped sol solution was allowed to age at ambient temperature in the dark for 16-20 hours before it was spun cast onto a cleaned coverslip at 6100 rpm for 70 seconds. These conditions resulted in a 203 ± 15 nm thick film as determined by Atomic Force Microscopy (AFM), Figure 2.3. Film step edges were formed by selectively removing the film from the coverslip support with a

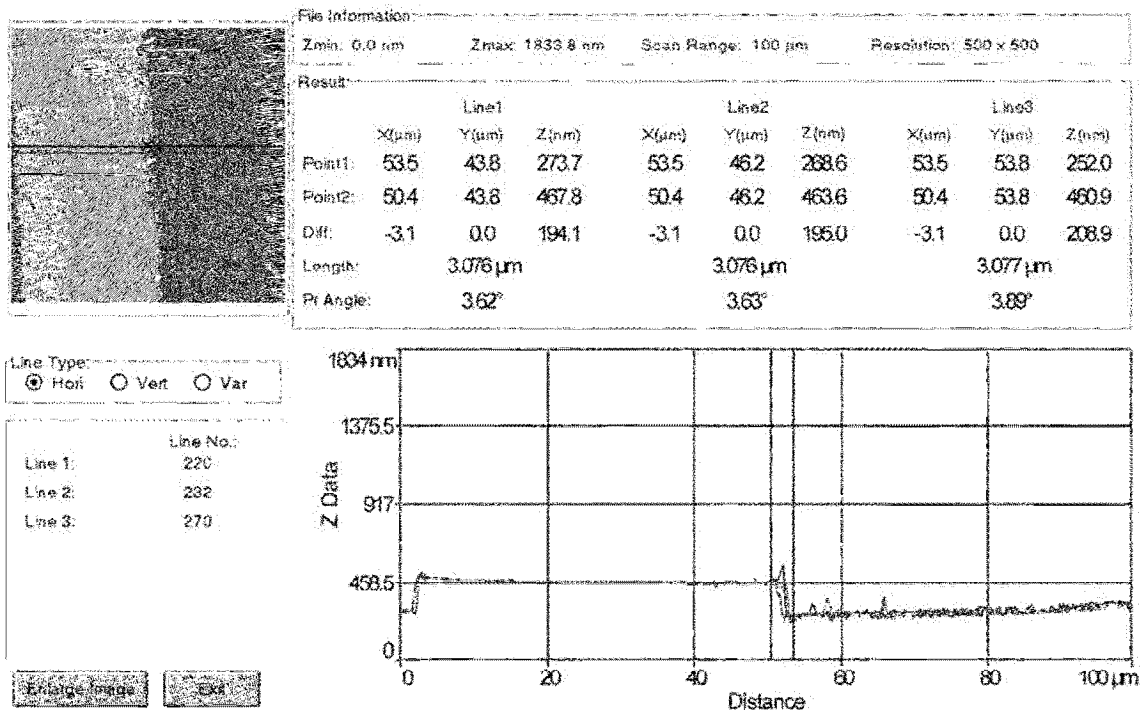

Figure 2.3. Sol-gel film thickness was measured by AFM. The film was mechanically removed from the coverslip support and the resulting step edge imaged to determine the film height. The spin coating procedure provided a 203 ± 15 nm thick sample.

fresh razor blade. The coverslip was then blown clean with nitrogen to remove loose film fragments and imaged by AFM. The height difference between the smooth film and coverslip surface was used to estimate the film thickness. Films soaked in water did not vary significantly from this thickness after drying, indicating that the films remained stable when soaked in water.

2.3.3 Thin Film Sample Identification

Dry films prepared for analysis and tested on the same day they were spin-cast were considered fresh films, while films tested the next day, after the film aged overnight in the dark, were considered one day old samples (day one, or d1). Fresh film fluorescence images often contained signal streaking, indicating continued active dye translational motion within the films.[2,3] Allowing the films to age an additional day reduced streaking, improved the image quality, and increased the percentage of molecules successfully relocated to the laser focus for subsequent fluorescence testing. For these reasons, day one films were preferred. However, testing was also performed on fresh films to characterize the change in mobility with aging.

To test sample behavior when equilibrated with a solvent, samples were attached to a cuvette section with epoxy and the cuvette filled with the test solvent. Since ethanol was found to dissolve the epoxy, vacuum grease was instead used to seal the ethanol samples. Samples not exposed to a liquid during testing were considered dry films, while samples exposed to a liquid reference the liquid contained in the cuvette. Samples designated as "wet" indicate equilibration with water. Silica sol-gel films were examined while equilibrated with water, ethanol, different pH buffers, and solutions containing sodium cyanide. The buffer pHs were selected to promote conditions favorable to guest-

host repulsion as a method to control guest-host interactions. Although it has been reported that extensive flushing with concentrated phosphate buffers promotes silica dissolution in chromatography columns,[4-6] our current procedure uses low phosphate concentrations, low organic solvent content, limited buffer volume, and a static equilibration, instead of dynamic flushing. This is expected to minimize the phosphate impact on our silicate films.[4-6] The sample films were left for at least 30 minutes (and more typically 2-3 hours) to ensure thermal equilibrium and film solvation before testing.

2.3.4 Dip-coated Thin Films

Silica thin films were also formed using the dip-coating technique (Figure 2.4).[7-10] In this technique an extended coverslip (6 cm) is placed within a large reservoir containing the liquid sol solution. The coverslip is then withdrawn (vibration and draft free) from the sol reservoir at a constant rate. The sol surface tension and solvent evaporation rapidly form and age the thin silica sol-gel film formed on the withdrawn coverslip. The vibration free withdrawal can be accomplished with a vibration free motor, or by harnessing the smooth downward force provided by a float resting on top of an emptying water column. I assembled a dip-coating apparatus based on the water column

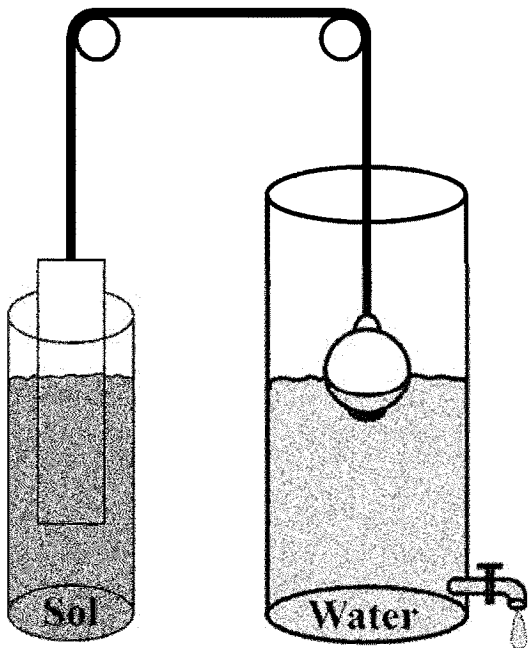

Figure 2.4. Dipcoating apparatus showing a coverslip in the sol solution reservoir on the left side of the figure. The coverslip is connected by ribbon to the float resting on top of the emptying water column on the right. The dipcoating withdrawal rate is thus determined by the rate that the water is drained out of the water column.

arrangement with the intention to compare the spin and dip-coated film environments. However, I was unable to optimize the dip-coating parameters to obtain satisfactorily reproducible films. I especially struggled with the need to isolate the apparatus from drafts, and identifying an appropriate ribbon material to connect the float and coverslip without binding on the guide rods.

2.3.5 Silica Nanoparticles

The silica sol-gel internal structure depends on the relative rates of two processes, the rates of hydrolysis and condensation. If the hydrolysis rate is fast while the condensation rate is slow, there will be a silanol functional group abundance available to condense with the growing sol-gel polymer.[11,12] The slow condensation rate would favor adjacent hydroxyl group bonding in the structure, producing a denser, more ordered network.[11,12] Spin or dip-coating this solution leads to a continuous smooth silica thin film, with the procedure described in Section 2.3.2. On the other extreme, if the condensation rate is much faster than the hydrolysis rate, highly branched silica nanoparticles (SNP) result.[11,12] Since the silanol condensation proceeds more rapidly, when hydrolysis does occur, the silanol formed reacts with the first free silanol encountered, leading to a silica sol-gel polymer that grows randomly in all directions.[12] Dip-coating a SNP solution leads to an ordered SNP layer on the substrate with voids between the particles.[13] The change in sol-gel structure is illustrated in Figure 2.5 for the sol (top row) to gel (bottom row) transition as the hydrolysis and condensation rates are altered by pH (horizontal axis).

Our investigation focused on the change in probe behavior within the phosphoric acid hydrolyzed silica sol-gel thin films and the ammonium hydroxide catalyzed SNP

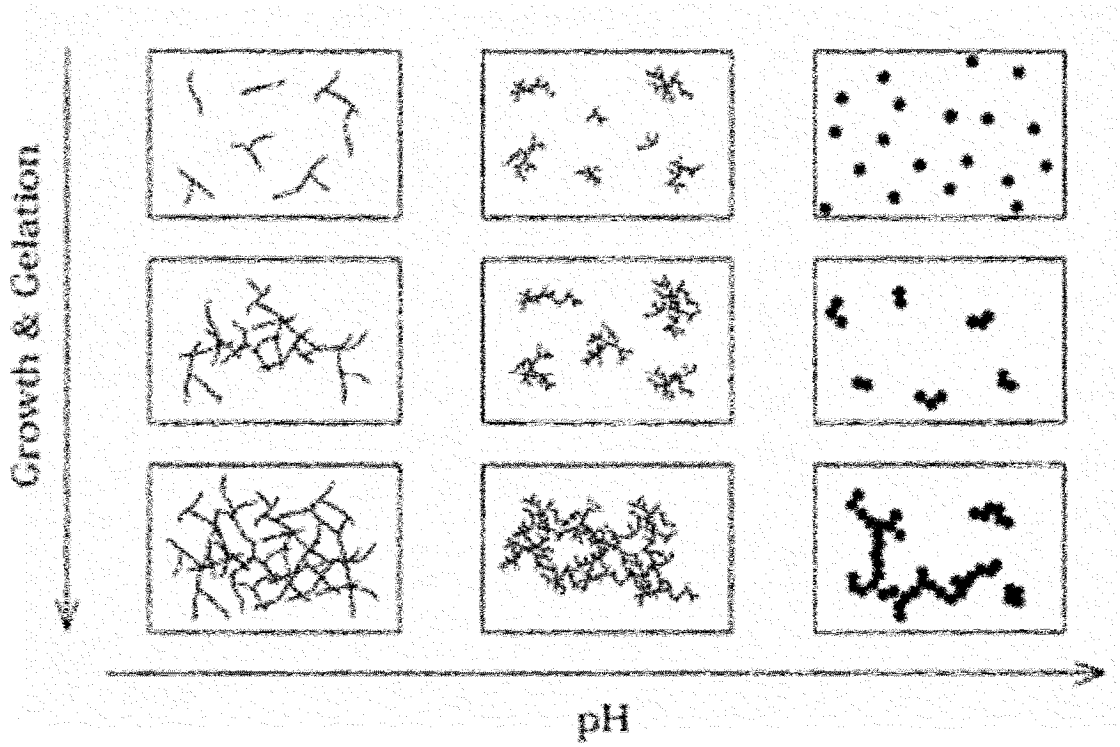

Figure 2.5. The final sol-gel structure depends on the silane concentration and the reaction rates of both hydrolysis and condensation. While at low pH ranges a more ordered three dimensional cross linked network is formed, at high pH ranges aggregates and nanoparticles are preferentially formed. (figure taken from Gallagher,D.; Ring, T. A. *Chimia* **1989**, *43*, 298-304)

environments. For this investigation I collaborated with Dr. Becky Abraham, who prepared the SNP samples based on the Stöber method,[14] while I prepared the related thin film samples. I also prepared and tested the TRITC in SNP samples after her departure. The SNP were prepared by initially combining 50 μL 30% NH_4OH, 490 μL 100% EtOH, and 10 μL dye dissolved in 100% EtOH. To this was added 35 μL TEOS, which was immediately vortexed and sonicated for 20 minutes at room temperature. After sonication, the SNP growth was halted by the addition of acetone (500 μL). At this stage the particles were approximately 250 nm in diameter. Smaller or larger particles can be obtained by altering the condensation (sonication) time. The SNP were then centrifuge settled, and the liquid decanted off. They were rinsed once with EtOH and six to ten

times with acetone, centrifuging between each rinse, to remove the excess free dye remaining in the reaction solution. After rinsing, the SNP were suspended in 100 μL EtOH for storage and testing. The SNP hydrolysis rate is dependent on the reaction water content. Thus the water present in the 95% EtOH, or the addition of dye dissolved in water, accelerates the SNP growth rate and leads to larger nanoparticles.[15] EtOH suspended SNP were spotted on to a clean coverslip, and the SNP samples were tested as described in Section 2.4 after the EtOH evaporated. Figure 2.6 illustrates the correlation between the observed dye fluorescence emission and the SNP physical location. By

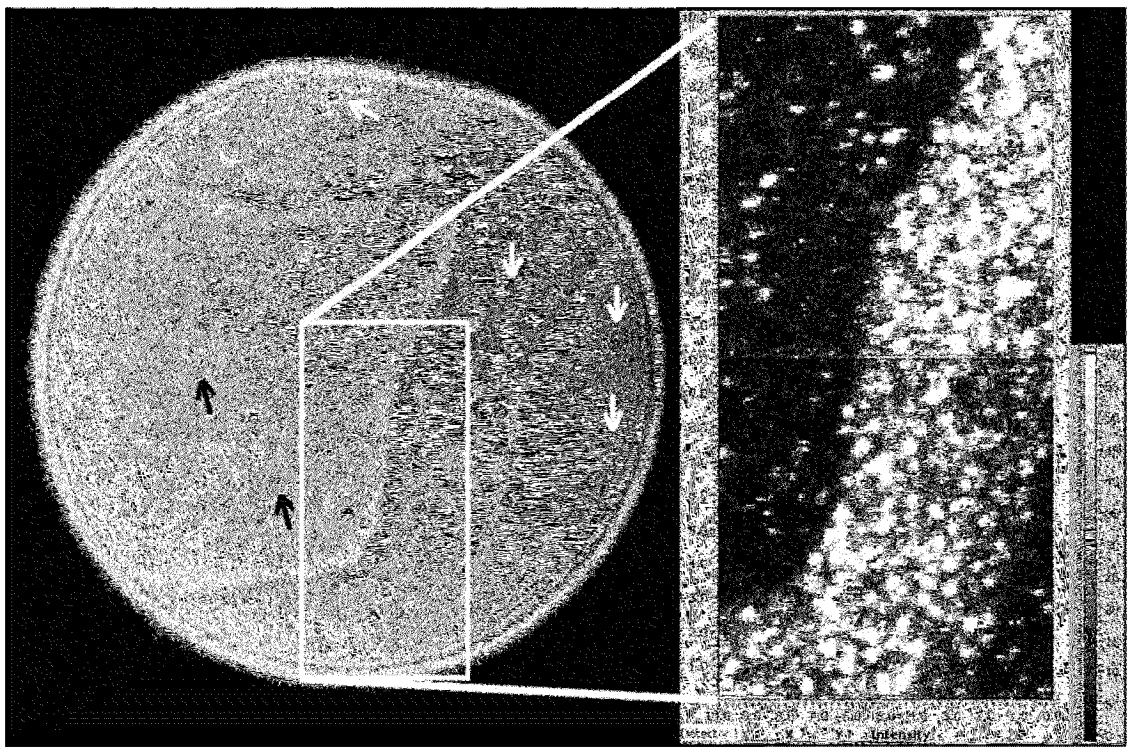

Figure 2.6. At 200 nm diameter the SNP are on the border of being optically resolvable. On the left is a transmission image showing SNP that have aggregated into larger optically resolvable structures during solvent evaporation. The black arrows indicate individual SNP that appear as fuzzy grey spots. The white arrows indicate optical system abrasions that appear as sharp white rimmed circles. On the right, two (10 μm × 10 μm) fluorescence emission images have been combined to illustrate the correlation between sample fluorescence emission and dye doped SNP location.

adjusting the dye concentration to obtain one entrapped dye for every 10-100 SNP, single molecule spectroscopy can be performed on isolated dye molecules within the SNP aggregate structures. Some SNP samples were modified to covalently attach TRITC to the silica matrix through aminopropylsilane (APS) incorporation. Dr. Abraham prepared the SNP covalently bound samples which are discussed further in Chapter 7. Entrapped and covalently bonded dye comparison should expand our understanding of dye rotational freedom and stability within the silica sol-gel pores.

2.3.6 TMOS Samples

Like TEOS, Tetramethyl orthosilicate (TMOS) can also be used to form silica sol-gel. The TMOS silica sol-gels formed demonstrate increased biomolecule compatibility relative to the TEOS based sol-gels. Termed biogels, the TMOS preparation involves addition of protein or enzyme containing buffer to a sol solution to accelerate the condensation reaction and stabilize the entrapped biomolecule.[16-19] Biogel thin films are often prepared by dip-coating to eliminate the harsh spincoating centrifugal stress on biomolecules. During my first year, I worked to prepare TMOS encapsulated horseradish peroxidase (HRP) thin films for single chemiluminescent molecule enzyme detection. To form the TMOS sol solution 562.5 μL TMOS, 120.0 μL double distilled water, and 11.25 μL 0.01 M HCl were combined, vortexed and sonicated for 20 minutes. To 20 μL of the TMOS sol solution, 20 μL polyvinyl alcohol and 80 μL 0.1 M HRP in 50 mM TRIS-HCl pH 8.0 buffer were added. A thin film was formed by rolling 40 μL of the sol-gel solution on top the coverslip to provide even coverage. The sol-gel gelation rate is determined by the buffer concentration and volume added to the sol solution.

Due to a number of factors, I was unable to obtain single HRP results and decided to instead focus on the TEOS thin film projects. During the TMOS work I did observe a green product that forms only when the HRP, luminal (substrate), and peroxide were combined and the chemiluminescent solution added to the TMOS sol solution. However, the product evaded identification.

2.4 INSTRUMENTATION

Single molecule spectroscopy has been made possible through recent improvements in detector sensitivity, laser excitation intensity, and the ability to reproducibly control movements with nanometer precision. These improvements, combined with high laser dye fluorescence quantum yields, have made single molecule detection and testing possible. This section focuses on our single molecule confocal microscope instrument and the work performed in constructing it.

2.4.1 Instrumentation Set-up

For reference, a simplified confocal laser microscope diagram is provided in Figure 2.7. The instrument itself was assembled on an optical table that rests on four nitrogen gas filled pneumatic pistons that suspend the table on a gas cushion, causing it to float. This minimized vibrational disturbances that would otherwise destabilize optical alignment. To perform laser spectroscopy, confocal or otherwise, a laser excitation source is required. Each instrument was constructed to permit use of either a helium-neon or an air cooled argon-ion laser excitation source (Figure 2.7 left side). The helium-neon laser provides 543.5 nm excitation, while the argon-ion laser provides 514 nm, 488 nm, and 457 nm excitation wavelengths, as well as several other minor wavelengths not currently used. The helium-neon source was used to excite $DiIC_{12}$, SRB, and NR, while

the 514 nm argon-ion line was used for R6G, and TRITC. ORG was excited with the 488 nm argon-ion laser line. Argon-ion wavelength isolation was obtained by spatially filtering the laser through a prism and blocking the undesired wavelengths from continuing along the beampath with an adjustable aperture (not pictured).

The excitation light was passed through ½- and ¼- waveplates, as needed, to ensure that the excitation light was circularly polarized. Circularly polarized excitation was used to guarantee that the final polarization distribution was not biased by preferential excitation of molecular dipoles aligned with a linear excitation source. Neutral density optical filters were used to adjust the excitation power before it was

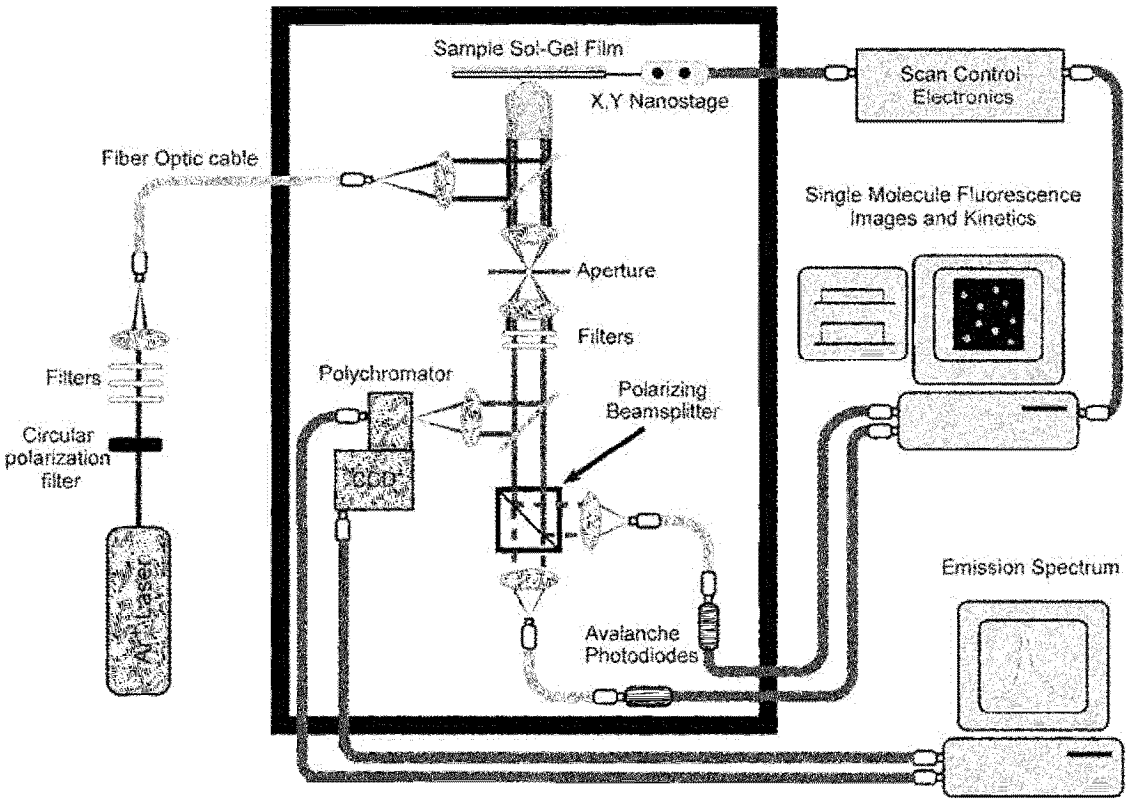

Figure 2.7. Above is a simplified diagram for the confocal laser microscope arrangement used to test single fluorescent molecules. The fiber optic and other cables pass through the black plexiglass box that isolates the sample, microscope, CCD camera, and detectors from stray light, connecting the laser source and computer controls to the interior positioning and detection systems.

coupled into a single-mode optical fiber by a 10× objective for transfer into the "black box". The optical fiber also served as a 3.3 μm diameter spatial filter. The sample and detection systems are isolated from room light to prevent false signals. Initially this was accomplished with black plasticboard, which is a corrugated black plastic version of cardboard. However, this did not adequately seal the instrument from external light sources. Therefore my earliest modification to the system was constructing a black plexiglass and aluminum rail light sealed box. The box constructed for the second instrument was sufficiently sealed to permit testing under normal room lighting without a detectible increase in the background. However, to reduce the risk of overloading the detectors, sample testing continued to be performed in the dark.

After transfer into the box, the laser was collimated by a 10× objective and directed into the epi-illumination port of an inverted microscope (Nikon, TE-200 or TE-300). Inside the microscope the laser passed through an interference filter, and was reflected up to a 100× microscope objective (Nikon, CFI Achromat oil immersion lens 1.25 N.A.) by a dichroic beamsplitter (Chroma Technology). Power within the focused laser spot was varied according to the testing conditions and dye to obtain suitable signal intensity and dye survival lifetime for each investigation. The laser power was varied by adjusting the laser focus into the initial coupler or placing neutral density filters in the beampath. Since the microscope optics and optical fiber can alter the laser polarization, the ½- and ¼- waveplates were adjusted to provide circularly polarized light at the sample stage.

The sample coated coverslip was placed on a nano-positioning stage containing positional feedback electronics (Melles Griot "NanoBlock," or Queensgate "NPS-XY-

100A") mounted at the microscope objective focal plane. For instrument 2 this was accomplished by custom mounting the Queensgate nanostage to the inverted microscope via a ¼ inch thick aluminum plate platform machined personally to permit the objective to pass through both the mount and nanostage. The nanostages facilitate raster scanning to image the molecule location, as well as molecule relocation to the objective focal point for fluorescence testing. Sample fluorescence was collected by the same 100× objective, passed through the dichroic beamsplitter, and directed out the microscope side port through a 100 μm aperture positioned at the first image plane. Fluorescence diverging from the aperture was then collimated by an achromatic lens and passed through a notch filter (Kaiser Optical Systems) and/or long-pass filter (Omega Optical, ALPHA Technology) to eliminate residual laser excitation and scattered light before it was directed to a polarizing beamsplitter cube. The beamsplitter cube resolved the fluorescence into two orthogonally polarized components which we arbitrarily designated as parallel ($I_{//}(t)$) and perpendicular ($I_{\perp}(t)$). Two achromatic lenses coupled the polarization resolved fluorescence into multimode optical fibers for simultaneous detection by two separate avalanche photodiode (APD) detectors (Perkin Elmer, SPCM-AQR).

To collect sample fluorescence spectra, or images, the beampath could be switched so that the collimated light was focused through an achromatic lens onto a CCD camera for imaging. To collect sample fluorescence spectra (instrument 1) the achromatic lens focused the sample fluorescence onto a polychromator connected to a CCD array (Acton, SpectraPro 150 and Roper Scientific, SpectruMM). Instrument 2 was built to permit wide area total internal refraction (TIR) excitation and imaging (Figure

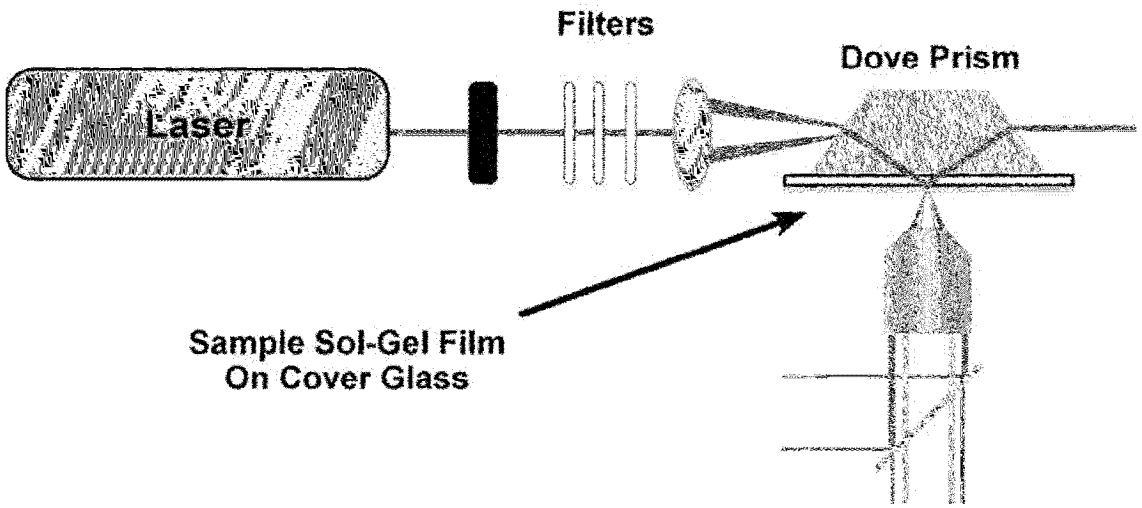

Figure 2.8. Instrument 2 was constructed to permit wide area sample excitation using total internal refraction. Rather than reflecting off the dichroic beamsplitter, the excitation light was focused through a dove prism that refracts the excitation off the sol-gel air interface above the microscope objective. The fluorescence then follows the path illustrated in Figure 2.7. Since a wide area is excited the entire area can be imaged simultaneously using a CCD camera, rather than the single location monitored by an APD.

2.8). Rather than coupling the laser into the fiber optic cable for transfer into the box and through the microscope, the TIR arrangement passed the laser through a small hole in the box and directed it through a dove prism mounted above the microscope objective. The sample coated coverslip was mounted sol-gel side down on the dove prism bottom with immersion oil. The achromatic lens and beampath position were adjusted to focus the prism refracted beam directly over the microscope objective which imaged the sample fluorescence. While Dr. Abraham and I were successful in setting up the TIR optics, the CCD camera was not sufficiently sensitive to image single molecule fluorescence emission.

2.4.2 Labview© Programming

Both instrument 1 and 2 have their nanostage position and APD detector signals controlled through custom written Labview© virtual instrument interfaces (Figure 2.9). Since the nanostages were from different suppliers, and the detectors used different

detector-computer interface cards, each instrument required unique programming solutions to function correctly. Instrument 1 was built around a Melles Griot x-, y-, z-axis piezoelectric nanostage that combines manual course and regional adjustment controls with a digital controller, which enabled micrometer to nanometer adjustment. The digital controller permits adjustment directly through the controller, or indirectly through the Labview© software interface. Instrument 2 was built with an x-, y- axis Queensgate piezoelectric system which was accessed solely through the computer

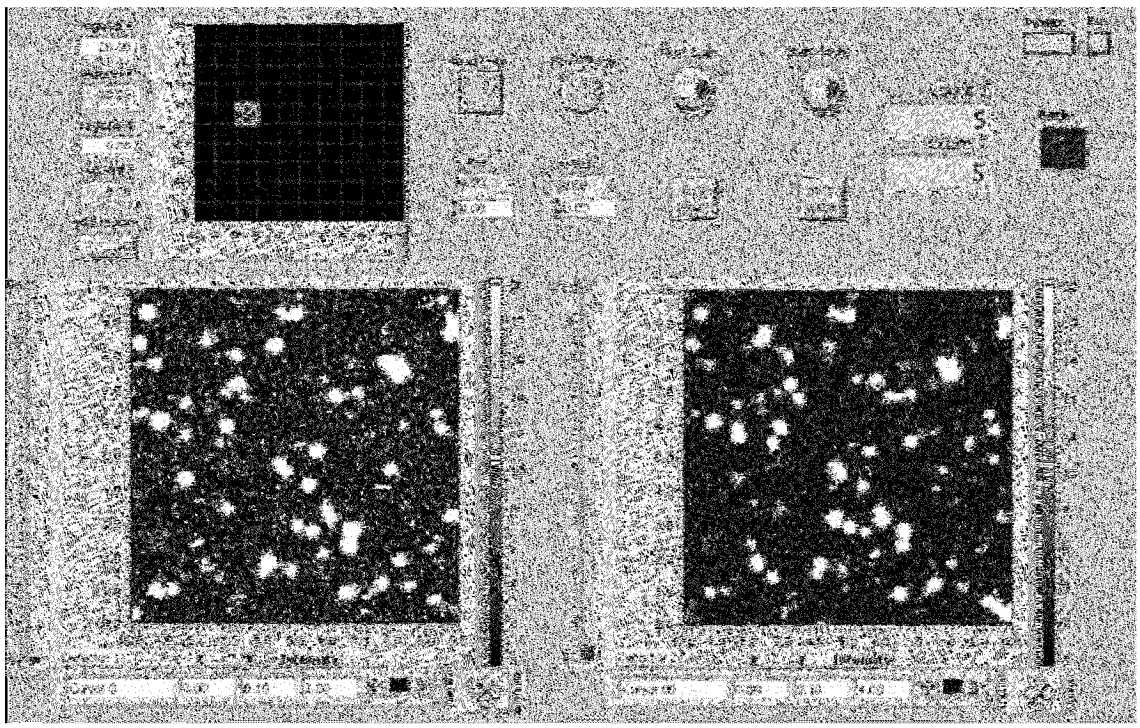

Figure 2.9. The instrument 2 Labview© virtual instrument interface in is shown above. The interface controls both the nanostage position and collects the orthogonal detector signals. An X-Y raster scan over a 10 × 10 μm area (start scan control) constructs a fluorescence intensity image for each detector. These images were used to identify the dye molecule position for relocation to the laser focus (move stage control) to record a fluorescence intensity time trace (Start count control). Since the nanostage position for this instrument is entirely computer controlled, the overall regional stage position is determined by the X, Y regional position and goto region controls. This absolute position permits assembling images to construct a larger image, as well as correlation of sample response to optically visible sol-gel structures.

addressed controller, preventing manual adjustment (except for non-reproducible physical coverslip relocation). The Queensgate stage provides 10 nm position precision within its 120 μm × 120 μm range. Thus the Labview© interface had to be written from scratch to accommodate the changes in nanostage, detectors, and to select the regional sample area (Figure 2.9).

The second virtual instrument control interface accomplished this through regional position controls that selected a 10 μm × 10 μm area within the 120 μm × 120 μm stage range (Figure 2.9 goto region controls). That 10 μm × 10 μm selected area was raster scanned in 100 nm step increments (100 × 100 pixels) and the two fluorescence polarized images (one for each detector) displayed (Figure 2.9 start scan control). The dye location was determined from the fluorescence spot maximum, and the molecule relocated to the objective focal point for further testing (Figure 2.9 move stage control). The molecule fluorescence was accumulated every 50 ms and displayed in real time before it was saved (Figure 2.9 start count control). The greatest interface programming difficulty was discovering how to initialize communication between the computer and Queensgate controller, since the provided protocols did not function properly. Since assembly, the second instrument has logged over 1600 hours of use.

2.5 DATA ANALYSIS

2.5.1 Molecule Classification

The single molecule mobility was determined by calculating its emission polarization ($P(t)$) according to Equation 2.1. The statistical $P(t)$ average ($\overline{P}$) was also

$$P(t) = \frac{GI_{//}(t) - I_{\perp}(t)}{GI_{//}(t) + I_{\perp}(t)} \qquad \textbf{2.1}$$

calculated to aid mobility classification. Since APD detectors have different sensitivities and optical component birefringence, isotropic emission from a moderately concentrated dye solution was used to obtained a scaling factor (G) that was applied to $I_{//}(t)$. This correction was collected daily to correct for asymmetric response between the parallel and perpendicular detection channels, when applied it forces the isotropic dye solution $\overline{P}$ to zero. All subsequent $I_{//}(t)$ measurements for the same day included this correction factor.

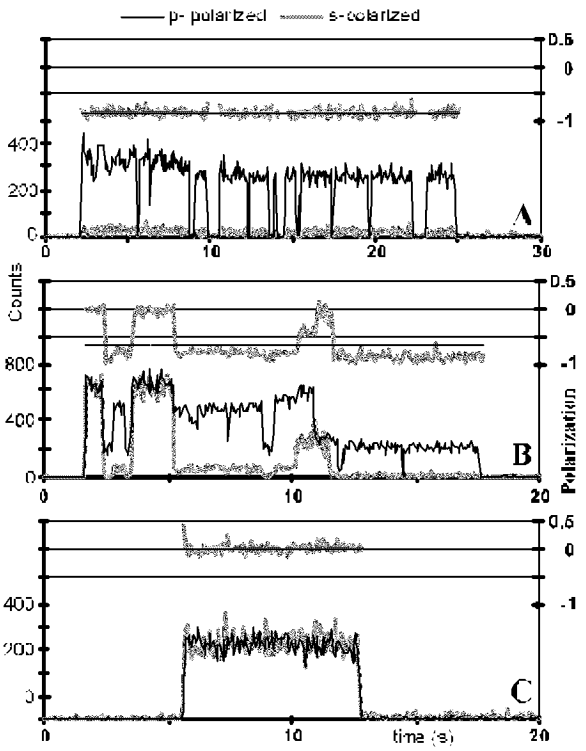

Figure 2.10. Molecule kinetic traces presenting the $I_{//}$ and $I_{\perp}$ detector signals in grey and black at the bottom of each panel. The corresponding polarization (grey) and average polarization (black line) values are shown in the top of each panel. A: Displays a fixed molecule trace, B: an intermediate molecule, and C: a freely tumbling molecule.

In addition to the scaling factor, the $\overline{P}$ standard deviation (σ_{iso}) from the dye solution was also used as a $\overline{P}$ single molecule uncertainty reference. Thus, a molecule will be designated as 'tumbling' if its $\overline{P}$ is within $\pm\,\sigma_{iso}$ of zero polarization (Figure 2.10 C). On the other hand, $\overline{P}$ for an immobilized molecule can range from -1 to 1, depending on its orientation. As a result, a molecule is designated as a 'fixed' molecule if its $|\overline{P}|$ is greater than σ_{iso} (Figure 2.10 A). If a molecule changes its orientation, a regional $\overline{P}$ change

during measurement, it will be assigned as an 'intermediate' molecule (Figure 2.10 B). It is worth noting that our classification scheme is unable to differentiate between a tumbling molecule and a fixed molecule aligned 45° to the parallel and perpendicular axes. Consequently, the uncorrected tumbling molecule percentage reported should be treated as an upper limit.

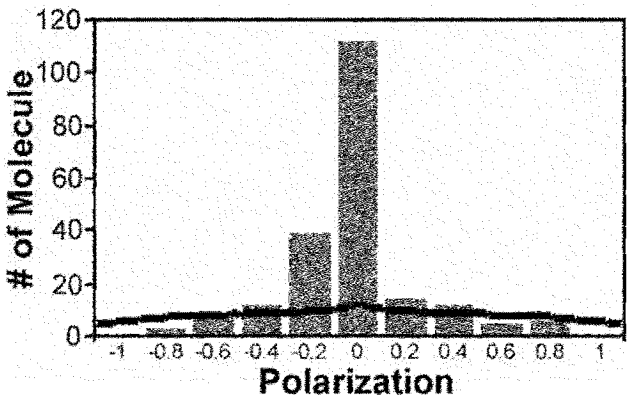

Figure 2.11. A $DiIC_{12}$ $\overline{P}$ histogram. The black line shows the Equation 2.3 theoretical fit based on a randomly oriented fixed molecule set. Due to high numerical aperture effects a fixed molecule set will contain a small population with zero polarization. The higher than theoretical zero polarization population observed indicated a high tumbling or intermediate molecule population in the actual sample.

2.5.2 High Numerical Aperture Correction

The tumbling classification uncertainty can be partly alleviated by statistical modeling to estimate the population incorrectly assigned due to fixed molecule orientation alignment and the high numerical aperture (N.A.) microscope objective depolarization effect.[20] In Figure 2.11, we present the $\overline{P}$ distribution determined for 212 $DiIC_{12}$ molecules. Due to the high N.A. depolarization effect, a randomly oriented

$$I_{ll} = I_{tot}\left(K_1 x^2 + K_2 y^2 + K_3 z^2\right) \quad \textbf{2.2a}$$

$$I_{\perp} = I_{tot}\left(K_2 x^2 + K_1 y^2 + K_3 z^2\right) \quad \textbf{2.2b}$$

$$K_1 = \tfrac{3}{32}\left(5 - 3\cos\theta_{obj} - \cos^2\theta_{obj} - \cos^3\theta_{obj}\right) \quad \textbf{2.2c}$$

$$K_2 = \tfrac{1}{32}\left(1 - 3\cos\theta_{obj} + \cos^2\theta_{obj} - \cos^3\theta_{obj}\right) \quad \textbf{2.2d}$$

$$K_3 = \tfrac{1}{8}\left(2 - 3\cos\theta_{obj} + \cos^3\theta_{obj}\right) \quad \textbf{2.2e}$$

$$\text{N.A.} = n\sin\theta_{obj} \quad \textbf{2.2f}$$

emission dipole with component (x, y, z) will contribute to I_{ll} and $I_{\perp}$ according to Equations 2.2a and 2.2b.[20,21] Where the objective optical axis is parallel to the z-axis, I_{tot} is the total emission intensity, n is the immersion oil index of refraction , and K_1, K_2, K_3 and N.A. are defined in Equations 2.2 c-f. Substituting I_{ll} and $I_{\perp}$ in Equation 2.1 with Equation 2.2a and 2.2b gives the emission dipole polarization expression shown in Equation 2.3. When the N.A. is low, $K_1 >> K_2$ and K_3, and Equation 2.3 reduces directly back to Equation 2.1. When the N.A. is high, K_2 and K_3 are no longer negligible and the

$$P = \frac{(K_1 - K_2)(x^2 - y^2)}{(K_1 + K_2)(x^2 + y^2) + 2K_3 z^2} \qquad \textbf{2.3}$$

dipole polarization distribution will skew toward zero polarization, creating a peak at the distribution center, rather than the trough predicted by Equation 2.1 alone. [22] For a 1.25 N.A. oil immersion microscope objective, n = 1.52, θ_{obj} = 55.32°, K_1 = 0.2611, K_2 = 0.0025, and K_3 = 0.0597. The polarization histogram in Figure 2.11 clearly suggests that the dye $\overline{P}$ distribution did not conform to a randomly oriented fixed molecule distribution inside the sol-gel silicate film. The poor fit at zero $\overline{P}$ suggests that more molecules exhibited zero polarization than the depolarization effect alone could account for. This was a strong indication that the sample also contains tumbling or intermediate molecules in addition to fixed molecules. These molecules emit isotropic fluorescence or provide lifetime averaged zero fluorescence polarization. According to the theoretical fit to 212 molecules, there would be about 12 fixed molecules mistakenly designated as tumbling molecules. These 12 incorrectly assigned molecules have emission dipole projections on the x-y plane that make a 45° angle to the x-axis, rendering the measured polarization zero, leading to the incorrect assignment. Based on these statistics, the High

N.A. influence on mobility is corrected for by reassigning tumbling molecule population, equal to approximately 5% of the fixed molecule population, to the fixed classification. Mobilities corrected in this fashion are designated as High N.A. corrected values.

2.5.3 Error Calculation

The errors indicated for mobility classification percentages were calculated under a binomial sampling distribution assumption using Equation 2.4. The error is calculated in the number of molecules whose classification is uncertain, where p is the molecule

$$\text{Error} = (p\ q\ n)^{1/2} \qquad \textbf{2.4}^{23}$$

fraction within the classification considered, q is the molecule fraction not within that classification (1- p), and n is the total molecules sampled. As the sampling size increases a more representative sample is obtained and the error associated with non-representative sample selection decreases. Whenever possible an approximately 200 molecule, or larger, sample size was sought to reduce the sampling error.

2.5.4 Visual Basic Analysis Macros

The virtual instrument interface saved the kinetic trace information as two numeric text documents consisting of the detector values, these values required additional analysis to be usable. Data analysis was performed in Excel© via several Visual Basic© macro programs that simplify and speed the analysis process. The earliest macro version was programmed by C. Ricardo Viteri to accommodate molecule orientation determination using the signal ratio from the two detectors. Since then I modified the program to use the polarization equation as well as many other revisions. The current version decreased data analysis time by a factor of ten, reduced the manual input required, and saved the files five times smaller than early versions. The main analysis

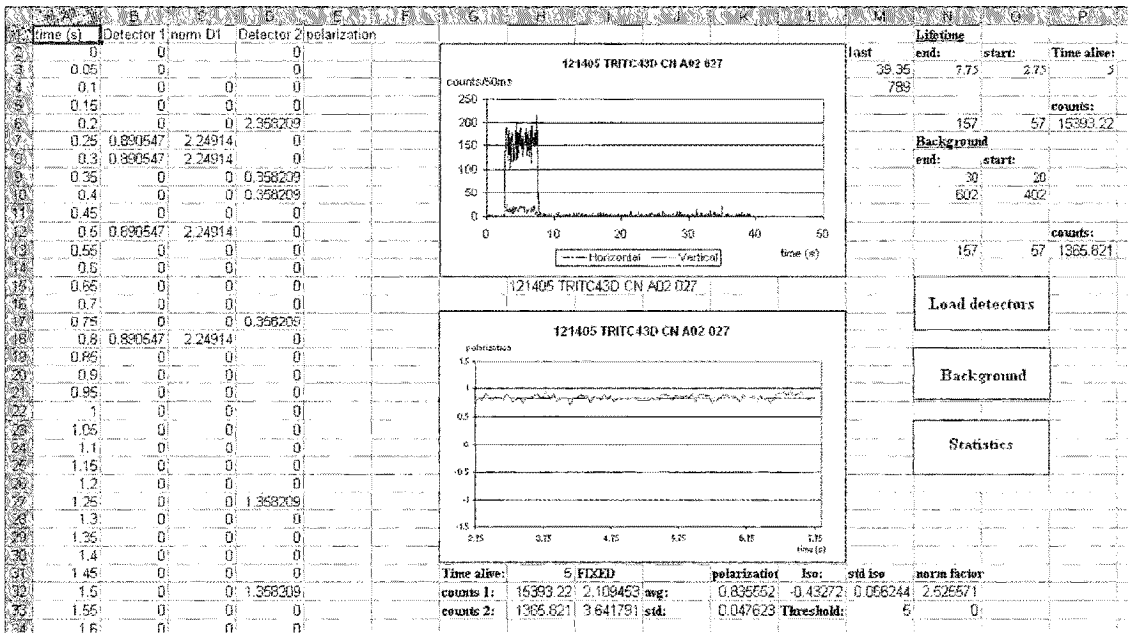

Figure 2.12. The Excel© facilitated kinetic trace data analysis workspace using Visual Basic© programmed macros. Each rectangular button in column N/O executes a programmed command series that loads, calculates, or modifies the data for numerical and graphical interpretation.

workspace is shown in Figure 2.12. The rectangular buttons that span columns N and O (load detectors, background, and statistics) were connected to Visual Basic© executable macro programs. The load detector button, for example, extracted the file name for molecule identification, extracted the detector values, added the experiment time, graphed the data relative to time, named the graphs, applied a correction factor (section 2.5.2), and located the final data point for use by other macros. While the programmed steps could be done manually, the macros greatly sped the process and reduced repetitive user actions. The other macros on the page, based on user input, subtracted a background value from the detector signals; calculated the average polarization value, the total counts, the time alive, and the polarization standard deviation; and graphed the incremental polarization over the selected molecule lifetime range. Other macro

programs collect the molecule information for printing or property histogram analysis. The primary polarization analysis program is included in Appendix C for reference.

2.6 TEM

Chapter 9 will further explain our use of gold nanoparticles to template the sol-gel pore size. Here I would like to mention the Transmission Electron Microscopy (TEM) characterization that accompanied this experiment. Before pores with a known size can be templated by the gold nanoparticles, the gold nanoparticle size must be determined. Since gold absorbs electrons well, the gold nanoparticles provide good TEM image contrast despite their small diameter. Gold nanoparticle sample images were acquired (JOEL 2000-FX) on film or by electronic detector and the images converted to electronic data files, Figure 2.13. From those files nanoparticle size and distribution profiles were

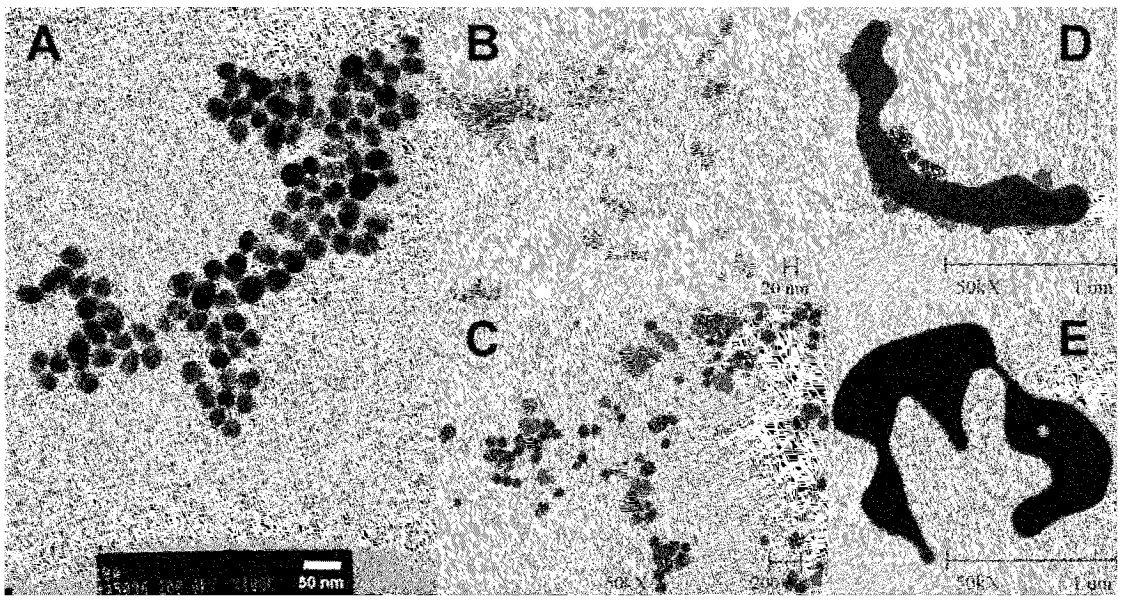

Figure 2.13. Gold nanoparticles were imaged via transmission electron microscopy. A: and B: show well behaved nanoparticle samples with diameters approximately 30 and 14 nm. Larger nanoparticles become less regular as they grow. C: shows gold triangles and other shapes that made some samples unsuitable for pore templating. Continued nanoparticle growth can lead to intriguing abstract, but unusable, micron sized particles (D and E).

compiled by manual pixel count, or Adobe Photoshop© plugin manipulation. The presence of multiple size distribution peaks in some samples indicated multiple nanoparticle nucleation stages that would increase the templated pore size uncertainty. Figure 2.13 A and B show well behaved gold nanoparticle samples, where the distribution is fairly homogeneous. As the particles grow larger (A ~30 nm, B ~14 nm) they tend to become less regular in shape. Samples unsuitable for our purposes contained gold triangles, Figure 2.13 C, or other irregular particle shapes that would complicate sample analysis, Figure 2.13 D and E. Significant gold nanoparticle preparation and characterization was required before pore templating could begin.

2.7 CONCLUSION

The experimental procedures and skills presented here represent aspects common to the sample preparation and testing reported in the following chapters. This chapter documented the foundational work that makes these subsequent analyses possible. It included the work I performed in setting up our second confocal instrument, as well as my efforts to improve the data analysis process. AFM and TEM sample characterization also served to expand my knowledge and skills to other microscopy techniques.

Chapter II References

(1) Depending on the dye volume used the additional ethanol needed to make-up the 5 uL was not necessarily added. This was done to reduce the risk of sample contamination due to repeated container opening and pipette tip contact.

(2) Hou, Y.; Higgins, D. A. *J. Phys. Chem. B* **2002**, *106*, 10306.

(3) Higgins, D. A.; Collinson, M. M.; Saroja, G.; Bardo, A. M. *Chem. Mater.* **2002**, *14*, 3734.

(4) Kirkland, J. J.; Henderson, J. W.; DeStefano, J. J.; van Straten, M. A.; Claessens, H. A. *J. Chromatogr., A* **1997**, *762*, 97.

(5) Tindall, G. W.; Perry, R. L. *J. Chromatogr., A* **2003**, *988*, 309.

(6) Claessens, H. A.; van Straten, M. A.; Kirkland, J. J. *J. Chromatogr., A* **1996**, *728*, 259.

(7) Huang, M. H.; Soyez, H. M.; Dunn, B. S.; Zink, J. I. *Chem. Mater.* **2000**, *12*, 231.

(8) Lu, Y. F.; Ganguli, R.; Drewien, C. A.; Anderson, M. T.; Brinker, C. J.; Gong, W. L.; Guo, Y. X.; Soyez, H.; Dunn, B.; Huang, M. H.; Zink, J. I. *Nature* **1997**, *389*, 364.

(9) Nishida, F.; McKiernan, J. M.; Dunn, B.; Zink, J. I.; Brinker, C. J.; Hurd, A. J. *J. Am. Ceram. Soc.* **1995**, *78*, 1640.

(10) Huang, M. H.; Dunn, B. S.; Soyez, H.; Zink, J. I. *Langmuir* **1998**, *14*, 7331.

(11) Leite, C. A. P.; de Souza, E. F.; Galembeck, F. *J. Braz. Chem. Soc.* **2001**, *12*, 519.

(12) Gallagher, D.; Ring, T. A. *Chimia* **1989**, *43*, 298.

(13) Iskandar, F.; Abdullah, M.; Yoden, H.; Okuyama, K. *J. Sol-Gel Sci. Technol.* **2004**, *29*, 41.

(14) Stoeber, W.; Fink, A.; Bohn, E. *J. Colloid and Interface Sci.* **1968**, *26*, 62.

(15) Park, S. K.; Do Kim, K.; Kim, H. T. *Colloid Surf. A-Physicochem. Eng. Asp.* **2002**, *197*, 7.

(16) Diaz, A. N.; Peinado, M. C. R.; Minguez, M. C. T. *Anal. Chim. Acta* **1998**, *363*, 221.

(17) Ellerby, L. M.; Nishida, C. R.; Nishida, F.; Yamanaka, S. A.; Dunn, B.; Valentine, J. S.; Zink, J. I. *Science* **1992**, *255*, 1113.

(18) Smith, K.; Silvernail, N. J.; Rodgers, K. R.; Elgren, T. E.; Castro, M.; Parker, R. M. *J. Am. Chem. Soc.* **2002**, *124*, 4247.

(19) Chen, J.-P.; Wang, H.-Y. *Biotechnol. Tech.* **1998**, *12*, 851.

(20) Ha, T.; Laurence, T. A.; Chemla, D. S.; Weiss, S. *J. Phys. Chem. B* **1999**, *103*, 6839.

(21) Axelrod, D. *Biophys. J.* **1979**, *26*, 557.

(22) Garcia-Parajo, M. F.; Koopman, M.; Van Dijk, E. M. H. P.; Subramaniam, V.; Van Hulst, N. F. *Proc. Natl. Acad. Sci. U.S.A.* **2001**, *98*, 14392.

(23) Parratt, L. G. *Probability and Experimental Errors in Science: An Elementary Survey*; John Wiley and Sons: New York, 1961.

Chapter III

Guest-Host Charge-Charge Interactions within Silica Sol-Gel

3.1 CHAPTER ABSTRACT

Our results indicate that long-range coulombic interactions influence guest rotational mobility to a measured extent within silica sol-gel. The nanoscopic confinement imposed by the silica sol-gel matrix on a highly polarizable guest molecule may favor guest-host interactions contributed by shorter range interactions, such as van der Waals or hydrogen bonding. Alternatively, it is possible that the interaction is dominated by physical confinement due to molecular templating or collapse of the silica pore. Charge-charge repulsion between a negatively charged guest and the negatively charged silica surface increased the guest rotational mobility within the silica sol-gel. Positively charged and neutral guests displayed similar rotational mobility distributions, both of which were less mobile than that seen for the negatively charged guest. When solvated, samples show an increased charge influence on mobility due to increasing counter ion dissociation and tumbling freedom. A 24% maximum in tumbling molecules was obtained for Oregon Green 514 equilibrated with a pH 7 buffer. However, the ever present fixed molecule population likely indicates that guest molecule physical immobilization always plays a significant role in determining guest mobility. We also identified a class of molecules that change rotational mobility behavior over time. These intermediate molecules, when combined with the traditional immobilized (fixed) and freely tumbling rotational mobility classifications, help to more fully characterize the observed dye behavior.

3.2 INTRODUCTION

The sol-gel process is an attractive method for creating organic-inorganic and bio-inorganic materials from alkoxide precursors. The room temperature hydrolysis and condensation reactions permit the incorporation of various optically,[1-6] chemically,[7,8] and biologically[9-12] active guest molecules within the porous silica host matrix. The porous silica structure, combined with high optical clarity[4] and mechanical strength,[6,13] make silica sol-gel an ideal material for optical sensor applications.[7,14] Already, materials sensitive to pH,[7,15,16] solvent polarity,[17,18] guest mobility,[18-20] and various enzyme substrates[9,11,13,21] have been created through the sol-gel process, and in several cases used for quantitative measurements. Silica sol-gel host matrices have been shown to selectively stabilize encapsulated organic and biological molecules, increasing both laser dye photostability[1,22-24] and enzyme structural integrity.[14,21,25,26] However, guest molecule leaching[27] and biomolecule structural changes during sol-gel incorporation[25,28,29] continue to be ongoing concerns. The guest molecule trapped within the mesoporous sol-gel matrix is expected to experience substantial surface interaction, which directly impacts the guest molecule mobility. Differing degrees of surface interaction provide the widely varied molecular mobility behaviors that have been observed.[30-34] Such a broad molecular mobility distribution inevitably leads to diverse guest molecule physical and chemical properties, since each molecule experiences a unique local environment. To take full advantage of silica sol-gel's potential in optical systems, and reduce unwanted effects, an increased understanding about the guest molecule's interaction with the local environment is necessary.[19]

A molecule's tendency to freely diffuse in a solvent or adsorb on a surface, is the cumulative product of many interactions.[35-37] In the most general consideration, a molecule's tendency to adsorb or freely diffuse is determined by the tendency to associate with the solvent and the attraction toward the surface. A large difference in these two opposing forces leads to predominantly solvated or adsorbed molecules. While hydrophobic interactions are often assumed to be the sole force controlling adsorption behavior, other forces that contribute to adsorption include the electrical double layer effect,[37,38] electrostatic interactions,[35,36] dispersion forces,[37,38] and hydrogen bonding.[39,40] Representative methods used to investigate the extent to which these forces contribute to dye adsorption include NMR,[41-43] varying the host composition and structure,[17,22,27,44-48] additive inclusion,[6,22,23] varying the guest molecule physical attributes,[22] modifying the silicate surfaces,[49,50] or altering the solvents in contact with the sample.[16,51,52]

In attempts to reduce organic dye leaching into the solvent, as well as maximize dye incorporation, previous studies have added hydrophobic organically modified silicates to the sol-gel host.[19,21,27,47] This results in a silica sol-gel host more hydrophobic than the solvent, improving the hydrophobic organic guest retention rate. Studies have also sought to optimize biomolecule stability within silica sol-gel, typically by reducing the sol-gel alcohol content and adding buffers during the condensation stage.[9-11] These preparation changes result in an internal solvent composition less likely to denature the biomolecule during the encapsulation process. Both the organic silicate inclusion and biological buffer addition seek to influence guest properties through host environment modification. Dye diffusion rates through silica based materials have also been studied as a function of dye charge.[35,36] These tests indicate that charge attraction to the surface

increases dye adsorption and decreases the bulk diffusion rates. This exemplifies an investigation into guest interactions based on guest variation. These studies hint at trends in guest mobility that depends on guest-host electrostatic interactions; however, since they are bulk measurements, they do not necessarily reveal the range of individual interaction that are taking place.

In order to investigate the interaction range more fully it is worthwhile to consider the interactions on a molecular level, since individual molecules can exist only in a single state at any given time.[53] Studying properties in this way removes the averaging effect, allowing the static and dynamic environmental property distribution to be studied.[1,44,53-57] Single molecule studies also provide a more direct comparison between theoretical and experimental results.[56] Since the silica sol-gel internal structure and local environments are heterogeneous,[1,19,44,54] the local environment distribution will produce a range of guest-host interactions that must be accounted for in any analysis. Single molecule spectroscopy permits guest molecule grouping based on similar responses, which are subsequently analyzed under the assumption that they represent similar environments or interactions with the host.[16,18,24] Strong guest-host interaction reduces or prevents guest mobility. Using single molecule spectroscopy, we have previously demonstrated that an immobilized guest has higher photostability than its mobile counterpart.[24]

In this work we examine charge-charge interactions influence on guest molecule mobility entrapped within a silica sol-gel host matrix. Owing to the extensive structural and chemical heterogeneities found inside sol-gel silicates, we employ single molecule spectroscopy to examine how coulombic interaction is manifested at the molecular level.[1,58] We employed molecular mobility to monitor the degree to which coulombic

interaction specifically contributes to guest-host interaction. We assume that stronger guest-host interaction (Coulombic attraction) will hinder guest molecule rotational motion, whereas a weak guest-host interaction will favor freely tumbling guest molecules. To assist in this investigation individual molecules were classified as "tumbling", "fixed", and "intermediate" if they exhibited zero, non-zero, and varying emission polarization, respectively.[24,59]

It is worth noting that time-resolved fluorescence anisotropy examines pico- to nanosecond sample responses,[60-62] EPR and NMR examine micro- to millisecond responses,[41,43] while our classification scheme follows fluorescence polarization changes occurring on time scales ranging from several hundred milliseconds, to seconds, or even minutes. Our ability to determine molecular mobility at the single molecule level also helps to eliminate the guest-host interactions influence on fluorescence quantum yield that, if not corrected for, will inevitably skew an ensemble-measured mobility distribution to favor the stronger fluorescence population. Our classification scheme was selected to provide a link between our measured values and the four identified sol-gel pore environment regions (the free liquid, the interfacial region, the pore wall, and constrained regions).[18,24] Our "tumbling" classification corresponds to the free liquid, the "intermediate" classification to the liquid-pore wall interface, and the "fixed" classification includes both molecules adsorbed to the pore wall and molecules physically immobilized within a constricted region.

Two theories have been proposed to account for fixed guest molecules within these constrained regions. In the first theory, known as templating, a guest molecule promotes silica bond formation around itself acting as a template, or mold, for the final

sol-gel structure.[14,63] This is similar to the molding and casting used to produce many macroscopic objects (such as toy cars), however in this case the mold remains around the guest molecule preserving the initially templated conformation. In the second theory, a guest within a larger pore is immobilized when the supporting solvent is removed and the pore collapses.[1,15,18,20,45] In this situation the guest is constrained due to the force exerted by the pore walls that have collapsed around it. This force is believed to deform some guests away from their initial conformation. Regardless of the process that forms the constricted region, the observed result is a reduction in guest molecule motion.

3.3 RESULTS AND DISCUSSION

3.3.1 Dry Sol-Gel Films

3.3.1.1 Day One Dry Films

The chemical structures for the four dyes, Rhodamine 6G (R6G), Nile Red (NR), sulforhodamine B (SRB), and Oregon Green 514 (ORG), used as probes in this experiment are show in Figure 3.1. R6G, SRB, and ORG share an easily identified common core molecular skeleton. R6G contains an iminium ion and is regarded as a positively charged probe molecule. Since the positive R6G charge delocalizes throughout the entire xanthene moiety, the iminium proton normally does not participate in acid-base

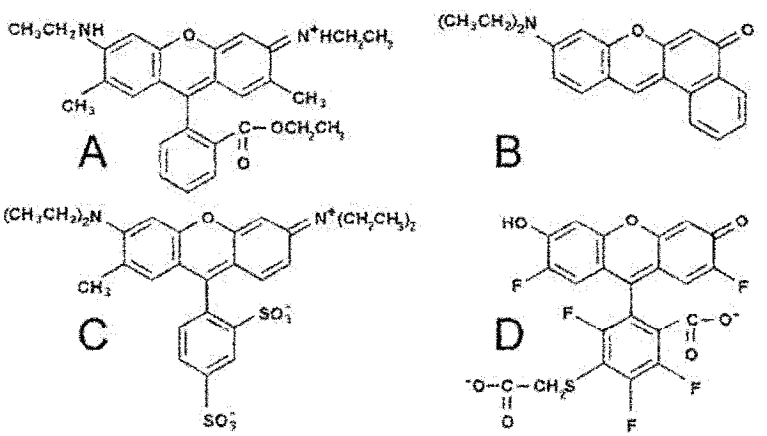

Figure 3.1. Chemical structure for the organic dye molecules used to probe dye-silica sol-gel charge-charge interactions. A) rhodamine 6G (R6G), B) Nile Red, C) sulforhodamine B, D) Oregon Green 514.

equilibria. R6G fluorescence is therefore quite insensitive to external pH variations near physiological conditions. At high pH however, for example pH 12, the R6G ester group will undergo base-catalyzed hydrolysis (pKa ~ 11) to become a R6G zwitterion.[64] For the negatively charged probe molecule, we chose ORG over fluorescein due to its higher photostability. Similar to fluorescein, ORG's fluorescence properties are pH sensitive. Depending on the surrounding pH, an ORG molecule can be weakly or strongly fluorescent based on the phenolic protonation state. Since the phenolic proton has a low pK_a value (*via infra*), its fluorescence gradually becomes insensitive to pH greater than 6.0. The carboxylic acid groups also have relatively low pK_a values that provide additional negative charge to the molecule (up to three negative net charge). In this study, ORG is regarded as a negatively charged probe molecule because, by default, at the single molecule level it is more difficult to observe and test the weakly fluorescent neutral ORG molecules. SRB like R6G contains an iminium ion; however its sulfate groups make it a zwitterion with a negative one net charge. Nile Red (NR) is a neutral dye with a skeletal structure different from the other three dyes.

These dyes were selected to provide a range of possible guest charged states and coulombic interactions (attraction, none, or repulsion respectively) with the negative silica surface. The mobility distributions obtained for R6G, NR, and ORG in dry day one films are presented in Figure 3.2. The low R6G tumbling molecule population suggests that R6G interacts strongly with the silicate matrix, presumably through coulombic attraction. But, R6G and NR present mobilities that are virtually identical, indicating that they experience similar degree of surface interactions. This occurs even though R6G is expected to possess a positive charge and NR ($pK_a = 1.00 \pm 0.05$) is neutral.[65] In addition

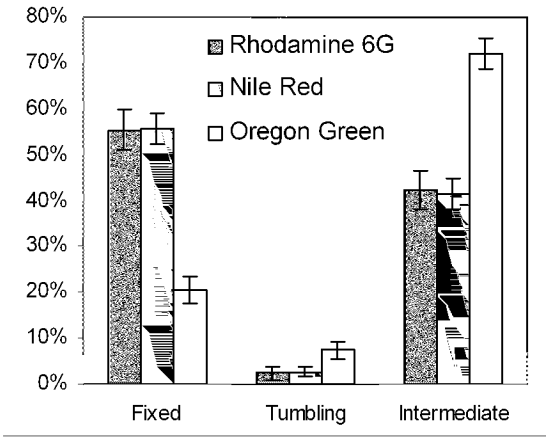

Figure 3.2. Rhodamine 6G (R6G), Nile Red, and Oregon Green mobility comparison within day one dried sol-gel films. Notice that the mobility distributions for R6G and Nile Red are statistically identical; indicating that charge attraction does not significantly alter the mobility distribution. In contrast Oregon Green shows significantly greater mobility than either R6G or Nile Red, as demonstrated by greater tumbling and intermediate populations.

to fixed and tumbling molecules, there is a sizable "intermediate" molecule population in both samples. Through single molecule measurements we can identify these molecules that occasionally switch polarization, indicating weaker silica surface interactions. These molecules jump between different fixed orientations or temporarily dissociate from the surface and freely tumble in the solvent during the course of a measurement, resulting in a change in emission polarization ($P(t)$). Figure 3.3 presents two different examples of

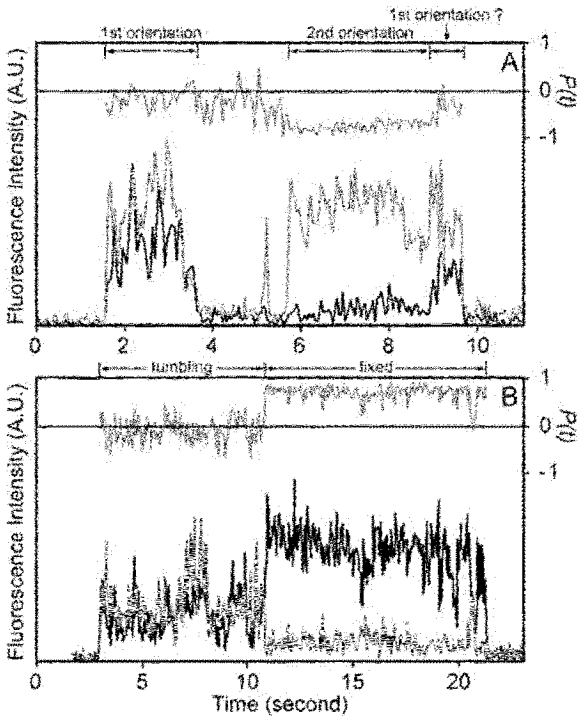

Figure 3.3. Intermediate ORG molecule fluorescence time trace examples. Panel A illustrates a molecule that switches between two fixed orientations, both with a negative average orientation polarization. The molecule in panel B would be best described as a tumbling molecule that becomes fixed. Single molecule photobleaching is indicated by the abrupt fluorescence intensity drop at the end of each trace. The lower black and gray lines in each panel represent $I_{//}(t)$ and $I_{\perp}(t)$, respectively. The additional gray line near the top of each panel represents the corresponding $P(t)$ at each time unit.

intermediate molecule behavior.

A slight but noticeable increase in the tumbling molecule percentage can be seen when cationic R6G and neutral NR are compared to anionic ORG (Figure 3.2). A larger decrease in the fixed molecule percentage for ORG relative to R6G and NR is also observed. From these results we reach two conclusions. First, since the sol-gel surface is assumed to have a negative charge (point of zero charge = 2.5 pH),[35,39] due to the structural similarity between R6G and ORG, the increase in the ORG tumbling molecule population can likely be attributed to coulombic repulsion between ORG and the silica surface. However, the variation is lower than expected if the entire ORG population is negatively charged and repelled from the surface. Second, the similarity in R6G and NR results indicates that charge attraction does not significantly enhance immobilization. The lower than expected molecular charge influence on mobility could be attributed to dye adsorption on the pore walls, or through pore collapse, due to solvent evaporation during film aging. Moreover, without a solvent present the dye will be unable to dissociate from the counter ion, rendering most molecules neutral and eliminating the expected differences in charge. Within the dry day one films this physical immobilization appears to dominate other forces in most local environments, leaving a reduced number of isolated pores fully or partially solvated.[12,16] The slight increase in tumbling ORG mobility seen could represent the mobility contributed by molecules isolated in pores that still contain solvent, that solvent would then allow them to dissociate from their counter ion.

3.3.1.2 Fresh Dry Films

The R6G, SRB, and ORG fresh film results support both the charge repulsion influence on mobility trend and the hypothesis that physical entrapment dominates the dry day one films. As seen in Figure 3.4 the opposite charge between R6G and ORG results in a 7-fold difference in the freely tumbling molecule population, from 2% for R6G to 14% for ORG. The overall increase in tumbling molecule population appears to correspond to an increase in negative charge (positive R6G, negative zwitterionic SRB, and negative ORG). Support for a generalized increase in fresh film mobility relative to day one films includes: a reduction in the fixed R6G molecule percentage relative to the day one films (from 56% ± 4% to 23% ± 3%), an increase in the ORG tumbling molecule percentage (from 7% ± 2% to 14% ± 2%), the streaking behavior observed while imaging, and gradual fluorescence spot (dye) relocation between consecutive imaging scans of the same fresh sample area. Both image streaking and spot relocation indicate active dye translational motion within the films on the sample imaging time scale.[44,66]

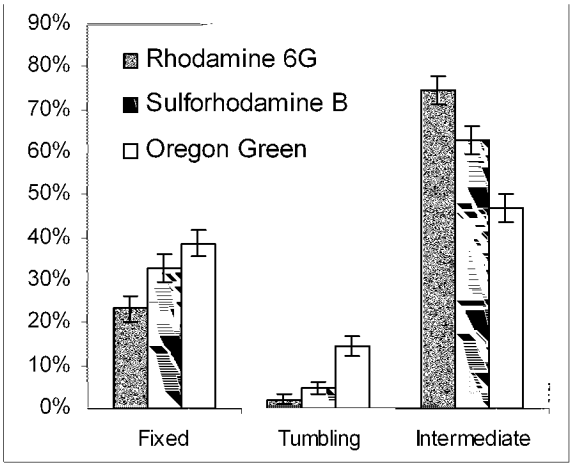

Figure 3.4. Rhodamine 6G, sulforhodamine B, and Oregon Green comparison within fresh dry films. For both fixed and tumbling categories an increase in population is seen as the probe negativity increases.

A reduction in guest mobility as the film ages agrees with our current understanding of the sol-gel condensation process. After gelation the silica bonds continue to form, reducing the pore size as the silica network grows and ages. At the

same time the solvent evaporates from the film (ethanol first and then water), reducing pore solvation and leading to pore collapse.[67] Due to our method's inability to track and test molecules with significant translational motion, the fresh film results are expected to underestimate the highly mobile molecule population. The dye molecules with significant translational motion would be expected to contribute to the tumbling or intermediate molecule populations if they were tracked, since they are obviously not fixed. Thus for the fresh films, and also for the equilibrated films, our results represent the dye molecules sufficiently encapsulated to prevent, or reduce, free translational diffusion within the film rather than the complete representation including all molecular mobilities present within the film. This could explain the counter-intuitive increase in fresh film fixed molecule population as the guest negativity increases. Since the most mobile molecules are least likely to be sampled, a higher fixed molecule fraction will be obtained.

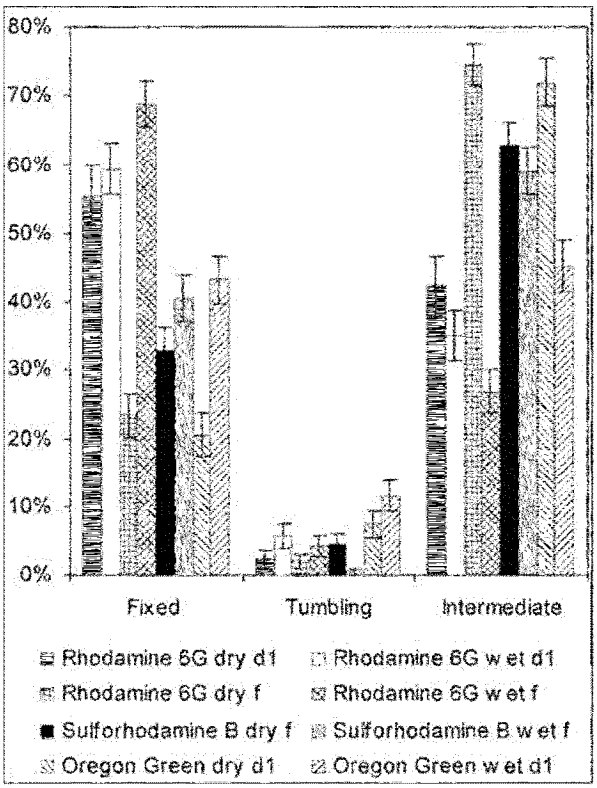

Figure 3.5. Water equilibrated (wet) films compared to their corresponding dry films (dry) on the day they were formed (fresh - f) and one day after (d1). In each pair an increase in fixed molecules is seen on the addition of water, also in all cases except sulforhodamine B an increase in tumbling molecules is observed as well.

3.3.2 Water Equilibrated Films

To increase the pore and guest solvation, dry films (fresh and day

one) were equilibrated with double distilled water and the subsequent change in mobility was investigated. Based on these results two comparison sets are possible; water equilibrated films (wet) compared to their corresponding dry film, and the water equilibrated film trend as the guest charge is varied. In all four dry and equilibrated film pairs, Figure 3.5, the water equilibrated films demonstrate an increase in fixed molecules relative to the dry film, as well as a corresponding decrease in intermediate molecules. As was the case for the fresh films, this is likely due to selectively detecting fully encapsulated molecules in the equilibrated films, due to free dye translation or leaching. In addition to the increase seen in fixed molecule population, both R6G and ORG show an increase in tumbling molecules while SRB shows a decrease in tumbling molecules.

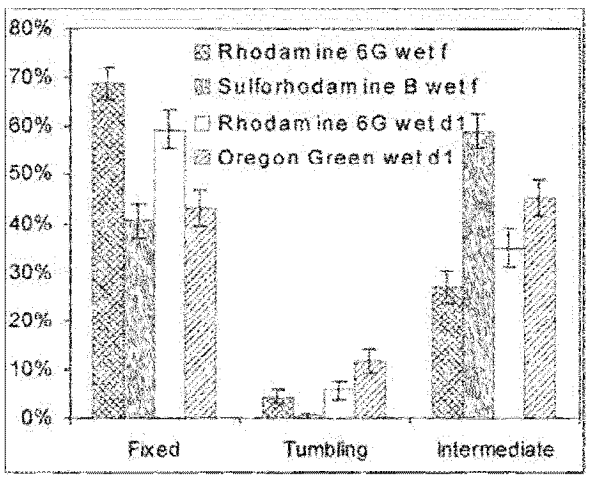

Figure 3.6. Water equilibrated (wet) film populations comparing freshly formed (f) sulforhodamine B and one day old (d1) Oregon Green films to rhodamine 6G (R6G, f and d1). While there is a decrease in fixed molecule population for zwitter-ionic sulforhodamine B there is no corresponding increase in tumbling molecules. For Oregon Green there is both a decrease in fixed molecules and an increase in tumbling molecules indicating increased mobility relative to R6G.

SRB's zwitter-ionic nature ($pK_a < 1.5$) complicates conclusive analysis since the cationic center can promote immobilization while the anionic centers experience surface repulsion that would favor solvation.[35,39] In addition other researchers indicate that SRB has the potential to form immobilizing hydrogen bonds to the silica surface as well.[35,39]

Neglecting SRB, comparison of R6G and ORG in water equilibrated films reinforces the increased mobility trend with charge repulsion. From

Figure 3.6, it is evident that water equilibrated R6G films contain a significantly higher fixed molecule population relative to ORG, while ORG has greater tumbling and intermediate molecule populations. The increase in R6G fixed molecule population and decrease in intermediate population, indicates fewer R6G silica surface reorientations corresponding to increased surface attraction. Bi-exponential fluorescence anisotropy decays and high residual fluorescence anisotropy have been reported for R6G and oxazine dyes encapsulated inside alcogels.[20,39,68,69] These observations were respectively attributed to different R6G local environments and strong R6G adsorption to the alcogels silica surface, which would restrict rotational motions. Our results directly demonstrate that R6G global reorientation is largely prohibited in both the dry and wet films, but restricted rotational motions remain.

A more in-depth dye dwell time analysis investigating intermediate molecule reorientations is under consideration and would provide increased insight into the relationship between the kinetic rates of dye adsorption and desorption and molecular charge. Film solvation by water provides the dye greater rotational freedom, as well as an increased dye molecule fraction in the charged state due to counter-ion dissociation. These changes result in the observed increase in charge's influence on the rotational mobility.

3.3.3 ORG Thin Films

3.3.3.1 Thin Film pH Determination

The relatively small dry ORG tumbling molecule populations observed may imply that (i) coulombic interaction alone does not determine molecular mobility in silica sol-gel and/or (ii) the acidic TEOS sample preparation hydrolysis led to a lower internal sample

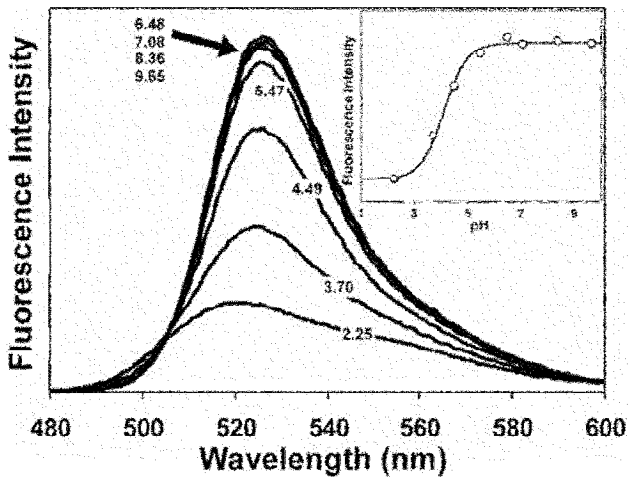

Figure 3.7. ORG emission spectra for pH buffered solutions. All spectra were recorded with a fluorometer using 457 nm excitation. Inset: Data points were obtained by integrating the fluorescence intensity from 465 nm to 600 nm for each emission spectrum. The solid line is a fit to the Henderson-Hasselbalch equation, which gives an estimated ORG pK_a value of 4.1±0.1.

pH and rendered both ORG and the silica surface neutral (isoelectric point = 2.0 ± 0.2).[70] This would reduce coulombic repulsion between ORG and the silica surface and produce fewer tumbling molecules. Figure 3.7 shows the ORG emission spectra for a series of pH buffered ORG solutions when excited at 457 nm. As the pH increases, anionic ORG becomes the dominant species and the ORG fluorescence intensity increases. According to the Henderson-Hasselbalch fit depicted in the Figure 3.7 inset, the ORG phenolic pK_a value was determined to be 4.1±0.1.[71] Thus it is expected that the coulombic repulsion between ORG and a silica surface would diminish if the internal silica sol-gel film pH drops below 4.1.

To estimate the internal silica sol-gel film pH, Figure 3.8, we compared the normalized bulk ORG fluorescence spectra in a dry film, ORG dissolved in different pH buffers, and ORG in films equilibrated with various pH buffers. All spectra were collected using 488nm excitation. It is apparent from Figure 3.8 that the ORG emission spectra in solutions are considerably narrower than those obtained for equilibrated ORG films. The solution spectra also exhibit a systematic peak maximum blue-shift from 535 nm to 526 nm with increasing pH, whereas the film spectra peak maxima remain relatively unchanged at 526±1 nm, regardless of the external pH. The ORG emission

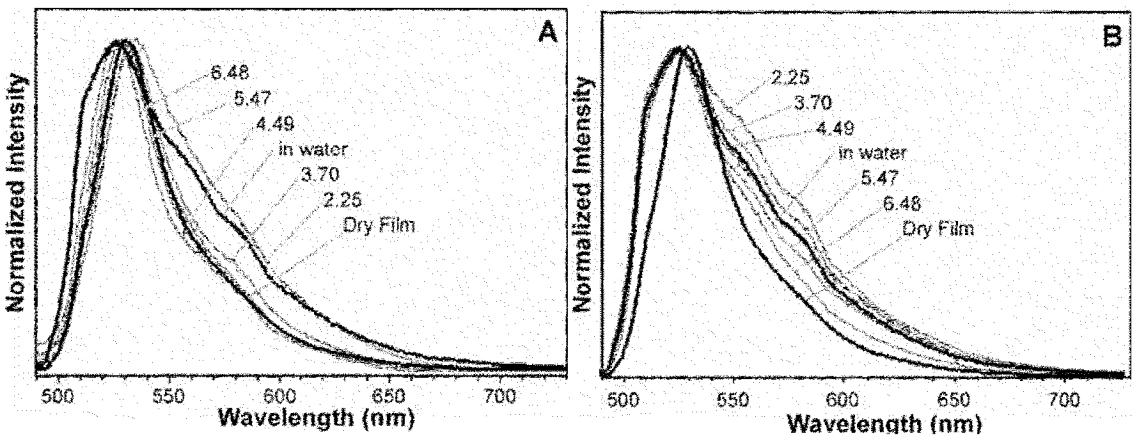

Figure 3.8. Panel A: ORG solution emission spectra in pH buffers (gray lines) and ORG dry silica sol-gel film emission spectra before and after equilibration with water (black lines). Panel B: ORG silica sol-gel film emission spectra after equilibration with pH buffers (gray lines). ORG dry silica sol-gel film emission spectra before and after equilibration with water are shown as black lines. All spectra shown were collected on a confocal microscope using 488 nm excitation.

broadening evident in the wet films clearly reflects the heterogeneous silica sol-gel environment. Surprisingly the dry ORG film fluorescence spectrum contains a narrow peak located at 531 nm that strongly resembles the ORG pH 4.49 solution spectrum. While it is unlikely that a ORG dry film would experience a more solution-like environment than the wet film, an intriguing alternative explanation is that the narrow peak reflects a more homogeneous dry film internal environment. The exact cause of this interesting phenomenon is unclear and is under investigation. If the dry film internal pH was indeed close to 4.49, then both ORG and the silica surface should be negatively charged and the potential for coulombic repulsion would be improved. That would help explain why encapsulated ORG displays more tumbling molecules than R6G. Meanwhile, the ORG emission spectra are significantly broadened when equilibrated with either water or pH buffers, indicating that the encapsulated ORG molecules were exposed to a more heterogeneous and dynamic environment once solvated. The ORG

emission spectrum broadening also confirmed that, despite encapsulation, the ORG molecules were still able to interact with external reagents. Since a dramatic reduction in ORG emission was observed when solvated, we believe that the dynamic interaction between encapsulated ORG and water is responsible for both the spectral broadening and ORG fluorescence quenching. Interestingly the water equilibrated ORG film emission spectrum indicates that the internal pH lies between 4.49 and 5.47, similar to the dry film internal pH. This suggests that water did not significantly alter the internal silicate film pH, which remained close to 5.0±0.5.

3.3.3.1 Effect of pH Variation on ORG Mobility

To explore how external pH can alter the silica sol-gel encapsulated ORG mobility we measured the ORG mobility distributions under a range of film environments. Since the ORG negative charge is dependent on the dye protonation state, we first sought to alter the dry film internal pH by adding sodium hydroxide immediately before spin-casting. Our assumption was that the added NaOH would neutralize the residual catalytic phosphoric acid to provide an internal film pH around 9. While an increase in tumbling molecules relative to both

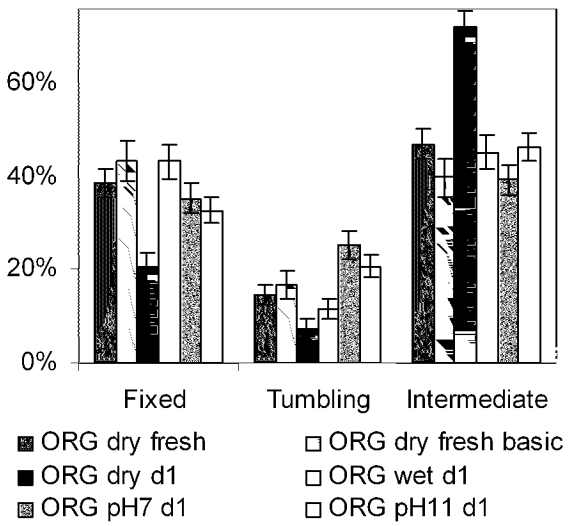

Figure 3.9. Oregon Green rotational mobility distributions as the sol-gel local environment is altered; freshly formed (fresh), sodium hydroxide added (basic), day one (d1), water (wet) and buffer equilibrated (pH 7 and pH11) films are displayed. As environmental changes are made that favor charge repulsion an increase in tumbling molecule population is generally observed.

the fresh and day one ORG dry films was observed, as shown in Figure 3.9, the NaOH addition also greatly increased the sol-gel condensation rate, generating micrometer silica particles within the films. Our conclusion from this experiment was that the base did not simply alter the internal pH, but also acted to catalyze silica nanoparticle formation, resulting in an altered internal silica network as well. The two processes inseparability prevents us from drawing meaningful conclusions about charge repulsion's influence on mobility in this case. It also demonstrates the need to make external pH adjustments to the film after sol-gel condensation is completed.

Next, as reported in part in section 3.3.2, day one ORG dry films were equilibrated with water to increase pore solvation, which also increased the internal pH through catalytic phosphoric acid dilution. Direct pH measurement on the water, acid dilution calculations, and a calibration curve using the concentrated ORG sample fluorescence emission spectrum[59] all indicate an internal pH around 4.5 for the water equilibrated films. Theoretically, with a $pK_a = 4.1 \pm 0.1$[59,72] most ORG molecules (86%, as per the Henderson-Hasselbalch equation) should be deprotonated and repelled by the negatively charged silica surface (point of zero charge = 2.5 pH)[35,39] at this pH. This said, the 4% increase in tumbling molecule population above the dry day 1 sample was considerably less than expected. This could signal a lower than indicated internal pH, unaccounted for stabilizing forces that promote ORG protonation, or that charge repulsion does not greatly influence mobility due to other dominating forces (such as physical confinement). Subsequently, day one films were equilibrated with 50 mM phosphate buffers (pH 7 or pH 11) to ensure that accessible ORG exclusively existed in the anionic form (99.9%+). In both cases the tumbling molecule population (25 ± 3%

and 21 ± 2%) was double that seen in the water equilibrated sample (12 ± 2%) and triple the dry day one sample population (7 ± 2%). This trend in mobility demonstrates that charge repulsion does contribute significantly to guest mobility under appropriately controlled conditions. We recognize that the 25% maximum tumbling molecule population reported here does not constitute the dominant force controlling molecular mobility. However, it does indicate the measurable and significant role that charge-charge repulsion plays in influencing mobility. The large increase in tumbling molecules also represents a concrete first step towards externally controlling guest mobility by manipulating charge-charge interactions.

3.3.4 Polarization Distribution Analysis

3.3.4 High Numerical Aperture Correction

Since we use a two dimensional orientation projection to classify the molecules, the molecular emission dipole spatial orientation produces a fraction of fixed molecules that are classified improperly as tumbling molecules by the polarization calculation, shown in Equation 3.1 (for expanded discussion see Chapter 2). This depolarization

$$P(t) = (I_{ll}(t) - I_{\perp}(t)) / (I_{ll}(t) + I_{\perp}(t)) \qquad \textbf{3.1}$$

effect is a consequence of using a high numerical aperture (N.A.) microscope.[24,73,74] Theoretically, based on a randomly oriented emission dipole's contribution (x, y, z) to

$$P = \{(K_1 - K_2)(x^2 - y^2)\} / \{ (K_1 + K_2)(x^2 + y^2) + 2K_3 z^2 \} \qquad \textbf{3.2}\ [24]$$

$I_{ll}(t)$ and $I_{\perp}(t)$, and assuming the objective optical axis is parallel to the z-axis, a fixed emission dipole polarization becomes Equation 3.2. For the low N.A case, where $K_1 >> K_2$ and K_3, Equation 3.2 reduces to Equation 3.1. For the high N.A. case, where K_2 and K_3 are no longer negligible, a random fixed emission dipole polarization set's

polarization will skew towards zero. In our case, using a N.A = 1.25 with immersion microscope oil (n = 1.52) we obtain an objective angle of 55.32° and values of 0.2611, 0.0025, and 0.0597 for K_1, K_2, and K_3 respectively. Since K_2 and K_3 are significant, the fixed dipole polarization distribution will follow Equation 3.2 resulting in a peak at zero polarization, rather than the minima predicted by Equation 3.1. This peak represents the molecules mistakenly classified as tumbling by our method when they are in fact fixed with an emission dipole angle that contributes equally to both $I_{//}(t)$ and $I_{\perp}(t)$. Based on the fixed molecule population identified in our experiments, the number of mistakenly classified tumbling molecules can be estimated and corrected for. Since this is a statistical correction to the population, it does not specifically identify the tumbling molecules that are misclassified.

3.3.4 Corrected Mobility Distribution Analysis

Taking into account the high N.A. correction, a more distinct contrast in behavior is observed based on molecular charge. As seen in Table 3.1, the only dye that retains a consistent tumbling molecule population, in all environments, is anionic ORG with 6-24% tumbling molecules after correction. For R6G, SRB, and NR the majority of molecules previously considered tumbling are reclassified as fixed, retaining less than 1-3% tumbling population after correction. Since the R6G, SRB, and ORG core molecular structures are the same, the substitute groups must account for the variations observed in dye mobility. Specifically, anionic charge repulsion promotes ORG mobility, while the R6G cationic charge contributes a lesser degree to adsorption. The 24% tumbling molecules for ORG day 1 pH 7 represents a maximum in charge repulsion dependent molecular mobility control, while the 22% fixed molecule population for dry day 1 ORG

Table 3.1. Dye mobility populations (A) before the high N.A. correction is taken into account and (B) after the high N.A. correction is applied. In C the total molecules for each dye set is indicated.

Dye	A			B			C
	Fixed	Tumbling	Intermediate	Fixed	Tumbling	Intermediate	Number of Molecules
rhodamine 6G dry d1	56% ± 4%	2% ± 1%	42% ± 4%	58% ± 4%	0% ± 0%	42% ± 4%	130
rhodamine 6G wet d1	59% ± 4%	6% ± 2%	35% ± 4%	62% ± 4%	3% ± 2%	35% ± 4%	160
rhodamine 6G dry fresh	23% ± 3%	2% ± 1%	75% ± 3%	25% ± 3%	1 % ± 1%	74% ± 3%	193
rhodamine 6G wet fresh	69% ± 3%	4% ± 1%	27% ± 3%	72% ± 3%	1% ± 1%	27% ± 3%	190
Nile Red dry d1	56% ± 3%	3% ± 1%	41% ± 3%	58% ± 3%	0% ± 0%	42% ± 3%	226
sulforhodamine B dry fresh	33% ± 3%	4% ± 1%	63% ± 3%	34% ± 3%	3% ± 1%	63% ± 3%	199
sulforhodamine B wet fresh	40% ± 3%	1% ± 0%	59% ± 3%	41% ± 3%	0% ± 0%	59% ± 3%	200
Oregon Green dry fresh	39% ± 3%	14% ± 2%	47% ± 3%	41% ± 3%	12% ± 2%	47% ± 3%	241
Oregon Green dry fresh basic	43% ± 4%	17% ± 3%	40% ± 4%	46% ± 4%	14% ± 3%	40% ± 4%	143
Oregon Green dry d1	21% ± 3%	7% ± 2%	72% ± 3%	22% ± 3%	6% ± 2%	72% ± 3%	175
Oregon Green wet d1	43% ± 4%	12% ± 2%	45% ± 4%	46% ± 4%	9% ± 2%	45% ± 4%	190
Oregon Green pH 7 d1	35% ± 3%	25% ± 3%	40% ± 3%	37% ± 3%	24% ± 3%	39% ± 3%	221
Oregon Green pH 11 d1	33% ± 3%	21% ± 2%	46% ± 3%	35% ± 3%	19% ± 2%	46% ± 3%	269

represents a immobilization minimum. This minimum might indicate the molecule population confined within the dried films by physical entrapment. This could explain the contradiction between our results that charge-charge attraction represents a minor influence on co-condensed guest molecule mobility in silica sol-gel, and the strong influence electrostatic interaction has on molecular diffusion within naturally occurring silica based strata.[35,36] Since molecular diffusion in those studies was measured with tracer dyes introduced long after the geological silicate network was established, this may signify the importance of entrapment, or molecular templating, in determining silica sol-gel mobility.

Our results agree with cationic and neutral dye fluorescence anisotropy studies within sol-gel monoliths that indicate hindered but not complete loss of guest mobility upon entrapment.[20,40,69] The bi-exponential anisotropy decay observed is traditionally attributed to both an adsorbed state and separate freely tumbling state. In contrast to the traditional interpretation our results indicate an effective mobility partitioning into fixed and intermediate (or hindered) states, rather than freely tumbling, for most samples. The fact that intermediate molecules alternate between mobility states adds support to fluorescence anisotropy interpretation using hindered, rather than free rotation terms. Since these intermediate molecules change their emission polarization over very long time scales, they could escape detection by previous steady-state and time-resolved ensemble measurements. Those studies would only indicate intermediate molecule partitioning behavior as either fixed or tumbling, since it would not observe the transient state. Our results are in part consistent with those obtained from a recent NMR study on small solute molecules in tetramethyl orthosilicate (TMOS) monoliths. Based on the

NMR results the existence of tumbling, fixed, and transitioning molecules was proposed for cationic guests, though their respective populations were not quantified.[41] However, our identification of fixed molecule populations for both neutral and anionic guests deviates drastically from the NMR results.[41] This may result from additional hydrophobic interactions and hydrogen bonding made possible by our larger organic probe molecules, or differences in the TEOS and TMOS sol-gel structure due to precursor choice and preparation procedure.

In this report, mobility distributions have been largely explained using the four-region pore model advocated by Zink and coworkers.[18] Implicit in the four-region model is a relatively static silica host with an internal framework that continues to evolve slowly long after gelation. For the more dynamic silica host that likely exists near gelation, an alternative silica particle growth model has been proposed.[75-77] This model interprets dye fluorescence anisotropy decay as the rotational rate for a probe molecule bound to a freely rotating silica particle.[60] The probe bound particle size is extracted from the fluorescence anisotropy decay rate and the effect that the particle size has on the perceived viscosity. Particle sizes have been calculated in this manner through the sol-gel gelation point.[60,75-77] The contention between these two models centers on interpreting the anisotropy decay as either local viscosity variances or changing particle size. There is no disagreement that condensation continues after gelation, with the macroscopic gel network gradually assimilating particles and particle aggregates. Thus, starting from the particle growth model near gelation, when dried and aged, the particles will aggregate and form a silica matrix containing solvent filled voids (pores), the interface between solvent and matrix, and potential locations where the pore dimensions

are comparable to the probe size. In short it becomes the four-region sol-gel interior interpretation. We believe that the four-region pore interior model and the particle growth model are compatible and can be combined to provide a fuller internal silica sol-gel structure description as the matrix develops over time and ages.

The discrepancies between our results and those obtained from NMR or time-resolved fluorescence anisotropy studies are likely related to this sample aging process.[41,60,75-77] While those investigations were conducted entirely on silica sol-gel monoliths, where internal solvent is retained for an extended time, our thin film samples generally contain less solvent due to the rapid evaporation associated with the spin coating process.[78] Due to this, our samples experience an accelerated aging process and resemble a dried, aged monolith with reduced guest mobility. Similar to our thin films, very high steady-state fluorescence polarization has also been reported for probes embedded in dip-coated thin films, where solvent evaporation and rapid pore collapse were believed to be responsible for the guest mobility reduction.[79] Further highlighting the stark contrast in guest mobility between thin film and monolith samples, single fluorescent molecule translational mobility trajectories inside silica sol-gel monoliths have been recently observed.[80]

3.4 CONCLUSION

For the first time, single molecule spectroscopy allowed us to monitor coulombic interaction's influence on guest molecule global rotational mobility inside a silica sol-gel host at a molecular level. By directly observing probe molecule global rotational motion over 50-ms intervals, our mobility classification is immune to the fluorescence depolarization effect of rapid segmental motions originating from immobilized

molecules. In an ensemble measurement this fluorescence depolarization effect can be mistakenly identified as tumbling molecules and tends to inflate the tumbling population. The ability to observe single molecule rotational motion also allows us to identify three mobility classes present in the silica sol-gel host. These classes provide an alternative interpretation for the bi-exponential decay components and high residual fluorescence anisotropy commonly found in dye ensemble measurements. Moreover, the intermediate molecule population revealed by single molecule spectroscopy will provide new insights into slow molecular dynamics that are unlikely to be captured by either conventional steady-state or time-resolved ensemble measurements.

Using charged dye molecules as probes, we demonstrate charge-charge interactions influence on guest molecule mobility trapped within a silica sol-gel host. By altering the film internal solvent content and pH through external liquid equilibration, the dye protonation and charged state was varied. In both dry and water equilibrated films, the anionic ORG charge repulsion from the surface resulted in an increased tumbling molecule population. In dry films, cationic and neutral guests displayed similar mobilities characterized by insignificant tumbling molecule populations, indicating a limited or canceled cationic charge influence on mobility. However, the R6G water equilibrated sample demonstrated an increase in fixed molecules, indicating an increased silica surface attraction when solvated. The increase in charge influence with the addition of water is attributed to counter ion dissociation and a reduction in physical immobilization upon solvation. In addition, pH buffers were shown to control the ORG charged state, increasing the tumbling molecule population by promoting charge repulsion.

While demonstrating that charge-charge interactions influence guest mobility, our results also indicate that charge-charge interactions are not necessarily the dominant immobilization force (less than 24% contribution to mobility as seen for ORG) within the silica sol-gel host. Other interactions including dye solvation, physical entrapment, hydrogen bonding, and hydrophobicity, appear to play significant roles in determining a guest's mobility. Further testing will seek to clarify the contributions that these other interactions make to mobility, as well as reveal how these forces work in concert. This knowledge will enable the eventual customization and control of guest-host charge-charge interactions and their associated properties, much as hydrophobicity has already been used to selectively place probe molecules in desired environments.[46,81]

Chapter III References

(1) Mei, E.; Bardo, A. M.; Collinson, M. M.; Higgins, D. A. *J. Phys. Chem. B* **2000**, *104*, 9973.
(2) De Matteis, F.; Prosposito, P.; Sarcinelli, F.; Casalboni, M.; Pizzoferrato, R.; Furlani, A.; Russo, M. V.; Vannucci, A.; Varasi, M. *J. Non-Cryst. Solids* **1999**, *245*, 15.
(3) Yariv, E.; Reisfeld, R. *Opt. Mater.* **1999**, *13*, 49.
(4) Casalboni, M.; Dematteis, F.; Francini, R.; Prosposito, P.; Senesi, R.; Grassano, U. M.; Pizzoferrato, R.; Gnappi, G.; Montenero, A. *J. Lumines.* **1997**, *72-74*, 475.
(5) Lai, D. C.; Dunn, B.; Zink, J. I. *Inorg. Chem.* **1996**, *35*, 2152.
(6) Reisfeld, R.; Yariv, E.; Minti, H. *Opt. Mater.* **1997**, *8*, 31.
(7) MacCraith, B. D.; McDonagh, C.; McEvoy, A. K.; Butler, T.; Okeeffe, G.; Murphy, V. *J. Sol-Gel Sci. Technol* **1997**, *8*, 1053.
(8) Walcarius, A.; Delacote, C. *Chem. Mater.* **2003**, *15*, 4181.
(9) Diaz, A. N.; Peinado, M. C. R.; Minguez, M. C. T. *Anal. Chim. Acta* **1998**, *363*, 221.
(10) Ellerby, L. M.; Nishida, C. R.; Nishida, F.; Yamanaka, S. A.; Dunn, B.; Valentine, J. S.; Zink, J. I. *Science* **1992**, *255*, 1113.
(11) Gill, I. *Chem. Mater.* **2001**, *13*, 3404.
(12) Zheng, L.; Brennan, J. D. *Analyst* **1998**, *123*, 1735.
(13) Tang, Y.; Dave, B. C. *Adv. Mater.* **1998**, *10*, 1536.
(14) Lan, E. H.; Dave, B. C.; Fukuto, J. M.; Dunn, B.; Zink, J. I.; Valentine, J. S. *J. Mater. Chem.* **1999**, *9*, 45.
(15) Nishida, F.; McKiernan, J. M.; Dunn, B.; Zink, J. I.; Brinker, C. J.; Hurd, A. J. *J. Am. Chem. Soc.* **1995**, *78*, 1640.
(16) Villegas, M. A.; Pascual, L. *J. Mater. Sci.* **2000**, *35*, 4615.
(17) Lobnik, A.; Wolfbeis, O. S. *J. Sol-Gel Sci. Technol* **2001**, *20*, 303.
(18) Dunn, B.; Zink, J. I. *Chem. Mater.* **1997**, *9*, 2280.
(19) Keeling-Tucker, T.; Brennan, J. D. *Chem. Mater.* **2001**, *13*, 3331.
(20) Narang, U.; Wang, R.; Prasad, P. N.; Bright, F. V. *J. Phys. Chem.* **1994**, *98*, 17.
(21) Gulcev, M. D.; Goring, G. L. G.; Rakic, M.; Brennan, J. D. *Anal. Chim. Acta* **2002**, *457*, 47.
(22) Yariv, E.; Schultheiss, S.; Saraidarov, T.; Reisfeld, R. *Opt. Mater.* **2001**, *16*, 29.
(23) Rahn, M. D.; King, T. A.; Gorman, A. A.; Hamblett, I. *Appl. Opt.* **1997**, *36*, 5862.
(24) Viteri, C. R.; Gilliland, J. W.; Yip, W. T. *J. Am. Chem. Soc.* **2003**, *125*, 1980.
(25) Lloyd, C. R.; Eyring, E. M. *Langmuir* **2000**, *16*, 9092.
(26) Chen, J. P.; Wang, H. Y. *Biotechnol. Tech.* **1998**, *12*, 851.
(27) Tapec, R.; Zhao, X. J. J.; Tan, W. H. *J. Nanosci. Nanotechnol.* **2002**, *2*, 405.
(28) Ferrer, M. L.; del Monte, F.; Mateo, C. R.; Gomez, J.; Levy, D. *J. Sol-Gel Sci. Technol* **2003**, *26*, 1169.
(29) Zheng, L.; Flora, K.; Brennan, J. D. *Chem. Mater.* **1998**, *10*, 3974.
(30) Dave, B. C.; Soyez, H.; Miller, J. M.; Dunn, B.; Valentine, J. S.; Zink, J. I. *Chem. Mater.* **1995**, *7*, 1431.
(31) Zheng, L. L.; Reid, W. R.; Brennan, J. D. *Anal. Chem.* **1997**, *69*, 3940.
(32) Jordan, J. D.; Dunbar, R. A.; Bright, F. V. *Anal. Chem.* **1995**, *67*, 2436.

(33) Doody, M. A.; Baker, G. A.; Pandey, S.; Bright, F. V. *Chem. Mater.* **2000**, *12*, 1142.
(34) Flora, K. K.; Brennan, J. D. *Chem. Mater.* **2001**, *13*, 4170.
(35) Kasnavia, T.; Vu, D.; Sabatini, D. A. *Ground Water* **1999**, *37*, 376.
(36) Sabatini, D. A. *Ground Water* **2000**, *38*, 651.
(37) Rosen, M. J. *Surfactants and Interfacial Phenomena*, 2nd ed.; John Wiley and Sons: New York, 1989.
(38) Adamson, A. W.; Gast, A. P. *Physical Chemistry of Surfaces*, 6th ed.; John Wiley and Sons: New York, 1997.
(39) Ferrer, M. L.; del Monte, F. *Langmuir* **2003**, *19*, 650.
(40) Ferrer, M. L.; del Monte, F.; Levy, D. *J. Phys. Chem. B* **2001**, *105*, 11076.
(41) Wheeler, K. E.; Lees, N. S.; Gurbiel, R. J.; Hatch, S. L.; Nocek, J. M.; Hoffman, B. M. *J. Am. Chem. Soc.* **2004**, *126*, 13459.
(42) Handel, H.; Gesele, E.; Gottschall, K.; Albert, K. *Angew. Chem., Int. Edit.* **2003**, *42*, 438.
(43) Komori, Y.; Hayashi, S. *Phys. Chem. Chem. Phys.* **2003**, *5*, 3777.
(44) Higgins, D. A.; Collinson, M. M.; Saroja, G.; Bardo, A. M. *Chem. Mater.* **2002**, *14*, 3734.
(45) Huang, M. H.; Dunn, B. S.; Soyez, H.; Zink, J. I. *Langmuir* **1998**, *14*, 7331.
(46) Hernandez, R.; Franville, A. C.; Minoofar, P.; Dunn, B.; Zink, J. I. *J. Am. Chem. Soc.* **2001**, *123*, 1248.
(47) Hirashima, H.; Imai, H.; Fukui, Y. *J. Sol-Gel Sci. Technol* **2003**, *26*, 383.
(48) Lu, Y.; Ganguli, R.; Drewlen, C. A.; Anderson, M. T.; Brinker, C. J.; Gong, W.; Guo, Y.; Soyez, H.; Dunn, B.; Huang, M. H.; Zink, J. I. *Nature* **1997**, *389*, 364.
(49) Gellermann, C.; Storch, W.; Wolter, H. *J. Sol-Gel Sci. Technol* **1997**, *8*, 173.
(50) Chia, S.; Cao, J.; Stoddart, J. E.; Zink, J. I. *Angew. Chem., Int. Edit.* **2001**, *40*, 2447.
(51) McCain, K. S.; Hanley, D. C.; Harris, J. M. *Anal. Chem.* **2003**, *75*, 4351.
(52) McCain, K. S.; Harris, J. M. *Anal. Chem.* **2003**, *75*, 3616.
(53) Moerner, W. E.; Orrit, M. *Science* **1999**, *283*, 1670.
(54) Wang, H. M.; Bardo, A. M.; Collinson, M. M.; Higgins, D. A. *J. Phys. Chem. B* **1998**, *102*, 7231.
(55) Orrit, M. *J. Chem. Phys.* **2002**, *117*, 10938.
(56) Jung, Y. J.; Barkai, E.; Silbey, R. J. *J. Chem. Phys.* **2002**, *117*, 10980.
(57) Yip, W. T.; Hu, D. H.; Yu, J.; Vanden Bout, D. A.; Barbara, P. F. *J. Phys. Chem. A* **1998**, *102*, 7564.
(58) Bardo, A. M.; Collinson, M. M.; Higgins, D. A. *Chem. Mater.* **2001**, *13*, 2713.
(59) Gilliland, J. W.; Yokoyama, K.; Yip, W. T. *Chem. Mater.* **2004**, *16*, 3949
(60) Geddes, C. D. *J. Fluoresc.* **2002**, *12*, 343.
(61) Flora, K. K.; Brennan, J. D. *J. Phys. Chem. B* **2001**, *105*, 12003.
(62) Tleugabulova, D.; Zhang, Z.; Brennan, J. A. *J. Phys. Chem. B* **2003**, *107*, 10127.
(63) Lu, Y. F.; Cao, G. Z.; Kale, R. P.; Prabakar, S.; Lopez, G. P.; Brinker, C. J. *Chem. Mater.* **1999**, *11*, 1223.
(64) El Baraka, M.; Deumie, M.; Viallet, P.; Lampidis, T. J. *Journal of Photochemistry and Photobiology A-Chemistry* **1991**, *62*, 195.
(65) Stuzka, V.; Simanek, V. *Collect. Czech. Chem. Commun.* **1973**, *38*, 194.

(66) Hou, Y. W.; Higgins, D. A. *J. Phys. Chem. B* **2002**, *106*, 10306.
(67) Narang, U.; Jordan, J. D.; Bright, F. V.; Prasad, P. N. *J. Phys. Chem.* **1994**, *98*, 8101.
(68) Hungerford, G.; Suhling, K.; Ferreira, J. A. *Journal of Photochemistry and Photobiology A-Chemistry* **1999**, *129*, 71.
(69) del Monte, F.; Ferrer, M. L.; Levy, D. *J. Mater. Chem.* **2001**, *11*, 1745.
(70) Park, G. A. *Chem. Rev.* **1965**, *65*, 177.
(71) The pKa was originally incorrectly reported as 3.69 +/- 0.08 in the Chemistry of Materials publication. It has been corrected at all occurrences in this dissertation
(72) The original published reference misreports the pKa value as 3.7.
(73) Axelrod, D. *Methods in Cell Biology* **1989**, *30*, 333.
(74) Bopp, M. A.; Jia, Y.; Haran, G.; Morlino, E. A.; Hochstrasser, R. M. *Appl. Phys. Lett.* **1998**, *73*, 7.
(75) Birch, D. J. S.; Geddes, C. D. *Phys. Rev. E: Stat. Phys., Plasmas, Fluids, Relat. Interdiscip. Top.* **2000**, *62*, 2977.
(76) Geddes, C. D.; Karolin, J.; Birch, D. J. S. *J. Fluoresc.* **2002**, *12*, 135.
(77) Tleugabulova, D.; Duft, A. M.; Zhang, Z.; Chen, Y.; Brook, M. A.; Brennan, J. D. *Langmuir* **2004**, *20*, 5924.
(78) Brinker, C. J.; Hurd, A. J.; Schunk, P. R.; Frye, G. C.; Ashley, C. S. *J. Non-Cryst. Solids* **1992**, *147*, 424.
(79) Huang, M. H.; Soyez, H. M.; Dunn, B. S.; Zink, J. I. *Chem. Mater.* **2000**, *12*, 231.
(80) Hellriegel, C.; Kirstein, J.; Brauchle, C.; Latour, V.; Pigot, T.; Olivier, R.; Lacombe, S.; Brown, R.; Guieu, V.; Payrastre, C.; Izquierdo, A.; Mocho, P. *J. Phys. Chem. B* **2004**, *108*, 14699.
(81) Minoofar, P.; Hernandez, R.; Franville, A. C.; Chia, S. Y.; Dunn, B.; Zink, J. I. *J. Sol-Gel Sci. Technol* **2003**, *26*, 571.

Chapter IV

Solvent Effect on Mobility and Photostability of Organic Dyes Embedded Inside Silica Sol-Gel Thin Films

4.1 CHAPTER ABSTRACT

This chapter focuses on rhodamine 6G (R6G), sulforhodamine B (SRB), Oregon Green 514 (ORG), and didodecyl-3,3,3',3'-tetramethylindocarbocyanine ($DilC_{12}$) mobility and photostability in dry and equilibrated (water or ethanol) silica sol-gel thin films. Positively charged R6G remained immobilized, regardless of the solvent. Negative zwitterionic SRB was primarily immobilized in both solvent media, likely due to hydrogen bonding, and other short range interactions. While R6G photostability significantly decreased in solvent media, due to enhanced solvent interactions, hydrogen bonding appeared to retard solvated SRB molecular motions increasing its photostability. Hydrophobic interactions were proposed responsible for the high $DiIC_{12}$ mobility found in dry films, while hydrophobic chain attraction toward the less polar silica matrix was considered responsible for the $DiIC_{12}$ tumbling to intermediate population transfer in solvated films. $DiIC_{12}$ in water and ethanol covered films displayed similar photostability due to similar silica environments and hydrophobic chain dynamics.

4.2 INTRODUCTION

Organic and biological molecule incorporation into nanoporous silica sol-gel hosts has garnered significant attention in recent years. Aside from being biocompatible, the porous inorganic silica matrix has on numerous occasions been demonstrated to enhance encapsulated guest molecule thermodynamic stability, mostly through molecular

motion restriction.[1-5] Thus proteins were shown to display higher melting temperatures,[6-8] function even under hostile conditions,[9,10] exhibit extended shelf life,[11,12] and organic dyes reportedly acquire exceptional photostability when trapped inside silica sol-gel matrices.[13-15]

A guest molecule will experience a dramatic increase in surface interactions on encapsulation, which inevitably restrict molecular motions. This has spawned careful investigations into how the sol-gel formation process alters molecular motions as well as the surface's influence on nanoscopiclly confined guest molecules. Indeed, probe steady-state fluorescence polarization increased in dip-coated sol-gel thin films as they aged, indicating a progressively constricted matrix environment.[16] Similarly, fluorescent time-resolved anisotropy clearly reveals slowed rotational dynamics during the sol to gel transition. This decrease was attributed to continued silica nanoparticle growth, with the probe molecules adsorbed to the growing particles.[17-19] Relatively slow translational motions have been uncovered within organically modified silica films.[20] In addition, active translational motions have even been found in extensively dried monolith samples.[21] These intriguing phenomena not only reflect the wide range of molecular motions supported by the nanoporous silica sol-gel network, it also reveals potentially diverse physical and chemical properties available to an encapsulated guest molecule. Thus, understanding the factors that influence molecular motions inside a silica sol-gel host should help improve our control over encapsulated guest molecule behavior.

The nanoscopic confinement imposed by a silica sol-gel host both directly restricts guest molecule motions, and influences solvation dynamics. Not surprisingly, solvation dynamics inside a silica sol-gel host are much slower than those in bulk water.[22]

Also, unlike the bulk liquid, multiple diffusion components are needed to describe solvation inside a silica host. While one component generally resembles bulk solvation, a noticeably slower component is attributed to the silica surface retardation effect that results from confinement.[23-25] This slowed dynamic interaction between a guest molecule and its surrounding solvent potentially alters the guest's photophysical properties. For example, we have previously used single-molecule spectroscopy to examine both an encapsulated probe's photophysical properties and mobility simultaneously, confirming that an immobilized probe has higher photostability than its tumbling counterpart.[26] In a subsequent attempt to manipulate molecular mobility using electrostatic interactions, we discovered that Coulombic attraction contributes a minor amount to immobilization inside silica sol-gel.[27,28] Thus, immobilization is likely facilitated by short-range interactions such as van der Waals interaction, hydrogen bonding, physical confinement, hydrophobic interaction, or even molecular templating.[29,30]

To further advance silica sol-gel composite material development and gain further control over molecular dynamics inside nanoporous silica hosts, we continue to examine Coulombic interaction, hydrogen bonding, and solvation dynamics influence on encapsulated probe molecule mobility and photostability in dry, water, and ethanol equilibrated films. Rhodamine 6G (R6G), sulforhodamine B (SRB),

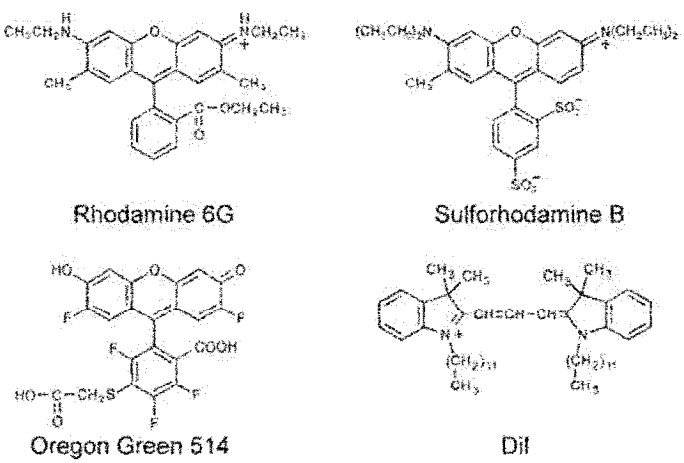

Figure 4.1. R6G, SRB, ORG, and $DiIC_{12}$ molecular structures.

Oregon Green 514 (ORG), and didodecyl-3,3,3',3'-tetramethylindocarbocyanine ($DiIC_{12}$) were chosen to represent cationic, zwitterionic, anionic, and hydrophobic probes, respectively (molecular structures shown in Figure 4.1). More importantly, the strongly acidic SRB sulfonic groups ($pK_a < 1.5$)[31] provide an excellent opportunity to examine hydrogen bonding inside a moderately acidic porous silica environment (isoelectric point = 2.0 ± 0.2).[32] We were able to use single-molecule spectroscopy to compare subtle mobility and photostability changes as both the probe and solvent hydrogen bonding capability varied. In addition, hydrophobic interactions influence was investigated through the $DiIC_{12}$ response toward different solvent media.

4.3 RESULTS AND DISCUSSION

4.3.1 Photostability Measurement

In addition to facilitating mobility classification, fluorescence intensity time traces were used to determine single molecule survival lifetimes in order to reveal the photodegradation kinetic changes on nanoscopic encapsulation. The survival lifetime is defined as the time it takes to photo-degrade the molecule under continuous excitation. This parameter can be directly inferred from the fluorescence intensity time trace and serves as a reliable photostability measure. Accordingly, a collection of single-molecule survival lifetimes was used to construct a "molecule fraction remaining fluorescent ($F(t)$)" *vs* "time elapsed (t)" histogram. The decay in $F(t)$ was fit to single- or bi-exponential components according to Equation 4.1 where τ_1, τ_2, and $\langle\tau\rangle$ are decay time

$$F(t) = a_1 \exp(-t/\tau_1) + a_2 \exp(-t/\tau_2) \quad \textbf{4.1a}$$

$$F(0) = a_1 + a_2 = 1 \quad \textbf{4.1b}$$

$$\langle\tau\rangle = a_1\tau_1 + a_2\tau_2 \quad \textbf{4.1c}$$

constants used to compare probe molecule photostability across different mobilities and environments. Since the survival lifetime is strongly influenced by the excitation rate, all experiments were conducted with an approximately constant excitation power density (~917 $W \cdot cm^{-2}$) to permit genuine photostability comparison.

In addition to the survival lifetime, the dye photostability was characterized using photobleaching quantum yield (ϕ_b) analysis. ϕ_b were calculated according to Equation 4.2

$$\phi_b = \frac{\eta \phi_f}{N_{total}} \qquad \textbf{4.2}$$

where η is the instrument detection efficiency, ϕ_f is the probe fluorescence quantum yield, and N_{total} is the total photons recorded in a fluorescence intensity time trace before the molecule photobleached.[33,34] In our calculations we assumed a 10% detection efficiency. Table 4.1 summarizes the ϕ_f values used to determine ϕ_b based on probe and solvent. All ϕ_f values were determined using R6G in ethanol as a standard reference, which was assumed to be 0.95 under both 514 nm and 543 nm excitation.[35] The dry sample ϕ_b were calculated using the ϕ_f obtained in ethanol. Since $DiIC_{12}$ is only slightly soluble in water, it also used the ϕ_f for ethanol to calculate ϕ_b. The ϕ_b values from many single molecules were then used to construct a "molecule fraction with equal or lower ϕ_b ($F(\phi_b)$)" vs "ϕ_b" histogram. Similar to $F(t)$, the $F(\phi_b)$ decay was fit to single-

Table 4.1. R6G, SRB, and $DiIC_{12}$ fluorescence quantum efficiencies in water and ethanol. The R6G ϕ_f was assumed to be 0.95 and was used as a reference standard. $DiIC_{12}$ was practically insoluble in water.

Dye	ϕ_f in water	ϕ_f in ethanol	Excitation Wavelength (nm)
R6G	0.90	0.95	514
R6G	0.52	0.95	543
SRB	0.15	0.43	543
$DiIC_{12}$	–	0.07	543

or bi-exponential components from which ϕ_1, ϕ_2, and $\langle\phi_b\rangle$ were extracted. To minimize statistical errors, about 200 molecules were studied for each sample.

4.3.2 Solvent Effect on Mobility in Dry Films

Dye molecule translational mobility in freshly formed silicate films was investigated by recording consecutive fluorescence images for a 10 μm × 10 μm sample area. The fluorescence spot spatial distribution between consecutive images was compared. Since image acquisition took approximately 12 minutes, only diffusion on a comparable timescale could be tracked. Dye molecules with higher diffusion rates, if observed at all, would appear as fluorescence streaks in the images. Figure 4.2 provides two R6G fluorescence image sets where each image was taken approximately 12 minutes after the preceding image. The two image sets represent orthogonally polarized emission ($I_{//(t)}$ and $I_{\perp(t)}$) collected from the same sample area. These images effectively display R6G diffusion over the first hour immediately after the sample was spun-cast. Because subsequent investigation would immerse the sample in solvent, it was deliberately overloaded with R6G to offset dye loss upon wetting. The high R6G number density shown is atypical for single-molecule investigations, but that most fluorescence spots represent isolated molecules was indirectly supported by: (*i*) The proportionate number density increase relative to single-molecule films doped with 10-fold less R6G. (*ii*) Discrete intensity jumps associated with blinking and photobleaching that were widely displayed in many fluorescence spot time traces. (*iii*) Frequent observation of fluorescence polarization that conformed to a single emission dipole. Even so, the high R6G number density inevitably resulted in fluorescence spot clustering, rendering some molecules spatially unresolved (less than 200-300 nm separation). It is unlikely that

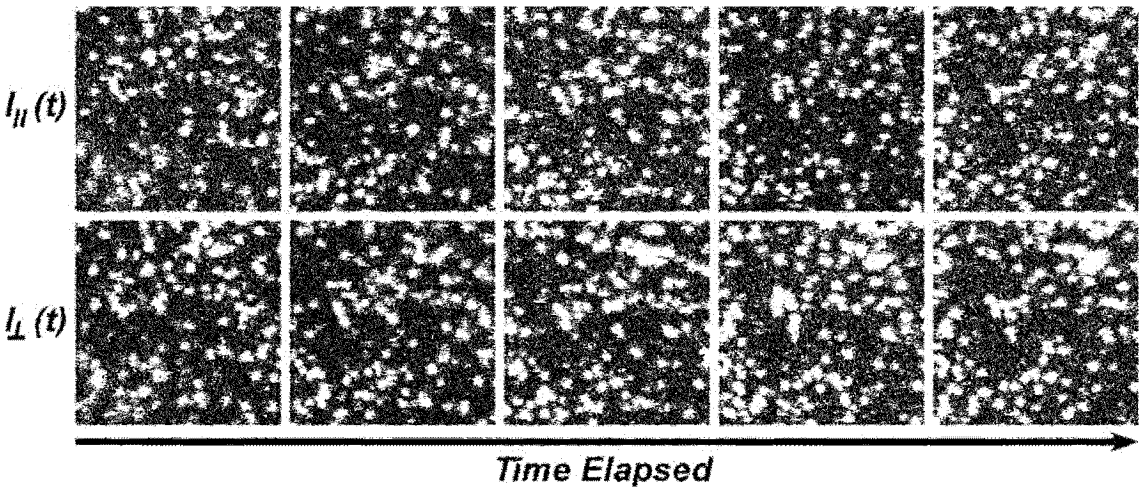

Figure 4.2. Fluorescence image series documenting R6G dry film evolution shortly after the spin-coating process. Since it took approximately 12 minutes to complete a scan, this image series illustrates the gradual decrease in R6G translational motion inside a fresh film over the first hour. The first and second rows represent images recorded from the same 10 μm × 10 μm sample area but constructed from different $I_{//}(t)$ and $I_{\perp}(t)$ detection channels.

these fluorescence clusters were aggregates since both R6G *H*- and *J*-aggregates are expected to occur at significantly higher concentrations.[36-38]

The image series in Figure 4.2 provides a glimpse at encapsulated R6G mobility for the first hour immediately after the film was spun-cast. A freely tumbling R6G molecule should emit isotropic fluorescence and produce an equal fluorescence intensity spots in each polarization-resolved image pair. For an immobilized R6G molecule the fluorescence spot intensity in the polarization-resolved images can vary greatly, depending on its orientation. Immobilized R6G examples are evident in Figure 4.2 and are recognized by the emission intensity disparity between the polarization-resolved images. It is also apparent that many fluorescent spots in the polarization-resolved images display similar emission intensity. This implies that many R6G molecules retain significant rotational freedom. The exceptional freedom enjoyed by R6G at this early stage of silica sol-gel encapsulation is further demonstrated by comparing the first two

images within each polarization set. Here, R6G translational motion was significant enough that the two images do not quite resemble one another even though they were acquired from the same area only 12 minutes apart

When the fluorescence spots were monitored for an hour, by comparing the first and the last images within each polarization set, significant movement beyond the ± 20 nm nano-stage repetition accuracy was observed for over 80% of the fluorescence spots. Translational motion on this timescale practically precludes individual molecule mobility classification since they could not be located for the necessary time trace acquisition. However, they were sufficiently immobilized that most R6G molecule emission was still visualized as diffraction-limited fluorescent spots in these images. This is further supported by the few fluorescence streaks present in these images, since streaky images would strongly indicate moderate translational motion occurring inside the silica sol-gel samples.[39] The image series within each polarization set also suggest that R6G translational motion gradually slowed down as the sample aged. This could result from (*i*) smaller pore formation through the ongoing silanol condensation reaction, (*ii*) silicate pore collapse due to solvent evaporation, or (*iii*) that R6G molecules diffused irreversibly into smaller pores and became severely constrained. Consequently, there is improved fluorescent spot location correlation between the last two images as opposed to the first two images within each polarization set. Disparity in emission intensity between fluorescent spots in the last polarization-resolved image pair also increased as the sample aged and more R6G molecules became immobilized. Even so, the last two images in the polarization sets reveal that R6G diffusion was not completely arrested after aging for

one hour. This agrees with the molecular diffusion recently observed inside extensively aged silica sol-gel monoliths prepared in a similar fashion.[21]

4.3.3 Wet Films

As illustrated in Figure 4.3, equilibrating the sample in water did more than just enhance R6G mobility, more dramatically approximately half the R6G molecules disappeared due to leaching. Being quite soluble in water, most encapsulated R6G would partition favorably into the aqueous medium and readily diffuse away from the silica sol-gel matrix surface. This would leave behind potentially solvated R6G that does not have unrestricted access to leaching channels, or R6G trapped inside small pores where confined solvation was prevalent, a condition that favors immobilization. Indeed, Figure 4.3 reveals a remarkable emission intensity contrast between the polarization-resolved images for most R6G molecules that remain, indicating that they were immobilized. As

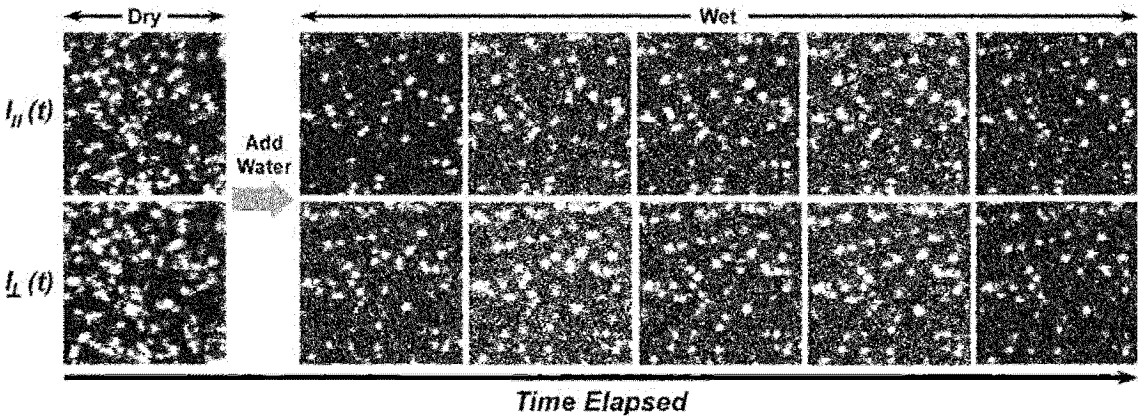

Figure 4.3. Fluorescence image series for R6G before and after the film was equilibrated with water. Significant R6G population is lost upon wetting, probably due to leaching. The remaining R6G molecules are quite immobile since little translational motion is observed over time. The two rows show the orthogonal $I_{//}(t)$ and $I_{\perp}(t)$ detection channels. Since the wet sample fluorescence is considerably less than the dry sample (compare the dry and first wet image), a higher excitation intensity was used starting with the second wet sample image. This increased the background and a more saturating grayscale was applied to better illustrate the single molecule locations. The gradual decrease in both signal and background fluorescence is probably due to dye photobleaching under repeated scanning.

an additional proof for extensive R6G immobilization, the images show that most R6G retained its original position even after one hour in water (compare the second and last images in each polarization set). This is in stark contrast to the dry sample shown in Figure 4.2, which displayed significant molecular diffusion over a one-hour span.

Although not shown, a similar but less dramatic trend was also found in the SRB fluorescence images where the fixed molecule percentage was slightly increased at the expense of mobile intermediate and tumbling molecules in the water-immersed sample. While the silicate film internal pH in water (pH = 5.0±0.5)[27] was sufficient to deprotonate both SRB sulfonic acid groups (pK_a < 1.5)[31] to provide a zwitterion with a negative one net charge, charge-charge surface repulsion was apparently not strong enough to make SRB a more mobile guest than R6G. This is consistent with our previous finding that charge-charge interaction is not a major factor in determining mobility.[27,28] Even with a range of one to three negative charges, mobile ORG was not the dominant species found in our films. Molecular imprinting and shorter range electrostatic interactions may play a more prominent role in controlling the guest molecule mobility under nanoscopic confinement.[29,30] Alternatively, the SRB negative charges may be shielded by a special hydrogen bonding network as illustrated in Figure 4.4.[40] Despite the negative charges, this SRB form could be effectively immobilized near a silica surface through hydrogen bonding.

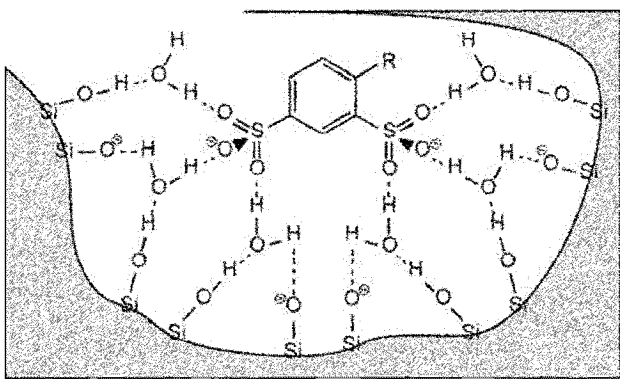

Figure 4.4. Special hydrogen bonding network that might hold SRB in place and help reduce molecular motions surrounding a silica sol-gel encapsulated SRB molecule. R represents the SRB xanthene ring.

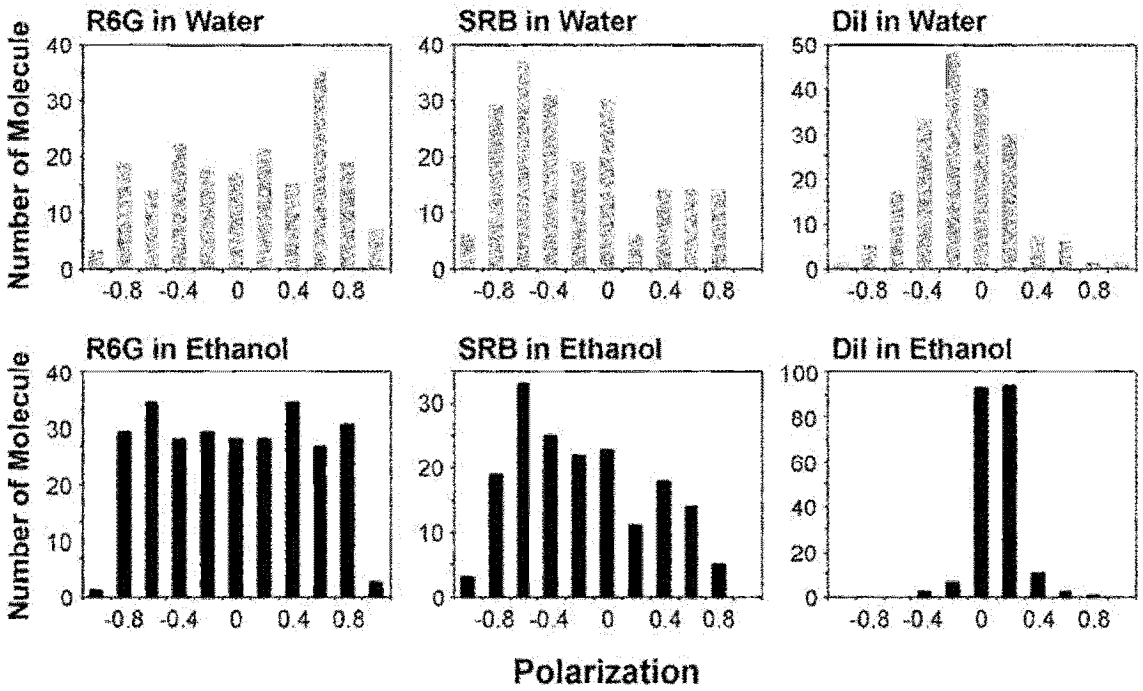

Figure 4.5. R6G, SRB, and $DiIC_{12}$ polarization distributions in water- and ethanol-covered films. Despite a considerable decrease in the tumbling molecule population relative to dry films, $DiIC_{12}$ still displays a higher mobility than R6G and SRB. This is illustrated by the $DiIC_{12}$ peaks around zero polarization that contain tumbling and intermediate molecules. The slight deviation from peaking at zero polarization in some histograms is most likely caused by insufficient statistics.

The relatively flat polarization distributions shown in Figure 4.5 further illustrate that both R6G and SRB were mostly immobilized upon wetting. Finally, even with the two anionic sulfonic groups, SRB could have been immobilized on the silica surface through its cationic imino group, as adsorption experiments have clearly demonstrated that SRB is attracted to both cationic and anionic aquifer materials such as sandstone and limestone, respectively.[31,41]

Despite a positive charge on $DiIC_{12}$, the polarization distribution peak around zero, Figure 4.5, indicates that $DiIC_{12}$ displays considerable mobility in water. This could imply that the micro-environment surrounding the remaining $DiIC_{12}$ molecules is quite different from either R6G or SRB. The higher mobility displayed by $DiIC_{12}$ could be due

to poor molecular imprinting disrupted by the constant and non-directional floppy aliphatic tail motions during the sol-gel formation process. Moreover, the tails hydrophobic nature might have increased mobility by preventing $DiIC_{12}$ from strongly adhering to the hydrophilic silicate surface. Our previous $DiIC_{12}$ study revealed that it exhibited high mobility in dry silicate films.[26] Relative to those dry films, the distribution illustrated in Figure 4.5 actually represents a dramatic reduction in $DiIC_{12}$ mobility upon wetting. Contrary to R6G and SRB, $DiIC_{12}$ leaching was not significant (data not shown), presumably due to the poor $DiIC_{12}$ solubility in water. Interestingly, despite $DiIC_{12}$'s greater solubility in ethanol, a similar lack of $DiIC_{12}$ leaching in ethanol was observed, implying $DiIC_{12}$'s preference for the less polar silica matrix (ethanol and silica glass dielectric constants ε are 25.3 and 3.81, respectively). However, similar to R6G and SRB, the remaining $DiIC_{12}$ were not found to diffuse from their original positions overtime and might have been physically trapped despite their higher mobility.

It is also worth pointing out that the R6G emission intensity in water was considerably less than that from the dry sample. The emission intensity decrease is not R6G specific since the same effect was observed for the other dyes we examined. Nor does the effect appear unique to the silica matrix since it was reported to occur to polyelectrolyte film entrapped probes examined under water.[42] It is therefore quite possible that radiation less relaxation was enhanced by the increase in dynamic interactions between an encapsulated dye and its surrounding solvent molecules upon wetting. Alternatively, the dielectric media presence above a silicate film might alter our instrument's fluorescence collection efficiency. While the latter was unlikely to be a

major factor, it nevertheless might lead to a partial decrease in probe molecule emission intensity.

4.3.4 Mobility Distributions

Table 4.2 summarizes the single molecule R6G, SRB, $DiIC_{12}$, and ORG mobility classification distributions for dry and wet films. Since these results are later used for the lifetime and ϕ_b exponential curve fittings, the tumbling populations are not corrected for high numerical aperture influences. That correction does not specifically identify the misclassified molecules. According to the distributions, the primary mobility displayed by R6G and SRB in dry films was intermediate. This contribution was somewhat less in ORG due to charge-charge repulsion that led to a noticeable increase in tumbling molecules. The intermediate and tumbling molecule preferential leaching in water and ethanol have resulted in an apparent fixed molecule percentage increase for R6G, SRB, and ORG. Of the remaining molecules, the

Table 4.2. Dye mobility distributions in dry, water, and ethanol covered silica sol-gel films. All mobility results are from fresh films except the dry $DiIC_{12}$, which is a compilation of aged film results and the ORG H_2O which is a day one film.

Dye		Fixed (%)	Intermediate (%)	Tumbling (%)
R6G	Dry	23±3	75±3	2±1
	H_2O	69±3	27±3	4±1
	EtOH	57±3	42±3	1±1
SRB	Dry	33±3	63±3	4±1
	H_2O	40±3	59±3	1±0
	EtOH	58±4	39±4	3±1
$DiIC_{12}$	Dry	39±4	14±2	47±4
	H_2O	33±3	56±4	11±2
	EtOH	48±3	38±3	14±2
ORG	Dry	39±3	47±3	14±2
	H_2O	43±4	45±4	12±2

intermediate molecules are more suitable to illustrate the solvent effect on guest-host interactions since they are most likely to lie at the solid-liquid interface. Assuming the sol-gel film structural and chemical environments are identical in all samples, any difference in guest-host interaction between SRB, ORG, and R6G should originate directly from the different dye subsistent groups. For example, the propensity for an intermediate molecule to leave the surface for an extended period of time, or temporarily leave the surface and change orientation, depends on how well the solvent can stabilize the molecule relative to the silicate surface. Consequently, multiply charged species are expected to be better stabilized in water (ε = 80.1 at 293 K) than on a less polar silicate surface (ε = 3.81 at 293 K). This may help explain the decreasing intermediate molecule percentage found for SRB (triply charged), ORG (single to triple charged), and R6G (singly charged) in water as the maximum localized charge number decreases. This trend becomes less apparent in a less polar solvent like ethanol (ε = 25.3 at 293 K). It is worth noting that we deliberately exclude the $DiIC_{12}$ mobility distributions in this comparison due to its different molecular skeleton.

The high $DiIC_{12}$ tumbling molecule percentage (47%) in the dry film demonstrates the molecule's hydrophobic nature and its disfavor toward immobilization on a hydrophilic silica surface. This mismatch in polarity is so dominant that Coulombic attraction between the oppositely charged $DiIC_{12}$ and silica surface appears unimportant. The Coulombic attraction is likely further weakened by a close counter ion association in solvent. The high tumbling hydrophobic guest percentage is an indication of a relatively non-polar solvent environment inside the dry film, presumably due to ethanol that had not completely vaporized during the spin-coating process. Ethanol was also produced by

ongoing condensation reactions between Si–OH and unhydrolyzed Si–OEt as the sample aged. There was a substantial decrease in the tumbling $DiIC_{12}$ percentage when the solvent was replaced with water, reflecting its poor solubility in an aqueous medium. Consequently, the mobility was dominated by intermediate molecules, which may indicate that $DiIC_{12}$ preferred neither the silica surface nor the aqueous liquid medium. In the less polar ethanol, however, $DiIC_{12}$ appeared to retain greater mobility. Although not seen in fluorescence image scans, the $DiIC_{12}$ solvation in ethanol might have led to a minor leaching problem, which is evident by the small increase in the fixed $DiIC_{12}$ molecule percentage.

4.3.5 Solvent Effect on Photostability

It is worth noting that different organic dyes possess different photobleaching pathways, hence each dye's photostability depends strongly on its own photobleaching mechanism. Photobleaching mechanisms are complicated and are a rarely explored research area due to the difficulty in identifying the non-fluorescent photo-products. Depending on the excitation intensity, photobleaching can be either a single- or a multi-photon process. Given the low excitation intensity (~1 $kW \cdot cm^{-2}$) employed in the current studies, multi-photon photobleaching processes are unlikely. At low intensity and under ambient atmosphere, the primary photobleaching process is believed to be photo-oxidation. In this process, reactive singlet oxygen is generated by the dye triplet state interaction with a ground state oxygen molecule, which then oxidizes a dye molecule into either a non-fluorescent or an off-resonance product. Spectroscopic evidence for peroxide and di-epoxide products have been found among single terrylene molecule photo-products.[43]

The single-photon R6G photobleaching mechanism has been examined recently. In the simplest case, a three-level mechanism model formed by the S_0, S_1, and T_1 states is sufficient to describe photobleaching kinetics.[44] A more elaborate model adds an extra single-photon photobleaching pathway that involves a radical anion intermediate level, which can also accommodate multi-photon photobleaching processes.[45] Although no photobleaching study on SRB or ORG has been reported, since R6G, SRB, and ORG are all built from a xanthene skeleton, it makes us believe that they share a similar photo-oxidation reaction pathway during photobleaching. In all three, the conjugated xanthene moiety forms the dye fluorophore. For example, in fluorescein (also possessing a xanthene skeleton) photo-oxidation was investigated using a three-level model to explore singlet oxygen scavengers effect on photo-oxidation.[46-48] Evidence for photo-induced intersystem crossing from S_1 to T_1 in $DiIC_{12}$ has also allowed a three-level model photobleaching mechanism to develop. However, unlike xanthene, the $DiIC_{12}$ cyanine moiety can undergo a *cis-trans* isomerization reaction that complicates photobleaching description. Although not directly investigated in $DiIC_{12}$, *cis-trans* isomerization in molecular analogs, such as Cy3 and Cy5, have been studied and its implications to photobleaching examined.[49,50] In general, all organic dyes exhibit higher photostability in an oxygen-depleted atmosphere, signifying the photo-oxidation role in single-photon photobleaching processes. As a result, factors that accelerate oxygen diffusion are expected to reduce photostability. This may explain the shorter survival lifetime found in our wet samples (except for SRB) relative to the dry samples, since the films' porous framework could swell on solvation.[51,52]

Table 4.3. Survival lifetime analysis based on mono- and bi-exponential decay functions

Dry	Category	a_1	τ_1 (second)	a_2	τ_2 (second)	$\langle r^2 \rangle$	$\langle \tau \rangle$ (second)
Dry							
R6G	Fixed	0.59±0.03	10±1	0.41±0.03	82±5	0.994	39.5±5.4
	Intermediate	0.22±0.01	11±1	0.78±0.01	103±1	0.999	82.8±2.1
DiIC$_{12}$	Fixed	0.84±0.02	13±1	0.16±0.02	130±31	0.995	31.7±8.4
	Tumbling	0.81±0.02	4.3±0.2	0.19±0.01	64±7	0.998	15.6±2.2
SRB	Fixed	1.0	20±1	-	-	0.989	20±1
	Intermediate	0.95±0.02	28±1	0.05±0.03	442±631	0.992	48.7±46.3
Water							
R6G	Fixed	0.49±0.01	3.0±0.1	0.51±0.01	32±3	0.995	17.8±1.9
	Intermediate	1.0	26±1	-	-	0.994	26±1
DiIC$_{12}$	Fixed	0.43±0.02	1.1±0.1	0.57±0.02	11±1	0.996	6.7±0.9
	Intermediate	0.54±0.05	5.9±0.5	0.46±0.05	28±3	0.996	16.1±3.3
	Tumbling	1.0	9.8±0.8	-	-	0.858	9.8±0.8
SRB	Fixed	0.27±0.1	1.9±0.1	0.73±0.01	38 ± 1	0.998	28.3±1.3
	Intermediate	1.0	76±1	-	-	0.995	76±1
Ethanol							
R6G	Fixed	0.63±0.02	4.2±0.2	0.37±0.02	38±3	0.994	16.7±2.1
	Intermediate	0.05±0.01	3±2	0.95±0.01	33±1	0.996	31.5±1.4
DiIC$_{12}$	Fixed	0.32±0.01	3.3±0.3	0.68±0.01	30±1	0.997	21.5±1.1
	Intermediate	0.33±0.04	7±1	0.67±0.04	48±3	0.991	34.5±4.5
	Tumbling	1.0	13±1	-	-	0.972	13±1
SRB	Fixed	0.40±0.01	5.4±0.3	0.60±0.01	80±2	0.997	50.2±2.2
	Intermediate	0.17±0.02	11±1	0.83±0.02	113±3	0.997	95.7±5.1

After the probes were separated into different mobility classes, the photostability in each class was determined by measuring its survival time against photo-degradation under continuous illumination. In Table 4.3, we summarize the R6G, $DiIC_{12}$, and SRB survival lifetimes recorded for dry, water-covered, and ethanol-covered films. The tumbling R6G and SRB photostabilities are not included due to insufficient tumbling molecule populations to support statistically meaningful analysis. Although the molecules have been grouped into different mobility classes, two distinct survival lifetimes are generally required to characterize their photostabilities. This suggests that mobility alone cannot account for the heterogeneous guest behavior found in silica sol-gel hosts. It is quite plausible that different local environments surround the molecules within each mobility class, hence contributing to the observed photostability heterogeneity. In addition, the cyanine dye *cis-trans* isomerization reaction may broaden the photostability distribution for $DiIC_{12}$, adding to the observed inhomogeneous behavior.[50] On the other

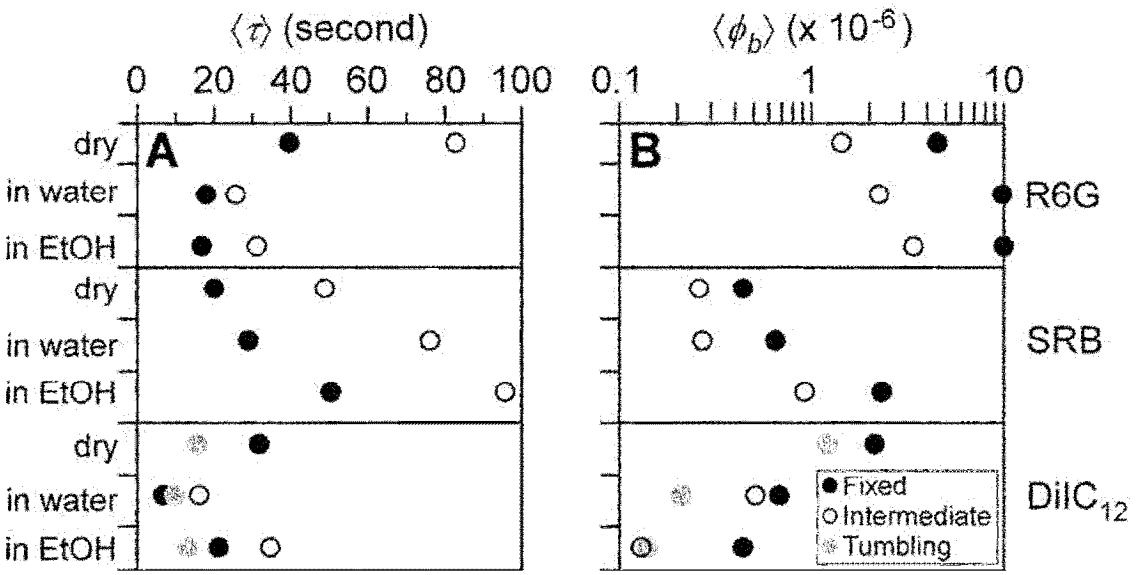

Figure 4.6. (A) The average survival lifetime $\langle\tau\rangle$ and (B) the average photobleaching quantum yield $\langle\phi_b\rangle$ for R6G, SRB, and $DiIC_{12}$ in dry, water-covered, and ethanol-covered films. For a better presentation, error bars are not shown.

hand, Berglung pointed out that multi-exponential photobleaching lifetimes obtained from single-molecule and ensemble measurements may be an artifact caused by a non-uniform laser excitation profile and is not necessarily due to sample heterogeneity.[53] Since the excitation profile employed in this study is more Gaussian-like than uniform, and that spatial heterogeneity is ubiquitous in sol-gel silicates, the inhomogeneous survival lifetimes we observed are likely influenced by all the above mentioned factors.

To facilitate comparison, the average probe survival lifetime $\langle \tau \rangle$ under each experimental condition was calculated and plotted in Figure 4.6A. According to the figure, intermediate molecules appear noticeably more photo-stable relative to fixed molecules. This observation applies to dry, water-covered, and ethanol-covered R6G and SRB. Since the longer a molecule survives the greater the probability a polarization change will occur, this higher intermediate photostability could be an artifact of their high intrinsic photostabilities. In addition, the intermediate R6G and SRB survival lifetimes could be skewed toward longer lifetimes by a few exceptionally photostable molecules. This is evident for intermediate SRB in dry films by the huge error associated with its τ_2. However this effect becomes less apparent in $DiIC_{12}$, presumably due to a lower photostability. In view of this potential artifact, the intermediate molecule photostability will not be further discussed.

In addition to survival lifetime, photostability for the same data sets were calculated using photobleaching quantum yield (ϕ_b).[33,34] This method allows direct photostability comparison between different dyes, regardless of their excitation rate and ϕ_f values. It also permits dye ϕ_b comparison in different solvent media, hence eliminating excitation efficiency and ϕ_f changes resulting from solvation. By excluding the solvation

Table 4.4 Photobleaching quantum yield (ϕ_b) based on mono- and bi-exponential decay functions

Dry	Category	a_1	ϕ_1 ($\times 10^{-6}$)	a_2	ϕ_2 ($\times 10^{-6}$)	$\langle r^2 \rangle$	$\langle \phi_b \rangle$ ($\times 10^{-6}$)
Dry							
R6G	Fixed	0.34±0.02	10.9±2.5	0.66±0.02	1.20±0.12	0.988	4.52±1.10
	Intermediate	1.0	1.43±0.02	-	-	0.969	1.43±0.02
DiIC$_{12}$	Fixed	0.36±0.01	0.30±0.04	0.64±0.01	3.16±0.17	0.992	2.13±0.10
	Tumbling	1.0	1.21±0.01	-	-	0.992	1.21±0.01
SRB	Fixed	1.0	0.44±0.01	-	-	0.981	0.44±0.01
	Intermediate	1.0	0.26±0.01	-	-	0.986	0.26±0.01
Water							
R6G	Fixed	0.78±0.01	3.00±0.09	0.22±0.01	33.9±3.8	0.996	9.81±1.18
	Intermediate	1.0	2.24±0.06	-	-	0.974	2.24±0.06
DiIC$_{12}$	Fixed	0.38±0.01	0.08±0.01	0.62±0.01	1.06±0.04	0.994	0.68±0.03
	Intermediate	0.92±0.02	0.21±0.01	0.08±0.02	3.82±2.20	0.992	0.51±0.25
	Tumbling	1.0	0.21±0.01	-	-	0.973	0.21±0.01
SRB	Fixed	0.64±0.01	0.20±0.02	0.36±0.01	1.44±0.24	0.992	0.65±0.11
	Intermediate	0.74±0.04	0.11±0.01	0.26±0.04	0.74±0.25	0.976	0.27±0.10
Ethanol							
R6G	Fixed	0.76±0.01	2.82±0.07	0.24±0.01	33.1±2.7	0.998	9.98±0.88
	Intermediate	0.89±0.05	1.84±0.17	0.11±0.05	15.6±11.8	0.981	3.39±2.11
DiIC$_{12}$	Fixed	0.88±0.03	0.11±0.01	0.12±0.03	2.75±1.87	0.962	0.44±0.31
	Intermediate	1.0	0.13±0.01	-	-	0.979	0.13±0.01
	Tumbling	1.0	0.14±0.01	-	-	0.943	0.14±0.01
SRB	Fixed	0.54±0.01	0.38±0.03	0.46±0.01	4.59±0.30	0.993	2.32±0.16
	Intermediate	0.49±0.01	0.18±0.01	0.51±0.01	1.64±0.07	0.997	0.92±0.04

electronic effects, ϕ_b serves as a complementary indicator to survival lifetime and provides information regarding solvation's effect on photokinetics. Moreover as long as photobleaching is kept to a single-photon process, ϕ_b should be insensitive to excitation intensity variations between measurements and therefore especially useful for comparing data collected over an extended time period. Since ϕ_b represents the probability that a molecule will photobleach per excitation, a decrease in ϕ_b corresponds to an increase in molecule photostability.

The ϕ_b analysis results are summarized in Table 4.4 and the averaged photobleaching quantum yields $\langle\phi_b\rangle$ are presented as a log plot in Figure 4.6B. Similar to the survival lifetime analysis, many decays in Table 4.4 were only well fit with a bi-exponential function, indicating the silica sol-gel sample's spatial heterogeneity. On the other hand, the number of mono-exponential decays in the ϕ_b analysis is greater than in the survival lifetimes, Table 4.3. The additional heterogeneity retained in the survival lifetime analysis is probably caused by local environment changes to the excitation efficiency or ϕ_f, which is to some extent accounted for in the ϕ_b analysis. Excluding these electronic effects, it becomes clear from the bi-exponential fitting results in Table 4.4 that all fixed molecules (with the exception of the dry SRB sample) exhibit heterogeneous photobleaching kinetics. This is consistent with the idea that a disorganized solid silica framework would influence oxygen diffusion in a region specific fashion. In contrast, the tumbling molecules in Table 4.4 show mono-exponential ϕ_b decay behavior. This suggests that tumbling molecules experience more homogeneous photobleaching kinetics, probably due to a consistent oxygen supply in larger and more accessible silica

pores. Intermediate molecules exhibit both mono-and bi-exponential decays, reflecting their interfacial location where the oxygen supply may vary.

4.3.5.1 Rhodamine 6G

According to Figure 4.6A, the fixed R6G survival lifetime decreased by half when equilibrated with water or ethanol. This could result from an increase in solvent molecule dynamic interactions within the wet samples. It is well known that reducing dynamic interactions helps limit relaxation processes that lead to encapsulated dye molecule photodegradation. This explains why fixed molecules exhibit a higher photostability than tumbling molecules.[26] This kinetic influence is demonstrated by the larger $\langle \phi_b \rangle$ for R6G in ethanol and water relative to the dry sample, Figure 4.6B. Based on the lifetimes alone water or ethanol might have caused an unexpected increase in excitation efficiency, shortening the R6G survival lifetime, and leading to an apparent decrease in photostability. But, in this case the R6G ϕ_b trend shows that the lifetime and number of photons emitted were both reduced by the solvent interaction. This corresponds to our observation that under constant excitation power the dye fluorescence intensity decreased after solvation. Since both $\langle \tau \rangle$ and $\langle \phi_b \rangle$ for fixed R6G in water and ethanol are within experimental error to one another, this suggests the solvents influenced R6G–silica interactions in a similar fashion, both electronically and kinetically. This can be explained since (*i*) R6G is readily soluble in both water and ethanol. Thus, R6G is equally well solvated in either solvent. (*ii*) R6G cannot hydrogen bond; it is therefore unlikely to differentiate between water and ethanol based on their hydrogen bonding abilities. (*iii*) Fixed molecules that do not leach into the solvent medium are likely trapped in small pores with only a thin solvent shell separating the molecules and the silica surface. It has

been reported that solvation dynamics in confined liquids are usually slower than those in the bulk liquid, due to a more viscous liquid layer adjacent to the solid surface.[22-25,54-63] Although solvation dynamics are generally faster in water than in ethanol,[55,56] this surface drag is expected to slow down solvation dynamics in our samples considerably and minimize the difference between water and ethanol.

4.3.5.2 Sulforhodamine B

Compared to R6G, the SRB $\langle\tau\rangle$ and $\langle\phi_b\rangle$ analysis results appear less consistent with one another. The $\langle\tau\rangle$ indicates that water and ethanol extend the dye lifetime over that of the dry sample, but the $\langle\phi_b\rangle$ indicates that the dye survives fewer excitations in the solvents. Unlike R6G, SRB solvation does not appear to enhance the excitation efficiency since it did not lead to shorter $\langle\tau\rangle$ values. Thus, the solvent-covered samples display a decreased photostability due to increased solvent molecule dynamic interactions. Although SRB and R6G share a similar molecular skeleton, SRB is quite different from R6G in two major aspects. First, SRB is multiply charged and zwitterionic at moderate pH ($pK_a < 1.5$). With an internal pH over 1.5 in both dry and water-equilibrated films,[27] the two SRB sulfonic groups will deprotonate and provide the molecule a net negative charge. Second, the two SRB sulfonic groups are able to hydrogen bond protic solvents such as water or ethanol as illustrated in Figure 4.4.[40]

With multiple charges, SRB has a strong dipole moment that can arrange surrounding solvent molecules into a highly directional solvation shell. This solvation shell generates a polarization field that is constantly disrupted, hence weakened, by bulk solution random molecular motions. However, under the porous silica sol-gel matrix enforced nanoscopic confinement the solvation shell polarization field will presumably

be weakened to a lesser extent, as a result of (*i*) a relatively static silica framework that reduces random molecular motions and (*ii*) the reduced polarization field perturbation associated with the relatively less polar silica surface influence.[61] Since fixed SRB that do not leach into a solvent medium are more likely to be confined in small pores, both effects are expected to be significant. A stronger polarization field surrounding SRB will hinder molecular motions and slow solvation dynamics relative to those observed in bulk liquids. Moreover, hydrogen bonding may also help anchor SRB directly or indirectly to the silica surface and further discourage random molecular motions, as illustrated in Figure 4.4. Very high initial (r_0) and residual (r_∞) fluorescence anisotropy values have been observed for silica sol-gel encapsulated SRB, indicating that nanoscopic confinement severely constrains SRB motion.[64] With molecular motions subdued, dynamic interactions that lead to photodegradation will be less probable.

This is evident in the increase in $\langle \phi_b \rangle$ for fixed SRB in ethanol relative to water. The less polar ethanol is expected to produce a weaker polarization field than water, thus permitting more dynamic molecular motions, making the molecule more susceptible to photodegradation. However, the increase in $\langle \tau \rangle$ would seem to contradict this, potentially indicating that the bulk obtained ϕ_f was not appropriate for the confined hydrogen bonded system, which could also provide stabilizing non-photodegradation relaxation pathways. The higher $\langle \tau \rangle$ and $\langle \phi_b \rangle$ indicate that SRB in ethanol is both longer lived and simultaneously less photostable. Since $\langle \tau \rangle$ and $\langle \phi_b \rangle$ in water and dry films are similar to each other it may imply that SRB is mostly solvated by water in the dry film. This potential preference for water over the less polar ethanol can be understood in light of the strong dipole moment associated with the multiply charged zwitterionic SRB molecule.

4.3.5.3 Didodecyl-3,3,3',3'-tetramethylindocarbocyanine

$DiIC_{12}$ is the most non-polar probe employed in this study and it was also the least consistent in $\langle\tau\rangle$ and $\langle\phi_b\rangle$ behavior between the three environments. Despite its positive charge $DiIC_{12}$ is almost insoluble in water, but readily soluble in ethanol. The poor $DiIC_{12}$ solubility in polar environments will probably keep it closely counter ion associated inside the silica sol-gel matrix, weakening charge attraction. As a result, $DiIC_{12}$ in dry films likely sought to preferentially associate with residual ethanol, a poly-condensation reaction side product of the silica sol-gel formation process. Thus, it is not difficult to see why $\langle\tau\rangle$ for tumbling $DiIC_{12}$, and to a lesser extent fixed $DiIC_{12}$, in dry films are similar to those in ethanol (Figure 4.6A). More importantly, the figure indicates that the increased fixed survival lifetime relative to tumbling $DiIC_{12}$ is maintained in both dry and ethanol-covered films. This photostability contrast becomes more apparent when only the fixed and tumbling $DiIC_{12}$ major component survival lifetimes in Table 4.3 are considered. A greater than 2-fold longer fixed $DiIC_{12}$ survival lifetime is observed relative to tumbling $DiIC_{12}$ in both dry (ratio of τ = 13:4.3) and ethanol covered (ratio of τ = 30:13) films. This relationship was not preserved in the water covered $DiIC_{12}$ sample.

A somewhat different picture emerges when the $\langle\phi_b\rangle$ values are considered, Figure 4.6B. Although $DiIC_{12}$ in a dry film may be solvated by ethanol, Figure 4.6B suggests that the ethanol-covered sample exhibits very different photobleaching kinetics. In both dry and ethanol covered films the tumbling populations became more stable relative to fixed; while in water the fixed molecules remain less stable but more comparable to the ethanol covered sample. The decreased tumbling $\langle\phi_b\rangle$ likely represents an increase in the ϕ_f for the tumbling state relative to the fixed state. The fuller solvation experienced by

the tumbling $DiIC_{12}$ would weaken the counter ion's influence on the fluorophore, as well as increase collisional quenching of the triplet state. Both water and ethanol covered samples in Figure 4.6B register a noticeable decrease in $\langle\phi_b\rangle$ (greater photostability) compared to dry $DiIC_{12}$. The decrease in the oxygen diffusion rate through the solvent relative to the air filled pores might explain the decreased solvent ϕ_b. But, for both $DiIC_{12}$ and SRB the ϕ_b's appear to indicate that they are more photostable than R6G, an accepted standard of photostability. At least some of this apparent photostability might be due to the unexpectedly low ϕ_f values obtained for $DiIC_{12}$ and SRB (Table 4.1). $DiIC_{12}$ especially presented problems in determining ϕ_f due to surface adsorption during the experiment. Higher ϕ_f values would shift the ϕ_b more in line with the R6G values obtained. This could also indicate that the ethanol like ϕ_f assumption used to calculate the dry sample ϕ_b was not appropriate due to silica surface influence on the dye photophysical properties within the pores.

Perhaps the most prominent $DiIC_{12}$ feature in Figure 4.6A is that its survival lifetime is shorter and spans a narrower range than R6G or SRB in all environments. The shorter survival lifetime may result from the $DiIC_{12}$ unique molecular dynamics associated with the two floppy aliphatic chains. The narrow $DiIC_{12}$ survival lifetime range found in water and ethanol covered films may imply that molecular dynamics dominate solvated $DiIC_{12}$ photobleaching kinetics and that they do not vary significantly in different media. The insensitivity toward water or ethanol is demonstrated by the similarity in fixed and tumbling molecule $\langle\phi_b\rangle$ values in both solvent media, Figure 4.6B, even though their lifetimes vary significantly. The lack of solvent sensitivity could be related to the highly non-polar $DiIC_{12}$ aliphatic chains minimizing their free energy by

pushing the chains toward the less polar silica sol-gel matrix in either water or ethanol. This would explain why $DiIC_{12}$ in a dry film does not readily leach into water or ethanol when covered by solvent. Similar hydrophobic and hydrophilic interactions have already been utilized to control fluorescent donor and acceptor molecule placement inside mesoporous silica sol-gel hosts to examine energy transfer.[65,66] Since molecular dynamics associated with the aliphatic chains are believed responsible for $DiIC_{12}$'s accepted low photostability, the lack of major chain-solvent interaction differences may explain why $DiIC_{12}$ photostability appears relatively insensitive to the external solvent. Even though the tertiary amine in the $DiIC_{12}$ imidazole core may participate in hydrogen bonding and potentially enhance photostability, the nitrogen is more likely to be heavily involved in π-π conjugation and show little hydrogen bonding tendency. Examining the silica sol-gel encapsulated $DiIC_{12}$ photostability in a more non-polar solvent medium like n-hexane would help release the aliphatic chains from the silica matrix and provide new insight into the relationship between $DiIC_{12}$ solvation dynamics and photostability.

4.4 CONCLUSION

Using fluorescent probes that carry different (*i*) molecular charges, (*ii*) hydrogen bonding capabilities, and (*iii*) hydrophobic interaction propensities, we have began to delineate these three factors' respective influence on encapsulated guest molecule mobility and photostability. The surprisingly high zwitterionic SRB immobilization was attributed to hydrogen bonding that helps lock the molecule into a relatively fixed position under nanoscopic confinement. This hydrogen bonding effect not only influenced SRB mobility, but also slowed solvation dynamics surrounding the molecule such that SRB photostability was maintained, even in wet samples. With no hydrogen

bonding to reduce molecular motions, R6G experienced a dramatic drop in survival lifetime due to enhanced guest-solvent interactions. Coulombic repulsion's influence was readily observed in anionic ORG where the tumbling molecule percentage was found to be considerably higher than R6G and SRB despite a similar molecular skeleton. Hydrophobic interactions pertaining to $DiIC_{12}$'s aliphatic chains continue to dominate the molecular properties in dry, water, and ethanol covered samples. Since both water and ethanol are more polar than the silica host, $DiIC_{12}$ was likely pushed toward the solid-liquid interface where the non-polar aliphatic chains could interact more favorably with the silica matrix. This transferred the tumbling $DiIC_{12}$ population into intermediate population with a relatively narrow survival lifetime range in dry, water-, and ethanol-covered samples.

Chapter IV References

(1) Nguyen, D. T.; Smit, M.; Dunn, B.; Zink, J. I. *Chem. Mater.* **2002**, *14*, 4300.
(2) Jin, W.; Brennan, J. D. *Anal. Chim. Acta* **2002**, *461*, 1.
(3) Flora, K. K.; Brennan, J. D. *Chem. Mater.* **2001**, *13*, 4170.
(4) Eggers, D. K.; Valentine, J. S. *J. Mol. Biol.* **2001**, *314*, 911.
(5) Badjic, J. D.; Kostic, N. M. *Chem. Mater.* **1999**, *11*, 3671.
(6) Zheng, L.; Brennan, J. D. *Analyst* **1998**, *123*, 1735.
(7) Zheng, L.; Flora, K.; Brennan, J. D. *Chem. Mater.* **1998**, *10*, 3974.
(8) Lan, E. H.; Dave, B. C.; Fukuto, J. M.; Dunn, B.; Zink, J. I.; Valentine, J. S. *J. Mater. Chem.* **1999**, *9*, 45.
(9) Li, J.; Tan, S. N.; Oh, J. T. *Journal of ElectroAnal. Chem.* **1998**, *448*, 69.
(10) Van Unen, D.-J.; Engbersen, J. F. J.; Reinhoudt, D. N. *Biotechnol. Bioeng.* **2001**, *75*, 154.
(11) Shtelzer, S.; Braun, S. *Biotechnology and Applied Biochemistry* **1994**, *19*, 293.
(12) Aylott, J. W.; Richardson, D. J.; Russell, D. A. *Analyst* **1997**, *122*, 77.
(13) Avnir, D.; Levy, D.; Reisfeld, R. *J. Phys. Chem.* **1984**, *88*, 5956.
(14) Suratwala, T.; Gardlund, Z.; Davidson, K.; Uhlmann, D. R.; Watson, J.; Bonilla, S.; Peyghambarian, N. *Chem. Mater.* **1998**, *10*, 199.
(15) Yariv, E.; Schultheiss, S.; Saraidarov, T.; Reisfeld, R. *Opt. Mater.* **2001**, *16*, 29.
(16) Huang, M. H.; Soyez, H. M.; Dunn, B. S.; Zink, J. I. *Chem. Mater.* **2000**, *12*, 231.
(17) Geddes, C. D.; Birch, D. J. S. *J. Non-Cryst. Solids* **2000**, *270*, 191.
(18) Geddes, C. D.; Karolin, J.; Birch, D. J. S. *J. Phys. Chem. B* **2002**, *106*, 3835.
(19) Tleugabulova, D.; Zhang, Z.; Brennan, J. D. *J. Phys. Chem. B* **2003**, *107*, 10127.
(20) Martin-Brown, S. A.; Fu, Y.; Saroja, G.; Collinson, M. M.; Higgins, D. A. *Anal. Chem.* **2005**, *77*, 486.
(21) Hellriegel, C.; Kirstein, J.; Braeuchle, C.; Latour, V.; Pigot, T.; Olivier, R.; Lacombe, S.; Brown, R.; Guieu, V.; Payrastre, C.; Izquierdo, A.; Mocho, P. *J. Phys. Chem. B* **2004**, *108*, 14699.
(22) Pal, S. K.; Sukul, D.; Mandal, D.; Sen, S.; Bhattacharyya, K. *J. Phys. Chem. B* **2000**, *104*, 2613.
(23) Loughnane, B. J.; Fourkas, J. T. *J. Phys. Chem. B* **1998**, *102*, 10288.
(24) Loughnane, B. J.; Farrer, R. A.; Scodinu, A.; Reilly, T.; Fourkas, J. T. *J. Phys. Chem. B* **2000**, *104*, 5421.
(25) Loughnane, B. J.; Farrer, R. A.; Fourkas, J. T. *J. Phys. Chem. B* **1998**, *102*, 5409.
(26) Viteri, C. R.; Gilliland, J. W.; Yip, W. T. *J. Am. Chem. Soc.* **2003**, *125*, 1980.
(27) Gilliland, J. W.; Yokoyama, K.; Yip, W. T. *Chem. Mater.* **2004**, *16*, 3949.
(28) Gilliland, J. W.; Yokoyama, K.; Yip, W. T. *J. Phys. Chem. B* **2005**, *109*, 4816.
(29) Lu, Y.; Cao, G.; Kale, R. P.; Prabakar, S.; Lopez, G. P.; Brinker, C. J. *Chem. Mater.* **1999**, *11*, 1223.
(30) Fireman-Shoresh, S.; Avnir, D.; Marx, S. *Chem. Mater.* **2003**, *15*, 3607.
(31) Kasnavia, T.; Vu, D.; Sabatini, D. A. *Ground Water* **1999**, *37*, 376.
(32) Park, G. A. *Chem. Rev.* **1965**, *65*, 177.
(33) Fleury, L.; Sick, B.; Zumofen, G.; Hecht, B.; Wild, U. P. *Mol. Phys.* **1998**, *95*, 1333.
(34) Lill, Y.; Hecht, B. *Appl. Phys. Lett.* **2004**, *84*, 1665.

(35) Drexhage, K. H. Structure and Properties of Laser Dyes. In *Dye Lasers*; 2nd ed.; Schafer, F. P., Ed.; Springer-Verlag: Berlin, 1977; Vol. 1; pp 144.
(36) Blonski, S. *Chem. Phys. Lett.* **1991**, *184*, 229.
(37) Lin, C. T.; Mahloudji, A.M.; Li, L.; Hsiao, M.W. *Chem. Phys. Lett.* **1992**, *193*, 8.
(38) del Monte, F.; Mackenzie, J. D.; Levy, D. *Langmuir* **2000**, *16*, 7377.
(39) Bardo, A. M.; Collinson, M. M.; Higgins, D. A. *Chem. Mater.* **2001**, *13*, 2713.
(40) Li, Q.; Weng, S.; Wu, J.; Zhou, N. *J. Phys. Chem. B* **1998**, *102*, 3168.
(41) Sabatini, D. A. *Ground Water* **2000**, *38*, 651.
(42) Li, Y.; Yip, W. T. *Langmuir* **2004**, *20*, 11039.
(43) Christ, T.; Kulzer, F.; Bordat, P.; Basche, T. *Angew. Chem., Int. Edit.* **2001**, *40*, 4192.
(44) Eggeling, C.; Volkmer, A.; Seidel, C. A. M. *ChemPhysChem* **2005**, *6*, 791.
(45) Zondervan, R.; Kulzer, F.; Kol'chenko, M. A.; Orrit, M. *J. Phys. Chem. A* **2004**, *108*, 1657.
(46) Periasamy, N.; Bicknese, S.; Verkman, A. S. *Photochem. Photobiol.* **1996**, *63*, 265.
(47) Song, L.; Varma, C. A. G. O.; Verhoeven, J. W.; Tanke, H. J. *Biophys. J.* **1996**, *70*, 2959.
(48) Gaigalas, A. K.; Wang, L.; Cole, K. D.; Humphries, E. *J. Phys. Chem. A* **2004**, *108*, 4378.
(49) Ha, T.; Xu, J. *Phys. Rev. Lett.* **2003**, *90*, 223002.
(50) Widengren, J.; Schwille, P. *J. Phys. Chem. A* **2000**, *104*, 6416.
(51) Hou, Y. W.; Bardo, A. M.; Martinez, C.; Higgins, D. A. *J. Phys. Chem. B* **2000**, *104*, 212.
(52) Hou, Y.; Higgins, D. A. *J. Phys. Chem. B* **2002**, *106*, 10306.
(53) Berglund, A. J. *J. Chem. Phys.* **2004**, *121*, 2899.
(54) Loughnane, B. J.; Farrer, R. A.; Scodinu, A.; Fourkas, J. T. *J. Chem. Phys.* **1999**, *111*, 5116.
(55) Vajda, S.; Jimenez, R.; Rosenthal, S. J.; Fidler, V.; Fleming, G. R.; Castner, E. W., Jr. *J. Chem. Soc., Faraday Trans.* **1995**, *91*, 867.
(56) Horng, M. L.; Gardecki, J. A.; Papazyan, A.; Maroncelli, M. *J. Phys. Chem.* **1995**, *99*, 17311.
(57) Sarkar, N.; Datta, A.; Das, S.; Bhattacharyya, K. *J. Phys. Chem.* **1996**, *100*, 15483.
(58) Sarkar, N.; Das, K.; Datta, A.; Das, S.; Bhattacharyya, K. *J. Phys. Chem.* **1996**, *100*, 10523.
(59) Datta, A.; Pal, S. K.; Mandal, D.; Bhattacharyya, K. *J. Phys. Chem. B* **1998**, *102*, 6114.
(60) Baumann, R.; Ferrante, C.; Kneuper, E.; Deeg, F.-W.; Braeuchle, C. *J. Phys. Chem. A* **2003**, *107*, 2422.
(61) Baumann, R.; Ferrante, C.; Deeg, F. W.; Brauchle, C. *J. Chem. Phys.* **2001**, *114*, 5781.
(62) Halder, A.; Sen, S.; Das Burman, A.; Patra, A.; Bhattacharyya, K. *J. Phys. Chem. B* **2004**, *108*, 2309.
(63) Hazra, P.; Chakrabarty, D.; Chakraborty, A.; Sarkar, N. *Chem. Phys. Lett.* **2003**, *382*, 71.

(64) Ferrer, M. L.; del Monte, F. *Langmuir* **2003**, *19*, 650.
(65) Minoofar, P. N.; Dunn, B. S.; Zink, J. I. *J. Am. Chem. Soc.* **2005**, *127*, 2656.
(66) Minoofar, P.; Hernandez, R.; Franville, A. C.; Chia, S. Y.; Dunn, B.; Zink, J. I. *J. Sol-Gel Sci. Technol.* **2003**, *26*, 571.

Chapter V

Our Evolving View of $DiIC_{12}$ Guest-Host Interactions

5.1 CHAPTER ABSTRACT

The conclusions for dry $DiIC_{12}$ in Chapter 4 are revisited in light of two $DiIC_{12}$ fresh film data sets. These $DiIC_{12}$ fresh film results indicate lower fixed and tumbling mobility than that seen for the previously reported dry sample. This is likely due to differences in sample preparation and testing conditions. These differences, together with the new mobility, lifetime, and photobleaching quantum yield results we obtained indicate that the previous dry $DiIC_{12}$ results are not suitable for direct comparison to the equilibrated samples. However, they do illustrate the influence of sample preparation and testing conditions on guest-host interactions. In contrast, the fresh $DiIC_{12}$ film mobilities obtained from the more recent data sets are in trend with those previously observed for water and ethanol equilibrated films. In addition, the fresh film average lifetimes and average photobleaching quantum yields are comparable to those seen for the EtOH equilibrated sample. The fresh $DiIC_{12}$ results display behavior similar to that seen for SRB, R6G, and ORG on solvent addition; however the $DiIC_{12}$ photostability appears less dependent on the solvent identity compared to the other dyes.

5.2 INTRODUCTION

While reviewing the results reported in Chapter 4, we began to question the appropriateness of using the dry $DiIC_{12}$ results for comparison with the equilibrated films. At issue is the difference in the dry $DiIC_{12}$ sample preparation and testing conditions relative to the equilibrated film samples. A dry fresh film $DiIC_{12}$ sample

prepared under conditions similar to the equilibrated films was identified and on analysis it provided results significantly different from the first $DiIC_{12}$ dry sample. Since there were two conflicting data sets available, it was decided that a third data set was necessary to clarify which results were more appropriate for comparison with the equilibrated samples. Testing on the third $DiIC_{12}$ data set was completed in January 2006. This chapter shares how our understanding of the $DiIC_{12}$ silica sol-gel interactions has evolved as additional information has become available.

5.3 RESULTS AND DISCUSSION

5.3.1 Sample Testing, Preparation, and Identification History

The dry $DiIC_{12}$ sample reported previously (DiI A – the aged $DiIC_{12}$ sample) was prepared in 2002 when the two detector $I_{//(t)}$ and $I_{\perp(t)}$ measurements were first implemented. The sample was prepared by combining 1.95 μL 1/100 v/v phosphoric acid, 100.0 μL double distilled water, 353.3 μL 95% EtOH, and 176.8 μL TEOS. To that solution 4.8 μL $DiIC_{12}$ in 95% EtOH was added after sonication, to produce a 1:8:7 TEOS:ethanol:water molar ratio solution that is virtually identical to our other samples. However, this sample was sonicated for 2 hours at room temperature (~25°C), rather than the 0°C ice bath used with later experiments. One indication that this temperature difference altered the sol-gel structure is the 363 ± 20 nm film thickness measured for this sample. The sample preparation sonicated at 0°C results in a 203 ± 15 nm thick film when spin-cast under the same conditions. This difference in film thickness probably resulted from an increase in the sol viscosity caused by the increased hydrolysis and condensation rates at elevated temperature. The DiI A sample was then tested when the film was between 4 and 13 days old as part of an ongoing study into the change in $DiIC_{12}$

lifetime with aging. In the DiI A experiment, while the excitation power used for photobleaching measurements was monitored for consistent intensity, the actual excitation power intensity was not recorded. It is also unknown whether an emphasis was placed on selecting molecules that appeared brightly in both polarized scan images during the initial two detector testing trials. This selection process would bias the resulting dye polarization values towards a higher zero polarization population.

After the aging study, our preparation procedure was altered to that described in Chapter 2. The main change in preparation was the temperature at which the sample sonicates. A 0°C ice bath was selected to provide a more reproducible sonication temperature, and sample testing was performed on the fresh or day one films. Molecules were selected equally from both detector images and did not necessarily appear bright in both detectors simultaneously. Since a highly polarized molecule will not appear equally in both detectors, this broadens the molecule polarization distribution sampled to better reflect the silica sol-gel environment. Laser power monitoring and documentation was instituted to track the laser source stability and sample testing conditions. As a result, the investigations into charge-charge interactions and solvent influence on mobility (Chapters 3 and 4) were collected with an average power density of approximately 917 $W \cdot cm^{-2}$. This includes the fresh $DilC_{12}$ sample (DiI F1) prepared using the 0°C preparation procedure. The DiI F1 sample results differed appreciably from those obtained from DiI A. Based on similar sample preparation conditions the DiI F1 sample should be more appropriate for comparison to the equilibrated samples. But, with two conflicting results available, an additional data set was necessary to confirm the fresh $DilC_{12}$ sample results. A second $DilC_{12}$ fresh sample (DiI F2) was prepared and tested in

January 2006 at a 923 $W \cdot cm^{-2}$ power density. This places the DiI F2 excitation intensity slightly higher than the DiI F1 intensity, but well within the range used for the solvent equilibrated samples.

5.3.2 $DiIC_{12}$ Mobility

The mobility populations for the dry and solvent equilibrated $DiIC_{12}$ films are shown in Figure 5.1 and Table 5.1. It is clearly evident that the DiI A mobility differs drastically from the other $DiIC_{12}$ samples, as well as from the other dye mobilities we have collected up to this point (Chapter 3 Table 3.1), due to its high tumbling population. For comparison, the ORG pH 7 sample has the next highest tumbling population of only 25%, even though it has three negative charges (Chapter 3 Table 3.1). This high tumbling mobility makes the DiI A sample unusual. The DiI F1/F2 mobilities are shown side by side in Figure 5.1 where it can be seen that they are more or less within sampling error of one another. These two fresh film mobilities correspond well even though they were

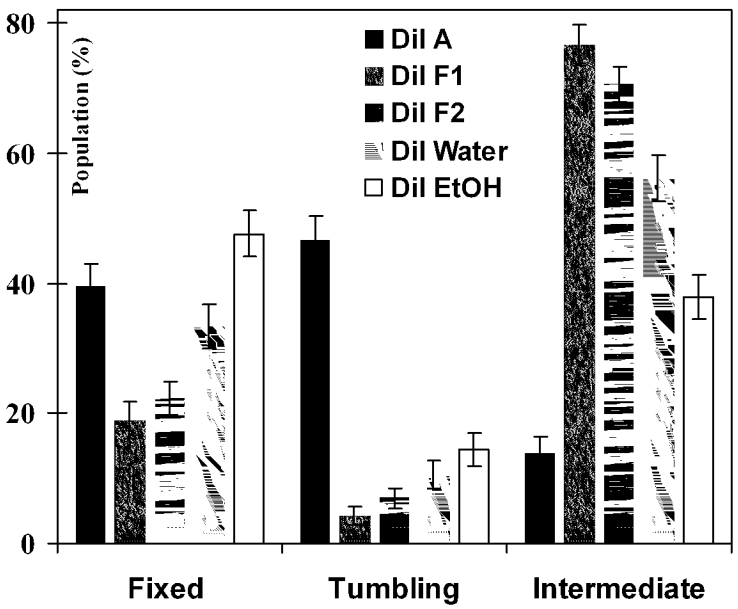

Figure 5.1. $DiIC_{12}$ mobility populations for dry (DiI A, DiI F1, DiI F2) and solvent equilibrated films. The DiI A sample was prepared at 25° and combines results from films aged 4 to 13 days after spincoating. DiI F1/F2 and the solvent equilibrated samples were all fresh films prepared at 0°. The DiI A mobility differs greatly from the fresh film mobilities, indicating that the preparation and testing conditions significantly alter dye mobility.

prepared and tested nearly four years apart. If the DiI A mobilities are excluded from consideration, a familiar pattern emerges. The fixed and tumbling populations increase while the intermediate population decreases by the same amount as we progress from the dry fresh films, to water, to EtOH equilibrated samples. This is the same general mobility trend observed for SRB, and partially for R6G and ORG as well. This provides further evidence that preferential dye leaching leads to the observed increase in fixed molecule population on solvent addition. The averaged DiI F1/F2 fresh populations (20% fixed, 6% tumbling, and 74% intermediate) are very similar to those found in the ORG day one films (21% fixed, 7% tumbling, and 72% intermediate). The high fresh $DiIC_{12}$ intermediate population indicates that $DiIC_{12}$ has a similar distain for the silica sol-gel surface as the negatively charged ORG, even though $DiIC_{12}$ has a positive charge. We propose that the $DiIC_{12}$ aliphatic tails may hinder immobilization and result in the small fixed molecule population. Like R6G and SRB, counter ion dissociation and solvation in the less polar EtOH likely lead to the increase seen in tumbling population on solvation, while preferential leaching increases the fixed population. Interestingly there remains a 20% minimum fixed population across all dye samples, potentially representing those dye

Table 5.1. $DiIC_{12}$ mobilities indicating the population in percentage and number of molecules.

Dye	Fixed (%)	Tumbling (%)	Intermediate (%)
DiI A	39 ± 4 % 77	47 ± 4 % 27	14 ± 2 % 91
DiI F1	19 ± 3 % 36	4 ± 1 % 8	77 ± 3 % 145
DiI F2	22 ± 3 % 61	7 ± 2 % 19	71 ± 3 % 192
DiI H_2O	33 ± 3 % 63	11 ± 2 % 106	56 ± 4 % 20
DiI EtOH	48 ± 3 % 99	14 ± 2 % 79	38 ± 3 % 30

molecules physically confined regardless of the guest-host interaction strength. This physical immobilization could result from either pore templating or pores collapsing. In addition, the mobility change between the dry and water equilibrated films is approximately the same magnitude as the change between the water and EtOH films; with the fixed population increasing approximately 14% and the tumbling population approximately 4 %.

Table 5.2. $DiIC_{12}$ Survival lifetime analysis based on single- and bi-exponential decay functions using Excel©. All fittings were reevaluated to normalize the fitting parameters used.

Dry	Category	a_1	τ_1 (second)	a_2	τ_2 (second)	$\langle r^2 \rangle$	$\langle \tau \rangle$ (second)
DiI A	Fixed	0.38±0.02	2.3±0.2	0.62±0.02	17.2±0.6	0.9986	11.6±0.5
	Tumbling	0.77±0.07	5.0±0.5	0.23±0.08	64±66	0.9971	18±16
	Intermediate	0.25±0.04	2.5±0.8	0.75±0.04	31±2	0.9952	24±2
DiI F1	Fixed	0.65±0.04	4.4±0.4	0.35±0.04	50±8	0.9963	20±3
	Tumbling	1.0	7.4±0.5	-	-	0.9826	7.4±0.5
	Intermediate	0.31±0.02	9±1	0.69±0.03	54±2	0.9977	40±2
DiI F2	Fixed	0.68±0.02	2.6±0.2	0.32±0.02	37±4	0.9968	14±2
	Tumbling	1.0	6.9±0.5	-	-	0.9647	6.9±0.5
	Intermediate	0.85±0.03	18.3±0.7	0.15±0.03	105±25	0.9984	31±5
$DiIC_{12}$ Water	Fixed	0.43±0.02	1.12±0.09	0.57±0.02	11.4±0.5	0.9983	7.0±0.4
	Tumbling	1.0	11±1	-	-	0.9187	11±1
	Intermediate	0.53±0.05	5.9±0.6	0.47±0.06	26±3	0.9981	15±2
$DiIC_{12}$ EtOH	Fixed	0.32±0.01	3.2±0.2	0.68±0.01	29.7±0.8	0.9983	21.1±0.7
	Tumbling	0.6±0.4	8±3	0.4±0.4	31±25	0.9895	16±15
	Intermediate	0.26±0.04	6±1	0.74±0.04	43±2	0.9960	33±2

5.3.2 DilC$_{12}$ Lifetime and Photobleaching Quantum Yield

Differences between DiI A and DiI F1/F2 are also evident in the average survival lifetime ($\langle\tau\rangle$) and average photobleaching quantum yield ($\langle\phi_b\rangle$) values presented in Table 5.2, Table 5.3, and Figure 5.2. To identify how the molecular mobility influenced the dye stability, the survival lifetime and photobleaching quantum yield (ϕ_b) values were refit to single and bi-exponential decay functions in Excel©. For the DiI A sample, the refitting places the fixed $\langle\tau\rangle$ shorter than the tumbling $\langle\tau\rangle$. This results from a change in the fixed molecule lifetime minor component from 130 to 2.26 which was accompanied by an $\langle r^2\rangle$ increase from 0.995 to 0.9986. Nonetheless, when only the $\langle\tau\rangle$ major component for the fixed DiI A molecules is considered, it remains approximately three times more stable than the tumbling molecules. The intermediate molecule lifetimes are included in Figure 5.2, showing that the intermediate population has the longest lifetime in all samples, potentially due to the increased probability of reorientation that longer lived molecules face.

As seen in Figure 5.2A and Table 5.2, $\langle\tau\rangle$ for the DiI A and DiI F1/F2 samples are significantly different. The DiI A $\langle\tau\rangle$ distribution is most similar to the water equilibrated sample. Since the $\langle\tau\rangle$ order and narrow distribution in the DiI A sample resembles the water equilibrated sample, it possibly reflects the more aged and developed sol-gel matrix environment due to the higher sonication temperature and extended drying time. This would agree with other silica sol-gel drying studies that show ethanol evaporating from the sol-gel before water, as evidenced by polarity changes.[1-5] However, since the excitation power used to investigate the DiI A sample was not recorded, the lifetime and photostability differences could instead be related to excitation power differences. The

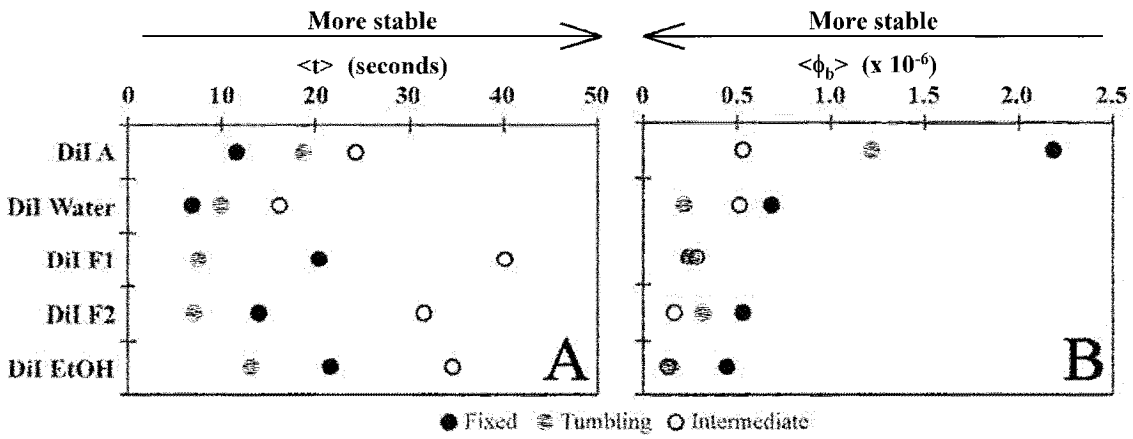

Figure 5.2. The $DiIC_{12}$ $\langle\tau\rangle$ (A) and $\langle\phi_b\rangle$ (B) values are presented by sample and mobility class above. The DiI F1/F2 $\langle\tau\rangle$ values correlate well to each other and to the EtOH equilibrated sample and match the equilibrated sample $\langle\phi_b\rangle$ values and spacing better than DiI A does. Based on $\langle\phi_b\rangle$ the DiI A sample is less stable than the fresh samples, potentially reflecting the dryer, more developed DiI A silica sol-gel structure.

survival lifetimes obtained from the DiI F1/F2 samples correlate well to the ethanol equilibrated sample. This similarity to the EtOH sample potentially indicates $DiIC_{12}$ solvation in residual EtOH within the DiI F1/F2 fresh films. The decrease in the water equilibrated lifetimes relative to both the fresh and EtOH equilibrated films suggest a less stable $DiIC_{12}$-water interaction.

Comparison of the fitted lifetimes reveals another interesting pattern. In general the tumbling and intermediate molecule photobleaching quantum yields fit well to single-exponential decay functions, while the fixed molecules require a second component to accurately describe the decay. The more homogeneous behavior observed in the tumbling and intermediate decays likely indicate their accessibility to solvent dissolved oxygen while tumbling or at the solvent-surface interface. The bi-exponential decay observed for fixed molecules would then represent two, or more, fixed molecule environments. One decay could correspond to dye adsorption on the surface, where it

remains readily accessible to solvent dissolved oxygen, while the other could represent sites more isolated from the solvent medium through greater matrix incorporation.

When the $\langle\phi_b\rangle$ trends are considered, Figure 5.2B and Table 5.3, the fresh film $DiIC_{12}$ results roughly resemble one another. The $\langle\phi_b\rangle$ value similarity indicates that the DiI F1/F2 films and the solvent equilibrated fresh films experience a similar degree of photostability, regardless of the solvent medium. If the DiI A sample is an accurate representation of the aged sample response, the reduced DiI A photostability relative to

Table 5.3. $DiIC_{12}$ photobleaching quantum yield analysis based on single- and bi-exponential decay functions using Excel©. All fittings were reevaluated to normalize the fitting parameters used.

Dry	Category	a_1	ϕ_1 ($\times10^{-6}$)	a_2	ϕ_2 ($\times10^{-6}$)	$\langle r^2\rangle$	$\langle\phi_b\rangle$ ($\times10^{-6}$)
DiI A	Fixed	0.38±0.02	0.31±0.03	0.62±0.02	3.3±0.2	0.9969	2.2±0.1
	Tumbling	1.0	1.20±0.01	-	-	0.9963	1.20±0.01
	Intermediate	1.0	0.53±0.02	-	-	0.9936	0.53±0.02
DiI F1	Fixed	0.12±0.02	0.005±0.003	0.88±0.02	0.27±0.01	0.9951	0.23±0.01
	Tumbling	1.0	0.26±0.02	-	-	0.9642	0.26±0.02
	Intermediate	0.96±0.02	0.133±0.005	0.04±0.02	4±8	0.9960	0.3±0.4
DiI F2	Fixed	0.55±0.04	0.15±0.01	0.45±0.04	0.98±0.01	0.9974	0.52±0.06
	Tumbling	0.95±0.17	0.20±0.05	0.05±0.18	3±24	0.9795	0.3±1.2
	Intermediate	1.0	0.160±0.001	-	-	0.9968	0.160±0.001
$DiIC_{12}$ Water	Fixed	0.37±0.02	0.080±0.007	0.63±0.02	1.04±0.04	0.9975	0.69±0.3
	Tumbling	1.0	0.194±0.009	-	-	0.9846	0.194±0.009
	Intermediate	0.90±0.02	0.206±0.008	0.10±0.02	3±1.2	0.9969	0.5±0.1
$DiIC_{12}$ EtOH	Fixed	0.85±0.03	0.11±0.01	0.14±0.04	2±1	0.9846	0.85±0.02
	Tumbling	1.0	0.140±0.006	-	-	0.9796	0.140±0.006
	Intermediate	1.0	0.13±0.02	-	-	0.9906	0.13±0.02

the fresh and solvent equilibrated films could indicate a stability decrease due to solvent evaporation. Although the fresh films are not in contact with a solvent, they usually retain residual solvent within their porous silica structure. As the solvent evaporates from the film, the oxygen diffusion rate through the film would increase, since the oxygen would pass through air filled pores rather than solvent filled pores. This increased oxygen supply would make the dye molecules less stable due to a greater access to oxygen for photo-oxidation.

When the $DiIC_{12}$ $\langle\tau\rangle$ and $\langle\phi_b\rangle$ in Figure 5.2 are compared to R6G and SRB in Figure 5.3 few of our previous conclusions concerning the differences between dyes are altered. The main change is that $DiIC_{12}$ no longer appears greatly stabilized on solvent addition. Rather, the fresh $DiIC_{12}$ film photostability appears more indifferent to solvent identity than either R6G or SRB. This is seen in the broader R6G and SRB $\langle\tau\rangle$ and $\langle\phi_b\rangle$ distributions in Figure 5.3, and narrow $\langle\phi_b\rangle$ $DiIC_{12}$ distribution in Figure 5.2.

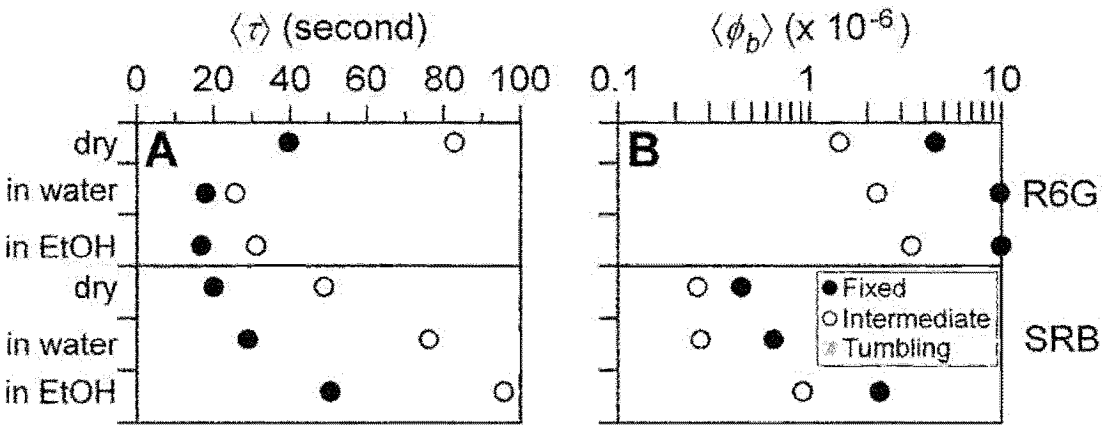

Figure 5.3. A partial reproduction of Figure 4.6 showing the average survival lifetime $\langle\tau\rangle$ (A) and the average photobleaching quantum yield $\langle\phi_b\rangle$ (B) for R6G and SRB in dry, water, and ethanol equilibrated films. When comparing to Figure 5.2 remember that the figure scales are different.

5.3.3 Summary of Modifications Made to the Previous DiIC$_{12}$ Conclusions

Based on the most recent DiIC$_{12}$ fresh film results, some of our conclusions in Chapter 4 must be modified. First, since the DiI F1/F2 samples lack a high tumbling population, the statement that the hydrophobic dye nature results in increased tumbling mobility within the dry sample should be modified. Instead the hydrophobic nature likely contributes to increased mobility through the large intermediate populations seen with the fresh DiI F1/F2 samples. The differences in DiI A and DiI F1/F2 mobilities demonstrate the importance of preparation and testing conditions on sample mobility. These differences may account for the unusually high tumbling population observed in the DiI A sample. When the same procedure is used to prepare all the samples, the fixed, tumbling, and intermediate mobility behavior on solvent addition is consistent with the trend observed for R6G, SRB, and ORG. This supports the belief that dye solvation increases the fixed molecule population through preferential leaching of highly mobile molecules.

Another refinement to the understanding of the silica sol-gel environment involves the longer fixed $\langle\tau\rangle$ relative to the tumbling $\langle\tau\rangle$. For the fresh DiI F1/F2 samples the average fixed molecule lifetime is greater than the tumbling molecule lifetime, but the $\langle\tau\rangle$ no longer breaks down for direct comparison between the individual exponential fitting components. This is in part due to the single exponential tumbling molecule survival lifetime decays.

Another change to the previous conclusions is that the fresh DiIC$_{12}$ $\langle\tau\rangle$ behavior becomes more consistent with the ethanol equilibrated DiIC$_{12}$ behavior. This is evident

in the broader fixed, tumbling, and intermediate survival lifetime distribution in the fresh samples, and the improved fresh and EtOH lifetime value correlation. The fresh dry $\langle \phi_b \rangle$ values are also in better agreement with the solvated fresh films than the DiI A sample, producing $DiIC_{12}$ $\langle \phi_b \rangle$ clustering at low values. That the DiI A sample appears less photostable (larger $\langle \phi_b \rangle$ values) than the fresh films makes intuitive sense, since residual solvent in the fresh films would slow oxygen diffusion through the fresh films relative to the air filled pores in the aged sample. However, without knowing the actual DiI A excitation power a definite conclusion cannot be reached.

The fresh film results support the conclusion that the hydrophobic dye preferentially associates with residual EtOH rather than the hydrophilic silica surface in the dry films, as seen by the $\langle \tau \rangle$ and $\langle \phi_b \rangle$ results. This preference could contribute to the high intermediate $DiIC_{12}$ population observed even though $DiIC_{12}$ is positively charged. A lack of strong solvent and silica surface attraction could account for the apparent indifference that the $DiIC_{12}$ $\langle \phi_b \rangle$ shows toward the solvents. This would indicate that neither water nor EtOH protected the dye from oxidation on solvation, even though EtOH is a better solvent for $DiIC_{12}$ than water.

5.4 CONCLUSION

Based on recent results obtained from $DiIC_{12}$ fresh films, the previously reported dry $DiIC_{12}$ sample appears inappropriate for direct comparison to the solvent equilibrated samples, due to different sample preparation procedures. This has led us to modify some previous conclusions concerning the $DiIC_{12}$ interactions with the silica sol-gel host. Based on the fresh film results the $DiIC_{12}$ mobility/solvation trend resembles that observed for R6G, ORG, and SRB. The similarities in $\langle \tau \rangle$ and $\langle \phi_b \rangle$ for the fresh and EtOH

films provide stronger evidence that $DiIC_{12}$ preferentially associates with residual EtOH within the fresh films. While the major survival lifetime component alone no longer indicates a higher stability for fixed molecules relative to their tumbling counterpart, the $\langle \tau \rangle$ values continue to support greater stability for fixed molecules. Finally, the decrease in $\langle \phi_b \rangle$ for the aged $DiIC_{12}$ sample could point to the importance of solvent in reducing photo-oxidation, by slowing oxygen diffusion through the sol-gel pores. Further single molecule study will continue to evolve our understanding of the complex interactions between organic guest molecules and the silica sol-gel host matrix.

Chapter V References

(1) Nishida, F.; McKiernan, J. M.; Dunn, B.; Zink, J. I.; Brinker, C. J.; Hurd, A. J. *J. Am. Ceram. Soc.* **1995**, *78*, 1640.

(2) Mei, E.; Bardo, A. M.; Collinson, M. M.; Higgins, D. A. *J. Phys. Chem. B* **2000**, *104*, 9973.

(3) Lobnik, A.; Wolfbeis, O. S. *J. Sol-Gel Sci. Technol.* **2001**, *20*, 303.

(4) Narang, U.; Wang, R.; Prasad, P. N.; Bright, F. V. *J. Phys. Chem.* **1994**, *98*, 17.

(5) Narang, U.; Jordan, J. D.; Bright, F. V.; Prasad, P. N. *J. Phys. Chem.* **1994**, *98*, 8101.

Chapter VI

Nanomolar Oregon Green pH Response within a Silica Sol-gel Host

6.1 CHAPTER ABSTRACT

This chapter further develops the dye Oregon Green 514 (ORG) that we previously studied. Our results indicate that ORG thin silica sol-gel films function as an optical sensor, even at nanomolar concentrations, this is in spite of dye leaching and photobleaching over time. This low concentration range bridges the single molecule studies we previously performed and the higher concentration bulk averaged behavior. In our results we identify response hysteresis due to delayed solvent diffusion into isolated pores and silica sol-gel film degradation in high pH phosphate buffers. Our observations concerning ORG fluorescence spectra changes on silica sol-gel encapsulation and confocal testing are also reported.

6.2 INTRODUCTION

Increased sol-gel process understanding has prompted new sol-gel based materials and technology discoveries and developments. This is especially evident in the increased interest shown in silica sol-gel sensors. Silica sol-gel is an appealing optical material due to its high mechanical strength,[1,2] optical clarity,[3] porosity,[4-7] processability, and relative low cost. Investigators seek to customize sol-gel material response for specific sensor environments and optical applications by modifying the silica sol-gel properties.[8,9] Not only are the silica sol-gel properties varied, but the techniques used to investigate these properties are diverse as well. Techniques used to investigate sol-gel properties include

absorbance,[10,11] fluorescence,[12-14] time resolved spectroscopy,[13,15,16] single molecule spectroscopy,[17-20] NMR,[21-23] IR,[24,25] TEM,[26] and X-ray diffraction.[27-29] While single molecule spectroscopy inherently reports on local properties, most techniques provide a "bulk" time, or number, averaged response. The understanding gained from these investigations typically focuses on the organic-inorganic and bio-inorganic composite material's ability to either protect or confine guest molecules within the silica sol-gel host matrix. When used as a host material, silica sol-gel has been shown in some cases to increase laser dye photostability[18,30-32] and selectively stabilize enzyme structural integrity.[8,33-35] However, dye retention over time and bio-molecule encapsulation remain areas that require further development.

One interesting property for sensor development is the silica sol-gel matrix porosity, which permits both guest confinement and solvent accessibility. The pore existence enables guest molecule encapsulation within a confined environment while retaining guest molecule activity and native protein conformation.[8,33-37] In addition, the pore interconnection allows solvent and small molecules to diffuse into the sol-gel matrix where they can interact with the confined guest.[36,37] This is especially attractive for biosensor applications, since an active enzyme can be confined within the solid silica host and still remain accessible to externally available substrates. The silica matrix is also optically clear which makes it ideal for optical sensor development. By confining an environmentally responsive guest within the transparent sol-gel matrix the indicator is localized for improved detection and recovery, while minimizing the restriction on external solvent exchange.[10,12,16,24,38-40] Silica sol-gel materials sensitive to pH,[9-12,34,41]

pharmaceutical products in blood,[40,42] gases,[24,39] and selected ions have all been reported.[43-47]

Another important property for an optical sensor is response time. Silica sol-gel monoliths have proved less than ideal in this area since a monolith can take hours or days to fully respond to external changes.[5,41] One method to increase sensor response time over the monolith is to reduce the thickness to form a thin sol-gel film. A shorter diffusion path length increases the response rate to the external environment, but thin films experience accelerated drying and sol-gel pore collapse.[48,49] The shorter diffusion path length also corresponds to a reduced optical path length, decreasing the desired optical response intensity. In order to overcome the decreased signal intensity resulting from the reduced optical path length, increased indicator concentrations have been used,[41] and the excitation interaction path length has been enhanced by using an optical waveguide,[9,41,47,50] or sol-gel coated optical fiber.[9,11,40] While pH response has been investigated on the single molecule level, where it was used to determine the change in molecular pK_a distributions with buffer variation,.[51] sensor response is typically investigated using high indicator concentrations (μM – mM) to overcome the low response intensity. These high indicator concentrations tend to overwhelm, or mask, detrimental influences on sensor response (such as inhomogeneous solvent access, preferential leaching, or dye photobleaching) by providing an intense average response. To fully exploit silica sol-gel's sensor potential, we must seek to better understand the underlying interactions involved, in order to eventually control the environment and guest-host interactions to provide optimized sensor response.

With this goal in mind, this work evaluates the pH response of nanomolar Oregon Green 514 (ORG) confined within silica sol-gel thin films for further development as a pH sensor. This system was also selected to gain a fuller understanding of indicator behavior at a concentration that bridges the transition between single molecule and bulk averaged behavior. A low concentration sample that approaches the single-molecule limit should provide a sample more sensitive to potential detrimental influences that will reveal the most about the environmental effects on the indicator. Here we expand on our previous single molecule investigation into the influence that charge-charge interactions have on guest rotational mobility within silica sol-gel. In it we observed that ORG fluorescence intensity as well as single molecule rotational mobility varied with pH in silica thin films.[19,20] In this study we focus on the spectroscopic ORG thin film response when subjected to repeated buffer exposure, and evaluate an appropriate method for analyzing the thin film pH sensor response.

6.3 RESULTS AND DISCUSSION

6.3.1 ORG Spectral Response in Solution Characterized

Oregon Green 514, structure presented in Figure 6.1, is a fluorinated fluorescein derivative. The highly electronegative fluoride atoms attached withdrawal electron density from the phenolic group, reducing the phenolic group pK_a from 7 to approximately 4.7.[52-54] However, the apparent pK_a has been shown to vary between 3.77 to 4.7 based on the detection technique and

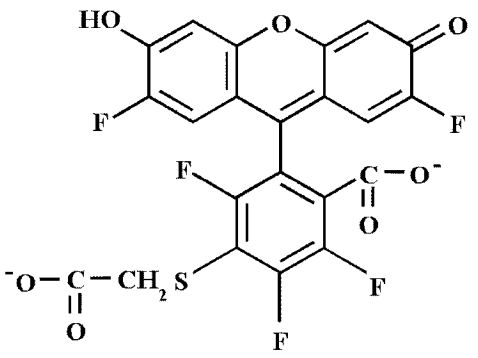

Figure 6.1. Chemical structure of Oregon Green 514.

sample testing parameters, since the parameters provide selective dye protonation state excitation and/or detection.[53,55] The phenolic proton is only one of three acidic protons in ORG, but due to its location on the xanthene moiety it is the only one that significantly influences the optical response. ORG has a trianionic charge when fully deprotonated. However, due to its optical activity, only the phenolic proton pK_a is considered here.

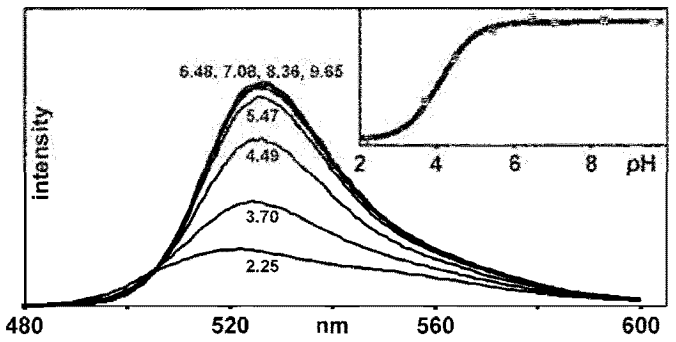

Figure 6.2. ORG bulk solution fluorescence spectra excited at 457 nm and monitored by a fluorometer. As the pH increases the peak sharpens, the peak maximum red shifts, and spectrum intensity reaches a plateau, indicating full phenolic group deprotonation. In the insert, the titration curve based on the total area under the peak is presented. The solid line indicates the Henderson-Hasselbalch fit to the solution response with a pK_a of 4.1.

As seen in Figure 6.2, ORG in bulk solution (457 nm excitation) responds to pH variation with changes in both emission intensity and wavelength. As the phenolic proton is removed, the dye extinction coefficient increases with a subsequent increase in fluorescence emission.[52,53,55] Concurrent with the fluorescence emission intensity increase is a red shift in the solution peak maximum as the pH increases from 2.2 to 9.7. In addition, the 524 nm peak comes to dominate the 554 nm shoulder seen in the pH 2.2 spectrum. Integrating the emission spectrum area provides a suitable variable for monitoring the pH response in solution and was fit to the Henderson-Hasselbalch equation. This fit provides a standard curve for determining an unknown environment's pH as well as the ORG solution pK_a. The bulk ORG solution excited at 457 nm provided a pK_a value of 4.1, see Figure 6.2.[20,56]

6.3.2 ORG Film Equilibration Response Rate and Hysteresis

After characterizing the ORG solution response, the 34 nM ORG silica sol-gel film response to buffers as a function of time was monitored to determine an appropriate equilibration time and testing parameters for accurate pH determination. The spectral response was monitored by accumulating a single spectrum over the first 2 minutes of every 5 minute period for at least two hours. Film response was monitored to determine the equilibration rates for water, pH 2.3, pH 7, and pH 9.7 buffers. In all four cases the dry to solvated transition occurred rapidly with a reasonably consistent normalized spectrum obtained within the first five to ten minutes after buffer addition. Monitoring the film over the next two hours indicated a steady state with an occasional random intensity jump or spectral shift that returned to the common response range on the next accumulation. These variations come from using a low concentration sample. While the time trials indicate that solvent equilibration was reached within the first 10 minutes we decided to wait 20 to 30 minutes to ensure a steady state before further testing. The cycled pH results reproducibility supports this choice.

For comparison, a 5 minute equilibration time with a 30 second accumulation regiment was evaluated. Significant hysteresis in the pH response curve was observed for the 5 minute equilibration regiment that is not present in the 20 minute sample. Hysteresis effects have been reported for other rapidly cycled silica sol-gel films, with the hysteresis diminishing during continued use.[47] This hysteresis is attributed to dye contained within isolated, slowly equilibrating pores.[47,51] The retarded diffusion rate into the isolated pores results in a wider local environment distribution contributing to the total signal, this alters both the emission peak intensity and shape. Continued buffer

cycling allows the dye within these isolated pores to reach a steady state pH response, thereafter contributing a constant response to the total film signal.[47] Potentially the observed hysteresis could be reduced, and the film response rate increased, by cycling the buffers until a steady state signal was achieved. This is the solution predominantly used by other groups when studying sensor response. Alternately, the hysteresis could potentially be reduced by pre-equilibrating the film in an appropriate mid-range buffer before use, initially establishing the steady state pH in the isolated pores. However, that would require a careful determination of the required steady state pH. For this work the 20 minute equilibration time was deemed sufficient.

6.3.3 Thin Film Spectral Response Characterization and Measurement

While ORG fluorescence responds readily to pH variation in solution, an identical response within the silica sol-gel host environment cannot be assumed. Silica sol-gel is a heterogeneous host environment. Even assuming complete TEOS hydrolysis, the protonated or deprotonated silanol distribution could influence the film response by locally buffering the guest as the solution approaches the silanol pK_a, reported to be between 4.5 - 9.[51,57,58] In addition, unreacted surface

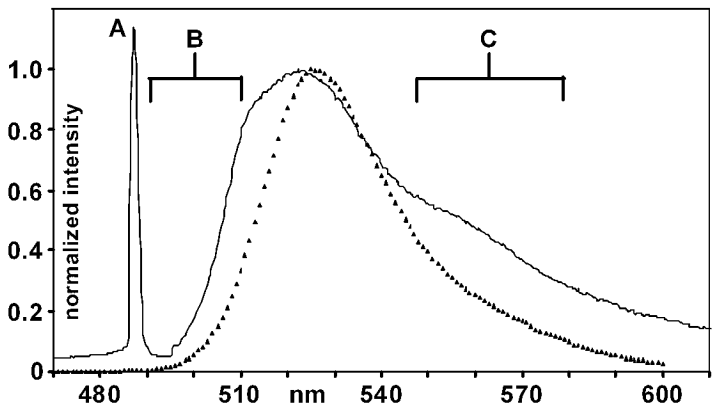

Figure 6.3. The normalized ORG pH 7 solution fluorescence (dotted) spectrum collected on a fluorometer, excited at 457 nm. and the normalized ORG pH 7 sol-gel thin film (solid) spectrum collected on a confocal microscope excited at 488 nm. Features identified in the confocal spectrum include the 488 nm laser spike (A), the long-pass filter cutoff effects beginning around 510 nm (B), and the shoulder (C) which is more prominent relative to the peak than in the solution spectra.

ethoxy groups and the random pore architecture increase the local environment heterogeneity. The spectroscopic response is modified by the 488 nm excitation and accompanied dye extinction coefficient change. In addition the dichroic beamsplitter, notch, and bandpass filters cumulatively cutoff fluorescence shorter than 510 nm. Figure 6.3 presents the peak normalized fluorescence spectra for ORG pH 7 bulk solution and pH 7 buffered ORG silica sol-gel films. The most prominent difference between the two spectra is the residual laser feature at 488 nm. This proved useful as an internal wavelength calibration reference. On encapsulation in sol-gel and buffered at pH 7, the ORG peak blue shifted from 525 nm to 522 nm, broadened, and the 554 nm shoulder increases in prominence relative to the peak. These differences are likely the result of high local environmental heterogeneity. Completely isolated pores would retain a low pH due to residual phosphoric acid catalyst, while slightly accessible pores would exhibit slowed equilibration rates. Both the ORG excitation efficiency and fluorescence intensity decreased on protonation.

Unlike the 547 nm excited bulk solution, where the peak maximum red shifts with an increase in pH (Figure 6.2), the confocal tested solution and sol-gel samples demonstrate a slight peak maximum blue shift with increased pH. Beginning around 510 nm on the ORG thin film sol-gel peak (Figure 6.3) the dichroic beamsplitter and longpass filtering effect becomes evident by the drop in fluorescence intensity that deforms the peak shape. The short wavelength cutoff alters the total area under the peak for all pHs, but there is a proportionately greater influence on the low pH values due to the lower intensities and broader peaks at low pH. The low ORG concentration used to characterize the response, and the corresponding low fluorescence, makes the signal more

susceptible to random and systematic variations in the intensity. Some intensity influences identified were local concentration variations, dye photobleaching, leaching, and variations in the emission maximum due to local environment heterogeneity. The combined influence on the total area over time and nonuniform pH impact is seen in Figure 6.4. On repeated sample cycling the pH 3.6 spectra intensity decreased 20% while the pH 6.6 spectra only decreased 10%. This unequal intensity decay makes the area a less reliable pH indicator for the nanomolar ORG silica thin films, even though it is an appropriate variable for monitoring the solution pH.

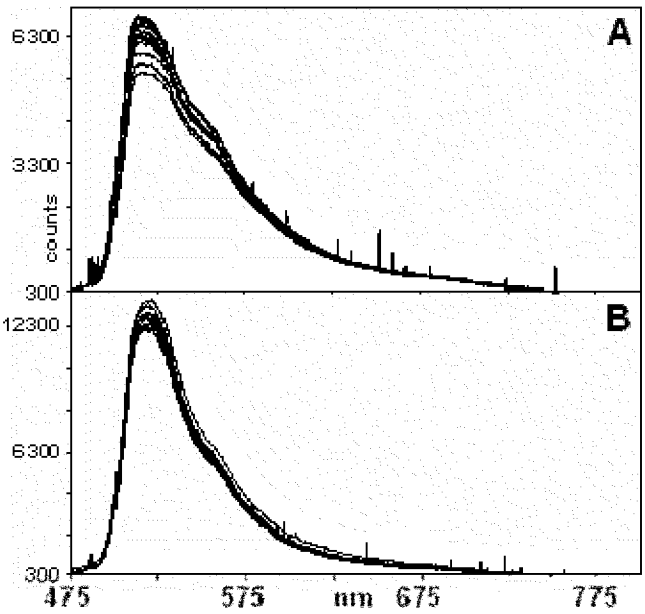

Figure 6.4. Due to the ORG intensity decrease over time, the thin film intensity was deemed an unreliable pH indicator. Shown are the spectra collected during 7 buffer cycles for the pH 3.6 (A) and pH 6.6 (B) data points. The pH 3.6 intensity maximum decreased ~20%, and the pH 6.6 decreased ~10%.

To determine the most appropriate parameter for monitoring the pH response, several analysis options were used on two pH 7 to 2 cycles. The results are shown in Figure 6.5. In addition to the total area, the 524 nm peak to 554 nm shoulder intensity ratio, and the ratio taken from both two and three Gaussian peak fits to the spectra were evaluated. The primary obstacle to using the intensity to monitor thin film pH is the decrease in signal over time, due to dye leaching and photobleaching, Figure 6.4 and 6.5A. Random fluctuations in the spectrum intensity were also observed in spectra

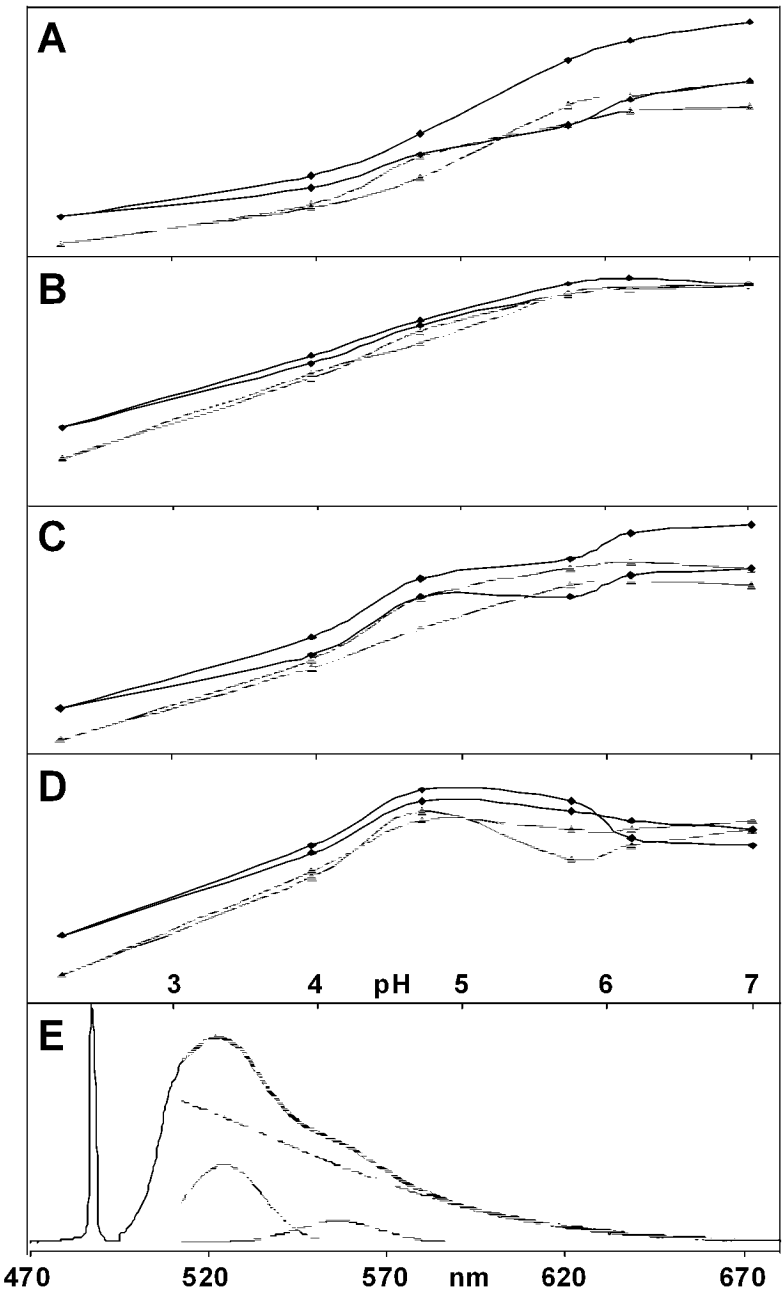

Figure 6.5. Panels A - D present the results obtained for two thin film buffer cycles analyzed by four different techniques; total area under the curve (A), the 524 nm peak to 554 nm shoulder intensity ratio (B), the intensity ratio based on a two Gaussian peak fit (C), and the intensity ratio based on a three Gaussian peak fit (D). Of the four techniques the peak shoulder intensity ratio (B) demonstrated the best reproducibility. Panel E indicates the three Gaussian peak fit (grey portion of the spectrum) to the ORG pH 7 spectrum, and the individual Gaussian peaks. The rapid emission cutoff around 510 nm is believed to be a major contributor to error in C and D. To properly fit the data a large contribution from an unrealistic and broad Gaussian wing is required (E). Fittings were performed using Excel©.

sequentially obtained at the same pH, increasing the potential error. To reduce the signal dependence on these random and systematic intensity changes, the 524 nm peak to 554 nm shoulder intensity ratio was evaluated. This ratio provided a more reliable response than the total area alone, as shown in Figure 6.5B. Some deviation in the response remained evident, so the spectra were fit with two and three Gaussian peak functions in an attempt to further reduce the response variability. Conceptually the two peak Gaussian fit would correspond to a two state acid-base equilibrium model, while the three peak Gaussian fit takes into account potential contributions from a ORG neutral, cationic, dianionic, or trianionic state to the fluorescence. Oregon Green 488 is a more fully characterized dye that is structurally related to ORG. For Oregon Green 488 the neutral and monoanionic states have the same emission spectra, while the cationic state has a low intensity and blue shifted emission.[55] The fitted peak to shoulder intensity ratios are shown in Figure 6.5C and 6.5D, as well as a representative three peak Gaussian fit to the spectrum in Figure 6.5E.

Neither Gaussian fitting provided a more reproducible response than the intensity ratio, which also requires less data analysis. Surprisingly the two Gaussian fit ratio for the most part reproduces the integrated area response, indicating continued intensity dependence. The three Gaussian fit ratio also showed greater intensity dependence than the simple peak to shoulder ratio. While the third Gaussian peak at 460 nm (25 nm beyond the 488nm excitation) appears centered near the cationic Oregon Green 488 peak maximum, tempting us to identify it as the ORG cationic state, the high intensity is inconsistent with the cationic Oregon Green 488 response.[55] In addition, the 510 nm filter cutoff makes accurate peak maximum extrapolation for identification purposes

problematic. The Gaussian fittings inability to provide a more reproducible response is likely due to the filter cutoff and sample heterogeneity. To include sample heterogeneity in the fitting model would require a two or three Gaussian profile for each local dye environment, which is not mathematically practical. Within the silica sol-gel films the intensity alone does not function as a reliable pH indicator, leaving the peak-shoulder ratio as the more reliable pH measure. This agrees with recent two wavelength emission ratio use to determine pK_a values for single SNARF molecules in silica sol-gel, as well as the wider emission ratio use to monitor pH in both sol-gel and biological systems.[34,51,53,59-61] Thus, the emission ratio has been demonstrated to be appropriate for concentrations spanning the range from single molecule to bulk averaged concentrations.

6.3.4 ORG Henderson-Hasselbalch Fitting

With an appropriate monitoring variable selected, the ratio change on pH variation must be analyzed. The ratio response cycles (one cycle corresponds to sequential buffer equilibration from high pH to low pH and back to high pH) were fit by a linear equation, polynomial functions, and the Henderson-Hasselbalch equation, to determine the most appropriate response description. A linear function can describe the response satisfactorily (R values often over 0.99) when the response below pH 6 is considered. Polynomial fits to the data work best near the pK_a, but add curvature not present in the original data. Either function could prove useful in determining pH over a limited response range, but they do not provide the physical insight that the Henderson-Hasselbalch equation offers. From the Henderson-Hasselbalch equation the pK_a, relative acidic and basic state populations, and the protonated and deprotonated state emission intensities can be estimated. The Henderson-Hasselbalch equation (Equation 6.1) was

$$pH = pK_a - Log\ (\ [HA] / [A-]) \quad \textbf{6.1}$$

$$10\ (pK_a - pH) = [HA] / [A-] = x / 1 \quad \textbf{6.2}$$

$$f_{HA} = x / (x + 1) \qquad f_{A-} = 1/ (x + 1) \quad \textbf{6.3}$$

rearranged to solve for the protonated (HA) to deprotonated (A-) state concentration ratio in terms of the pH and pK_a values (Equation 6.2). The protonated (f_{HA}) and deprotonated (f_{A-}) state dye fractions were determined from the concentration ratio (Equation 6.3). The total response intensity depends on the maximum intensity for each state and dye population fraction in that state (Equation 6.4). Substituting the population fractions

$$I_{total} = I_{HA} \cdot f_{HA} + I_{A-} \cdot f_{A-} \quad \textbf{6.4}$$

found from the Henderson-Hasselbalch equation, into Equation 6.4 provides the total sample response as a function of pH, pK_a, the maximum protonated (I_{HA}) and deprotonated (I_{A-}) state intensities (Equation 6.5). Each buffer cycle was then

$$I_{total} = [1 / (x + 1)]\ (x\ I_{HA} + I_{A-}) \quad \textbf{6.5}$$

numerically evaluated to find the three unknown parameters: pK_a, I_{HA}, I_{A-}. Since this is a general solution to the Henderson-Hasselbalch equation, it can fit the total fluorescence spectra area or the peak to shoulder intensity ratio as desired. As previously observed for silica sol-gel film pH response, the intensity ratio response range in the bulk solution was larger than that observed for the doped silica films. This is due to optical filtering influences and the silica sol-gel environment heterogeneity.[51] Dye that resides within pores isolated from the buffer provides a constant acidic response in the films that is not present in the bulk solution. We believe this acidic response is also responsible for the enhanced shoulder prominence relative to the peak in the silica thin films. While this

reduces the dynamic response range, it does not reduce the ability to detect and analyze the pH response.

6.3.5 Oregon Green Thin Film pH Response

Early in the experimental process ORG thin film response was evaluated for the pH 2 to 11 range. Shown in Figure 6.6 is the response recorded over the first 1½ cycles of that range. Figure 6.6 shows the total spectra area, peak to shoulder intensity ratio, and the Henderson – Hasselbalch fit to the average first cycle intensity ratio values from pH 2 to 7. While the response ratio is reproducible over the first cycle, the pH 11 response is atypical of the expected pH titration curve. The expected curve is demonstrated by the solution response in Figure 6.2. The fully deprotonated sample should reach a plateau value similar to the pH 7 value. Not evident in the intensity ratio analysis, Figure 6.6B, but shown by the integrated area, Figure 6.6A, is the 30% increase in the pH 7 emission for the 2nd half of the first cycle and the 95% decrease

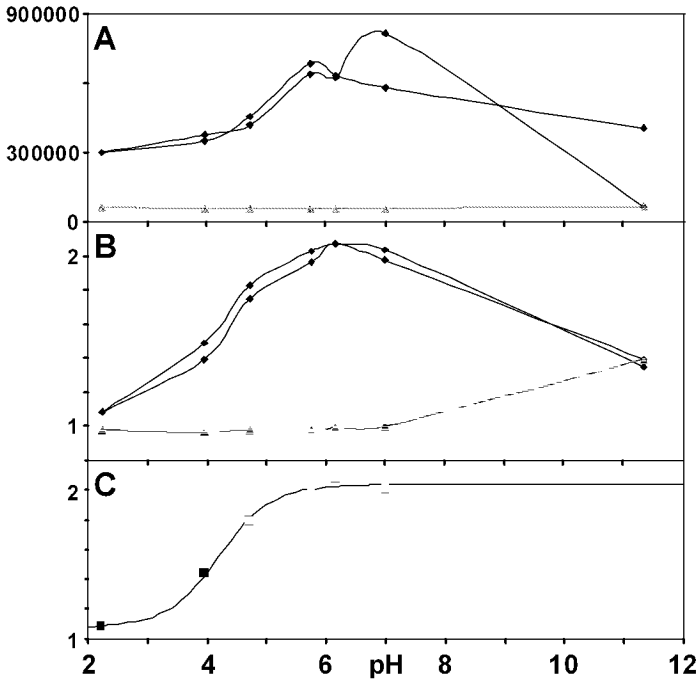

Figure 6.6 Total spectra area (A) and peak to shoulder intensity ratio response (B) for an ORG thin film cycled from pH 11 to 2. After one complete cycle (black data points) the film failed and became unresponsive (grey data points). Using the average first cycle ratios (C - squares) the Henderson-Hasselbalch fit (C - solid line) was calculated for the pH 2 – 7 range. It is readily apparent that the pH 11 ratio is inconsistent with the expected Henderson-Hasselbalch response and that repeated exposure to high pH conditions degraded the film response.

in pH 11 intensity relative to the initially measured value. Since the dye is expected to be fully deprotonated and most fluorescent at high pH, this deviation is unexpected. It indicates a ratio reproducible, but unidentified influence on the phenolic proton at high pH. Potentially a non-acid base interaction, a fluorescence quenching effect, an unidentified adsorption effect, or silanol deprotonation influence at high pH. After returning to pH 11 the film intensity became negligible and the intensity ratio no longer responded to pH variations. The sudden drop in film response is attributed to a catastrophic film failure resulting from rinsing process mechanical stress and silica solubility in high pH inorganic buffers. These combined influences likely resulted in film separation from the coverslip support. Silica sol-gel film separation from a supporting substrate and film degradation along film defects have been previously observed under high pH conditions.[10] While we previously reported ORG single molecule rotational mobilities in silica films equilibrated with pH 7 and 11 phosphate buffers, the low buffer volume, low inorganic ion concentration, and lack of rinsing stress permitted the films to remain stable for the experiment duration under the harsh conditions.[19,20] Chromatographic studies demonstrate that organic buffer use, such as citrate and HEPES, reduces silica stationary phase dissolution and increases the silica phase lifetime.[62-64] Taking these factors into consideration, subsequent testing limited the film exposure to organic buffers (citrate and HEPES) below pH 7.5, providing increased film stability and signal reproducibility. The rinsing process was also modified to reduce mechanical stress on the film. Fresh buffer was added along the cuvette wall and the used buffer was removed via suction tubing to prevent direct contact with the film surface.

These new conditions enabled the film to withstand continuous testing over 36 hours, corresponding to 7 complete buffer cycles and more than 210 rinsing steps, Figure 6.7. The cycled ratio relative standard deviation for each pH value was 2% or less over the experiment. Error in the estimated buffer pH increased with displacement from the pK_a due to the Henderson-Hasselbalch curve's asymptotic shape. A less consistent film response was obtained from films soaked overnight in pH 2 and 7 buffers between testing cycles. These films showed a change in the film response on extended buffer immersion. Part of this change was due to an increased hysteresis while isolated pores recovered a steady state condition. In addition, the dynamic range decayed more rapidly after soaking overnight in the pH 7 HEPES buffer. Both hysteresis and leaching influences should be moderated by using a midrange pH storage buffer (~pH 5).

Based on our single molecule studies, the decrease in dynamic range is the average fluorescence manifestation of the increased ORG rotational mobility, resulting from increased charge repulsion. In the single molecule studies, an increase in rotational mobility increases the potential that the molecules diffuse within the constraining pore (longer distance translational diffusion removes the single molecule from the instrument

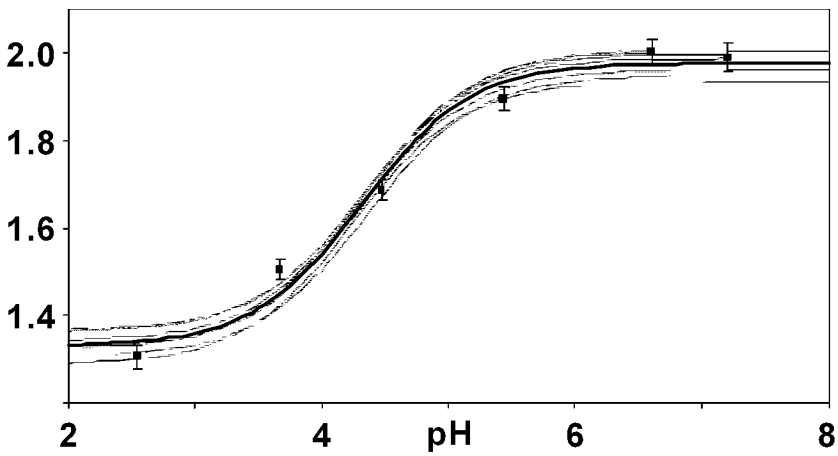

Figure 6.7. Average (black) and individual (grey) Henderson-Hasselbalch fits for seven buffer cycles over a 36 hour period. The black data points indicate the average value and the ~2% cycle standard deviation at each pH.

observation range). If the interconnected pores lead to the surface, without a constraining region smaller that the dye, a leaching channel to the surface is formed. On long immersion in buffers that promote guest host repulsion, the fully isolated dye that contributes to the fluorescence shoulder feature remains in the film, while the leachable dye that contributes to the peak emission eventually diffuses into the surrounding buffer. This reduction in the peak intensity reduces the peak-shoulder ratio. This influence would not be as evident at higher bulk concentrations since each dye molecule contributes a reduced amount to the total fluorescence and emits a fraction of its maximum emission intensity. In the bulk sample, individual dye molecule leaching or photobleaching is compensated for by the remaining bulk dye ensemble. The molecules remaining slightly increase their emission by absorbing the excitation light no longer absorbed by the missing molecule, minimizing its loss.

In the nanomolar films studied here, each molecule emits closer to its maximum emission yield. Therefore, when it is removed by bleaching, or leaching, the other molecules are less able to compensate for the loss. Thus in the nanomolar sample, even a small degree of leaching from the film, while an undetectable concentration in the solvent, becomes readily evident in the film intensity and the peak-shoulder ratio as well. Using the nanomolar ORG sample permits us to directly and rapidly observe changes in the film response due to leaching, rather than relying on the storage solution dye concentration as a measure of dye leaching. The low sample concentration reveals the processes occurring.

6.4 CONCLUSION

ORG doped silica sol-gel thin film performance as an optical pH sensor was critically evaluated. The high fluorescence quantum yield and change in extinction coefficient upon dye protonation permits pH determination even at nanomoler ORG concentrations.[52] These low concentrations also provide an increased understanding of sensor function and behavior. While sensor performance under these conditions is not at the level desired for analytical applications, several modifications to the system could be made to improve performance.

To make a thin film ORG sensor practical for application, effort should focus on ways to improve the film response time and cycling rate. Response hysteresis reduction through midrange pH buffer pre-equilibration must be further investigated. While cycling to obtain a steady-state condition has been used to achieve minute response times for other silica sol-gel sensors,[47] ultimately the limiting rate will be the solvent diffusion rate through the film. The diffusion rate could be improved by making thinner silica films, or increasing the silica film porosity. Making thinner or more porous films would require slight preparation modifications, but the new films must be evaluated for mechanical strength, adherence to the substrate, and resistance to dye leaching as the dye-solvent interactions increase.

A higher ORG concentration could also be used. The associated fluorescence intensity increase would influence sensor optimization and response in several ways. It would reduce the spectrum accumulation time, reduce the need for multiple accumulations, decrease the laser excitation intensity needed, decrease the system sensitivity to random intensity variations that result from non-uniform dye distribution,

and reduce the dye leaching and photobleaching influence on the response. These effects would correspond to an improved sampling rate, increased dye lifetime, and an improved response intensity and ratio stability. However, care must be taken to avoid over doping the films, since there is the potential for dye self quenching at high concentrations.

The pH range limitation imposed by silica dissolution is an issue common to all silica based materials, including chromatography columns.[62-65] While it prevents silica thin film application in high pH environments, silica remains a viable support material for low to mid range pH's, including biological environments. The choice of ORG with a 4.1 pK_a as the silica guest compliments the silica operational range. Since ORG is fully deprotonated above pH 7, the high pH limitation does not reduce the sensor functional range. Coating exposed host silanol groups with a protecting group might increase the silica host operational range by reducing silica dissolution,[63] but the resulting influence on the ORG environment might compromise response.

ORG doped silica thin films demonstrate promise as a low- to mid- range pH sensor. Developing this potential will provide an additional tool to the field of optical sensors. But more important than a new optical sensor is the increased knowledge gained through further studying the transitional region between single molecule behavior and bulk averaged response.

Chapter VI References

(1) Reisfeld, R.; Yariv, E.; Minti, H. *Opt. Mater.* **1997**, *8*, 31.
(2) Tang, Y.; Dave, B. C. *Adv. Mater.* **1998**, *10*, 1536.
(3) Casalboni, M.; DeMatteis, F.; Francini, R.; Prosposito, P.; Senesi, R.; Grassano, U. M.; Pizzoferrato, R.; Gnappi, G.; Montenero, A. *J. Lumines.* **1997**, *72-4*, 475.
(4) Dunn, B.; Zink, J. I. *Chem. Mater.* **1997**, *9*, 2280.
(5) Dave, B. C.; Miller, J. M.; Dunn, B.; Valentine, J. S.; Zink, J. I. *J. Sol-Gel Sci. Technol.* **1997**, *8*, 629.
(6) Panitz, J.-C.; Geiger, F. *J. Sol-Gel Sci. Technol.* **1998**, *13*, 473.
(7) Koone, N. D.; Zerda, T. W. *J. Sol-Gel Sci. Technol.* **1997**, *8*, 883.
(8) Lan, E. H.; Dave, B. C.; Fukuto, J. M.; Dunn, B.; Zink, J. I.; Valentine, J. S. *J. Mater. Chem.* **1999**, *9*, 45.
(9) MacCraith, B. D.; McDonagh, C.; McEvoy, A. K.; Butler, T.; Okeeffe, G.; Murphy, V. *J. Sol-Gel Sci. Technol.* **1997**, *8*, 1053.
(10) Villegas, M. A.; Pascual, L. *J. Mater. Sci.* **2000**, *35*, 4615.
(11) Ben-David, O.; Shafir, E.; Gilath, I.; Prior, Y.; Avnir, D. *Chem. Mater.* **1997**, *9*, 2255.
(12) Nishida, F.; McKiernan, J. M.; Dunn, B.; Zink, J. I.; Brinker, C. J.; Hurd, A. J. *J. Am. Ceram. Soc.* **1995**, *78*, 1640.
(13) Ferrer, M. L.; del Monte, F. *Langmuir* **2003**, *19*, 650.
(14) Sackett, D. L.; Wolff, J. *Anal. Biochem.* **1987**, *167*, 228.
(15) Narang, U.; Wang, R.; Prasad, P. N.; Bright, F. V. *J. Phys. Chem.* **1994**, *98*, 17.
(16) Flora, K. K.; Brennan, J. D. *J. Phys. Chem. B* **2001**, *105*, 12003.
(17) Higgins, D. A.; Collinson, M. M.; Saroja, G.; Bardo, A. M. *Chem. Mater.* **2002**, *14*, 3734.
(18) Viteri, C. R.; Gilliland, J. W.; Yip, W. T. *J. Am. Chem. Soc.* **2003**, *125*, 1980.
(19) Gilliland, J. W.; Yokoyama, K.; Yip, W. T. *J. Phys. Chem. B* **2005**, *109*, 4816.
(20) Gilliland, J. W.; Yokoyama, K.; Yip, W. T. *Chem. Mater.* **2004**, *16*, 3949.
(21) Komori, Y.; Hayashi, S. *Phys. Chem. Chem. Phys.* **2003**, *5*, 3777.
(22) Wheeler, K. E.; Lees, N. S.; Gurbiel, R. J.; Hatch, S. L.; Nocek, J. M.; Hoffman, B. M. *J. Am. Chem. Soc.* **2004**, *126*, 13459.
(23) Dong, H.; Lee, M.; Thomas, R. D.; Zhang, Z.; Reidy, R. F.; Mueller, D. W. *J. Sol-Gel Sci. Technol.* **2003**, *28*, 5.
(24) Dulebohn, J. I.; Haefner, S. C.; Berglund, K. A.; Dunbar, K. R. *Chem. Mater.* **1992**, *4*, 506.
(25) Martinez, J. R.; Ruiz, F.; Vorobiev, Y. V.; Perez-Robles, F.; Gonzalez-Hernandez, J. *J. Chem. Phys.* **1998**, *109*, 7511.
(26) Hentze, H.-P.; Raghavan, S. R.; McKelvey, C. A.; Kaler, E. W. *Langmuir* **2003**, *19*, 1069.
(27) Garcia, J. A. M.; Valverde, G.; Zink, J. I. *Langmuir* **2003**, *19*, 4411.
(28) Garcia, M. J.; Valverde, G.; Cruz, D.; Franco, A.; Zink, J. I.; Minoofar, P. *J. Phys. Chem. B* **2003**, *107*, 2249.
(29) Minoofar, P. N.; Hernandez, R.; Chia, S.; Dunn, B.; Zink, J. I.; Franville, A.-C. *J. Am. Chem. Soc.* **2002**, *124*, 14388.
(30) Yariv, E.; Schultheiss, S.; Saraidarov, T.; Reisfeld, R. *Opt. Mater.* **2001**, *16*, 29.

(31) Rahn, M. D.; King, T. A.; Gorman, A. A.; Hamblett, I. *Appl. Opt.* **1997**, *36*, 5862.
(32) Mei, E.; Bardo, A. M.; Collinson, M. M.; Higgins, D. A. *J. Phys. Chem. B* **2000**, *104*, 9973.
(33) Lloyd, C. R.; Eyring, E. M. *Langmuir* **2000**, *16*, 9092.
(34) Gulcev, M. D.; Goring, G. L. G.; Rakic, M.; Brennan, J. D. *Anal. Chim. Acta* **2002**, *457*, 47.
(35) Chen, J. P.; Wang, H. Y. *Biotechnol. Tech.* **1998**, *12*, 851.
(36) Ellerby, L. M.; Nishida, C. R.; Nishida, F.; Yamanaka, S. A.; Dunn, B.; Valentine, J. S.; Zink, J. I. *Science* **1992**, *255*, 1113.
(37) Gill, I. *Chem. Mater.* **2001**, *13*, 3404.
(38) Lobnik, A.; Wolfbeis, O. S. *J. Sol-Gel Sci. Technol.* **2001**, *20*, 303.
(39) von Bueltzingsloewen, C.; McEvoy, A. K.; McDonagh, C.; MacCraith, B. D.; Klimant, I.; Krause, C.; Wolfbeis, O. S. *Analyst* **2002**, *127*, 1478.
(40) Wen-xu, L.; Jian, C. *Anal. Chem.* **2003**, *75*, 1458.
(41) Lee, J. E.; Saavedra, S. S. *Anal. Chim. Acta* **1994**, *285*, 265.
(42) Chen, L.-X.; Niu, C.-G.; Zeng, G.-M.; Huang, G.-H.; Shen, G.-L.; Yu, R.-Q. *Anal. Sci.* **2003**, *19*, 295.
(43) Kim, W.; Chung, S.; Park, S. B.; Lee, S. C.; Kim, C. *Anal. Chem.* **1997**, *69*, 95.
(44) Kimura, K.; Sunagawa, T.; Yokoyama, M. *Anal. Chem.* **1997**, *69*, 2379.
(45) Kimura, K.; Sunagawa, T.; Yajima, S.; Miyake, S.; Yokoyama, M. *Anal. Chem.* **1998**, *70*, 4309.
(46) Collinson, M. M.; Howells, A. R. *Anal. Chem.* **2000**, *72*, 702A.
(47) Yang, L.; Saavedra, S. S. *Anal. Chem.* **1995**, *67*, 1307.
(48) Brinker, C. J.; Hurd, A. J.; Schunk, P. R.; Frye, G. C.; Ashley, C. S. *J.f Non-Cryst. Solids* **1992**, *147-148*, 424.
(49) Huang, M. H.; Soyez, H. M.; Dunn, B. S.; Zink, J. I. *Chem. Mater.* **2000**, *12*, 231.
(50) Rivera, D.; Harris, J. M. *Langmuir* **2001**, *17*, 5527.
(51) Fu, Y.; Collinson, M. M.; Higgins, D. A. *J. Am. Chem. Soc.* **2004**, *126*, 13838.
(52) Haugland, R. P. *Handbook of Fluorescent Probes and Research Products*, 9th ed.; Molecular Probes: Eugene, OR, 2002.
(53) Lin, H. J.; Szmacinski, H.; Lakowicz, J. R. *Anal. Biochem.* **1999**, *269*, 162.
(54) Sun, W.-C.; Gee, K. R.; Klaubert, D. H.; Haugland, R. P. *J. Org. Chem.* **1997**, *62*, 6469.
(55) Orte, A.; Crovetto, L.; Talavera, E. M.; Boens, N.; Alvarez-Pez, J. M. *J. Phys. Chem. A* **2005**, *109*, 734.
(56) The original published reference misreports the pKa value as 3.7
(57) Ong, S.; Zhao, X.; Eisenthal, K. B. *Chem. Phys. Lett.* **1992**, *191*, 327.
(58) Smith, E. A.; Wirth, M. J. *J. Chromatogr., A* **2004**, *1060*, 127.
(59) Ribou, A. C.; Vigo, J.; Salmon, J. M. *J. Chem. Educ.* **2002**, *79*, 1471.
(60) Brasselet, S.; Moerner, W. E. *Single Mol.* **2000**, *1*, 17.
(61) Whitaker, J. E.; Haugland, R. P.; Prendergast, F. G. *Anal. Biochem.* **1991**, *194*, 330.
(62) Tindall, G. W.; Perry, R. L. *J. Chromatogr., A* **2003**, *988*, 309.
(63) Kirkland, J. J.; Henderson, J. W.; DeStefano, J. J.; van Straten, M. A.; Claessens, H. A. *J. Chromatogr., A* **1997**, *762*, 97.

(64) Claessens, H. A.; van Straten, M. A.; Kirkland, J. J. *J. Chromatogr., A* **1996**, *728*, 259.
(65) Kirkland, J. J.; van Straten, M. A.; Claessens, H. A. *J. Chromatogr., A* **1995**, *691*, 3.

Chapter VII

Comparison of TRITC Rotational Mobility and Photostability in Silica Thin Films, Silica Nanoparticles, and Covalently Bound to Silica Nanoparticles

7.1 CHAPTER ABSTRACT

While our previous studies focused on investigating silica thin films through guest molecule variation, in this chapter we instead compare guest mobility, lifetime, and photostability for two different silica sol-gel host structures. The silica nanoparticle (SNP) structure contains a more highly branched silica network than the silica thin films due to base catalyzed changes in the hydrolysis and condensation rates. The tetramethylrhodamine-5-isothiocyanate (TRITC) guest molecule mobility in thin films was found to change little on environmental variation, likely due to hydrogen bonding and charge attraction to the surface. In contrast, the less dense SNP structure facilitates greater guest rotational mobility than the thin films, as shown by the increased intermediate molecule populations. The covalently bound TRITC mobility was found to differ little from the unbound TRITC mobility in SNP. While SNP incorporation alone did not significantly alter the TRITC lifetime or photobleaching quantum yield (ϕ_b) relative to the thin films, covalent bonding to the surface was found to increase the TRITC lifetime. However, a corresponding decrease in the ϕ_b, indicating increased photostability, was not observed. This implies a greater number of, or more efficient, radiationless excited state deactivation pathways within the covalently bound TRITC doped SNP sample.

7.2 INTRODUCTION

Our previous investigations focused on studying silica sol-gel thin films for optical sensor development purposes. However, using the sol-gel process, silica nanoparticles (SNP) can also be formed from the same starting materials as the films. Switching to a basic sol-gel catalyst provides highly branched discrete silica particles, rather than films.[1] Most methods for forming monodisperse SNP are based on the Stöber method, which employs ammonia to catalyze the sol-gel reaction.[2] The differences in the acid and base catalyzed sol-gel structures are attributed to differences in the acid and base catalyzed hydrolysis and condensation reaction mechanisms.

In an acid catalyzed reaction, hydrolysis occurs rapidly through "a bimolecular displacement mechanism which substitutes a H^+ (hydronium ion) for an alkyl group (R)."[3] At low pH, the hydrolysis rate occurs more rapidly than the condensation rate, favoring a more linear cross-linked silica structure.[3] The slow condensation rate allows time for the added silicate monomer units ($Si(OH)_4$) to rearrange into a conformation favorable for further cross-linking to the growing silica polymer network. On the other hand, for basic catalyst the hydrolysis mechanism switches to a nucleophilic substitution reaction which proceeds much slower than the rapid condensation reaction.[3] One factor that influences the base catalyzed hydrolysis rate is the silicon atom substituent group identity. When an alkoxy group is replaced by an attacking OH^- nucleophile, the silicon atom gains positive charge and experiences decreased steric hindrance.[4] These changes promote hydrolysis of the remaining alkoxy groups, and the hydrolysis rate accelerates as each alkoxy group is removed.[4] However, if the silicon condenses with a large polymer unit before all the alkoxy groups are hydrolyzed, the bonded silica network will sterically

hinder hydrolysis of the remaining alkoxy groups.[4] In the base catalyzed reaction, since condensation is rapid, an approaching silicate monomer condenses with the polymer network before it can assume an orientation favorable for additional cross-linking. This rapid random monomer addition leads to discrete silica nanoparticles.

SNP formation begins with condensation between two silicate monomer units to form a nucleation center. As the number of silicon atoms in the silica polymer cluster increases, the peripheral silanol group acidity is increased, making the silanol more reactive, which leads to preferential monomer addition to the larger polymer networks.[4] The nucleation centers grow through monomer and aggregate addition until the available silica source is consumed. Thus the final nanoparticle size depends on both the nucleation center prevalence and the abundance of reagent silica. The reagent silica available is easily regulated by adjusting the silane volume or concentration added to the reaction. The nucleation center abundance depends on charge repulsion to stabilize the nucleation center population. As the nucleation centers grow in size, the increasing negative surface charge prevents large nucleation centers from aggregating due to mutual repulsion.[5-7] Positive ions added to the sol solution during SNP formation can decrease the nucleation center stability by reducing the negative surface charge, leading to increased aggregation.[5-7] Nucleation center stability reaches a minimum at the nucleation center isoelectric point.[7] At this point the fewest nucleation centers will survive to form a small number of large SNP. Cationic charge addition after the isoelectric point increases nucleation center stability through increased positive charge repulsion, leading to a larger number of smaller SNP.

Like the silica sol-gel thin films, SNP are used in a variety of applications including optical sensors,[8] biosensors supports,[9] fluorescent bioimaging tags,[10,11] DNA or drug delivery carriers,[12] reaction catalyst,[13] and chromatographic support phases.[14-17] SNP are an attractive material due to their high surface area and silica's low chemical reactivity and toxicity. Like the silica thin films, guest molecules can be trapped inside SNP to confine or protect the guest molecules within the silica host matrix.[5-7,10,18] The SNP surface can be modified to attach guest doped SNP as fluorescent tags for imaging and tracing, [10,11] or to use the SNP as a solid support phase for biosensor and catalytic applications.[9,12,13] For these applications, an increased understanding about the silica host interaction with the confined, or bound, guest is necessary to maximize guest stability. Since silica thin films and SNP are both silica based sol-gel materials, they may display similar guest interactions. However, as shown in the $DiIC_{12}$ investigation, the preparation conditions significantly influence guest behavior. Knowing that the SNP network is more highly branched than the films,[1] we cannot confidently extend our thin film based conclusions to the SNP environment. In addition, the SNP covalent surface

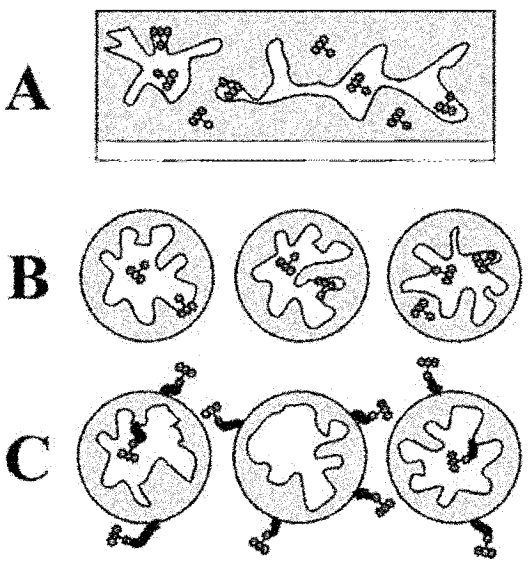

Figure 7.1. The three guest-host environments to be investigated are depicted to the left. The silica sol-gel film (A) is our reference environment where the dye is trapped within the pores or incorporated within the matrix. The doped SNP also traps the dye within the pores and matrix (B), but the more branched silica structure should be less physically restrictive. For the dye covalently bound to the SNP (C) the dye will be attached after SNP formation, ensuring it will reside within the pores, or on the SNP surface

modification used to attach organic and biological molecules to the SNP provides an opportunity to investigate more restricted guest molecule behavior.

With these considerations in mind we determined to compare guest dye mobility and photostability in three environments: (i) dye doped silica thin films, (ii) dye doped SNP, and (iii) dye covalently bound to SNP (Figure 7.1). The silica thin films will serve as our connection to previous studies while we investigate how the SNP structure modifies the guest behavior. The dye covalently bonded to the SNP surface should also reveal how covalent bonding influences the dye mobility and stability relative to the unbound dye physically trapped inside the SNP. In the thin film and unbound SNP samples, the dye should primarily reside within the pores left behind after condensation, but could become fully incorporated within the silica matrix. Since the SNP silica network contains greater branching, the dye doped in SNP is expected to display greater rotational mobility than the thin films, due to reduced physical confinement. While rhodamine 6 G (R6G) is appropriate to investigate the structural difference between the thin film and SNP, R6G cannot be covalently bound to the SNP (Figure 7.2). Instead, tetramethylrhodamine-5-

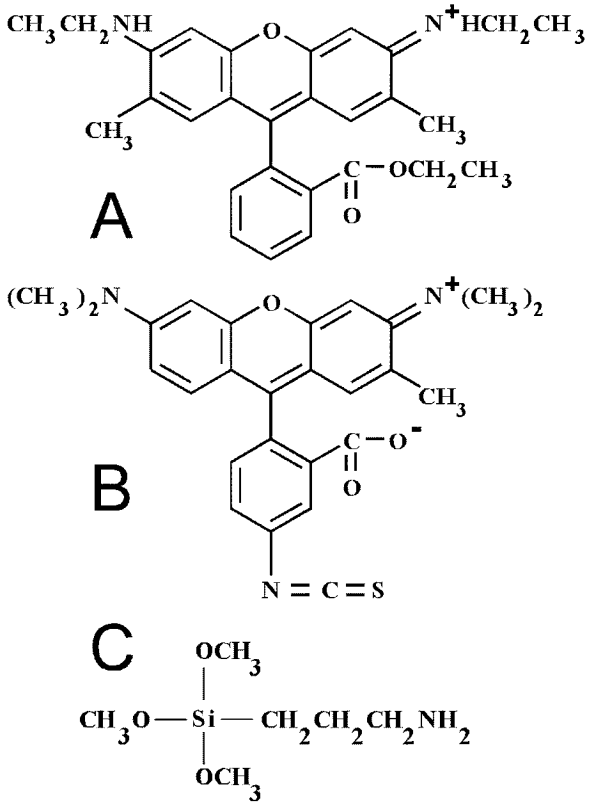

Figure 7.2. The chemical structures for R6G (A), TRITC (B), and APS (C) are shown above.

isothiocyanate (TRITC) was used to facilitate covalent attachment to the silica surface via the isothiocyanate functional group and 3-aminopropyl-trimethoxysilane (APS) (Figure 7.2 and 7.3). The TRITC covalently bond to the surface will make the dye "unleachable" into solution, eliminating the leaching problem common to doped silica materials. While it is assumed that the covalent bond does not alter the dye photostability, due to its distance from the fluorophore active moiety, it is unknown to what extent the bonding will influence dye mobility and photostability.

7.3 RESULTS AND DISCUSSION

7.3.1 SNP Preparation and TRITC Covalent Attachment

SNP samples where the dye is condensed with the silica precursor, similar to the thin film preparation procedure, are referred to as "doped" SNP samples. R6G and TRITC doped SNP were prepared using the Stöber method, with the reagent amounts adjusted to accommodate the small sample scale appropriate for our single molecule experiments.[2] The exact SNP preparation procedure used is documented in Chapter 2. In order to functionalize the SNP with APS for TRITC covalent bonding, a larger scale SNP preparation method was necessary.

The SNP amine functionalization procedure is based on the aqueous functionalization procedure reported by Choi and Chen.[11] The silica nanoparticles were prepared by combining 1.71 mL 30% NH_4OH, 13.8 mL 100% EtOH, and 0.61 mL TEOS with vigorous stirring until the solution turned cloudy, signaling SNP nucleation (approximately 5 minutes). After nucleation, the solution was moderately stirred for a total of 20 minutes at room temperature. After 20 minutes, the reaction was stopped by adding 1 M acetic acid until the solution reached pH 4 (about 100 mL 1 M acetic acid).

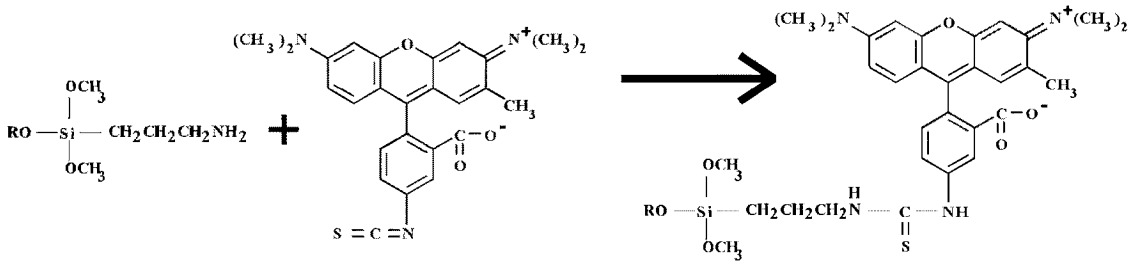

Figure 7.3. The TRITC-APS coupling reaction scheme is shown above. The TRITC isothiocyanate bonds to the APS previously attached to the SNP surface (R). This bond tethers the TRITC to the SNP.

The SNP/acetic acid solution was then refluxed at 80°C for 3 hours, reducing the total volume to 50 mL. After refluxing, 1.5 mL APS was added to the cooled solution with vigorous stirring for an hour to bond the APS to the SNP. Amine attachment to the SNP was confirmed by repeatedly rinsing the APS modified silica nanoparticles (APS-SNP) with acetone to remove unbound APS before adding salicylic aldehyde to the APS-SNP precipitate.[11] The bright yellow Schiff base produced shows that the SNP were functionalized by APS. A Schiff base was not observed when salicylic aldehyde was added to the final APS-SNP rinse solution. 8 mL APS-SNP solution and 2 mL TRITC dissolved in water were finally combined with stirring to form the TRITC-amine-SNP covalent bond as depicted in Figure 7.3.

APS-dye coupling can also be accomplished by combining APS with dye dissolved in anhydrous EtOH and allowing the solution to stir for 12 hours.[5] The amine coupled dye can then be added to the SNP reaction solution for co-condensation with the SNP matrix as it forms. However, the aqueous amine functionalization procedure was chosen over the anhydrous coupling procedure to ensure dye coupling to the surface, as well as its biocompatibility. Since the SNP are fully formed before the APS is added, TRITC will only be tethered to the pore interior or SNP exterior surfaces. In addition, the

aqueous procedure will permit extending this investigation to include tethered biomolecule mobility and stability in the future.

7.3.2 R6G Doped SNP Response

Due to our familiarity with R6G response in thin film environments we chose to use R6G for our initial SNP study. The previously reported R6G dry, water and EtOH equilibrated fresh film mobilities, as well as a new dry and water equilibrated day one film results are compared to the R6G doped SNP (R6G/SNP) mobility in Figure 7.4 and Table 7.1. As previously reported for the fresh films, there is an increase in the R6G fixed population on solvent addition. This proved true for the new day one water equilibrated sample as well, however the difference between the dry and water equilibrated fixed populations is less than that observed in the fresh films. This smaller change could signal that the dye's ability to leach decreased as the sample aged. This would reflect the more cross-linked silica structure present in the aged sample. The day one water equilibrated film mobility is also remarkably similar to the EtOH equilibrated fresh film mobility.

The R6G doped SNP mobility varies significantly from that seen for the majority of the thin film environments. In general it possesses a reduced fixed molecule population and increased tumbling and intermediate populations compared to the R6G film samples. This increased mobility likely results from the higher silica matrix branching due to the base catalyst. It is unlikely that residual catalyst caused the increased dye mobility, since a more basic internal solution would deprotonate surface silanol groups, and increase dye immobilization through greater charge-charge attraction. In addition, the SNP were washed repeatedly with EtOH and acetone to remove excess

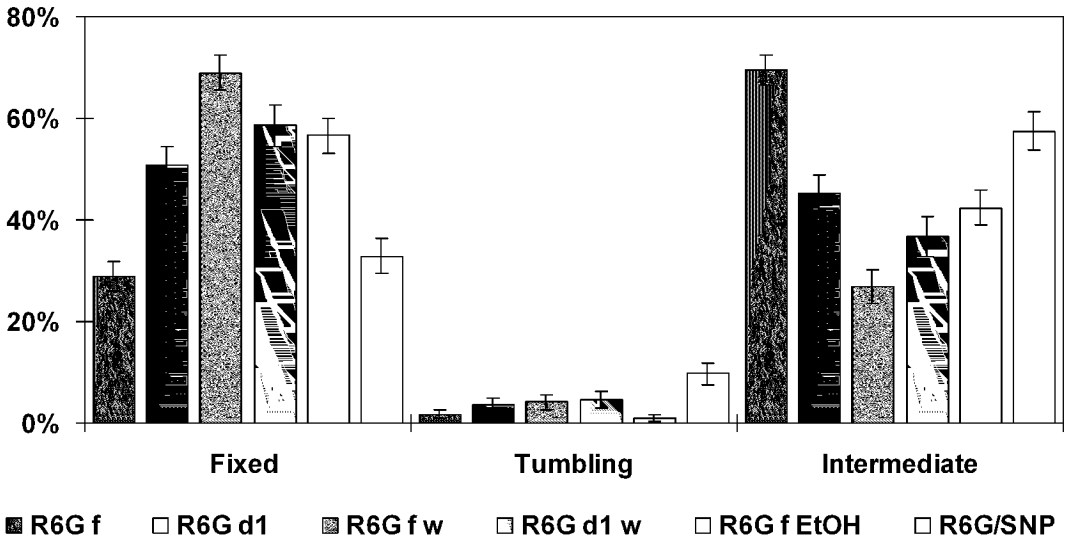

Figure 7.4. R6G mobilities for fresh, day one, water and EtOH equilibrated films, and R6G doped SNP. Within the silica films the fixed population increases with film age and on solvent addition. Even though the SNP were rinsed repeatedly, their mobility resembles the fresh film more than the solvent equilibrated films. This increased mobility likely indicates larger SNP pores due to the higher branched base catalyzed silica structure.

Table 7.1. R6G mobilities indicating the population in percentage and number of molecules.

Dye	R6G f	R6G d1	R6G f w	R6G d1 w	R6G f EtOH	R6G/SNP
Fixed (%)	29 ± 3% 69	51 ± 3% 110	69 ± 3% 131	58 ± 4% 89	57 ± 4% 116	33 ± 3% 61
Tumbling (%)	2 ± 1% 4	4 ± 1% 8	4 ± 2% 8	5 ± 2% 7	1 ± 1% 2	10 ± 2% 18
Intermediate (%)	69 ± 3% 167	45 ± 3% 98	27 ± 3% 51	37 ± 4% 56	42 ± 4% 87	57 ± 4% 107

dye and ammonium hydroxide before testing. Due to this rinsing the EtOH equilibrated film environment would be expected to be similar to the R6G/SNP sample, but R6G/SNP resembles the fresh film most. Since the SNP sample shows an increase in mobility relative to the EtOH film, the mobility difference is not due to dye solvation in EtOH.

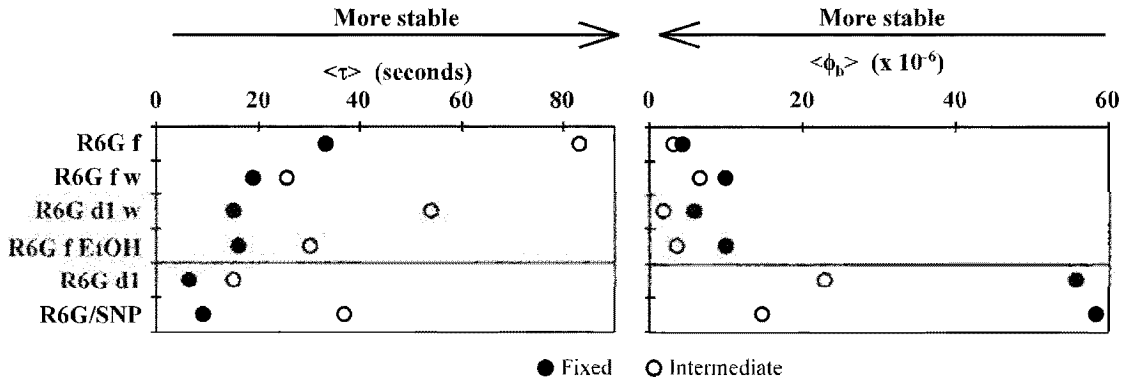

Figure 7.5. R6G $\langle \tau \rangle$ and $\langle \phi_b \rangle$ for thin film and SNP samples. Due to differences in excitation power and instrumentation the R6G day one and SNP samples cannot be directly compared to the other film results. Tumbling results are excluded due to small sample size.

Table 7.2. R6G Survival lifetime analysis based on single- and bi-exponential decay functions using Excel©. The R6G f and R6G EtOH tumbling results are not reported due to low populations.

Dye	Category	a_1	τ_1 (s)	a_2	τ_2 (s)	$\langle r^2 \rangle$	$\langle \tau \rangle$ (s)
R6G f	Fixed	0.39±0.02	4.8±0.4	0.61±0.02	51±2	0.9980	33±2
	Tumbling	-	-	-	-	-	-
	Intermediate	0.25±0.01	14.4±0.9	0.75±0.01	106±2	0.9992	83±2
R6G f w	Fixed	0.52±0.01	3.3±0.1	0.48±0.01	36±1	0.9979	18.9±0.8
	Tumbling	0.4±0.1	1.1±0.5	0.56±0.09	30±9	0.9821	17±6
	Intermediate	1.0	25.5±0.3	-	-	0.9970	25.5±0.3
R6G d1 w	Fixed	0.41±0.02	2.7±0.2	0.58±0.02	24±1	0.9972	15±1
	Tumbling	1.0	28±5	-	-	0.8362	28±5
	Intermediate	0.8±0.2	38±7	0.2±0.2	123±108	0.9962	54±37
R6G f EtOH	Fixed	0.62±0.02	3.9±0.2	0.38±0.02	36±3	0.9978	16±1
	Tumbling	-	-	-	-	-	-
	Intermediate	1.0	30.1±0.3	-	-	0.9983	30.1±0.3
R6G d1	Fixed	0.47±0.5	2.0±0.3	0.53±0.06	10±1	0.9955	6.4±0.9
	Tumbling	1.0	7.0±0.5	-	-	0.9792	7.0±0.5
	Intermediate	1.0	15.1±0.1	-	-	0.9966	15.1±0.1
R6G/SNP	Fixed	0.8±0.1	5.1±0.6	0.2±0.1	23±11	0.9968	9±4
	Tumbling	0.25±0.09	2±1	0.8±0.1	14±2	0.9916	11±2
	Intermediate	1.0	36.8±0.5	-	-	0.9945	36.8±0.5

Rather the similarity between the fresh film and R6G/SNP samples reflect the less confined silica structure present in both samples.

The R6G exponential fitted survival lifetimes are reported in Table 7.2, while the photobleaching quantum yields (ϕ_b) are in Table 7.3. The average survival lifetimes ($\langle\tau\rangle$) and average photobleaching quantum yields ($\langle\phi_b\rangle$) are displayed according to mobility in Figure 7.5. Most notable in Figure 7.5 is that the dry day one and R6G/SNP $\langle\tau\rangle$ and $\langle\phi_b\rangle$ appear much less photostable than the other dry and solvated films. This disparity reflects differences in the dry day one and R6G/SNP instrument collection efficiency and

Table 7.3. R6G photobleaching quantum yields based on single- and bi-exponential decay functions using Excel©. The R6G f and R6G EtOH tumbling results are not included due to low populations.

Dye	Category	a_1	ϕ_1 ($\times10^{-6}$)	a_2	ϕ_2 ($\times10^{-6}$)	$\langle r^2\rangle$	$\langle\phi_b\rangle$ ($\times10^{-6}$)
R6G f	Fixed	0.58±0.05	1.2±0.1	0.42±0.05	9±1	0.9952	4.3±0.8
	Tumbling	-	-	-	-	-	-
	Intermediate	0.96±0.03	1.33±0.08	0.04±0.03	42±121	0.9887	3±5
R6G f w	Fixed	0.78±0.01	3.00±0.09	0.22±0.02	34±4	0.9981	10±1
	Tumbling	1.0	4.1±0.4	-	-	0.9737	4.1±0.4
	Intermediate	0.94±0.04	2.0±0.2	0.06±0.04	75±202	0.9906	7±13
R6G d1 w	Fixed	0.5±0.1	2.6±0.4	0.5±0.1	9±1	0.9979	6±1
	Tumbling	0.2±0.5	2±3	0.8±0.5	7±3	0.9896	6±4
	Intermediate	1.0	1.8±0.4	-	-	0.9934	1.8±0.4
R6G f EtOH	Fixed	0.75±0.01	2.9±0.6	0.25±0.01	31±2	0.9992	9.9±0.6
	Tumbling	-	-	-	-	-	-
	Intermediate	0.86±0.06	1.8±0.2	0.14±0.06	13±8	0.9918	3±1
R6G d1	Fixed	0.84±0.02	22.1±0.4	0.16±0.02	234±58	0.9976	56±11
	Tumbling	1.0	14.3±0.8	-	-	0.9880	14.3±0.8
	Intermediate	0.67±0.05	9.0±0.7	0.33±0.05	51±8	0.9970	23±4
R6G/SNP	Fixed	0.98±0.05	30±3	0.02±0.05	1260±19800	0.9890	58±462
	Tumbling	1.0	39±2	-	-	0.9832	39±2
	Intermediate	1.0	14.6±0.2	-	-	0.9969	14.6±0.2

excitation power relative to the other four R6G films. All R6G samples were tested using 514 nm excitation. However, the R6G fresh, fresh and day one water equilibrated, and EtOH equilibrated samples were tested with an approximate 917 $W \cdot cm^{-2}$ power density, while the R6G day one and R6G/SNP were tested with a carefully reproduced 548 $W \cdot cm^{-2}$ power density on a separate instrument. These differences in the excitation power alter the excitation rate, making direct survival lifetime comparison impossible. At the same time, the results are puzzling since the samples excited by the lower excitation power (dry day one and R6G/SNP) have shorter lifetimes than those that experienced the higher excitation power. The large differences in the $\langle \phi_b \rangle$ values are likely the result of instrument collection efficiency differences that reduced the total photons recorded for the dry day one and R6G/SNP samples. The excitation power differences apparently had minimal influence on the mobility classifications. The dry day one sample presented here was excited with half the power used for the dry day one sample reported in Chapter 3, yet the two samples are almost within sampling error of one another (Chapter 3 R6G day one mobilities were: Fixed 56% ± 4%, Tumbling 2% ± 1%, and Intermediate 42% ± 4%). Comparison of the R6G dry day one and R6G/SNP results show that intermediate molecules were stabilized in the SNP environment since the intermediate lifetime increased and the associated ϕ_b decreased. The R6G fixed population photostability appears largely unaffected by the film and SNP structural differences.

7.3.3 TRITC Film and SNP Response

Like SRB and ORG used in previous studies, TRITC has the same core molecular skeleton as R6G (Figure 7.2). Major differences between TRITC and R6G include the isothiocyanate group that permits TRITC covalent bonding to the APS amine, the methyl

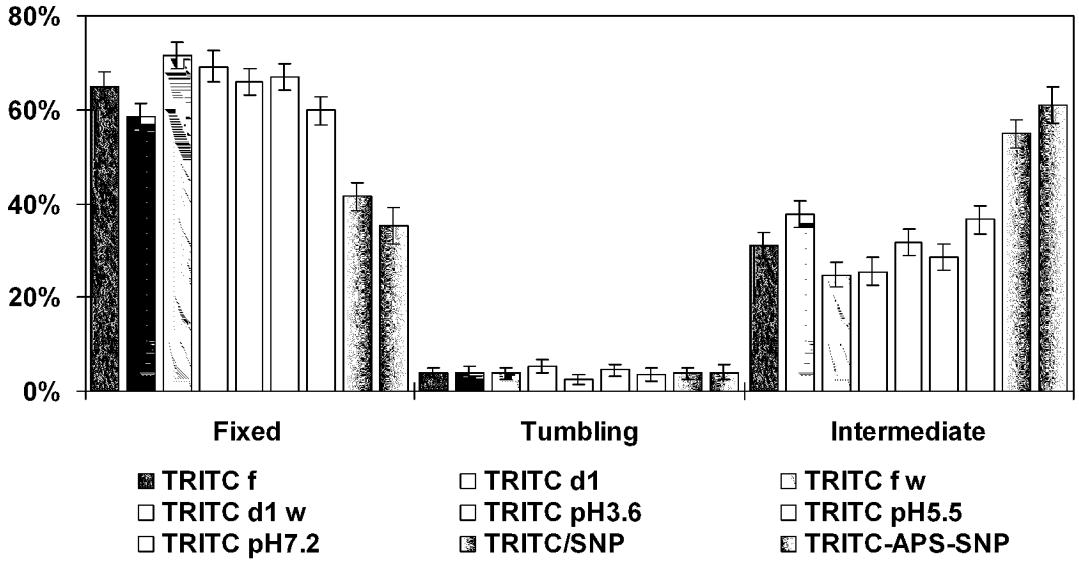

Figure 7.6. Unlike R6G the TRITC film mobilities appear largely insensitive to the film age, and water or pH equilibration. The TRITC films contain a greater fixed population than R6G, likely due to hydrogen bonding immobilization. Like the R6G doped SNP the TRITC SNP samples display reduced fixed and increased intermediate mobilities relative to the films. Surprisingly the TRITC doped and APS bound SNP show similar mobilities.

groups bound to the xanthene moiety nitrogens, and the carboxylic acid functional group that replaces the R6G ester on the bottom ring. Like SRB, TRITC is zwitterionic and the carboxylic acid functional group enables hydrogen bonding to the silica surface. The TRITC mobility in films and SNP are shown in Figure 7.6 and reported in Table 7.4. First, consider the TRITC film mobility in the dry, water, and pH buffered film environments. Surprisingly the TRITC film mobility is minimally influenced by the surrounding film environment. Dry and water equilibrated films were tested to check for preferential dye leaching and counter ion association related influences on mobility. There is an increase in the fixed population on solvent addition, but the change is not as large as that observed for other dyes. Solvent pH also had a minimal impact on the rotational mobility, even though the negatively charged carboxylic acid functional group

Table 7.4. TRITC mobilities presenting the population in percentage and number of molecules.

Dye	Fixed (%)	Tumbling (%)	Intermediate (%)
TRITC f	65 ± 3% 182	4 ± 1% 11	3 ± 3% 87
TRITC d1	58 ± 3% 175	4 ± 1% 12	38 ± 3% 113
TRITC f w	71 ± 3% 188	4 ± 1% 10	25 ± 3% 65
TRITC d1 w	69 ± 3% 144	5 ± 2% 11	26 ± 3% 53
TRITC pH 3.6	66 ± 3% 185	2 ± 1% 7	32 ± 3% 89
TRITC pH 5.5	67 ± 3% 181	4 ± 1% 12	29 ± 3% 77
TRITC pH 7.2	60 ± 3% 131	4 ± 1% 8	36 ± 3% 80
TRITC/SNP	41 ± 3% 111	4 ± 1% 10	55 ± 3% 147
TRITC -APS-SNP	35 ± 4% 53	4 ± 2% 6	61 ± 4% 92

should encourage increased mobility through charge-charge repulsion from the surface. Like SRB, TRITC hydrogen bonding is believed to dominate charge repulsion under nanoscopic confinement, resulting in the limited dye mobility variation observed. Since TRITC has a neutral net charge, cationic center attraction to the surface may act cooperatively with hydrogen bonding to immobilize the dye.

When the TRITC SNP mobilities are compared to the films, a difference is readily apparent (Figure 7.6). Both the TRITC doped SNP (TRITC/SNP) and the TRITC amine bound SNP (TRITC-APS-SNP) show increased intermediate populations and decreased fixed populations relative to the TRITC doped films. The SNP samples show this increased mobility even though they were repeatedly rinsed with acetone and EtOH to remove excess dye. The previous investigation into solvent equilibrated thin films indicated that solvent addition typically increases the fixed molecule population through mobile molecule preferential leaching. This reveals two things about the SNP samples. First, that doped TRITC is fully entrapped within the silica sol-gel nanoparticles, since the free dye was removed by rinsing. Second, as

proposed, the more branched SNP silica structure permits greater dye rotational mobility than the more cross-linked thin films. This is true in both the R6G/SNP and TRITC/SNP samples, despite TRITC's hydrogen bonding potential. Unexpectedly, the TRITC/SNP and TRITC-APS-SNP mobilities are similar, even though the TRITC-APS-SNP dye is covalently bound to the surface, which was expected to restrict the dye rotational freedom. The lack of significant change indicates that the intermediate molecule orientation changes involve surface reorientations rather than surface dissociation. Since APS contains multiple flexible sigma bonds, it does not appear to inhibit dye reorientation on the silica surface. A more detailed intermediate molecule transition analysis will be necessary to determine if fewer zero polarization reorientations occur within the TRITC-APS-SNP sample than in the TRITC/SNP sample. Comparing R6G/SNP mobility to both TRITC in SNP samples reveals that the R6G/SNP mobility is similar to the TRITC fixed and intermediate populations, but R6G has a greater tumbling population than either TRITC sample (Figure 7.7). The increased R6G tumbling freedom in the SNP is likely related to R6G's inability to hydrogen bond with the silica surface.

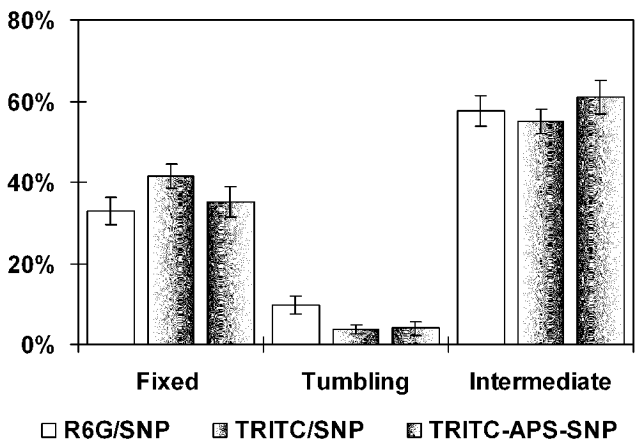

Figure 7.7. Mobility comparison between the three SNP samples. The R6G/SNP sample shows an increase in tumbling population relative to TRITC, probably due to R6G's inability to hydrogen bond. Surprisingly TRITC mobility changed little on covalent bonding to the SNP surface. This could indicate that dye intermediate behavior involves surface reorientations rather than complete surface dissociation.

Since the TRITC samples were all tested using the same conditions, the survival lifetimes and ϕ_b can be compared to elucidate host dependent differences in the TRITC photostability. Like the R6G day one films and R6G/SNP, the TRITC thin film and SNP samples were tested at 514 nm with a 548 $W \cdot cm^{-2}$ power density, allowing us to compare these two R6G samples to the TRITC results. The TRITC $\langle \tau \rangle$ results are presented in Figure 7.8, while the detailed $\langle \tau \rangle$ results are reported in Table 7.5. Like the TRITC mobility, there is surprisingly little change in the TRITC lifetimes across the silica thin film environments. This is seen in the consistent fixed molecule $\langle \tau \rangle$ position around 17 seconds. Although the tumbling $\langle \tau \rangle$ values are listed, the small tumbling molecule sample populations and the influence of high numeric aperture on fixed molecule misclassification introduce significant error. Thus, any conclusions based on these tumbling populations are tentative until larger sample sizes can be collected to confirm the results. The intermediate $\langle \tau \rangle$ is seen to be much more diverse than the fixed $\langle \tau \rangle$, reflecting the dynamic solvent-surface interface.

It is worth noting the similarity in the fresh TRITC film $\langle \tau \rangle$ and the TRITC/SNP $\langle \tau \rangle$ distributions (Figure 7.8). This similarity lends support to the conclusion that the fresh film and doped SNP samples share a similar degree of porosity. While it could instead indicate a similar degree of solvation in the SNP, due to the residual EtOH used to suspend the SNP, the disparity previously seen between the R6G/SNP and EtOH equilibrated thin film mobilities does not support this interpretation. An interesting trend emerges with the TRITC-APS-SNP sample, since the $\langle \tau \rangle$ increased relative to the unbound TRITC/SNP sample for all three mobility classes. The most dramatic $\langle \tau \rangle$ increase is seen for the TRITC fixed population, where the covalently bound fixed $\langle \tau \rangle$ is

Table 7.5. TRITC Survival lifetime analysis based on single- and bi-exponential decay functions using Excel©.

Dye	Category	a_1	τ_1 (s)	a_2	τ_2 (s)	$\langle r^2 \rangle$	$\langle \tau \rangle$ (s)
TRITC f	Fixed	0.42±0.02	3.2±0.2	0.58±0.02	21±1	0.9975	13.7±0.8
	Tumbling	1.0	3.9±0.3	-	-	0.9789	3.9±0.3
	Intermediate	1.0	40.2±0.6	-	-	0.9922	40.2±0.6
TRITC d1	Fixed	0.51±0.01	2.8±0.1	0.49±0.02	23±1	0.9978	12.4±0.6
	Tumbling	0.73±0.06	5.2±0.9	0.27±0.06	151±84	0.9915	45±2
	Intermediate	0.95±0.05	34±2	0.05±0.05	352±827	0.9945	49±42
TRITC f w	Fixed	0.78±0.03	7.8±0.4	0.22±0.03	54±11	0.9978	18±3
	Tumbling	0.3±0.1	2±1	0.7±0.1	30±7	0.9836	21±6
	Intermediate	1.0	46.5±0.4	-	-	0.9982	46.5±0.4
TRITC d1 w	Fixed	0.54±0.02	4.6±0.2	0.46±0.02	24±1	0.9989	13.4±0.8
	Tumbling	1.00	10.9±0.8	-	-	0.9790	10.9±0.8
	Intermediate	1.00	35.0±0.8	-	-	0.9947	35.0±0.8
TRITC pH 3.6	Fixed	0.56±0.03	5.2±0.3	0.44±0.03	26±3	0.9981	14±1
	Tumbling	1.0	13±1	-	-	0.9761	13±1
	Intermediate	0.37±0.05	16±6	0.63±0.04	84±2	0.9977	59±6
TRITC pH 5.5	Fixed	0.70±0.03	7.4±0.3	0.30±0.03	41±4	0.9984	18±2
	Tumbling	0.3±0.1	2±1	0.7±0.2	16±4	0.9814	12±4
	Intermediate	1.0	31.4±0.3	-	-	0.9975	31.4±0.3
TRITC pH 7.2	Fixed	0.53±0.04	3.8±0.3	0.47±0.04	21±2	0.9972	12±1
	Tumbling	1.0	10±1	-	-	0.9709	10±1
	Intermediate	0.7±0.1	27±4	0.3±0.2	103±45	0.9950	47±20
TRITC/ SNP	Fixed	0.45±0.03	4.1±0.4	0.55±0.03	27±2	0.9974	17±1
	Tumbling	1.0	3.7±0.3	-	-	0.9756	3.7±0.3
	Intermediate	1.0	43.4±0.2	-	-	0.9982	43.4±0.2
TRITC-APS-SNP	Fixed	0.82±0.03	13±1	0.18±0.03	219±92	0.9927	50±18
	Tumbling	0.2±0.1	0.5±0.7	0.8±0.1	14±3	0.9882	12±3
	Intermediate	0.95±0.03	37±2	0.05±0.03	578±896	0.9968	64±47

nearly three times larger than the unbound TRITC.

The $\langle \phi_b \rangle$ results are shown in Figure 7.8 and are reported in Table 7.6. Since the TRITC ϕ_f was not measured, a value of 0.85 was assumed when calculating ϕ_b for all TRITC samples. From the $\langle \phi_b \rangle$ results the most obvious trend is the reduced dry film fixed population photostability compared to the solvated and SNP samples (dry fixed $\langle \phi_b \rangle$ values around 40 versus 20's for the solvated films). This trend is opposite that seen in Chapter 4 for R6G and SRB. Since the dye survival lifetimes are unaffected, the greater photostability on solvent addition (based on decreased $\langle \phi_b \rangle$) indicates an increase in the average fluorescence emission in the dry films. This would account for the decreased number of photons emitted over a similar survival lifetime for the dry dye. Since, the

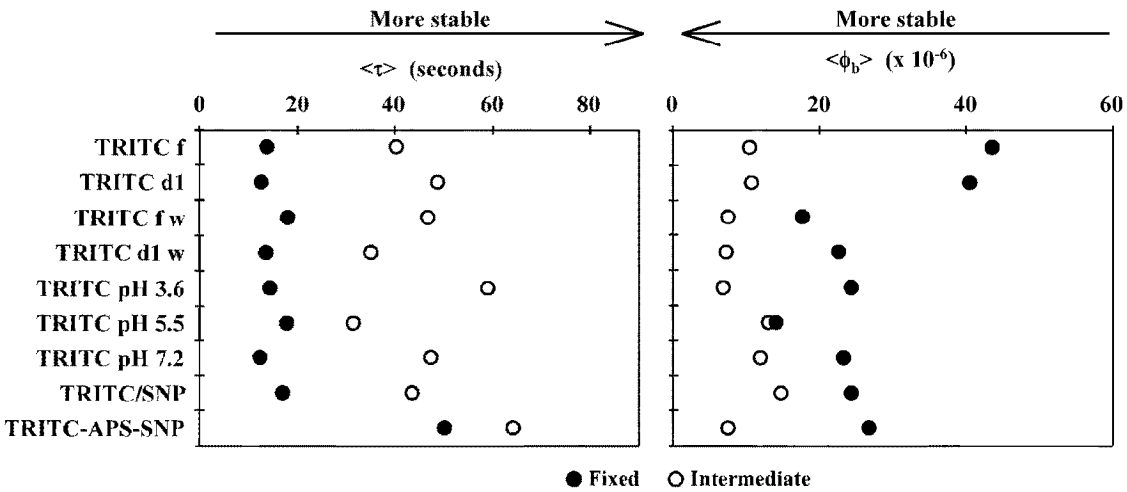

Figure 7.8. TRITC $\langle \tau \rangle$ and $\langle \phi_b \rangle$ for dry, water and buffer equilibrated films, TRITC doped SNP and APS bound SNP samples. In general, like the TRITC mobilities, the $\langle \tau \rangle$ and $\langle \phi_b \rangle$ appear fairly insensitive to the film environment as evident by the similarity in $\langle \tau \rangle$ and $\langle \phi_b \rangle$ values. Noticeable is the unusually unstable fresh and day one dry film fixed molecules, as indicated by the high $\langle \phi_b \rangle$. While the TRITC $\langle \phi_b \rangle$ appears little changed by SNP incorporation, covalent attachment increased the lifetime dramatically. Tumbling results are excluded due to small sample size.

Table 7.6. TRITC photobleaching quantum yields based on single- and bi-exponential decay functions using Excel©.

Dye	Category	a_1	ϕ_1 ($\times 10^{-6}$)	a_2	ϕ_2 ($\times 10^{-6}$)	$\langle r^2 \rangle$	$\langle \phi_b \rangle$ ($\times 10^{-6}$)
TRITC f	Fixed	0.75±0.01	15.4±0.3	0.25±0.01	129±9	0.9987	43.4±0.3
	Tumbling	1.0	41±3	-	-	0.9765	41±3
	Intermediate	0.90±0.03	4.5±0.2	0.10±0.03	61±33	0.9965	10±4
TRITC d1	Fixed	0.53±0.02	12.8±0.5	0.47±0.02	72±3	0.9988	40±2
	Tumbling	0.3±0.1	3±2	0.7±0.1	22±4	0.9931	16±4
	Intermediate	0.80±0.03	4.5±0.3	0.20±0.04	36±9	0.9952	11±2
TRITC f w	Fixed	0.64±0.07	9.2±0.7	0.36±0.07	33±5	0.9986	18±3
	Tumbling	0.7±0.2	6±2	0.3±0.2	53±51	0.9846	18±17
	Intermediate	0.82±0.07	4.1±0.3	0.18±0.07	22±9	0.9979	7±2
TRITC d1 w	Fixed	0.43±0.05	8.8±0.9	0.57±0.5	33±2	0.9984	22±2
	Tumbling	1.0	14±1	-	-	0.9609	14±1
	Intermediate	0.94±0.07	4.5±0.5	0.06±0.07	55±17	0.9938	7±10
TRITC pH 3.6	Fixed	0.63±0.03	8.0±0.4	0.37±0.03	52±5	0.9971	24±2
	Tumbling	1.0	5±1	-	-	0.9580	5±1
	Intermediate	0.95±0.02	3.7±0.1	0.05±0.02	72±84	0.9980	7±4
TRITC pH 5.5	Fixed	1.0	14.0±0.1	-	-	0.9965	14.0±0.1
	Tumbling	0.2±0.2	3±3	0.8±0.2	26±7	0.9848	21±7
	Intermediate	0.88±0.05	4.6±0.5	0.12±0.05	67±57	0.9842	12±8
TRITC pH 7.2	Fixed	0.26±0.03	6.4±0.8	0.74±0.03	29±1	0.9989	23±1
	Tumbling	1.0	9.5±0.7	-	-	0.9783	9.5±0.7
	Intermediate	0.89±0.03	4.7±0.3	0.11±0.04	71±51	0.9939	12±6
TRITC /SNP	Fixed	0.76±0.01	8.6±0.3	0.24±0.02	83±7	0.9986	27±2
	Tumbling	1.0	25±2	-	-	0.9796	25±2
	Intermediate	0.90±0.03	3.9±0.2	0.10±0.03	38±18	0.9962	7±2
TRITC-APS-SNP	Fixed	0.20±0.02	1.4±0.3	0.80±0.02	30±1	0.9957	24±1
	Tumbling	1.0	21±7	-	-	0.9576	21±7
	Intermediate	0.92±0.04	8.5±0.5	0.08±0.05	89±110	0.9939	15±9

samples were tested with the same excitation power this indicates a large ϕ_f change for TRITC on solvation due to counter ion dissociation, or a hydrogen bonding related ϕ_f change when a protic solvent is added. These changes could influence the total fluorescence emission through a molar absorbance coefficient change, or they could signify a change in fluorescence quantum yield due to changes in the radiationless excited state deactivation pathways. Within the dried samples, the close counter ion association with the dye likely reduces the molar absorption coefficient. The resulting "locally" high counter ion concentration for TRITC in the dry samples would also lead to excited state fluorescence quenching by the negative counter ion.[19]

A change in the TRITC ϕ_f is also indicated between the TRITC/SNP and TRITC-APS-SNP samples where the similar $\langle\phi_b\rangle$ values and longer $\langle\tau\rangle$ imply a reduced ϕ_f for the TRITC-APS-SNP sample. Since the bound TRITC has a longer average lifetime, it must have a reduced average quantum efficiency to emit the same total number of photons as the shorter lived TRITC/SNP sample. This indicates that the covalent bond, directly or indirectly, facilitated additional deactivation pathways that; extend the time spent in a dark state, increase the frequency that the dye transitions to a dark state, or reduce the TRITC excitation efficiency, which would lead to fewer emitted photons. Further investigation into the TRITC blinking kinetics and intermediate molecule reorientation dynamics should help identify the types of processes involved.

Since the R6G/SNP and TRITC SNP samples were tested under the same conditions, the $\langle\tau\rangle$ and $\langle\phi_b\rangle$ changes can be compared (Figure 7.9). For the ϕ_b calculation, R6G was assumed to have a ϕ_f of 0.95,[19] and TRITC was assumed to have a ϕ_f of 0.85. Because R6G has a near unity ϕ_f, any modification to the R6G structure would

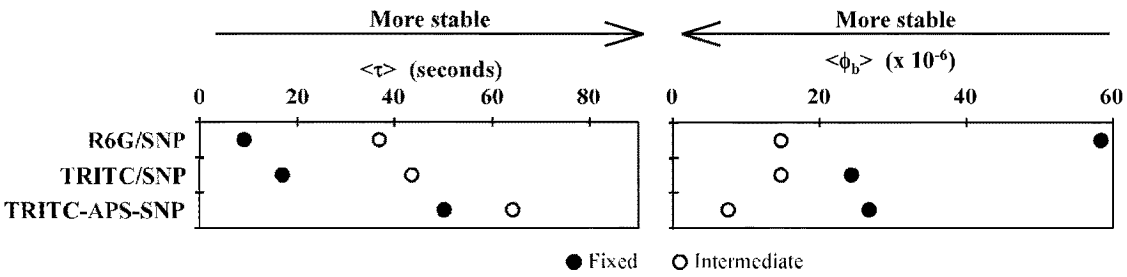

Figure 7.9. SNP sample $\langle \tau \rangle$ and $\langle \phi_b \rangle$ values. R6G appears less stable than TRITC in SNP as evident by the shorter lifetime and higher fixed population $\langle \phi_b \rangle$. For covalently bound TRITC a significant increase in the lifetime is seen. However, this increase is not matched by a corresponding increase in the $\langle \phi_b \rangle$. This could indicate changes in the TRITC excited state deactivation pathways, due to the TRITC-APS covalent bond to the silica surface. Tumbling results are excluded due to small sample size.

likely decrease the fluorescence efficiency, if it influences the efficiency at all. A TRITC ϕ_f below the 0.85 assumed value would decrease the $\langle \phi_b \rangle$ and improve the TRITC stability relative to R6G (Equation 4.2). A TRITC ϕ_f above 0.85 would slightly decrease the TRITC stability relative to R6G, but the TRITC fixed and tumbling $\langle \phi_b \rangle$ would remain approximately ½ to ¾ the R6G values. The TRITC/SNP and TRITC-APS-SNP samples both display longer fixed and intermediate lifetimes than the R6G/SNP sample. In addition, the R6G sample has a fixed $\langle \phi_b \rangle$ value approximately double that for the TRITC samples, indicating R6G is less photostable than TRITC within the SNP environment. The enhanced TRITC stability likely stems from the hydrogen bond immobilization which would reduce photooxidation favorable motions.

7.4 CONCLUSION

Based on the R6G and TRITC mobility distributions, we conclude that the more highly branched SNP matrix does facilitate increased dye rotational mobility relative to the silica sol-gel thin films. This is seen in the lower fixed populations and higher intermediate (and for R6G tumbling) populations in the SNP relative to the silica films.

The TRITC films also illustrate the dominant role that hydrogen bonding plays in determining dye rotational mobility, even as the solvent environment is altered. Covalent bonding to the SNP surface did not significantly alter the TRITC mobility distribution, indicating that the APS sigma bonds were flexible enough to not significantly inhibit molecular motions.

While SNP incorporation alone does not necessarily increase dye survival lifetime, or enhance dye photostability, covalent bonding to the surface led to a large increase in the TRITC survival lifetime ($\langle\tau\rangle$). That this lifetime increase was not accompanied by a corresponding decrease in $\langle\phi_b\rangle$ indicates that covalent bonding enhanced radiationless excited state deactivation pathways. The covalently bound dye's reduced average sample emission may also be related to increased time spent in the dark state, or a reduced absorption efficiency that leads to the low fluorescence emission. Further study of the free and bound TRITC blinking behavior and intermediate molecule reorientation kinetics may help elucidate the pathways that reduce the dye $\langle\phi_b\rangle$ on covalent bonding to SNP.

Chapter VII References

(1) Leite, C. A. P.; de Souza, E. F.; Galembeck, F. *J. Braz. Chem. Soc.* **2001**, *12*, 519.
(2) Stöber, W.; Fink, A.; Bohn, E. *J. Colloid Interface Sci.* **1968**, *26*, 62.
(3) Gallagher, D.; Ring, T. A. *Chimia* **1989**, *43*, 298.
(4) Van Blaaderen, A.; Kentgens, A. P. M. *J. Non-Cryst. Solids* **1992**, *149*, 161.
(5) Van Blaaderen, A.; Vrij, A. *Langmuir* **1992**, *8*, 2921.
(6) Imhof, A.; Megens, M.; Engelberts, J. J.; De Lang, D. T. N.; Sprik, R.; Vos, W. L. *J. Phys. Chem. B* **1999**, *103*, 1408.
(7) Shibata, S.; Taniguchi, T.; Yano, T.; Yamane, M. *J. Sol-Gel Sci. Technol.* **1997**, *10*, 263.
(8) Wen-xu, L.; Jian, C. *Anal. Chem.* **2003**, *75*, 1458.
(9) Hilliard, L. R.; Zhao, X.; Tan, W. *Anal. Chim. Acta* **2002**, *470*, 51.
(10) Santra, S.; Zhang, P.; Wang, K.; Tapec, R.; Tan, W. *Anal. Chem.* **2001**, *73*, 4988.
(11) Choi, H.; Chen, I. W. *J. Colloid Interface Sci.* **2003**, *258*, 435.
(12) Kneuer, C.; Sameti, M.; Haltner, E. G.; Schiestel, T.; Schirra, H.; Schmidt, H.; Lehr, C. M. *Int. J. Pharm.* **2000**, *196*, 257.
(13) Wu, D.-Y.; Chen, B.; Fu, X.-G.; Wu, L.-Z.; Zhang, L.-P.; Tung, C.-H. *Organic Letters* **2003**, *5*, 1075.
(14) Claessens, H. A.; van Straten, M. A.; Kirkland, J. J. *J. Chromatogr., A* **1996**, *728*, 259.
(15) Koehler, J.; Kirkland, J. J. *J. Chromatogr.* **1987**, *385*, 125.
(16) Kirkland, J. J.; Henderson, J. W.; DeStefano, J. J.; van Straten, M. A.; Claessens, H. A. *J. Chromatogr., A* **1997**, *762*, 97.
(17) Tindall, G. W.; Perry, R. L. *J. Chromatogr., A* **2003**, *988*, 309.
(18) Tapec, R.; Zhao, X. J. J.; Tan, W. H. *J. Nanosci. Nanotechnol.* **2002**, *2*, 405.
(19) Drexhage, K. H. Structure and Properties of Laser Dyes. In *Dye Lasers*; 2nd ed.; Schafer, F. P., Ed.; Springer-Verlag: Berlin, 1977; Vol. 1; pp 144.

Chapter VIII

Templating Silica Sol-Gel Pores with Gold Nanoparticles

8.1 CHAPTER ABSTRACT

This chapter provides preliminary results from an investigation into templating silica sol-gel pores around gold nanoparticles (GNP). Films containing tetramethylrhodamine-5-isothiocyanate (TRITC) and TRITC adsorbed to GNP were prepared and equilibrated with 50 mM sodium cyanide to dissolve the GNP pore template. A factor of ten increase in the excitation power relative to our previous TRITC samples was necessary, due to the increase in dye lifetime and decrease in fluorescence emission intensity on cyanide addition. When equilibrated with cyanide, the TRITC intermediate population increased slightly and the fixed population decreased. The GNP templated film's intermediate population also increased, giving a mobility distribution similar to that obtained for the silica nanoparticle samples. The templated film's fixed and intermediate molecule lifetimes increased, and the photobleaching quantum yields were lower than the untemplated reference sample. These preliminary results indicate that GNP templating increased TRITC mobility and photostability. Continued investigation will confirm these results, and determine the influence that pore diameter exerts on guest mobility and photostability.

8.2 INTRODUCTION

Our primary goal has been to develop strategies to control guest molecule mobility and photostability within silica sol-gel materials. The previous investigations into charge-charge interactions and the influence that solvent has on guest molecule

mobility indicate that physical immobilization plays a crucial role in determining guest mobility.[1-3] The 20% minimum in fixed molecule population observed in all samples likely corresponds to dye physically constrained within collapsed pores, dye within molecularly templated pores, or dye incorporated within the silica matrix without a pore. In the silica nanoparticle study, the dye location was controlled by covalent bonding to the surface after the silica matrix developed. However, the covalent bond prevents the guest molecule from freely diffusing within the pore. To study how confinement influences mobility and photostability we desire to selectively encapsulate unbound dye within pores of known dimensions.

Angstrom dimension pores have been templated in silica sol-gel using organic ligand substituent groups,[4] however the pyrolytic process used to remove the ligand template is not compatible with organic guest confinement. Surfactants,[5-9] living cells,[10] and liposomes[11] have also been used to template three dimensional structure in silica sol-gel materials. Unfortunately, these techniques do not provide the nanometer reproducibility and control necessary for a systematic study into confinement's influence on guest properties. The most promising templating technique appears to be that used to form "nanobubbles," which are hollow silica nanoparticles filled with a fluorophore such as fluorescein. In this technique fluorescein isothiocyanate was adsorbed to gold nanoparticles (GNP) through the gold-sulfur interaction, the GNP were then coated with a silica sol-gel layer to form nanometer sized silica nanoparticles around a gold core.[12] The gold core was then dissolved with sodium cyanide, leaving the adsorbed dye behind inside a solvent filled pore of the same dimensions as the GNP template.[12]

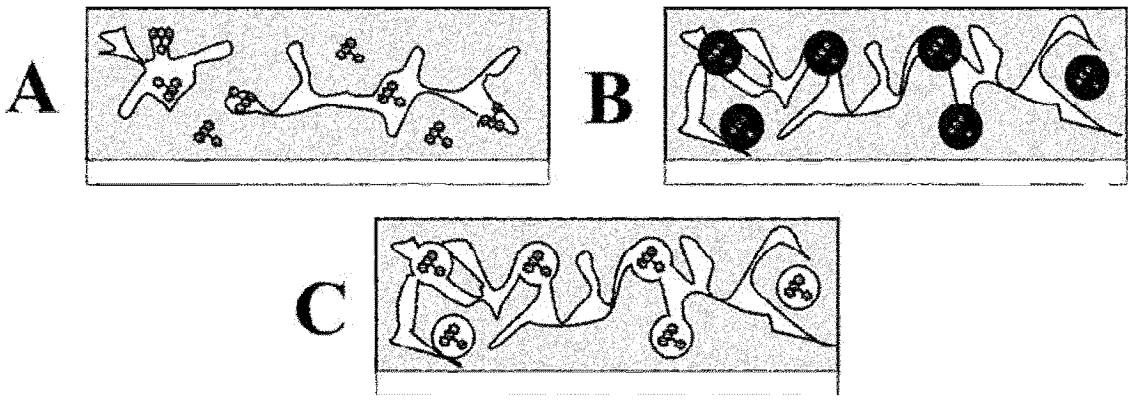

Figure 8.1. The untemplated pore structure (A) is expected to contain dye physically constrained by molecular templating, pore collapse around the dye, or by silica matrix incorporation. To influence the constrained molecule population, gold nanoparticles with dye adsorbed to the surface (B) were added to the sol solution and the silica structure allowed to form around the gold particles. Next, the gold was dissolved with cyanide, leaving the dye within open pores (C). These pores can be isolated from, or connected to the normal untemplated pore structure. Since the dye resides within the pores, the final mobility should be determined by the guest interactions with the surface.

By altering the GNP diameter used to template the silica sol-gel pores, we can investigate how confinement influences guest behavior as the pore size is varied. The GNP templating process is summarized in Figure 8.1. The GNP (with dye adsorbed to the surface) are added to the sol solution for incorporation within the developing silica sol-gel matrix. The silica sol-gel films are then allowed to dry and age to permit pore collapse around the GNP. Finally, cyanide is added to dissolve the GNP, leaving a pore behind that contains the guest molecule. Since the normal sol-gel pore structure is not altered by this templating process, the GNP diameter represents the minimum pore size that the dye is trapped inside. Interconnection with the nascent pore structure could increase the actual pore size surrounding the dye. Since pore collapse occurs before the GNP template is removed, physical confinement due to molecular templating, pore collapse, and matrix incorporation should be minimized, but cannot be completely

eliminated since dye adsorption is an equilibration process. This will free the molecule to allow hydrophobic, charge-charge, and other interactions to influence the encapsulated guest properties. In this study, GNP dimension variation will alter the degree of confinement so that the corresponding guest mobility and photostability can be tested. This chapter presents the preliminary results obtained for an untemplated tetramethylrhodamine-5-isothiocyanate (TRITC) reference sample and an initial gold templated TRITC sample equilibrated with cyanide.

8.3 RESULTS AND DISCUSSION

8.3.1 Gold Nanoparticle Preparation and Characterization

Monodisperse GNP were prepared using the Frens method,[13] which is based on the process reported by Turckevivh.[14] In the Frens method, a citrate solution is added to a boiling hydrogen tetrachloroaurate (III) ($HAuCl_4$) solution with stirring (Equation

$$\text{Au (III)} \xrightarrow[\text{heat}]{\text{citrate}} \text{Au (I)} \xrightarrow{\text{citrate}} \text{Au} \qquad 8.1$$

8.1).[13] The $HAuCl_4$ solution starts out orange in color due to the presence of Au^{+3}. Upon citrate addition to the boiling solution, Au^{+3} is reduced to Au^{+1}, and the solution becomes colorless. Within a few minutes the solution then turns a dark blue, that looks almost black, which indicates GNP nucleation. After turning dark blue, the solution changes a wine red color as the nanoparticle diameter increases. Growth of large nanoparticles (over ~70 nm in diameter) causes the solution to turn rust brown. This brown color also precedes the formation of micron or larger aggregates that precipitate out of solution. GNP nucleation and growth is fed by Au^{+1} reduction to Au^0 within the boiling citrate solution. Citrate serves several functions within the solution; it reduces Au^{+3} to Au^{+1} and then Au^0, it caps the GNP surface to slow growth, and it stabilizes GNP in solution to

prevent aggregation.[14,15] To avoid secondary GNP nucleation it is necessary that the glassware be extremely clean and free of foreign particulates. The glassware and stirbars used for GNP formation were cleaned with 0.1 M sodium cyanide to eliminate secondary nucleation catalyzed by residual GNP adsorbed to the surfaces. The final GNP diameter was controlled by adjusting the initial citrate concentration added to the $HAuCl_4$ solution. A small citrate to gold ratio results in large particles due to reduced nucleation and less efficient surface capping, while a large ratio provides a large number of nucleation sites and the GNP growth is capped more efficiently. By adjusting the citrate added, GNP between 11-40 nm diameter were successfully prepared. Larger GNP formed in this way tend to be irregular in shape (see Figure 2.13), but stepwise GNP growth from smaller seed particles could be used to reduce the irregularity in the large nanoparticle shape.[15,16] On the other extreme, smaller diameter GNP can be synthesized using $NaBH_4$, and control over the three dimensional GNP morphology can be exerted by changing the starting reactants and concentrations.[15-17]

Due to the pH sensitivity of the sol-gel hydrolysis and condensation rates, as well as the need to maximize dye adsorption to the GNP surface, it was necessary to remove the excess citrate from the GNP solutions. However, the citrate can not be entirely removed, since it stabilizes the GNP against aggregation.[14] Excess citrate was removed from the GNP solutions using a mixed ion-exchange resin (Amberlite MB-150 mixed bed ion-exchange resin – Sigma).[12,14] Approximately 0.35-0.4 g Amberlite and 25-30 mL GNP solution were combined, with stirring, to remove citrate from the GNP solutions. Solution conductance was monitored over time to track the citrate removal progress. Depending on the starting citrate concentration, a 20-30 minute Amberlite treatment was

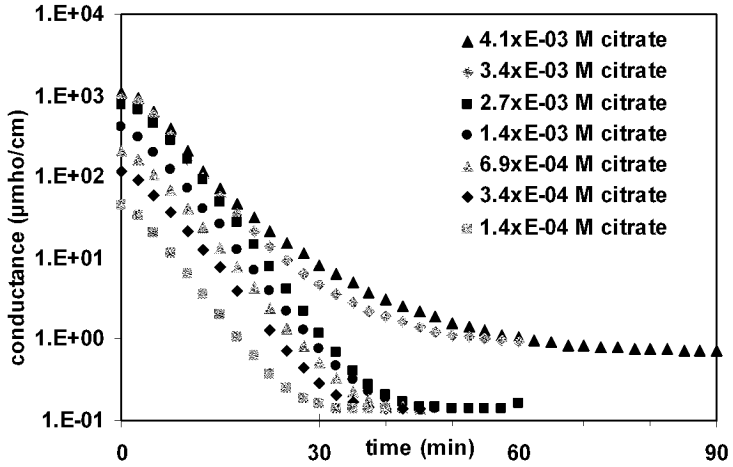

Figure 8.2. The change in conductance over time is presented for a series of citrate solutions to which Amberlite (0.35g) was added. Gold nanoparticle solutions with ~0.35-0.4g Amberlite added to 25 mL typical took 20-30 minutes to reach 10 μmho/cm. The actual time depended on the initial citrate concentration.

sufficient to reduce the GNP solution conductance below 10 μmho/cm (Figure 8.2). After which, the solution was filtered through glass wool to remove the used resin. The final solution conductance was adjusted to 10 μmho/cm, this corresponds to a 10^{-5} M citrate concentration which is sufficient to prevent aggregation.[14] The samples at 10 μmho/cm remained stable at room temperature over several months, while a solution reduced to 5 μmho/cm turned violet within a few days, indicating GNP aggregation.[14] Based on the change in UV absorbance, 90% of the GNP were recovered after the Amberlite treatment.

As stated in Chapter 2, GNP size was determined by imaging the samples with transmission electron microscopy (Figure 2.13). Samples that displayed a bimodal diameter distribution (indicating secondary nucleation occurred) were destroyed to prevent an inhomogeneous templated pore distribution. The GNP sample used for this preliminary result consisted of 10 ± 1 nm diameter particles and had a UV absorbance maximum at 521 nm. This nanoparticle absorbance maximum in the visible range results from a diameter dependent plasmon absorption band.[15] The GNP concentration was

estimated to be 2.7×10^{-8} M based on the starting $HAuCl_4$ mass, the bulk density of gold (18.9 g/cm^3), and the TEM measured diameter.[12]

8.3.2 Gold Nanoparticle Templated Sol-Gel Film Preparation

GNP with TRITC adsorbed to the surface were prepared by combining 1500 μL 2.7×10^{-8} M GNP solution and 1.5 μL 2.6×10^{-5} M TRITC dissolved in water. The combined solution was vortexed vigorously to ensure complete mixing and then allowed to sit for several hours to foster TRITC adsorption to the nanoparticle surface. These concentrations should provide a 1:0.96 GNP:TRITC molecule ratio. However, due to Poisson statistics, some particles are expected to contain no TRITC while others contained multiple TRITC molecules adsorbed. Several fluorescence kinetic traces in the preliminary data set indicated the presence of multiple fluorescence emitters and were discarded. Recalculation of the GNP concentration after use showed it to actually be 1.4×10^{-8} M, providing a GNP:TRITC ratio of 1:1.9. Future experiments will need to reduce the GNP:TRITC ratio, and/or the volume of solution used to prepare the sol solution to ensure single molecule investigation. The use of TRITC dissolved in water, rather than ethanol, was necessary since the GNP tend to aggregate on ethanol addition.

Due to the low GNP concentration, and suspension in water, the silica sol-gel preparation procedure reported in Chapter 2 was modified to accommodate GNP use. In the previous procedure, the guest dye (in ethanol) was added to the sol solution after sonication. For the GNP sample preparation the GNP solution replaced a portion of the 100 μL double distilled H_2O used to prepare the sol solution (for example 35 μL GNP and 65 μL double distilled H_2O). In addition, the GNP solution was added to the sol

before sonication. The sol solution was then allowed to sit overnight before spincoating, and testing was performed on the one day old thin film samples.

To remove the GNP template, a sealed cuvette containing 1 mL 50 mM sodium cyanide was attached to the coverslip and allowed to equilibrate with the film for at least two hours. Using Au_4 as an example, the GNP dissolution reaction is shown in Equation 8.2. The metallic gold particle is oxidized by cyanide in the presence of oxygen into a

$$Au_4 + 8NaCN + 2H_2O + O_2 \rightarrow 4NaOH + 4NaAu(CN)_2 \qquad \textbf{8.2}^{12}$$

soluble complex, leaving behind a pore where the particle used to be.[12] It is possible that some of the TRITC adsorbed GNP could be trapped within inaccessible regions of the silica sol-gel matrix, where the GNP are unable to dissolve to form a pore. However, due to gold's fluorescence quenching ability, it is not expected that the fluorescence emission from the dye adsorbed to GNP will be bright enough to observe.[12,18-21] For comparison to the nanoparticle templated films, a one day old TRITC film was equilibrated with cyanide to provide an untemplated response reference.

8.3.3 TRITC and Gold Nanoparticle Solution Absorbance

When TRITC was dissolved in cyanide (TRITC CN^-), the TRITC maximum peak absorbance (546 nm) intensity was found to increase relative to TRITC dissolved in water alone (TRITC H_2O), Figure 8.3. Both the TRITC CN^- and the cyanide solution with TRITC and GNP dissolved in it (TRITC GNP CN^-) show a 10 % increase in absorbance relative to the TRITC H_2O sample. The two cyanide solutions have nearly identical absorbance spectrums indicating that the GNP were dissolved by the cyanide solution (Figure 8.3.A). For the TRITC adsorbed to GNP sample (TRITC-GNP) there is also an increase in absorbance. Like many other dyes, the absorbance spectra for TRITC-

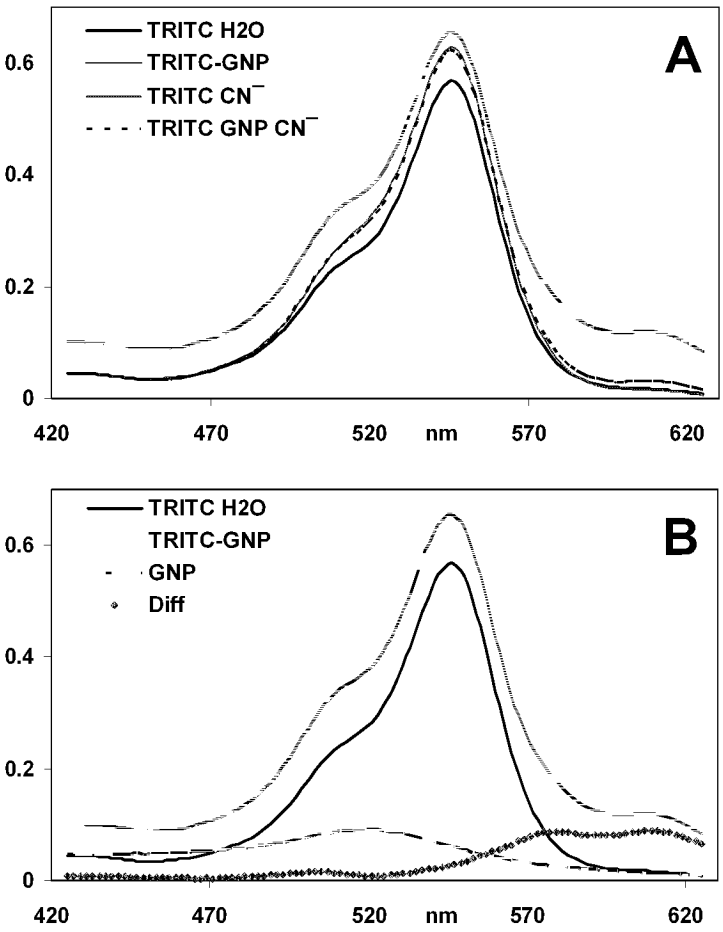

Figure 8.3. An increase in TRITC solution absorbance relative to water (TRITC H_2O) is seen for TRITC adsorbed to gold nanoparticles (TRITC-GNP), and when cyanide is the solvent (A). The cyanide dissolved TRITC (TRITC CN-) and solution containing both TRITC and gold nanoparticles dissolved in cyanide (TRITC GNP CN^-) give nearly identical spectra (A). While the 546 nm TRITC peak maximum does not change on adsorption to the gold nanoparticles (TRITC-GNP), an additional spectroscopic feature is evident (Diff) when the individual gold nanoparticle (GNP) and TRITC H_2O contributions are subtracted (B).

GNP is mostly the additive contributions from the individual gold nanoparticle (GNP) and TRITC H_2O absorbances.[22] However, when both the GNP and TRITC H_2O contributions are subtracted from the TRITC-GNP spectrum (Figure 8.3.B Diff), a TRITC adsorbed state spectroscopic feature is revealed around 550-620 nm.

8.3.4 Cyanide Equilibrated and Gold Nanoparticle Templated Mobilities

As described in Chapter 7, TRITC guest mobility varies little as the silica film environment changes. However, the TRITC mobility did increase when placed within the highly branched silica nanoparticle matrix, presumably due to a more open pore structure. While the previously studied TRITC buffer equilibrated samples showed

limited mobility change, the cyanide equilibrated sample (TRITC CN^-) shows a slight increase in mobility relative to the dry day one and equilibrated day one samples (Figure 8.4 and Table 8.1). The gold nanoparticle templated silica sol-gel sample (TRITC GNP CN^-) shows an increase in mobility relative to TRITC CN^-, as well as to the other TRITC thin film samples. The TRITC GNP

Table 8.1. TRITC mobilities presenting the population in percentage and number of molecules. For other TRITC mobilities see Table 7.4.

Dye	Fixed (%)	Tumbling (%)	Intermediate (%)
TRITC -SNP	41 ± 3% 111	4 ± 1% 10	55 ± 3% 147
TRITC -APS-SNP	35 ± 4% 53	4 ± 2% 6	61 ± 4% 92
TRITC d1	58 ± 3% 175	4 ± 1% 12	38 ± 3% 113
TRITC d1 w	69 ± 3% 144	5 ± 2% 11	26 ± 3% 53
TRITC CN-	54 ± 3% 148	4 ± 1% 11	42 ± 3% 117
TRITC GNP CN-	37 ± 3% 96	4 ± 1% 10	59 ± 3% 150

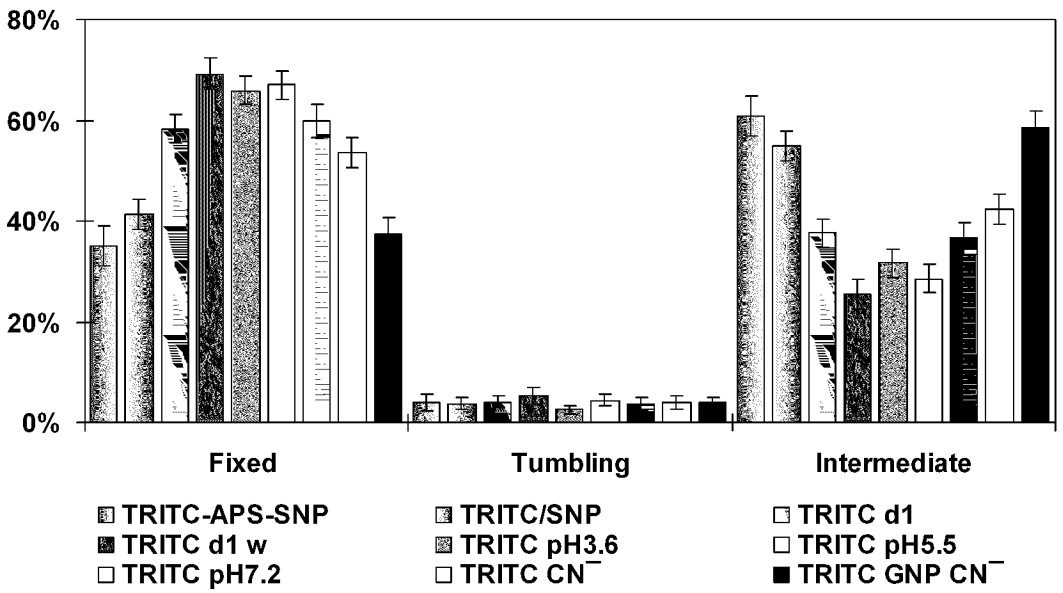

Figure 8.4. The mobility distributions for TRITC film and silica nanoparticle samples. For the cyanide equilibrated sample (TRITC CN^-), there is an increase in intermediate molecule mobility relative to most of the other thin film samples. For the gold nanoparticle templated sample (TRITC GNP CN^-), the TRITC intermediate mobility increased to that observed for the SNP samples.

CN^- mobility is nearly identical to that seen for both of the silica nanoparticle (SNP) samples, which could imply a decrease in physical confinement. Like all the other TRITC samples, hydrogen bonding to the silica surface likely inhibits TRITC from tumbling freely. Thus an anionic dye, such as Oregon Green 514, might be better suited to investigate the dependence of mobility on pore size. Alternately, the TRITC hydrogen bonding might be weakened through shielding, by adding a high ionic strength buffer after the GNP template is removed. Further study will discern how GNP templating and other influences synergistically influence guest mobility.

8.3.5 Cyanide Equilibrated and Templated Lifetimes and Photostabilities

The TRITC average survival lifetimes ($\langle\tau\rangle$) and average photobleaching quantum

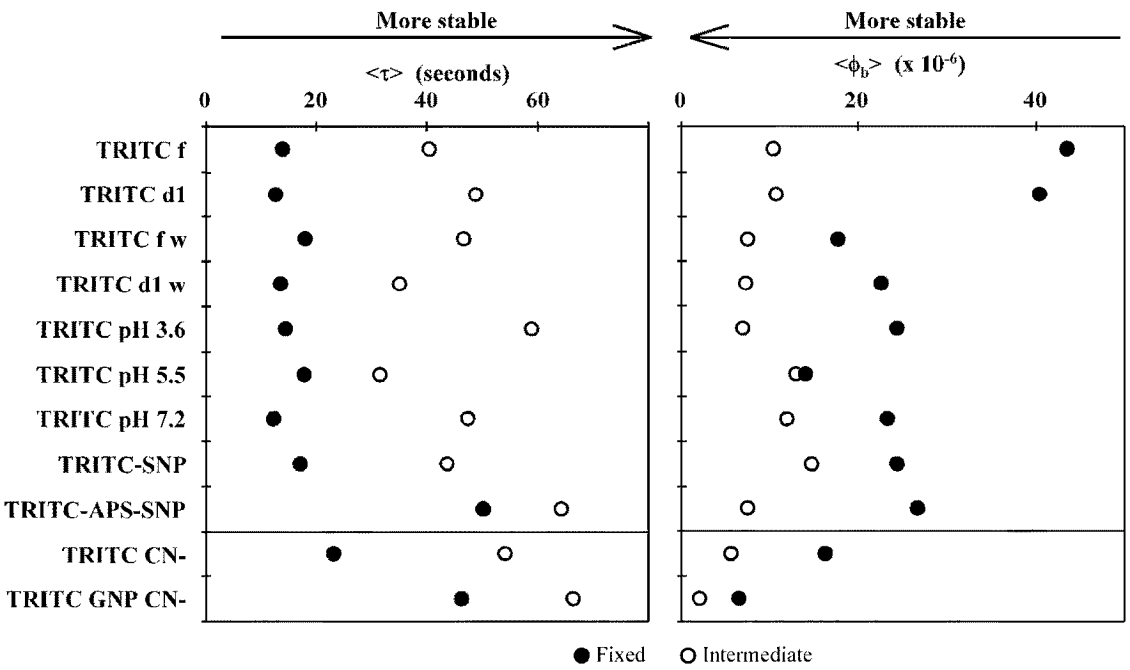

Figure 8.5. TRITC $\langle\tau\rangle$ and $\langle\phi_b\rangle$ for the previous dry and equilibrated TRITC samples, as well as the two new cyanide equilibrated samples. Direct comparison between the cyanide equilibrated and previous TRITC results can not be made, since the cyanide films required a 10 times higher excitation power density. The gold nanoparticle templated sample (TRITC GNP CN-) does show improved stability in both $\langle\tau\rangle$ and $\langle\phi_b\rangle$ relative to the untemplated film (TRITC CN^-). Tumbling results are excluded due to small sample size.

yields ($\langle\phi_b\rangle$) are shown in Figure 8.5 and Table 8.2 (refer to Table 7.5 and 7.6 for the previously reported TRITC lifetime and $\langle\phi_b\rangle$ values). Direct comparison between the two new cyanide equilibrated samples and the previous TRITC results is impossible, since the cyanide equilibrated samples were tested with a higher power density. The previous TRITC samples were tested with 550 $W \cdot cm^{-2}$, while the sodium cyanide equilibrated samples were tested with 5500 $W \cdot cm^{-2}$. This factor of ten increase in the excitation power was necessitated by the long lifetime and low fluorescence emission recorded for the cyanide equilibrated sample when excited with 550 $W \cdot cm^{-2}$. Surprisingly the TRITC CN^- $\langle\tau\rangle$ distribution is comparable to the other TRITC $\langle\tau\rangle$ results, even with the increase in excitation power (Figure 8.5). This indicates that cyanide as a solvent stabilized

Table 8.2. TRITC survival lifetime and photobleaching quantum yield analysis based on single- and bi-exponential decay functions using in Excel©.

Dye	Category	a_1	τ_1 (s)	a_2	τ_2 (s)	$\langle r^2\rangle$	$\langle\tau\rangle$ (s)
TRITC CN-	Fixed	0.37±0.01	3.9±0.3	0.63±0.01	34±1	0.9983	23.0±0.8
	Tumbling	0.5±0.3	2±2	0.5±0.3	21±15	0.9801	12±11
	Intermediate	1.0	54.1±0.5	-	-	0.9960	54.1±0.5
TRITC GNP CN-	Fixed	0.45±0.02	7.8±0.5	0.55±0.02	78±3	0.9976	46±2
	Tumbling	1.0	12.6±0.5	-	-	0.9928	12.6±0.5
	Intermediate	1.0	66.3±0.5	-	-	0.9980	66.3±0.5

Dye	Category	a_1	ϕ_1 ($\times10^{-6}$)	a_2	ϕ_2 ($\times10^{-6}$)	$\langle r^2\rangle$	$\langle\phi_b\rangle$ ($\times10^{-6}$)
TRITC CN-	Fixed	0.62±0.02	4.6±0.2	0.38±0.02	35±3	0.9971	16±1
	Tumbling	0.15±0.05	0.8±0.6	0.85±0.05	14±1	0.9957	12±1
	Intermediate	0.78±0.03	2.2±0.1	0.22±0.04	17±4	0.9960	6±1
TRITC GNP CN-	Fixed	0.62±0.01	0.93±0.05	0.38±0.01	15±1	0.9969	6.5±0.4
	Tumbling	0.3±0.3	2±2	0.7±0.3	12±6	0.9715	9±6
	Intermediate	0.83±0.03	0.92±0.05	0.17±0.03	7±2	0.9969	2.0±0.4

TRITC against photo-oxidation, while it also quenched the fluorescence emission. Since the solvent containing cuvette is sealed to isolate the cyanide, this might reduce the oxygen diffusion rate into the sample, reducing photobleaching. When TRITC GNP CN- is compared to TRITC CN^- (Figure 8.5) the fixed and intermediate $\langle\tau\rangle$s both increased, while all three $\langle\phi_b\rangle$ values decreased. Thus, the survival lifetimes and photobleaching quantum yields both indicate that the GNP templated sample is more photostable than the untemplated sample. The extent to which the pore physical confinement contributes to this increased stability will continue to be investigated by next altering the GNP size used to template the sol-gel pores.

8.4 CONCLUSION

The preliminary gold nanoparticle templated sample shows promise that pore size variation might be used to control guest mobility and photostability in the future. While hydrogen bonding interactions limit TRITC's ability to tumble freely, the intermediate molecule mobility increased to the same level observed within the silica nanoparticle samples. This increase is a significant change in mobility relative to the other TRITC film responses. Careful guest and solvent selection could potentially increase the guest mobility still further. The increased TRITC photostability observed for the gold nanoparticle templated film relative to the untemplated film also warrants further investigation. How will the survival lifetimes and photobleaching quantum yields change as the pore size decreases? And, will the increase in photostability remain when the film is placed in contact with other solvents? These and other questions will be answered by the continuing investigation into the relationship between guest properties and pore size.

Chapter VIII References

(1) Gilliland, J. W.; Yokoyama, K.; Yip, W. T. *Chem. Mater.* **2004**, *16*, 3949.
(2) Gilliland, J. W.; Yokoyama, K.; Yip, W. T. *J. Phys. Chem. B* **2005**, *109*, 4816.
(3) Gilliland, J. W.; Yokoyama, K.; Yip, W. T. *Chem. Mater.* **2005**, *17*, 6702.
(4) Lu, Y.; Cao, G.; Kale, R. P.; Prabakar, S.; Lopez, G. P.; Brinker, C. J. *Chem. Mater.* **1999**, *11*, 1223.
(5) Hentze, H.-P.; Raghavan, S. R.; McKelvey, C. A.; Kaler, E. W. *Langmuir* **2003**, *19*, 1069.
(6) Ferrer, M. L.; del Monte, F.; Levy, D. *J. Phys. Chem. B* **2001**, *105*, 11076.
(7) Garcia, J. A. M.; Valverde, G.; Zink, J. I. *Langmuir* **2003**, *19*, 4411.
(8) Sahu, K.; Roy, D.; Mondal, S. K.; Halder, A.; Bhattacharyya, K. *J. Phys. Chem. B* **2004**, *108*, 11971.
(9) Walcarius, A.; Delacote, C. *Chem. Mater.* **2003**, *15*, 4181.
(10) Chia, S. Y.; Urano, J.; Tamanoi, F.; Dunn, B.; Zink, J. I. *J. Am. Chem. Soc.* **2000**, *122*, 6488.
(11) Besanger, T.; Zhang, Y.; Brennan, J. D. *J. Phys. Chem. B* **2002**, *106*, 10535.
(12) Makarova, O. V.; Ostafin, A. E.; Miyoshi, H.; Norris, J. R.; Meisel, D. *J. Phys. Chem. B* **1999**, *103*, 9080.
(13) Frens, G. *Nature, Physical Science* **1973**, *241*, 20.
(14) Enustun, B. V.; Turkevich, J. *J. Am. Chem. Soc.* **1963**, *85*, 3317.
(15) Jana, N. R.; Gearheart, L.; Murphy, C. J. *Langmuir* **2001**, *17*, 6782.
(16) Brown, K. R.; Walter, D. G.; Natan, M. J. *Chem. Mater.* **2000**, *12*, 306.
(17) Gole, A.; Murphy, C. J. *Chem. Mater.* **2004**, *16*, 3633.
(18) Dulkeith, E.; Morteani, A. C.; Niedereichholz, T.; Klar, T. A.; Feldmann, J.; Levi, S. A.; van Veggel, F. C. J. M.; Reinhoudt, D. N.; Moller, M.; Gittins, D. I. *Phys. Rev. Lett.* **2002**, *89*, 203002/1.
(19) Gueroui, Z.; Libchaber, A. *Phys. Rev. Lett.* **2004**, *93*, 166108/1.
(20) Dubertret, B.; Calame, M.; Libchaber, A. J. *Nat. Biotechnol.* **2001**, *19*, 365.
(21) Du, H.; Disney, M. D.; Miller, B. L.; Krauss, T. D. *J. Am. Chem. Soc.* **2003**, *125*, 4012.
(22) Franzen, S.; Folmer, J. C. W.; Glomm, W. R.; O'Neal, R. *J. Phys. Chem. A* **2002**, *106*, 6533.

Chapter IX

Conclusion

The proceeding chapters provide a record of the research accomplished during the last five years. Included are the efforts to build the instrumentation, develop the data analysis macro programs used to process the results, and an investigation of nanomolar ORG thin film performance as an optical pH sensor. However, the primary research focus has been to develop an increased understanding about the molecular interactions that occur between guest molecules and the silica sol-gel host matrix. Each new understanding has provided a stepping stone toward the goal of influencing guest-host interactions, and through those interactions gain control over the material properties.

For the first time, single molecule spectroscopy has allowed us to monitor how molecular interactions influence guest molecule rotational mobility inside silica sol-gel thin films. Using fluorescence polarization detection, guest rotational motion was monitored and the observed behavior used to assign molecules to one of three mobility classes. The identification of the intermediate molecule population expands our understanding beyond simple fixed and tumbling motion, revealing the rich dynamics that are unlikely to be captured by conventional steady-state, or time-resolved ensemble measurements.

Investigation into the influence that charge-charge interactions have on guest molecule mobility revealed that anionic ORG repulsion from the negative silica surface increased the tumbling population in both dry and water equilibrated films. Buffers with different pH also influenced the ORG mobility by controlling the ORG protonation state

and anionic charge. Surprisingly, charge-charge attraction between cationic R6G and the negative surface did not reduce the guest mobility relative to neutral NR. This indicated that charge-charge attraction is one among many interactions that foster dye immobilization. These studies also revealed the importance of guest molecule dissociation from the counter ion, and suggest that physical immobilization plays an important role in determining guest mobility.

Sample equilibration with external solvents provided additional understandings about guest behavior. Solvent equilibration increased the observed fixed population, due to the preferential leaching of highly mobile molecules into the solvent. The increased molecular dynamics associated with solvent equilibration decreased R6G's average survival lifetime, while hydrogen bonding in SRB and TRITC reduced the influence of solvent dynamics relative to R6G. The hydrophobic $DiIC_{12}$ aliphatic chains and low solubility caused $DiIC_{12}$ to favor adsorption onto the silica surface. When solvated, however, $DiIC_{12}$ appeared to preferentially surround itself with an ethanol like solvent environment. Within these solvated samples there remained a 20 %, or greater, population that was physically immobilized by molecular templating, pore collapse, or matrix incorporation.

To investigate physical immobilization further, guest response was monitored within the more highly branched silica nanoparticle matrix. The silica nanoparticle environment was found to provide increased intermediate rotational motion relative to the silica thin films. In fact, both R6G and TRITC displayed similar mobility distributions in the silica nanoparticles, even though TRITC hydrogen bonding was expected to hinder guest mobility. Covalently bonding TRITC to the silica nanoparticle surface, with APS,

did not significantly alter the TRITC mobility distribution, but the dye survival lifetime increased. Unfortunately, the longer survival lifetime was not accompanied by a decrease in the photobleaching quantum yield, which suggested that photostability was not significantly enhanced. Physical immobilization was also investigated by templating the silica sol-gel pore size with gold nanoparticles. The gold nanoparticles should ensure dye placement within open pores, as well as provide control over the pore dimensions. While hydrogen bonding prevented TRITC from tumbling freely in the templated pores, the intermediate molecule population increased to the levels observed for the silica nanoparticle samples. The increased TRITC survival lifetime, and decreased photobleaching quantum yields, within the templated pores represent a promising advance toward greater molecular behavior control. Investigation will continue on the templated films to reveal the role that confinement plays in determining guest mobility and photostability.

The investigations reported here provide the groundwork for future studies into guest-host interactions in silica sol-gel. As our understanding of the molecular interactions improve, our ability to control guest behavior will increase. This will eventually allow us to customize and control silica sol-gel guest response for wider use in sensor and optics applications.

Appendix A

Publications

"Probing the dynamic guest-host interactions in sol-gel films using single molecule spectroscopy." Viteri, C. R.; Gilliland, J. W.; Yip, W. T. Journal of the American Chemical Society **2003** 125(7): 1980-87.

"Effect of Coulombic Interactions on Rotational Mobility of Guests in Sol-Gel Silicate Thin Films." Gilliland, J. W.; Yokoyama, K.; Yip, W. T. Chemistry of Materials **2004** 16(20): 3949-54.

"Comparative Study of Guest Charge-Charge Interactions within Silica Sol-Gel." Gilliland, J. W.; Yokoyama, K.; Yip, W. T. Journal of Physical Chemistry B. **2005** 109(11): 4824-28.

"Solvent Effect on Mobility and Photostability of Organic Dyes Embedded Inside Silica Sol-Gel Thin Films." Gilliland, J. W.; Yokoyama, K.; Yip, W. T. Chemistry of Materials. **2005** 17(26) 6702-6712.

Appendix B

"Probing the dynamic guest-host interactions in sol-gel films using single molecule spectroscopy"

Journal of the American Chemical Society ***2003*** *125(7): 1980-87.*

J|A|C|S
ARTICLES
Published on Web 01/21/2003

Probing the Dynamic Guest−Host Interactions in Sol−Gel Films Using Single Molecule Spectroscopy

C. Ricardo Viteri,† James W. Gilliland,‡ and Wai Tak Yip*,‡

Contribution from the Universidad San Francisco de Quito, Apartado 17-12-841, Quito, Ecuador and Department of Chemistry and Biochemistry, University of Oklahoma, Norman, Oklahoma 73019

Received April 15, 2002; E-mail: ivan-yip@ou.edu

Abstract: Organic dyes usually exhibit enhanced photostability when trapped inside sol−gel silicates. The enhanced photostability is attributed to the reduction of intramolecular motions that facilitate photodegradation. We report the simultaneous detection of mobility and photostability of sol−gel encapsulated didodecyl-3,3,3′,3′-tetramethylindocarbocyanine (DiI) using single molecule spectroscopy. Fluorescence from DiI was resolved into parallel and perpendicular polarization components and separately detected. On the basis of the calculated fluorescence polarization, single DiI molecules were classified into "tumbling" and "fixed". Out of 212 molecules investigated, 52% were found to be fixed. For the first time, the mobility of a guest molecule in sol−gel silicate can be directly correlated with its own photostability. Both tumbling and fixed molecules have shown to exhibit nonuniform photostability, indicative of the very heterogeneous guest−host interactions within each subgroup. The survival lifetimes for the majority of the tumbling and fixed molecules were found to be 4.3 and 13.1 s, respectively, demonstrating unequivocally that fixed molecules exhibit a higher photostability than tumbling molecules. These results are in accordance with a recent study on rhodamine 6 encapsulated in dried sol−gel silicates.

Introduction

The sol−gel process is a low temperature synthetic technique for the preparation of inorganic oxides. The synthesis is usually carried out at room temperature using metal alkoxide as a starting material.[1] One of the most widely used starting materials is tetraalkyl orthosilicate ($Si(OR)_4$), from which sol−gel silicate can be made. Scheme 1 illustrates the two reactions that best describe the sol−gel process. In the presence of water, silicon alkoxide first hydrolyzes into silanol, which then subsequently polycondensates with one another randomly into a porous and disorganized three-dimensional framework of silicon oxide. During the polycondensation process, many silanol groups will remain unreacted and distribute randomly throughout the entire sol−gel framework. Hence, sol−gel silicate is a porous material that is both structurally and chemically heterogeneous.

The porous nature of the sol−gel framework provides two distinctive advantages that are critical to the widespread application of sol−gel derived materials. First, it allows the trapping of many guest molecules introduced either before or after the polycondensation reaction. Indeed, the incorporation of organic dyes into porous silicate hosts using the sol−gel method has provided a valuable alternative to designing new optical materials. The preparation of dye-doped sol−gel composites is highly flexible, and the choice of inorganic substrate (host) and dye dopant (guest) is almost unlimited. If the host and guest are chosen properly, it is possible to tailor new photonic materials with desirable optical properties.[2] For examples, dye-doped silicate monoliths have been utilized in the fabrication of many solid-state devices including dye laser systems,[3−7] optical waveguide arrays,[8] and other photochromic materials.[9] Second, even though a guest molecule is well retained inside a sol−gel matrix, it can still interact with many external reagents that are small enough to diffuse through the porous framework. This second merit leads to the development of a wide array of chemical and biological sensors using sol−gel derived materials.[10] For examples, a pH sensing device can be constructed from a fluorescein-doped silica sol−gel matrix,[11] the spectral response of pyranine encapsulated inside a sol−gel silicate can be used to estimate the aqueous content in a

Scheme 1. Sol−Gel Process

$$Si(OR)_4 + nH_2O \xrightarrow{\text{hydrolysis}} Si(OR)_{4-n}(OH)_n + nROH$$

$$\equiv Si\text{-}OH + HO\text{-}Si\equiv \xrightarrow[\text{condensation}]{\text{poly-}} \equiv Si\text{-}O\text{-}Si\equiv + H_2O$$

† Universidad San Francisco de Quito.
‡ University of Oklahoma.

(1) Brinker, C. J.; Scherer, G. *Sol−Gel Science, The Physics and Chemistry of Sol−Gel Processing*; Academic Press: San Diego, CA, 1989.
(2) Reisfeld, R. *Opt. Mater.* **2000**, *16*, 1−7.
(3) McKiernan, J. M.; Yamanaka, S. A.; Dunn, B.; Zink, J. I. *J. Phys. Chem.* **1990**, *94*, 5652−5657.
(4) McKiernan, J. M.; Yamanaka, S. A.; Knobbe, E.; Fourcvicl, J.; Parvaneh, S.; Dunn, B.; Zink, J. I. *J. Inorg. Organomet. Polym.* **1991**, *1*, 87−103.
(5) Knobbe, E. T.; Dunn, B.; Fuqua, P. D.; Nishida, F.; Zink, J. I. In *Ultrastructure Processing of Advanced Materials*; Uhlmann, D. R., Ulrich, D. R., Eds.; John Wiley & Sons: New York, 1992; pp 519−529.
(6) Reisfeld, R.; Yariv, E.; Minti, H. *Opt. Mater.* **1997**, *8*, 31−36.
(7) Yariv, E.; Reisfeld, R. *Opt. Mater.* **1999**, *13*, 49−54.
(8) Yang, P. D.; Wirnsberger, G.; Huang, H. C.; Cordero, S. R.; McGehee, M. D.; Scott, B.; Deng, T.; Whitesides, G. M.; Chmelka, B. F.; Buratto, S. K.; Stucky, G. D. *Science* **2000**, *287*, 465−467.
(9) Levy, D. *Chem. Mater.* **1997**, *9*, 2666−2670.
(10) Liang, L. F.; Li, Y. T.; Yang, Y. C. *J. Pharm. Sci.* **2000**, *89*, 979−990.
(11) Villegas, M. A.; Pascual, L. *J. Mater. Sci.* **2000**, *35*, 4613−4619.

10.1021/ja026533k CCC: $25.00

Scheme 2. Route to Photodegradation of a Dye Molecule

$$^1\text{Dye} \xrightarrow{h\nu} {}^1\text{Dye}^*$$

$$^1\text{Dye}^* \xrightarrow{\text{intersystem crossing}} {}^3\text{Dye}^*$$

$$^3\text{Dye}^* + {}^3O_2 \xrightarrow{\text{triplet energy transfer}} {}^1\text{Dye} + {}^1O_2^*$$

$${}^1O_2^* + {}^1\text{Dye} \xrightarrow{\text{Oxidation}} \text{Oxidized Dye} \xrightarrow{\text{degradation}}$$

solution mixture,[12] the concentration of hydrogen peroxide can be accurately determined by measuring the chemiluminescence produced by a sol–gel encapsulated horseradish peroxidase biocomposite,[13] and glucose concentration can be routinely monitored by a glucose oxidase-doped silica sol–gel matrix.[14]

The rational design of solid-state photonic materials with desirable optical properties rests on our understanding of the interactions between an encapsulated molecule and its immediate surroundings. Accordingly, the study of optical properties of dye-doped solid hosts has been a subject of intense research.[11,15–24] There is increasing evidence to suggest that when an organic dye is trapped inside a sol–gel silicate, it exhibits a higher photostability.[15,25–28] The enhanced photostability of organic dyes found in a silica sol–gel host is arguably due to two major factors. The first one is the caging effect of the host on the dye molecules. When trapped inside a cavity of a physically comparable dimension, a dye molecule will experience hindered intramolecular motions. This reduction in intramolecular freedom is believed to enhance photostability by reducing the number of dynamic interactions that favor photodegradation. The second factor is reduced photo-oxidation. As illustrated by the series of reactions outlined in Scheme 2, photo-oxidation provides a major route to the destruction of an organic dye molecule. After a singlet excited dye molecule relaxes to a triplet state via intersystem crossing, it can easily transfer the excitation energy to a nearby oxygen molecule and produce a highly reactive singlet oxygen species ($^1\Delta_g$). This highly energetic oxygen molecule will then oxidize the dye nearby and lead to photodegradation of the dye molecule.[29–32] In particular, photo-oxidation occurs frequently inside a solvent host in which oxygen can diffuse freely toward a dye molecule. On the contrary, the densely networked environment inside a sol–gel silicate is believed to slow the diffusion of oxygen substantially, thereby minimizing photodegradation.[29,31]

It is worthwhile to point out that the postulation which suggests that hindered intramolecular motions will improve photostability is actually inferred from many different ensemble measurements.[7,21,33,34] However, a molecular property obtained from ensemble measurements is at best a statistical average of the observable. It is therefore almost impossible to interpret the relationship between different molecular properties measured from separate experiments. This is especially true in the case when dye molecules are trapped inside silica sol–gel films, where the pore size, pore shape, and the chemical environment between different pores are highly heterogeneous.[35] In other words, every encapsulated dye molecule is surrounded by a very different microenvironment. Hence, it remains uncertain if there really is a direct correlation between the intramolecular motions and photostability of a guest molecule encapsulated inside a sol–gel silicate host. As pointed out by Dunn et al., sol–gel encapsulated guest molecules generally reside in four different environments: (i) the interior of pores that are filled with liquid; (ii) the solid–liquid interface; (iii) the solid pore wall; and (iv) the constraining cleft region that extends deep into the pore wall.[21] As a result, a molecule trapped in different local environments is expected to display a different photophysical behavior.[36] Evidently, to better understand the origin of improved photostability of organic dyes encapsulated inside a silica sol–gel matrix, it is necessary to monitor the mobility and photostability of the dye molecules at the single molecule level.

Single molecule spectroscopy is an exciting new area of research. It aims at studying the physical and optical properties of individual molecules and thereby completely eliminates the statistical effect inherent to ensemble measurements. Recent advances in solid-state technology have allowed the optical detection of single molecules at room temperature.[37] The application of single molecule spectroscopy in both physical and biological sciences has been reviewed recently.[37–41] In this project, we will employ single molecule spectroscopy to study organic dyes trapped inside a silica sol–gel film in order to gain molecular-level insight into the caging effect on the optical properties of an encapsulated molecule. Of particular interest is how the mobility of a molecule relates to its own photostability. The successful application of sol–gel silicate derived photonic materials relies critically on the photostability of the dye dopants, which are highly sensitive to the nature of their

(12) Wasilewski, M.; Breiter, M. W. *J. Non-Cryst. Solids* **1997**, *220*, 52–57.
(13) Díaz, A. N.; Peinado, M. C. R.; Minguez, M. C. T. *Anal. Chim. Acta* **1998**, *365*, 221–227.
(14) Wu, X. J.; Choi, M. M. F.; Xiao, D. *Analyst* **1999**, *125*, 157–162.
(15) Avnir, D.; Levy, D.; Reisfeld, R. *J. Phys. Chem.* **1984**, *88*, 5956–5959.
(16) Suratwala, T.; Gardlund, Z.; Davidson, K.; Uhlmann, D. R.; Bonilla, S.; Peyghambarian, N. *J. Sol-Gel Sci. Technol.* **1997**, *8*, 973–978.
(17) Suratwala, T.; Gardlund, Z.; Davidson, K.; Uhlmann, D. R.; Watson, J.; Bonilla, S.; Peyghambarian, N. *Chem. Mater.* **1995**, *10*, 199–209.
(18) Suratwala, T.; Gardlund, Z.; Davidson, K.; Uhlmann, D. R.; Watson, J.; Peyghambarian, N. *Chem. Mater.* **1998**, *10*, 190–198.
(19) Yariv, E.; Schultheiss, S.; Saraidarov, T.; Reisfeld, R. *Opt. Mater.* **2001**, *16*, 29–38.
(20) Takahashi, Y.; Maeda, A.; Kojima, K.; Uchida, K. *J. Lumin.* **2000**, *87–9*, 767–769.
(21) Perez-Bueno, J. J.; Diaz-Flores, L. L.; Perez-Robles, J. F.; Espinoza-Beltran, F. J.; Ramirez-Bon, R.; Vorobiev, Y. V.; Gonzalez-Hernandez, J. *Microelectron. Eng.* **2000**, *51–2*, 667–675.
(22) Casalboni, M.; Dematteis, F.; Franzini, R.; Prosposito, P.; Sarcinelli, S.; Grassano, U. M.; Pizzoferrato, R.; Grappi, G.; Montenero, A. *J. Lumin.* **1997**, *72–4*, 475–477.
(23) De Matteis, F.; Prosposito, P.; Sarcinelli, F.; Casalboni, M.; Pizzoferrato, R.; Botrini, A.; Russo, M. V.; Vannucci, A.; Varasi, M. *J. Non-Cryst. Solids* **1999**, *245*, 15–19.
(24) Dunn, B.; Zink, J. I. *Chem. Mater.* **1997**, *9*, 2280–2291.
(25) Dubois, A.; Canva, M.; Brun, A.; Chaput, F.; Boilot, J. P. *Synth. Met.* **1996**, *81*, 305–308.
(26) Yogi, K.; Shibata, S.; Yano, T.; Yasumori, A.; Yamane, M.; Dunn, B. *J. Sol-Gel Sci. Technol.* **1995**, *4*, 67–73.
(27) Nishida, F.; Dunn, B.; McKiernan, J. M.; Zink, J. I.; Brinker, C. J.; Hurd, A. J. *J. Sol-Gel Sci. Technol.* **1994**, *2*, 477–481.
(28) Nishida, F.; McKiernan, J. M.; Dunn, B.; Zink, J. I.; Brinker, C. J.; Hurd, A. J. *J. Am. Ceram. Soc.* **1995**, *78*, 1640–1648.
(29) Rahn, M. D.; King, T. A.; Gorman, A. A.; Hamblett, I. *Appl. Opt.* **1997**, *36*, 5862–5871.
(30) Panzer, O.; Golubi, W.; Fischer, U. C.; Fuchs, H.; Mullen, K. *Adv. Mater.* **1998**, *10*, 1469–1472.
(31) Ahmad, M.; Rahn, M. D.; King, T. A. *Appl. Opt.* **1999**, *38*, 6337–6342.
(32) English, D. S.; Furube, A.; Barbara, P. F. *Chem. Phys. Lett.* **2000**, *324*, 15–19.
(33) Geddes, C. D.; Birch, D. J. S. *J. Non-Cryst. Solids* **2000**, *270*, 191–204.
(34) Wang, K.; Geiger, C.; Chen, L.; Swanson, B. *J. Am. Chem. Soc.* **2000**, *122*, 2398–2400.
(35) Wang, H. M.; Bardo, A. M.; Collinson, M. M.; Higgins, D. A. *J. Phys. Chem. B* **1998**, *102*, 7231–7237.
(36) Bardo, A. M.; Collinson, M. M.; Higgins, D. A. *Chem. Mater.* **2001**, *13*, 2713–2721.
(37) Xie, X. S.; Trautman, J. K. *Annu. Rev. Phys. Chem.* **1998**, *49*, 441–480.
(38) Moerner, W. E.; Orrit, M. *Science* **1999**, *283*, 1670–1676.
(39) Ginzewski, J. K.; Joachim, C. *Science* **1999**, *284*, 1683–1688.
(40) Mehta, A. D.; Rief, M.; Spudich, J. A.; Smith, D. A.; Simmons, R. M. *Science* **1999**, *283*, 1689–1695.
(41) Weiss, S. *Science* **1999**, *283*, 1676–1683.

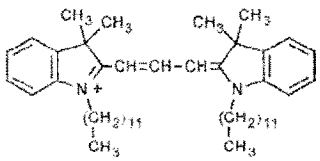

Figure 1. Molecular structure of DiI.

immediate surroundings. A better understanding of how an encapsulated molecule interacts with its local environment is therefore essential for the rational design of new photonic materials. This paper describes the single molecule spectroscopy of 1,1′-didodecyl-3,3,3′,3′-tetramethylindocarbocyanine (DiI) encapsulated in thin silica sol−gel films. We combine single molecule spectroscopy with fluorescence polarization detection to examine the correlation between the mobility and photostability of DiI encapsulated in the heterogeneous sol−gel silicate environment. Figure 1 illustrates the molecular structure of DiI.

Experimental Section

Materials. 99.9+% Tetraethyl orthosilicate (TEOS), spectrophotometric grade 95% ethanol, and 85 wt % phosphoric acid were purchased from Sigma-Aldrich. DiI was purchased from Molecular Probes. All chemicals were used without further purification. A phosphorous acid solution was prepared by diluting the 85 wt % stock solution 100 times using double-distilled water. Microscope cover glasses (Fisher Premium) were purchased from Fisher Scientific and were thoroughly cleaned before used.

Preparation of Sol Solution. TEOS sol solution was made from the acid hydrolysis of TEOS in an ethanol−water solution mixture in 1:8:7 molar ratios.[35,42] TEOS (177 μL) was first mixed with ethanol (358 μL), double-distilled water (100 μL), and the diluted phosphorous acid solution (2.0 μL). To facilitate hydrolysis, the solution mixture was sonicated for 2 h, during which time the temperature of the sonication bath was kept at 25 °C in order to minimize polycondensation. After sonication, the sol solution was slightly doped to 1.7 nM final dye concentration with a concentrated solution of DiI in ethanol. The DiI-doped sol solution was then allowed to age at ambient temperature in the dark for 24 h before it was used for thin silica sol−gel films preparation.

Casting of Sol−Gel Silicate Thin Films. Microscope cover glasses were used as the substrate for film casting. The cover glasses were cleaned by sonicating sequentially in 10% NaOH, acetone, and double-distilled water each for 20 min before used. To produce a thin sol−gel film for single molecule measurement, the aged DiI-doped sol solution (100 μL) was spin cast onto a cleaned cover glass at 6100 rpm for 70 s. The thickness of the film was determined by AFM to be 363 ± 20 nm. The sol−gel silicate films were allowed to age for three more days at ambient temperature in the dark before they were ready for single molecule measurement.

Single Molecule Spectroscopy. Fluorescence images of single DiI molecules were acquired by a home-built sample-scanning confocal microscope, which was based on an inverted microscope (Nikon, TE-200) and a nanopositioning stage equipped with position feedback electronics (Melles Griot, NanoBlock). Fluorescence images and kinetics traces from single DiI molecules were obtained under a continuous laser excitation at 543.5 nm, which is close to the λ_{max} of DiI encapsulated in a silica sol−gel monolith (551 nm), as illustrated in Figure 2. The laser excitation was delivered to the epi-illumination port of the microscope by a single-mode optical fiber, which also served as a 3.3 μm diameter spatial filter. The excitation laser that came out from the other end of the fiber was first collimated by a 10× objective,

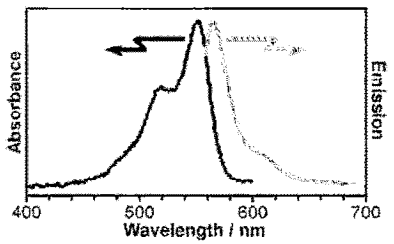

Figure 2. Absorption and emission spectra of DiI encapsulated in a sol−gel monolith. The emission spectrum was obtained from excitation at 551 nm.

filtered through a 543.5 nm interference filter, and then reflected up to a 100× microscope objective (Nikon, CFI Achromat oil immersion 1.25 N.A.) by a dichroic beam splitter (Chroma Technology). Fluorescence from single molecules collected by the same microscope objective was directed to exit from the side port of the microscope and clear a 100 μm aperture positioned at the first image plane. Fluorescence diverging from the aperture was then collimated with an achromatic lens and passed through a long-pass filter (Omega Optical, ALPHA Technology) to eliminate scattered laser excitation before it was directed to a polarizing beam splitter cube. The beam splitter cube resolved the fluorescence into a parallel ($I_\parallel$) and a perpendicular ($I_\perp$) polarization component that were subsequently detected by two separate avalanche photodiode (APD) detectors (Perkin-Elmer, SPCM-AQR).

Upon raster scanning of a sol−gel silicate sample, each APD detector would produce a fluorescence image from the same sample area with the respective fluorescence polarization. The spot sizes of DiI molecules in the images were mostly diffraction limited and were measured at ~280 nm. The typical size of a fluorescence image was fixed at 10 μm × 10 μm. To examine the photophysical properties of single molecules, a molecule was first chosen from a fluorescence image and then transported to the laser focus by the nanopositioning stage. The fluorescence kinetics trace of the chosen molecule could be collected by directing the collimated fluorescence to two separate APDs, where $I_\parallel(t)$ and $I_\perp(t)$ were simultaneously monitored by the APDs at a 50 ms dwell time upon continuous laser excitation. On the other hand, the emission spectrum of the molecule could be acquired by directing the collimated fluorescence to a polychromator (Acton, SpectraPro 150) equipped with a liquid-nitrogen cooled CCD camera (Roper Scientific, SpectruMM). To prevent the transmission profile of the dichroic beam splitter from clipping the short wavelength portion of the emission spectrum, single DiI molecules were excited at 514.5 nm, which is near to the first vibronic band of the molecule.

Polarization Measurements and Mobility Classification. To measure the fluorescence polarization of single DiI molecules, the linearly polarized laser excitation was first converted to a circularly polarized excitation with a 543.5 nm ¼ waveplate before it was coupled into the single-mode optical fiber. The use of a circularly polarized excitation ensures that the random orientation of single molecules parallel to the sample plane does not affect the excitation efficiency of each molecule. From the $I_\parallel(t)$ and $I_\perp(t)$ fluorescence kinetics traces, the polarization ($P(t)$) of fluorescence from single DiI molecules were calculated at all time according to

$$P(t) = \frac{I_\parallel(t) - I_\perp(t)}{I_\parallel(t) + I_\perp(t)} \qquad (1)$$

In addition to the time-dependent polarization $P(t)$, an average polarization ($\bar{P}$) together with its standard deviation ($\sigma_{\bar{P}}$) was also calculated as the statistical average of $P(t)$. To correct for the accumulated birefringence from various optical components as well as the different sensitivities of the two APDs, $\bar{P}$ values calculated from single molecules were always compared with the $\bar{P}$ of a concentrated DiI solution measured on the same day. Using the $\bar{P}$ determined from

(42) Mei, E.; Bardo, A. M.; Collinson, M. M.; Higgins, D. A. *J. Phys. Chem. B* **2000**, *104*, 9973−9980.

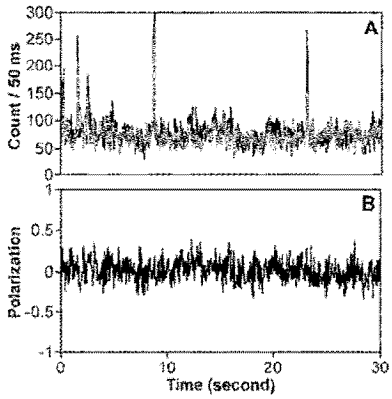

Figure 3. (A) $I_{\parallel}(t)$ (black) and $I_{\perp}(t)$ (gray) collected from a DiI in ethanol solution. (B) The polarization plot ($P(t)$) calculated from $I_{\parallel}(t)$ and $I_{\perp}(t)$ using eq 1.

the concentrated DiI solution as a reference for isotropic fluorescence, a DiI molecule could be assigned as "tumbling" or "fixed" accordingly.

Results and Discussions

Polarization of DiI Solution. The polarization of DiI in ethanol was determined from a 3.14 μM DiI in ethanol solution. Figure 3A shows the $I_{\parallel}(t)$ and $I_{\perp}(t)$ measured from the solution together with the calculated $P(t)$ in Figure 3B. It is fairly apparent that the signals from the two channels are not quite identical, with $I_{\parallel}$ usually larger than $I_{\perp}$, indicating the biased response from the $I_{\parallel}$ and $I_{\perp}$ detecting channels. This bias most likely resulted from the birefringence of various optical components plus any difference in the sensitivity of the two APD detectors. Assuming that the emission from a solution is isotropic, we applied a scaling factor to $I_{\parallel}(t)$ such that the calculated $\bar{P}$ of the solution was forced to zero. The same scaling factor would then be applied to all subsequent measurements of $I_{\parallel}(t)$ performed on the same day in order to eliminate any systematic error introduced by the instrument when calculating the fluorescence polarization of single molecules. In addition to the scaling factor, the standard deviation of the properly scaled $\bar{P}$ of the concentrated DiI solution (σ_{1sc}) was also calculated and subsequently used for the mobility classification of single DiI molecules. In our scheme, when the $\bar{P}$ of a single molecule is not within $\pm\sigma_{1sc}$ from zero polarization, the molecule will be classified as fixed.

Identification of Single DiI Molecules. A 363 nm thick silica sol–gel film prepared from a 1.7 nM dye-doped sol solution should contain approximately 37 molecules per fluorescence image area of 10 μm × 10 μm. Figure 4 shows a fluorescence image of DiI encapsulated in a sol–gel silicate film. It is a 100 pixel × 100 pixel image with each pixel representing a physical area of 100 nm × 100 nm. The signal at each pixel was integrated for 50 ms, and the typical background count rate was less than 10 counts. Many diffraction-limited fluorescence spots can be identified from the image with the number density agreeing reasonably well with the calculated number density. The emission spectrum shown in Figure 4B confirms that the fluorescence was indeed originated from DiI molecules. Single molecule emission from a majority of the fluorescence spots in the image was confirmed by their corresponding kinetics traces, where an abrupt drop of fluorescence intensity down to the

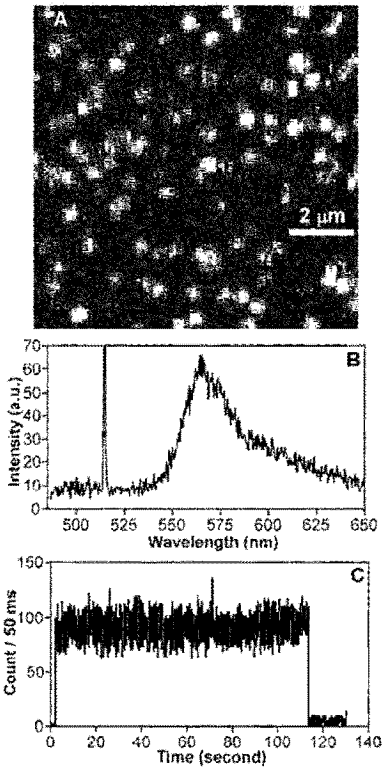

Figure 4. (A) Fluorescence image of DiI in a sol–gel silicate film. (B) The emission spectrum of a single DiI molecule when excited at 514.5 nm. (C) The fluorescence kinetics trace of a single DiI molecule.

background level was observed as a result of photobleaching (Figure 4C).

Single Molecule Studies of Silica Sol–Gel Films. The kinetics traces shown in Figure 5 exemplify the dynamic behavior displayed by DiI when it is encapsulated in sol–gel silicate. Unlike in polymer films, where the photophysics of DiI can mostly be described by a three-level system with negligible influence from guest–host interactions,[43,44] DiI in sol–gel silicate exhibits a much different behavior that is due to very rich dynamic interactions with its immediate surroundings. The observed intensity fluctuations in each kinetics trace are bigger than random shot noises, indicative of a second kind of dynamics occurring at a much faster time scale. Similar behavior has also been reported for rhodamine B and Nile Red encapsulated in silica sol–gel films.[36,42] In the case of rhodamine B, the intensity fluctuations were attributed to changes in the fluorescence quantum yield of the dye molecule because of rapid fluctuations in the environmental conditions.[42] It is highly probable that the same is happening to DiI when it is trapped inside a silica sol–gel film. Nevertheless, regardless of the exact origin of the intensity fluctuations, the survival time of each DiI molecule can still be accurately determined from the corresponding kinetics trace before the molecule is photobleached. The photostability of each molecule can then be directly inferred from the survival time measured.

(43) Trautman, J. K. *Proc. Robert A. Welch Found. Conf. Chem. Res.* 1995, 173–181.

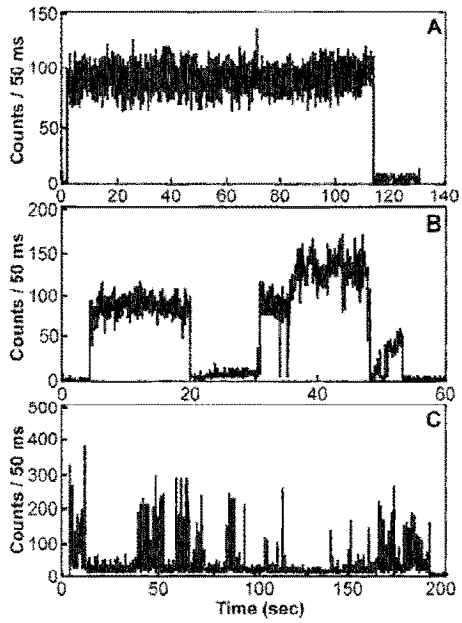

Figure 5. Examples of fluorescence trace from single DiI molecules with (A) single-level, (B) multilevel, and (C) multilevel-erratic transitions.

(i) Single Molecule Mobility. To determine if molecular motions contribute to the very rich dynamics observed, fluorescence polarization from single DiI molecules was measured using circularly polarized laser excitation. Figure 6 displays three fluorescence kinetics traces and the corresponding $\bar{P}(t)$ plots that are related to different kinds of mobility observed from silica sol–gel encapsulated DiI molecules. The $\bar{P}(t)$ plot in Figure 6A suggests that the molecule exhibits a fairly constant fluorescence polarization over time with $\bar{P} = 0.022 \pm 0.193$. The very small $\bar{P}$ indicates that the molecule is emitting isotropic fluorescence. This is possible if the molecule is free to tumble within its microcavity. Such behavior would be consistent with the notion that the molecule remains solvated at the interior of a pore that is filled with ethanol–water.[24] About 48% of the molecules from the aged 4-day old sample were found to exhibit such behavior. The molecule in Figure 6B also displays a fairly constant fluorescence polarization. Unlike the previous one, however, the fluorescence polarization of this molecule stays at -0.672 ± 0.065, which deviates substantially from zero. Accordingly, the molecule was assigned as a fixed molecule, suggesting that the molecule may be adhered to a pore wall, entrapped in a very small pore that prohibits rotation, or even buried deep inside a cleft such that the molecular motion is completely restrained.[24] When fluorescence dyes are used as tracers for undergroundwater studies, it is known that adsorptions of dye on mineral surfaces due to electrostatic interactions have a negative impact on the accuracy of hydrodynamic dispersion measurements.[45–47] The same argument may apply to sol–gel silicate at neutral pH, where the negatively charged surface tends to attract cationic dye molecules. Since DiI is a cationic dye, it is therefore possible that surface adsorptions due to electrostatic interactions may contribute significantly to the immobilization of DiI inside the sol–gel silicates thin films that we studied. On the other hand, electrostatic interactions may turn out to be irrelevant to the current investigation as the sol–gel films are prepared via the acidic hydrolysis of TEOS, leaving very few anionic sites available for electrostatic interactions inside the acidic sol–gel framework. Whether electrostatic interactions are responsible for the surface immobilization of most guest molecules inside sol–gel silicates is currently being investigated by comparing the polarization distributions of cationic rhodamine 6G and anionic sulforhodamine B molecules in sol–gel silicates. The results of this investigation will be reported elsewhere.[48]

Occasionally, a molecule may behave as neither tumbling nor fixed but a combination of both. In Figure 6C, we show a molecule that oscillates many times between tumbling and various fixed orientations. This behavior is clearly distinguished from the $\bar{P}(t)$ plot, where the fluorescence polarization of this molecule is shown to vary considerably throughout the entire investigation. The $\bar{P}$ of this molecule was determined to be -0.243 ± 0.307. The substantial amount of uncertainty accompanying $\bar{P}$ reflects the dramatic variation in the fluorescence polarization of the molecule because of continuous molecular reorientation. Such kind of behavior would be consistent with a molecule that is locating at the solid–liquid interface. For instances, the molecule may adhere to the silica surface when it collides with the silica sol–gel framework, whereas the molecule may tumble freely when it is swept away from the surface.[24]

It is worth mentioning that the rapid intensity fluctuations associated with the fluorescence kinetics traces of these three types of molecules are quite comparable to each other, indicating that reorientation of the entire molecule within the silica sol–gel framework does not contribute significantly to the observed intensity fluctuations. In addition, Figure 6C also suggests that the time scale of molecular reorientation for those oscillating molecules is much longer than the time scale of the rapid intensity fluctuations. This further eliminates molecular motion as a potential source of intensity fluctuations. Exactly what causes the rapid intensity fluctuations will be a subject of future investigations.[42]

In Figure 7, we present the distribution of $\bar{P}$ determined from a total of 212 single DiI molecules. Because of the depolarization effect of a high N.A. microscope objective, a randomly oriented emission dipole with component (x,y,z) will contribute to $I_{\parallel}$ and $I_{\perp}$, according to the following equations.[49,50]

$$I_{\parallel} = I_{tot}(K_1x^2 + K_2y^2 + K_3z^2) \quad (2a)$$

$$I_{\perp} = I_{tot}(K_2x^2 + K_1y^2 + K_3z^2) \quad (2b)$$

Where the optical axis of the objective is parallel to the z-axis, I_{tot} is the total emission intensity,

$$K_1 = {}^3/_{32}(5 - 3\cos\theta_{obj} - \cos^2\theta_{obj} - \cos^3\theta_{obj}) \quad (2c)$$

$$K_2 = {}^1/_{32}(1 - 3\cos\theta_{obj} + \cos^2\theta_{obj} - \cos^3\theta_{obj}) \quad (2d)$$

$$K_3 = {}^1/_{8}(2 - 3\cos\theta_{obj} + \cos^3\theta_{obj}) \quad (2e)$$

$$\text{N.A.} = n\sin\theta_{obj} \quad (2f)$$

(44) Yip, W. T.; Hu, D. H.; Yu, J.; Vandenbout, D. A.; Barbara, P. F. *J. Phys. Chem. A* **1998**, *102*, 7564–7575.
(45) Kasnavia T.; Vu, D.; Sabatini, D. A. *Ground Water* **1999**, *37*, 376–381.
(46) Sabatini, D. A. *Ground Water* **2000**, *38*, 651–656.
(47) Ray, K.; Nakahara, H. *J. Phys. Chem. B* **2002**, *106*, 92–100.

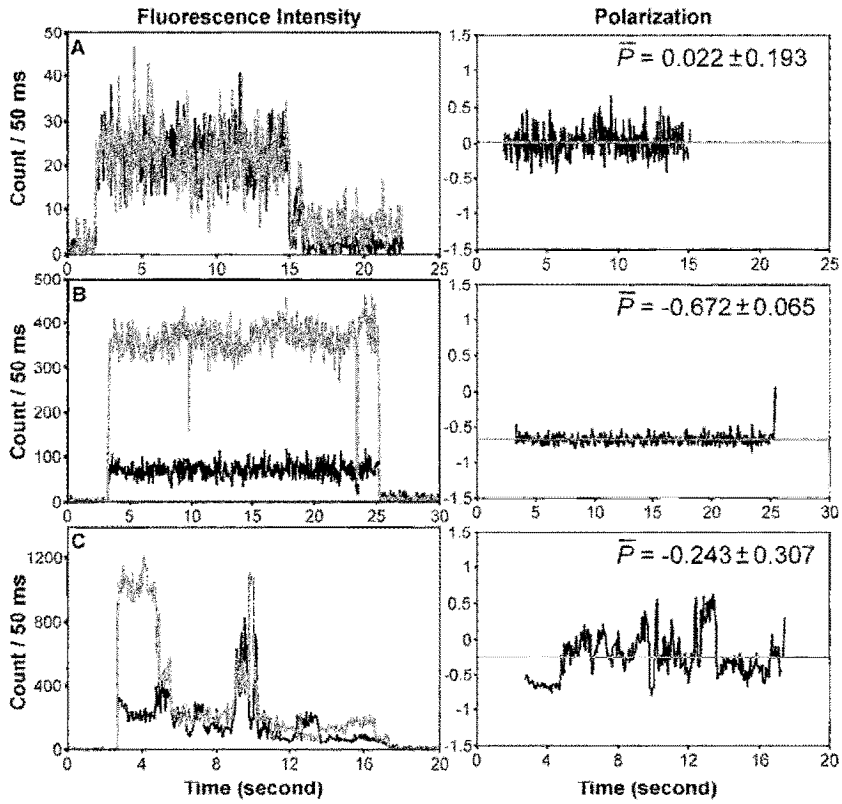

Figure 6. Fluorescence intensity and polarization of three single DiI molecules that display three different behaviors. (A) A molecule that tumbles freely with an average polarization close to zero. (B) A molecule that is completely immobilized with an average polarization equals −0.672. (C) A molecule that switches between tumbling and immobilized or between different orientations. Black and gray lines in the fluorescence traces represent $I_{\parallel}(t)$ and $I_{\perp}(t)$, respectively. The gray line in the polarization plot indicates the average polarization ($\bar{P}$) of the molecule.

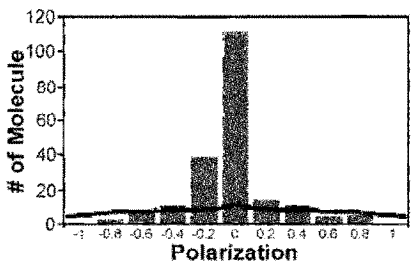

Figure 7. Histogram of $\bar{P}$. The solid line represents a theoretical fit that is based on applying eq 3 to a collection of fixed DiI molecules randomly oriented throughout the entire silica sol–gel framework.

Substituting $I_{\parallel}$ and $I_{\perp}$ in eq 1 with eqs 2a and 2b gives the polarization of the emission dipole as

$$P = \frac{(K_1 - K_2)(x^2 - y^2)}{(K_1 + K_2)(x^2 + y^2) + 2K_3 z^2} \qquad (3)$$

When N.A. is low, $K_1 \gg K_2$ and K_3, reducing eq 3 directly back to eq 1. When N.A. is high, K_2 and K_3 are no longer negligible and the polarization distribution of a collection of randomly oriented emission dipoles will skew toward zero polarization, creating a peak at the center of the distribution[51] instead of a trough that would have been predicted by eq 1 alone. For a 1.25 N.A. oil immersion microscope objective, $n = 1.52$, $\theta_{obj} = 55.32°$, $K_1 = 0.2611$, $K_2 = 0.0025$, and $K_3 = 0.0597$. The histogram in Figure 7 clearly suggests that the distribution of $\bar{P}$ does not conform to a collection of fixed DiI molecules that are randomly oriented inside a sol–gel silicate film. In fact, the very poor fit at $\bar{P}$ around zero suggests that there are more molecules exhibiting zero polarization than the depolarization effect can account for. This is a very strong indication that, in addition to fixed molecules, the sample also contains a lot of tumbling molecules, which give off isotropic fluorescence and thereby producing zero fluorescence polarization. There are altogether 101 tumbling molecules found, which account for 48% of the total number of DiI molecules we investigated. It is worth mentioning that, according to the theoretical fit, there will be about 12 fixed molecules mistakenly assigned to the group of 101 tumbling molecules. These 12% incorrectly assigned molecules have the projection of their emission dipoles on the $x-y$ plane making an angle about 45° from the x-axis.

(48) Manuscript in preparation.
(49) Axelrod, D. *Biophys. J.* **1979**, *26*, 557–573.
(50) Ha, T.; Laurence, T. A.; Chemla, D. S.; Weiss, S. *J. Phys. Chem. B* **1999**, *103*, 6839–6850.
(51) Garcia-Parajo, M. F.; Koopman, M.; van Dijk, E.; Subramaniam, V.; van Hulst, N. F. *Proc. Natl. Acad. Sci. U.S.A.* **2001**, *98*, 14392–14397.

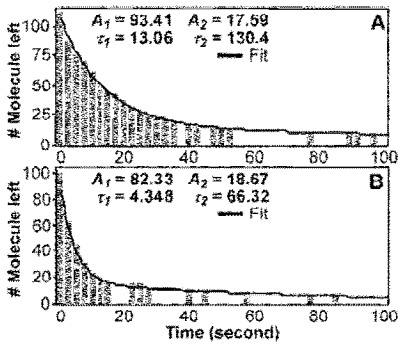

Figure 8. Survival histograms of single DiI molecules upon continuous excitation at 543.5 nm. (A) Fixed and (B) tumbling molecules. Both histograms are fitted with a biexponential decay function with the number of molecule left = $A_1 \exp(-t/\tau_1) + A_2 \exp(-t/\tau_2)$

rendering the measured polarization zero that eventually leads to the erroneous assignments.

(ii) Correlation Between Mobility and Photostability. Using the above technique, most single DiI molecules could be classified into two groups, namely "tumbling" and "fixed" molecules, with a different emphasis on the nature of their local environments, respectively. With this scheme, the effect of the local environment on the optical properties of silica sol–gel encapsulated DiI could be examined. For example, from the same set of fluorescence kinetics trace data, we could simultaneously classify the mobility and measure the photostability of every single DiI molecule. We compare in Figure 8 the histograms constructed from the photostability of the fixed and tumbling DiI molecules encapsulated in silica sol–gel films. Both histograms display biexponential decay kinetics, signifying further the heterogeneous nature of the silica sol–gel environment experienced by the molecules in each subgroup.

For the group of fixed molecules, it was expected that their optical properties would be extremely sensitive to the associated guest–host interactions, which depend critically on the nature of the point of contact upon DiI immobilization on a sol–gel silicate framework. While such kind of interactions should be highly heterogeneous, it is rather amazing to see that a biexponential decay function is sufficient to describe the photostability of the fixed molecules ($R^2 = 0.995$). Apparently, there are only a limited number of parameters that control the photostability of a fixed molecule despite the heterogeneity of its local environment. Figure 8A suggests that the survival lifetime of the majority (84%) of the 111 fixed molecules is 13.1 s. The remaining 16% of the fixed molecules exhibit a substantially higher photostability, with a survival lifetime approaching 130 s.

On the contrary, while one may expect that the photostability of the free DiI molecules would resemble DiI dissolved in ethanol and display a single exponential decay, it is truly surprising to see that a biexponential fit is required to describe the photostability of the free molecules shown in Figure 8B ($R^2 = 0.998$). Out of a total of 101 free molecules, 82 display a survival lifetime of 4.3 s. This relatively short survival lifetime accounts for 81% of the free molecules studied, with the remaining 19% exhibiting a longer survival lifetime of 66.3 s. It is unlikely that the longer-lived molecules in the biexponential decay are due to the presence of the erroneously assigned fixed molecules, as they constitute 19% of the total population instead of the 12% predicted by theory. Moreover, the survival lifetime of the majority of the fixed molecules is more than four times shorter than 66.3 s, making them an even less likely candidate for the observed longer lived molecules. It is therefore quite possible that some pores in the silica sol–gel film may be just big enough for a fully solvated molecule to tumble yet too small to leave the solvent shell of the molecule unperturbed while it is tumbling.[24,52–54] As a result, the optical properties of the free DiI may be quite different from those found in a DiI solution. At this point, the temporal resolution (50 ms) of our instrument is insufficient to distinguish the difference between hindered and truly free motions in single molecules. It is believed that time-resolved single molecule anisotropy measurements should provide additional insight into the optical properties and the nature of the local environment of this group of molecules.[55,56]

According to the histograms shown in Figure 8, our measurements suggest that the photostability of both the major and minor components of the fixed molecules is higher than the respective components of the free molecules. In particular, when only the major components are considered, our studies further indicate that the photostability of the fixed molecules is three times higher than the free molecules. This result is qualitatively consistent with previous studies on sol–gel monoliths, where an encapsulated dye usually exhibits enhanced photostability.[15,25,26] More importantly, this work establishes a direct correlation between the mobility and photostability of sol–gel encapsulated dye molecules. This level of microscopic information was previously unavailable in ensemble measurements. In addition, our enhancement factor is in remarkable agreement with the observed 4-fold increase in photostability exhibited by rhodamine B in dried silicate thin films relative to those in wet samples.[42] It is therefore very likely that when a film is dried and the solution content is completely vaporized, the dye dopants will be left immobilized on the surface of a silica sol–gel framework. Immobilization leads to the reduction of intramolecular motions, thereby reducing the number of dynamic interactions that lead to photodegradation, hence increasing photostability.

The suppression of oxygen diffusion probably plays an insignificant role in the observed improvement in photostability, since the thickness of our samples is only 363 ± 20 nm. On the other hand, the very high photostability displayed by the minor fraction (16%) of the fixed molecules is most likely due to a few molecules buried deep inside narrow clefts that are extremely difficult for oxygen gas to reach.

Conclusions

Using DiI as a fluorescence probe, the physical and optical properties of a silica sol–gel encapsulated guest molecule have been investigated with single molecule spectroscopy. Because of the capability of single molecule spectroscopy to decipher heterogeneous dynamics, this work has provided valuable insight

(52) Zheng, L. L.; Reid, W. R.; Brennan, J. D. *Anal. Chem.* **1997**, *69*, 3940–3949.
(53) Gottfried, D. S.; Kagan, A.; Hoffman, B. M.; Friedman, J. M. *J. Phys. Chem. B* **1999**, *103*, 2805–2807.
(54) Geddes, C. D.; Karolin, J.; Birch, D. J. S. *J. Phys. Chem. B* **2002**, *106*, 3835–3841.
(55) Hanns, G. S.; Sonnleitner, M.; Schutz, G. J.; Gruber, H. J.; Schmidt, T. *Biophys. J.* **1999**, *77*, 2864–2870.
(56) Schaffer, J.; Volkmer, A.; Eggeling, C.; Subramaniam, V.; Striker, G.; Seidel, C. A. M. *J. Phys. Chem. A* **1999**, *103*, 331–336.

into both the structural and chemical heterogeneity of the silica sol−gel environment. In this study, the mobility of single DiI molecules has been readily classified into tumbling and fixed, according to their respective fluorescence polarizations. The ability to separate the guest molecules into different subgroups provides a unique opportunity to examine the effect of guest−host interactions on the physical, chemical, and optical properties of each subgroup of guest molecules that are entrapped inside very different local environments. Such kind of microscopic information is critical to the rational design and fabrication of new photonic devices as well as sol−gel derived sensors and catalyst materials. Using single molecule spectroscopy to measure the mobility and photostability of silica sol−gel encapsulated DiI molecules simultaneously, the relationship between mobility and photostability has been established. It was found that DiI experiences a 3-fold increase in photostability upon immobilization, demonstrating unequivocally that hindered intramolecular motions do lead to higher photostability. It is expected that the application of this same technique to the study of other molecular properties as a function of mobility should yield further insight to the nature of the local environment surrounding a guest molecule and provide a better assessment on the impact of environmental heterogeneity on guest−host interactions within sol−gel derived materials. Finally, the very slow reorientation rate displayed by some DiI molecules that oscillate between tumbling and fixed also suggests that reorientation of the entire guest molecule does not have a significant contribution to the rapid intensity fluctuations observed in the fluorescence kinetics trace of single DiI molecules. The exact origin of the intensity fluctuations has yet to be determined.

Acknowledgment. W.T.Y. acknowledges Professor Matthew B. Johnson for performing the AFM measurement. This work was supported by the University of Oklahoma (startup funds) and the Petroleum Research Fund administered by the American Chemical Society.

JA026533K

Appendix C

Visual Basic© Data Analysis "Polarization" Macro

Attribute VB_Name = "Polarization"
'nu04 update 12/15/05
'added goto 67&68 conditions to corpaste delete cycle to eliminate deleting error for unused sheets

'nu update 11/17/05 and 11/29/05
'renamed spreadsheet name to version 4 (2Dpol_v.4)
'added paste command to detector1 sub to paste "name1" to cell H15 to provide access to the name for the histogram macro
'combined stathres and ratio subs to run sequentially off of one Excel button
'calculation of example ave and standard deviations removed when subs combined
'resizing of the graph in the stathres removed when subs combined
'changed location that threshold inputbox appears to avoid covering the graphs
'added selection command to the corrpaste sub to eliminate graph selected error
'macro version updated
'added section to corrpaste (and associated phrase in detector1 to save endrow value in cell I9) to delete unused spaces in order to reduce saved file size
'clarification notes added to corrpaste sub and isotropic sub

'Mu update 7/ 11-20 /05 James Gilliland
'spreadsheet name changed to 2Dpol_v.3 to reference modified spreadsheet
'in the detector1 sub 1 deleted the autofill of time and normalization through 2000 rows, and replaced with a logic statement to fill in the time and normalization while determining the end of the actual data.
'logic statement looks for 15 consecutive 0 values, "nulls," for both detector1 and 2 and calls that the end of the data
'the if loop also fills in the end time of the data into cell M3 automatically
'replaced references to "polarizibility" with "polarization" in program
'corpaste dialogue boxes and title altered to help clarify the input desired
'reformed background subtraction sub to combine both detector subtractions and simplify analysis by auto finding the end
'added clear step to detector1 to reduce carry over from previously loaded files
'detector1 cell selection changed to O9 to prepare for entering the background range
'corrected spelling errors

'Lambda update 5/23/05
'changed the delete of the laser spike added the last time to a replace of the rows with 0
' when loaded multiple times and the sample life time was over 200 s the delete step lead to a time mismatch

'Kappa update recorded 6/15/04 actual changes unknown
'added delete of 1st two times to cover 10^9 spike from new laser signal
'miscellaneous other changes not remembered.

'Iota version update 6/12/03
'added background sub and associated variables
'under corrpaste altered Stdev request phrase
'Changed detector1 autoselect to view chart for background choice rather than cell A2000 for editing
'update 6/16/03
'changed auto select detector to M3
'added range select O3 to background

'~10/29/03 personal updates
'changes in background times to bet fit the data
'second copy statement to make lifetime copying consistent, rather than intermittent

'Theta version update 8/22/02 James
'changed chart 3 range to include entire life time

```
'autoselect off of chart at end of Ratio sub
'version change in corrpaste

'eta version update 7/29/02
'added Name1, f, h, v, and polz as variables used
'chart naming relocated to detector1 sub from ratio sub, name taken from file name opened for detector1, return to A2000
'formula filling of polarization column taken from detector sub and placed in ratio sub to be based off of selected thresholds
'changed references in stathres sub to reference variable polz rather than cells(n,5), since that column is not filled until after thresholds are selected
'added clearing functions to Ratio sub to make sure current thresholds are graphed and old average cleared
'8/1/02 changed chart scale to 1.5 to -1.5

' Zeta version updated 7/18/02
'added print macro
'relocated std placement from Isotropic sub to import graphs sub
'auto select sheet 01 after running isotropic
'removed +/- 10 from average line of polarization chart
'replaced 2nd lifetime cells with single lifetime in stathres sub and to ratio sub
```

```
Option Base 1
Dim fileToOPen1, fileToOPen2, filename1, filename2, name1 As String
Dim l, n, b, a, d, p, inf, sup, t, f, bgs, bge, bgav1, bgav2, z, bgcone, bgctwo, last As Integer
Dim data(32000, 2)
Dim ratiodata(32000)
```

```
Sub Isotropic()
'sub used to obtain the sample isotropic value and place it on each page for use

sc = InputBox("Please, enter the polarization of the isotropic solution of the day:", "Scale Correction")
sc = Val(sc)
norm = ((1 - sc) / (1 + sc))
For n = 1 To 5
      sheet = "r0"
      sheet = sheet + Str(n)
      sheet = Left(sheet, 2) + Right(sheet, 1)
      Sheets(sheet).Select
      Cells(32, 12) = sc
      Cells(32, 14) = norm
Next n
      Sheets("r06").Select
      Cells(32, 12) = sc
      Cells(32, 14) = norm

   Sheets("r01").Select
End Sub
```

```
Sub detector1()
Attribute detector1.VB_Description = "Macro recorded 3/13/2002 by Ricardo"
Attribute detector1.VB_ProcData.VB_Invoke_Func = " \n14"

' 32000 rows of data used since that is the maximum that the graphs will do in a single series, more data can be imported, but a second series is needed to graph all of the data
```

```
Range("A2:E32000").Select
Selection.Clear

'Open file detector1
fileToOPen1 = Application _
   .GetOpenFilename("All Files (*.*), *.*")
Workbooks.Open Filename:= _
fileToOPen1

l = Len(fileToOPen1)
While Mid(fileToOPen1, l, 1) <> "\"
   l = l - 1
Wend
filename1 = Mid(fileToOPen1, l + 1, Len(fileToOPen1) - l - 1)

'chart name taken from file name
f = Len(filename1)
name1 = Mid(filename1, 1, f - 2)

'Select data from file of detector1 and paste in base file
 Windows(filename1).Activate
   Range("A1:A32000").Select
   Selection.Copy
   Windows("2Dpol v.4.xls").Activate
   Range("B2").Select
   ActiveSheet.Paste
   Range("C2").Select

   Windows(filename1).Activate
   ActiveWindow.Close
   Range("A2").Select

'Open file detector2
fileToOPen2 = Application _
   .GetOpenFilename("All Files (*.*), *.*")
Workbooks.Open Filename:= _
fileToOPen2

l = Len(fileToOPen2)
While Mid(fileToOPen2, l, 1) <> "\"
   l = l - 1
Wend
filename2 = Mid(fileToOPen2, l + 1, Len(fileToOPen2) - l - 1)

'Select data from file of detector2 and paste in base file
 Windows(filename2).Activate
   Range("A1:A32000").Select
   Selection.Copy
   Windows("2Dpol v.4.xls").Activate
   Range("D2").Select
   ActiveSheet.Paste
   Range("D2").Select
   Windows(filename2).Activate
   ActiveWindow.Close
'Fitting time
```

```
    Range("A2").Select
    ActiveCell.FormulaR1C1 = "0"
    Range("A3").Select
    ActiveCell.FormulaR1C1 = "0.05"
    Range("A4").Select
    ActiveCell.FormulaR1C1 = "0.1"

'addition of the time and normalization of detector1 while checking for the end of the data

For z = 2 To 32000
    perp = Cells(z, 2) + Cells(z + 1, 2) + Cells(z + 2, 2) + Cells(z + 3, 2) + Cells(z + 4, 2) + Cells(z + 5, 2)
+ Cells(z + 6, 2) + Cells(z + 7, 2) + Cells(z + 8, 2) + Cells(z + 9, 2) + Cells(z + 10, 2) + Cells(z + 11, 2) +
Cells(z + 12, 2) + Cells(z + 13, 2) + Cells(z + 14, 2)
    paral = Cells(z, 4) + Cells(z + 1, 4) + Cells(z + 2, 4) + Cells(z + 3, 4) + Cells(z + 4, 4) + Cells(z + 5,
4) + Cells(z + 6, 4) + Cells(z + 7, 4) + Cells(z + 8, 4) + Cells(z + 9, 4) + Cells(z + 10, 4) + Cells(z + 11, 4)
+ Cells(z + 12, 4) + Cells(z + 13, 4) + Cells(z + 14, 4)
If perp = 0 And paral = 0 Then
    endrow = z
    GoTo 42
    End If
Next z

42
    Cells(6, 9) = endrow
    Range("A2:A4").Select
    Selection.AutoFill Destination:=Range(Cells(2, 1), Cells(endrow, 1))
    Range("C2").Select
    ActiveCell.FormulaR1C1 = "=+RC[-1]*R32C14"
    Range("C2").Select
    Selection.AutoFill Destination:=Range(Cells(2, 3), Cells(endrow, 3))
    Range("A1").Select

    Cells(endrow - 1, 1).Select
    Selection.Copy
    Cells(3, 13).Select
    ActiveSheet.Paste
Cells(15, 8).Select
    Selection = name1

'renaming charts and setting options
ActiveSheet.ChartObjects("Chart 2").Activate
    ActiveChart.ChartTitle.Select
    Selection.Characters.Text = name1
    ActiveWindow.Visible = False
Windows("2Dpol v.4.xls").Activate
ActiveSheet.ChartObjects("Chart 3").Activate
    ActiveChart.ChartTitle.Select
    Selection.Characters.Text = name1
    ActiveWindow.Visible = False
Windows("2Dpol v.4.xls").Activate
Range("B2:D3").Select
    Selection = Null
Range("O9").Select

End Sub
```

```
Sub background()
'to subtract out the baseline background from each detector individually

Cells(2, 2) = Null
Cells(2, 4) = Null

'copies data to side for manipulation, provides backup for comparison before and after subtraction
Range("B1:B32000").Select
Selection.Copy
Range("Y1").Select
ActiveSheet.Paste

Range("D1:D32000").Select
Selection.Copy
Range("Z1").Select
ActiveSheet.Paste

'calculate average for two detectors over inputted range
   'detector1
bgs = Cells(10, 15)
bge = Cells(10, 14)
bgcone = 0
c = 0

For z = bgs To bge
   bgcone = bgcone + Cells(z, 25)
   c = c + 1
Next
bgav1 = bgcone / c

   'detector2
bgs = Cells(10, 15)
bge = Cells(10, 14)
bgctwo = 0
c = 0

For z = bgs To bge
   bgctwo = bgctwo + Cells(z, 26)
   c = c + 1
Next
bgav2 = bgctwo / c

'report of averages
Cells(32, 9) = bgav1
Cells(33, 9) = bgav2
last = Cells(4, 13)

Range("A1").Select
Selection.Copy

'use load detector endtime or request endtime of molecule to speed the background subtraction
   Range("M4").Select
   endrow2 = Cells(4, 13)
   If endrow2 <= 2 Then
      endtime = InputBox("Please enter the last time of the dye in seconds:", "endtime")
      endrow2 = ((endtime * 20) + 2)
```

```
    End If

'paste the equations to subtract the average background from detector1 and 2
    Range("B4").Select
    ActiveCell.FormulaR1C1 = "=+RC[23] - R32C9"
    Range("B4").Select
    Selection.AutoFill Destination:=Range(Cells(4, 2), Cells(endrow2, 2))

    Range("D4").Select
    ActiveCell.FormulaR1C1 = "=+RC[22] - R33C9"
    Range("D4").Select
    Selection.AutoFill Destination:=Range(Cells(4, 4), Cells(endrow2, 4))
    Range("A1").Select

'loop to set negatives to zero
For z = 2 To endrow2
    If Cells(z, 2) <= 0 Then
    Cells(z, 2) = 0
    End If

    If Cells(z, 4) <= 0 Then
    Cells(z, 4) = 0
    End If
Next z
Range("O3").Select
End Sub
```

```
Sub stathres()
Attribute stathres.VB_Description = "Macro recorded 3/13/2002 by Ricardo"
Attribute stathres.VB_ProcData.VB_Invoke_Func = " \n14"

Cells(31, 8) = Cells(3, 16)
'detector1
af = Cells(6, 14)
be = Cells(6, 15)
counts = 0
For p = be To af
    counts = counts + Cells(p, 3)
Next
Cells(32, 8) = counts
Cells(6, 16) = counts

'detector2
af = Cells(6, 14)
be = Cells(6, 15)
counts = 0
For p = be To af
    counts = counts + Cells(p, 4)
Next
Cells(33, 8) = counts
Cells(13, 16) = counts

'Ratio (detector1/detector2) average and stdev
If Cells(31, 8) >= t Then 'time alive detector1 > time alive detector2
    inf = Cells(6, 15): sup = Cells(6, 14) 'limits given by time alive from data of detector1
    Else
```

```
    inf = Cells(10, 15): sup = Cells(10, 14) 'limits given by time alive from data of detector2
  End If

  ActiveSheet.Select
  Cells(33, 13).Select

  'start of originally separate RATIO sub function
  'inputting molecule name and desired threshold values
  th1 = InputBox("Please, enter the threshold value that you want to apply to detector1 signal:",
"Threshold (horizontal)", , 100, 200)
  th2 = InputBox("Please, enter the threshold value that you want to apply to detector2 signal:",
"Threshold (vertical)", , 100, 200)
  th1 = Val(th1)
  Cells(33, 13) = th1
  th2 = Val(th2)
  Cells(33, 14) = th2

  'detector1
  af = Cells(6, 14)
  be = Cells(6, 15)
  counts = 0
  For p = be To af
    counts = counts + Cells(p, 3)
  Next
  Cells(32, 8) = counts
  Cells(6, 16) = counts

  'detector2
  af = Cells(6, 14)
  be = Cells(6, 15)
  counts = 0
  For p = be To af
    counts = counts + Cells(p, 4)
  Next
  Cells(33, 8) = counts
  Cells(13, 16) = counts

  'clears polarization column and average
  Range("E2").Select
  ActiveCell.FormulaR1C1 = Null
  Selection.AutoFill Destination:=Range("E2:E32000")

  Range("R2").Select
  ActiveCell.FormulaR1C1 = Null
  Selection.AutoFill Destination:=Range("R2:R32000")

  Range("F2").Select

  'polarization (detector1/detector2) average and stdev
  If Cells(31, 8) >= t Then 'time alive detector1 > time alive detector2
    inf = Cells(6, 15): sup = Cells(6, 14) 'limits given by time alive from data of detector1
    Else
    inf = Cells(10, 15): sup = Cells(10, 14) 'limits given by time alive from data of detector2
  End If
  c = 0 'average
  S = 0
```

```
For n = inf To sup
   If Cells(n, 3) > th1 And Cells(n, 4) > th2 Then
      Cells(n, 5) = "=(RC[-2]-RC[-1])/(RC[-2]+RC[-1])"
      c = c + 1
      S = S + Cells(n, 5)
      ratiodata(c) = Cells(n, 5)
   End If
Next n
avg = S / c
Cells(32, 11) = avg
k = 0 'stdev
For J = 1 To c
   k = k + (ratiodata(J) - avg) ^ 2
Next J

std = (k / c) ^ (1 / 2)
Cells(33, 11) = std

'adding average line to chart 3
af = Cells(6, 14)
be = Cells(6, 15)
counts = 0
For p = be To af
   Cells(p, 18) = avg
Next

'Improving the x-axis and y-axis scale of the plot polarization vs. time
ActiveSheet.ChartObjects("Chart 3").Activate
ActiveChart.Axes(xlCategory).Select
With ActiveChart.Axes(xlCategory)
   .MinimumScale = (inf - 2) / 20
   .MaximumScale = sup / 20
   .MinorUnitIsAuto = True
   .MajorUnitIsAuto = True
   .Crosses = xlAutomatic
   .ReversePlotOrder = False
   .ScaleType = xlLinear
   .DisplayUnit = xlNone
End With
ActiveSheet.ChartObjects("Chart 3").Activate
ActiveChart.Axes(xlCategory).Select
With ActiveChart.Axes(xlValue)
   .MinimumScale = -1.5
   .MaximumScale = 1.5
   .MinorUnitIsAuto = True
   .MajorUnitIsAuto = True
   .Crosses = xlCustom
   .CrossesAt = -1.5
   .ReversePlotOrder = False
   .ScaleType = xlLinear
   .DisplayUnit = xlNone

ActiveWindow.Visible = False
Windows("2Dpol v.4.xls").Activate
Range("N11").Select
End With
```

```
End
End Sub
```

```
Sub corrpaste()
Dim n As Integer
Dim title, day, sc, sheet As String

'loading of sample identification (name and age) and value to be used for molecule classification
dye = InputBox("Please enter the sample name:", "dye")
day = InputBox("Please, enter the sample age in days:", "Aging Time")

stdiso = InputBox("Please, enter the standard deviation you desire to use for classification as tumbling:",
"Classifying the molecules")
title = " "
title = dye + title + day + " day old samples"
Cells(1, 1) = title
Cells(52, 1) = title
Cells(1, 7) = "nu"
Cells(52, 7) = "nu"
stdiso = Val(stdiso)

'selection algorithm to make sure charts are not selected to remove chart selected error message

For n = 1 To 5
    sheet = "r0"
    sheet = sheet + Str(n)
    sheet = Left(sheet, 2) + Right(sheet, 1)
    Sheets(sheet).Select
    ActiveWindow.Visible = False
    Windows("2Dpol v.4.xls").Activate
    Range("N32").Select
    Cells(32, 13) = stdiso

Next n
    Sheets("r06").Select
    ActiveWindow.Visible = False
    Windows("2Dpol v.4.xls").Activate
    Range("N32").Select
    Cells(32, 13) = stdiso

'molecule classification algorithm based on polarization only

For n = 1 To 5
    sheet = "r0"
    sheet = sheet + Str(n)
    sheet = Left(sheet, 2) + Right(sheet, 1)
    Sheets(sheet).Select

    If Cells(32, 11) < (stdiso * (-1)) Or Cells(32, 11) > (stdiso) Then
      Cells(31, 9) = "FIXED"
      Else
      Cells(31, 9) = "TUMBLING"
    End If

Next n
```

```
    Sheets("r06").Select

    If Cells(32, 11) < (stdiso * (-1)) Or Cells(32, 11) > (stdiso) Then
       Cells(31, 9) = "FIXED"
       Else
       Cells(31, 9) = "TUMBLING"
    End If

'Paste Process to transfer the desired data from the individual pages to the prints page
'sheet 1

Sheets("r01").Select
   ActiveSheet.ChartObjects("Chart 2").Activate
   ActiveChart.ChartArea.Select
   ActiveChart.ChartArea.Copy
   ActiveWindow.Visible = False
   Windows("2Dpol v.4.xls").Activate
   Sheets("Print").Select
   ActiveSheet.ChartObjects("Chart 21").Activate
   ActiveChart.ChartArea.Select
   ActiveChart.Paste
   ActiveWindow.Visible = False
   Windows("2Dpol v.4.xls").Activate
   Sheets("r01").Select
   ActiveSheet.ChartObjects("Chart 2").Activate
   ActiveWindow.Visible = False
   Windows("2Dpol v.4.xls").Activate
   ActiveSheet.ChartObjects("Chart 3").Activate
   ActiveChart.ChartArea.Select
   ActiveChart.ChartArea.Copy
   ActiveWindow.Visible = False
   Windows("2Dpol v.4.xls").Activate
   Sheets("Print").Select
   ActiveSheet.ChartObjects("Chart 21").Activate
   ActiveWindow.Visible = False
   Windows("2Dpol v.4.xls").Activate
   ActiveSheet.ChartObjects("Chart 22").Activate
   ActiveChart.ChartArea.Select
   ActiveChart.Paste
   ActiveWindow.Visible = False
   Windows("2Dpol v.4.xls").Activate
   Sheets("r01").Select
   ActiveSheet.ChartObjects("Chart 3").Activate
   ActiveWindow.Visible = False
   Windows("2Dpol v.4.xls").Activate
   Range("G31:I33").Select
   Selection.Copy
   Sheets("Print").Select
   ActiveSheet.ChartObjects("Chart 22").Activate
   ActiveWindow.Visible = False
   Windows("2Dpol v.4.xls").Activate
   Range("A14").Select
   ActiveSheet.Paste
   Sheets("r01").Select
   Range("J31:N33").Select
   Application.CutCopyMode = False
   Selection.Copy
   Sheets("Print").Select
   Range("G14").Select
   ActiveSheet.Paste
'sheet 2
   Sheets("r02").Select
   ActiveSheet.ChartObjects("Chart 3").Activate
   ActiveWindow.Visible = False
   Windows("2Dpol v.4.xls").Activate
   ActiveSheet.ChartObjects("Chart 2").Activate
   ActiveChart.ChartArea.Select
   Application.CutCopyMode = False
   ActiveChart.ChartArea.Copy
   ActiveWindow.Visible = False
   Windows("2Dpol v.4.xls").Activate
   Sheets("Print").Select
   ActiveSheet.ChartObjects("Chart 23").Activate
   ActiveChart.ChartArea.Select
   ActiveChart.Paste
   ActiveWindow.Visible = False
   Windows("2Dpol v.4.xls").Activate
   Sheets("r02").Select
   ActiveSheet.ChartObjects("Chart 2").Activate
   ActiveWindow.Visible = False
   Windows("2Dpol v.4.xls").Activate
   ActiveSheet.ChartObjects("Chart 3").Activate
   ActiveChart.ChartArea.Select
   ActiveChart.ChartArea.Copy
   ActiveWindow.Visible = False
   Windows("2Dpol v.4.xls").Activate
   Sheets("Print").Select
   ActiveSheet.ChartObjects("Chart 23").Activate
   ActiveWindow.Visible = False
   Windows("2Dpol v.4.xls").Activate
   ActiveSheet.ChartObjects("Chart 14").Activate
   ActiveChart.ChartArea.Select
   ActiveChart.Paste
   ActiveWindow.Visible = False
   Windows("2Dpol v.4.xls").Activate
   Sheets("r02").Select
   ActiveSheet.ChartObjects("Chart 3").Activate
   ActiveWindow.Visible = False
   Windows("2Dpol v.4.xls").Activate
   Range("G31:I33").Select
   Selection.Copy
```

```
    Sheets("Print").Select
    ActiveSheet.ChartObjects("Chart 14").Activate
    ActiveWindow.Visible = False
    Windows("2Dpol v.4.xls").Activate
    Range("A31").Select
    ActiveSheet.Paste
    Sheets("r02").Select
    Range("J31:N33").Select
    Application.CutCopyMode = False
    Selection.Copy
    Sheets("Print").Select
    Range("G31").Select
    ActiveSheet.Paste
'sheet 3
    Sheets("r03").Select
    ActiveSheet.ChartObjects("Chart 3").Activate
    ActiveWindow.Visible = False
    Windows("2Dpol v.4.xls").Activate
    ActiveSheet.ChartObjects("Chart 2").Activate
    ActiveChart.ChartArea.Select
    Application.CutCopyMode = False
    ActiveChart.ChartArea.Copy
    ActiveWindow.Visible = False
    Windows("2Dpol v.4.xls").Activate
    Sheets("Print").Select
    ActiveWindow.SmallScroll Down:=21
    ActiveSheet.ChartObjects("Chart 15").Activate
    ActiveChart.ChartArea.Select
    ActiveChart.Paste
    ActiveWindow.Visible = False
    Windows("2Dpol v.4.xls").Activate
    Sheets("r03").Select
    ActiveSheet.ChartObjects("Chart 2").Activate
    ActiveWindow.Visible = False
    Windows("2Dpol v.4.xls").Activate
    ActiveSheet.ChartObjects("Chart 3").Activate
    ActiveChart.ChartArea.Select
    ActiveChart.ChartArea.Copy
    ActiveWindow.Visible = False
    Windows("2Dpol v.4.xls").Activate
    Sheets("Print").Select
    ActiveSheet.ChartObjects("Chart 15").Activate
    ActiveWindow.Visible = False
    Windows("2Dpol v.4.xls").Activate
    ActiveSheet.ChartObjects("Chart 16").Activate
    ActiveChart.ChartArea.Select
    ActiveChart.Paste
    ActiveWindow.Visible = False
    Windows("2Dpol v.4.xls").Activate
    Sheets("r03").Select
    ActiveSheet.ChartObjects("Chart 3").Activate
    ActiveWindow.Visible = False
    Windows("2Dpol v.4.xls").Activate
    Range("G31:I33").Select
    Selection.Copy
    Sheets("Print").Select
    ActiveSheet.ChartObjects("Chart 16").Activate
    ActiveWindow.Visible = False
    Windows("2Dpol v.4.xls").Activate
    Range("A48").Select
    ActiveSheet.Paste
    Sheets("r03").Select
    Range("J31:N33").Select
    Application.CutCopyMode = False
    Selection.Copy
    Sheets("Print").Select
    Range("G48").Select
    ActiveSheet.Paste
    ActiveWindow.SmallScroll Down:=24
'sheet 4
    Sheets("r04").Select
    ActiveSheet.ChartObjects("Chart 3").Activate
    ActiveWindow.Visible = False
    Windows("2Dpol v.4.xls").Activate
    ActiveSheet.ChartObjects("Chart 2").Activate
    ActiveChart.ChartArea.Select
    Application.CutCopyMode = False
    ActiveChart.ChartArea.Copy
    ActiveWindow.Visible = False
    Windows("2Dpol v.4.xls").Activate
    Sheets("Print").Select
    ActiveSheet.ChartObjects("Chart 17").Activate
    ActiveChart.ChartArea.Select
    ActiveChart.Paste
    ActiveWindow.Visible = False
    Windows("2Dpol v.4.xls").Activate
    Sheets("r04").Select
    ActiveSheet.ChartObjects("Chart 2").Activate
    ActiveWindow.Visible = False
    Windows("2Dpol v.4.xls").Activate
    ActiveSheet.ChartObjects("Chart 3").Activate
    ActiveChart.ChartArea.Select
    ActiveChart.ChartArea.Copy
    ActiveWindow.Visible = False
    Windows("2Dpol v.4.xls").Activate
    Sheets("Print").Select
    ActiveSheet.ChartObjects("Chart 17").Activate
    ActiveWindow.Visible = False
    Windows("2Dpol v.4.xls").Activate
    ActiveSheet.ChartObjects("Chart 18").Activate
    ActiveChart.ChartArea.Select
    ActiveChart.Paste
    Windows("2Dpol v.4.xls").SmallScroll
Down:=-12
    ActiveWindow.Visible = False
    Windows("2Dpol v.4.xls").Activate
    Sheets("r04").Select
    ActiveSheet.ChartObjects("Chart 3").Activate
    ActiveWindow.Visible = False
    Windows("2Dpol v.4.xls").Activate
    Range("G31:I33").Select
    Selection.Copy
```

```
    Sheets("Print").Select
    ActiveSheet.ChartObjects("Chart 18").Activate
    ActiveWindow.Visible = False
    Windows("2Dpol v.4.xls").Activate
    Range("A66").Select
    ActiveSheet.Paste
    Sheets("r04").Select
    Range("J31:N33").Select
    Application.CutCopyMode = False
    Selection.Copy
    Sheets("Print").Select
    Range("G66").Select
    ActiveSheet.Paste
'sheet 5
    Sheets("r05").Select
    ActiveSheet.ChartObjects("Chart 2").Activate
    ActiveChart.ChartArea.Select
    Application.CutCopyMode = False
    ActiveChart.ChartArea.Copy
    ActiveWindow.Visible = False
    Windows("2Dpol v.4.xls").Activate
    Sheets("Print").Select
    ActiveWindow.SmallScroll Down:=6
    ActiveSheet.ChartObjects("Chart 19").Activate
    ActiveChart.ChartArea.Select
    ActiveChart.Paste
    ActiveWindow.Visible = False
    Windows("2Dpol v.4.xls").Activate
    Sheets("r05").Select
    ActiveSheet.ChartObjects("Chart 2").Activate
    ActiveWindow.Visible = False
    Windows("2Dpol v.4.xls").Activate
    ActiveSheet.ChartObjects("Chart 3").Activate
    ActiveChart.ChartArea.Select
    ActiveChart.ChartArea.Copy
    ActiveWindow.Visible = False
    Windows("2Dpol v.4.xls").Activate
    Sheets("Print").Select
    ActiveSheet.ChartObjects("Chart 19").Activate
    ActiveWindow.Visible = False
    Windows("2Dpol v.4.xls").Activate
    ActiveSheet.ChartObjects("Chart 20").Activate
    ActiveChart.ChartArea.Select
    ActiveChart.Paste
    ActiveWindow.Visible = False
    Windows("2Dpol v.4.xls").Activate
    Sheets("r05").Select
    ActiveSheet.ChartObjects("Chart 3").Activate
    ActiveWindow.Visible = False
    Windows("2Dpol v.4.xls").Activate
    Range("G31:I33").Select
    Selection.Copy
    Sheets("Print").Select
    ActiveSheet.ChartObjects("Chart 20").Activate
    ActiveWindow.Visible = False
    Windows("2Dpol v.4.xls").Activate
    Range("A83").Select
    ActiveSheet.Paste
    Sheets("r05").Select
    Range("J31:N33").Select
    Application.CutCopyMode = False
    Selection.Copy
    Sheets("Print").Select
    Range("G83").Select
    ActiveSheet.Paste
    ActiveWindow.SmallScroll Down:=36
'sheet 6
    Sheets("r06").Select
    ActiveSheet.ChartObjects("Chart 3").Activate
    ActiveWindow.Visible = False
    Windows("2Dpol v.4.xls").Activate
    ActiveSheet.ChartObjects("Chart 2").Activate
    ActiveChart.ChartArea.Select
    Application.CutCopyMode = False
    ActiveChart.ChartArea.Copy
    ActiveWindow.Visible = False
    Windows("2Dpol v.4.xls").Activate
    Sheets("Print").Select
    ActiveSheet.ChartObjects("Chart 25").Activate
    ActiveChart.ChartArea.Select
    ActiveChart.Paste
    ActiveWindow.Visible = False
    Windows("2Dpol v.4.xls").Activate
    Sheets("r06").Select
    ActiveSheet.ChartObjects("Chart 2").Activate
    ActiveWindow.Visible = False
    Windows("2Dpol v.4.xls").Activate
    ActiveSheet.ChartObjects("Chart 3").Activate
    ActiveChart.ChartArea.Select
    ActiveChart.ChartArea.Copy
    ActiveWindow.Visible = False
    Windows("2Dpol v.4.xls").Activate
    Sheets("Print").Select
    ActiveSheet.ChartObjects("Chart 25").Activate
    ActiveWindow.Visible = False
    Windows("2Dpol v.4.xls").Activate
    ActiveSheet.ChartObjects("Chart 26").Activate
    ActiveChart.ChartArea.Select
    ActiveChart.Paste
    ActiveWindow.Visible = False
    Windows("2Dpol v.4.xls").Activate
    Sheets("r06").Select
    ActiveSheet.ChartObjects("Chart 3").Activate
    ActiveWindow.Visible = False
    Windows("2Dpol v.4.xls").Activate
    Range("G31:I33").Select
    Selection.Copy
    Sheets("Print").Select
    ActiveSheet.ChartObjects("Chart 26").Activate
    ActiveWindow.Visible = False
    Windows("2Dpol v.4.xls").Activate
    Range("A100").Select
```

```
    ActiveSheet.Paste                                   Sheets("Print").Select
    Sheets("r06").Select                                Range("G100").Select
    Range("J31:N33").Select                             ActiveSheet.Paste
    Application.CutCopyMode = False                     Range("A1").Select
    Selection.Copy

  ' Delete cycle to refresh empty cells and reduce the saved file size.  For some reason Excel likes to save files with "no value present" placeholders that increase the file size.
  ' This is especially the case when transferring empty cells during the load detectors sub, adjacent cells and other cells on screen are also filled these placeholder values.
  For n = 1 To 5
        sheet = "r0"
        sheet = sheet + Str(n)
        sheet = Left(sheet, 2) + Right(sheet, 1)
        Sheets(sheet).Select
        rowdelstart = Cells(6, 9)
        If rowdelstart = Empty Then GoTo 67
        Range("F34:Q2000").Select
        Selection.delete Shift:=xlUp

        Range(Cells(rowdelstart, 1), Cells(32000, 26)).Select
        Selection.delete Shift:=xlUp
        Range("A1").Select
  67
  Next n

        Sheets("r06").Select
        rowdelstart = Cells(6, 9)
        If rowdelstart = Empty Then GoTo 68

        Range("F34:Q2000").Select
        Selection.delete Shift:=xlUp

        Range(Cells(rowdelstart, 1), Cells(32000, 26)).Select
        Selection.delete Shift:=xlUp
        Range("A1").Select

  68
        Sheets("Print").Select
        Range("L21:T102").Select
        Selection.delete Shift:=xlUp
        Range("A1").Select

  End Sub
```

```
  Sub prints()
  ' prints Macro
  ' Macro recorded 7/18/2002 by  Yip Lab


     ActiveWindow.SelectedSheets.PrintOut From:=1, To:=2, Copies:=1, Collate _
        :=True
  End Sub
```

Appendix D

Abbreviations

σ_{iso}	emission polarization standard deviation obtained from an isotropic solution
ϕ_b	photobleaching quantum yield
ϕ_f	fluorescence quantum yield
τ	survival lifetime before photobleaching
$\langle\phi_b\rangle$	average photobleaching quantum yield
$\langle\tau\rangle$	average survival lifetime
AFM	Atomic Force Microscopy
APD	avalanche photodiode
APS	3-aminopropyl-trimethoxysilane
CCD	charge-coupled detector
CN^-	cyanide solution
$DiIC_{12}$	Didodecyl-3,3,3',3'-tetramethylindo-carbocyanine
EPR	electron paramagnetic resonance
EtOH	ethanol
$F(t)$	molecule fraction remaining fluorescent
f_{A-}	fraction of dye in the deprotonated state
f_{HA}	fraction of dye in the protonated state
G	polarization scaling factor
GNP	gold nanoparticle
H_2O	water
$HAuCl_4$	hydrogen tetrachloroaurate (III)
HEPES	2-[4-(2-Hydroxyethyl)-1-piperazine]ethanesulfonic acid
HRP	horseradish peroxidase
$I_{\perp}(t)$	polarized fluorescence intensity - perpendicular
I_{A-}	maximum deprotonated state intensity
I_{HA}	maximum protonated state intensity

$I_{//}(t)$	polarized fluorescence intensity - parallel
N.A.	numerical aperture
NMR	nuclear magnetic resonance
NR	Nile Red
OD	Optical Density
ORG	Oregon Green 514
ORMOSIL	Organically Modified Silane
$P(t)$	emission polarization
$\overline{P}$	statistical emission polarization average
R6G	rhodamine 6G
R6G/SNP	R6G doped in SNP
S_0	singlet ground electronic state
S_1	singlet first excited electronic state
SNP	silica nanoparticle
SRB	sulforhodamine B
T_1	triplet first excited electronic state
TEM	Transmission Electron Microscopy
TEOS	tetraethyl orthosilicate
TES	triethoxy silane
TIR	total internal refraction
TMOS	tetramethyl orthosilicate
TRIS-HCl	Tris (Hydroxymethyl) Aminomethane - Hydrogen Chloride
TRITC	tetramethylrhodamine-5-isothiocyanate
TRITC/SNP	TRITC doped in silica nanoparticle
TRITC-APS-SNP	TRITC covalently bonded to silica nanoparticle with 3-aminopropyl-trimethoxysilane